SYNTHESIS AND CHARACTERIZATION OF HIGH ASPECT RATIO RHODIUM NANOSTRUCTURES

A THESIS SUBMITTED TO THE

UNIVERSITY OF PUNE

FOR THE DEGREE OF DOCTOR OF PHILOSOPHY

IN

CHEMISTRY

By

BHASKAR R. SATHE

Dr. VIJAYAMOHANAN K. PILLAI

(Research Guide)

PHYSICAL AND MATERIALS CHEMISTRY DIVISION

NATIONAL CHEMICAL LABORATORY

PUNE – 411 008

INDIA

December 2010

Dedicated To

My Late

Grandfather….

DECLARATION

I, hereby declare that all the experiments embodied in this thesis entitled, **"SYNTHESIS AND CHARACTERIZATION OF HIGH ASPECT RATIO RHODIUM NANOSTRUCTURES",** submitted for the degree of Doctor of Philosophy in Chemistry, to the University of Pune have been carried out by me at the Physical and Materials Chemistry Division, National Chemical Laboratory, Pune, 411 008, India, under the supervision of Dr. Vijayamohanan K. Pillai. The work is original and has not been submitted in part or full by me, for any degree or diploma to this or to any other University.

Date: **BHASKAR RAMCHANDRA SATHE**

Physical and Materials Chemistry Division
National Chemical Laboratory
Pune – 411 008

Dr. Vijayamohanan K. Pillai
Scientist-H

Physical and Materials
Chemistry Division
National Chemical Laboratory
Pune – 411 008
INDIA

Tel: 91-020-2590 2588
Res: 91-020-2587 0307
Fax: 91-020-2590 2636
Email: vk.pillai@ncl.res.in

CERTIFICATE

This is to certify that the work incorporated in the thesis entitled, "**SYNTHESIS AND CHARACTERIZATION OF HIGH ASPECT RATIO RHODIUM NANOSTRUCTURES**", submitted by **Mr. Bhaskar Ramchandra Sathe,** has been carried out by him under my supervision at the Physical and Materials Chemistry Division, National Chemical Laboratory, Pune, 411 008, India. All the materials from other sources have been duly acknowledged in the thesis.

Research Guide
(Vijayamohanan K. Pillai)

Date :
Place : Pune

Acknowledgements

There are so many people, whose support, encouragement & inspiration are very much essential to accomplish major achievements in life, especially, if it involves the elements of fulfilling one's cherished dreams. For me, this thesis is such an important destiny & I am indeed, indebted to a lot of people for their well wishes & blessings, for completing this journey.

I would like to take this opportunity first, to pay my sincere admiration to Dr. K. Vijayamohanan, whose motivation, inspiration, encouragement & persistent guidance have lead me to bring my dream to reality. His knowledge is like an ever-expanding encyclopedia, which has all possible solutions to help me out of any problem. I must also mention that he is also a very good teacher & a wonderful research guide, which is often quite rare. His constant effort to imbue us with several, most essential habits, like weekly seminars & group meetings, monthly reports & daily planning, makes me confident to start an independent scientific carrier. He is also instrumental in teaching us to effectively communicate with people, to give a better presentation, to efficiently handle multitasking simultaneously and so on. My sincere regards and reverence are for him, forever. I also extend my sincere appreciation to Mrs. Manju for her motherly care, blessing & constant support. I would also like to offer my sincere admiration to Dr. I. S. Mulla for all his help, support, suggestion & advice during the course of this study.

I wish to thank Dr. S. Pal, Director (formal Head of Physical & Materials Chemistry Division) NCL, for providing me all the infrastructural facilities & for his constant encouragement. At this moment, I also would like to extend my sincere thanks to my former and present teachers, Profs. R. A. Mane, M. S. Shingare, T. K. Chondhekar, B. R. Arbad, V. G. Dongare (late), S. P. Korekar, A. S. Shitre, N. B. Jadav & H. Z. Jadhav for their gracious love, belief as they had built the foundation for this achievement. A special thanks to our collaborators, Drs. M. Aslam, D. Joag, M. A. More, M. K. Dongare & S. Umbarkar for their precious help & valuable discussions.

My heartfelt gratitude to Drs. Anil Kumar, P. A. Joy, S. B. Ogale, P. P. Wadgaonkar, Rahul Banerjee, Ashok Giri, B.L.V. Prasad, P. Poddar, V. Ravi, K. Sreekumar, M. Shelke & P. K. Ingale for their advice & help. I am highly indebted to Mr. A. B. Gaikwad, Dr. K. R. Patil, Mr. Gholap, Gajanan, Ketan & Naren for helping me a lot in characterising my samples. I also deeply acknowledge the appreciable help from Mr. Dipak & Mr. Punekar & the entire library staff for excellent facilities. Further, UGC & CSIR are gratefully acknowledged for the financial support.

I can never forget the help from my seniors, Drs. Jadabji, Nirmal, Trupti, Niranjan, Deepali & Meera for their mentoring & care during my initial research days. I would like to specially thank Dr. Bhalchandra (Dada) & Dr. Mahima (Chechi) for their constant encouragement & always being with me in all sorts of situations during my stay in NCL. I can never forget the special support, love & care with constant encouragement extended to me by Beena (Chottu) during the course of this work. My sincere thanks to Vinu & Dhanu for their love, support and timely help. My sincere thanks to the members of glassblowing, stores, purchase, workshop & security for their help during my stay in NCL.

A special thanks to all my labmates Kannan, Kuttan, Vivek, Sanjay, Pravin, Dhanraj, Mrudula, Joyashish, Ashivini, Bipin, Nilesh, Hussain, Ramireddy, Palani, Vinisha, Ranjeet & Vishal, who have helped me in all possible ways & have been my extended family during the tenure of my work at NCL. I wish to extend my thanks to my project students Kuttan & Viru for their love, constant efforts & enthusiasm.

I would also like to express my sincere thanks to all my divisional colleagues Nagesh, Mangesh, Pankaj, Vijay, Sanju, Shekhar, Sankar, Shraedha, Gitanjali, Sarita, Shabana, Lenin, Deepti, Sanjay, Manashi, Sudarshan, Priyanka, Vivek, Subhas, Vijay, Sreeja,Umesh & Khaja. I also extend my thanks to several other friends in NCL, Bapu, Arun, Ravi, Kishor, Rahul, Seema, Manoj, Vishal, Sandeep, Deu, Aaba, Ganesh, Prakash, Aaba, Satish, Suleman, Manmath, Dipak, Amit, Sumantra, Atul, Panchami, Sony, Smitha, Mehraj, Sambhji, Shared, Mahesh, Nagendra, Prakash, Satish, Dipak, Ankush, Nazrul, Vaibhav, Prasad & Pankaj. I have to express all my wholeheartedly gratitude to my dearest friends, Ad. Nilkhant, Rameshwar (Guru-mauli), Aaba, Sudhir, Sandeep, Nanasaheb, Sunder, Suresh, Rajiv, Om, Mahadhav, Surendra and Tukaraom without whose constant support and inspiration this would never have been possible. I also extend my special thanks to my collaborators Ankush, Ajay and Datta for their valuable help & support.

As always, it is impossible to mention everybody who had an impact on this work although there are those whose spiritual support is even more important. I find no words to express my feelings for my parents, Aai and Anna whose moral support, love & constant encouragement have helped me to complete this journey. This thesis is also a dream for my elder brother 'Madhukar' and Vaini 'Vaishali' whose support has always played a key role in my career. I wish to express my gratitude to my beloved younger brother 'Subhash', who has always inspired me at every stage of life & my studies as well. The presence of the little angels 'Aniket' & 'Abhijit' is always refreshing, making me feel relaxed, comfortable and which provides me energy to work. I wish to extend my sincere gratitude to my grandfather & all other relatives for their blessings & love. Finally, a very special appreciation is due to my fiancé Jyoti not only for her constant encouragement but also for her patience & understanding throughout.

Bhaskar Ramchandra Sathe

Table of Contents

Chapter 1

Chapter 2

Chapter 3

Chapter 4

Chapter 5

List of Abbreviations

Abbreviation	Expansion
ac	Alternating Current
AFM	Atomic Force Microscope
BE	Binding Energy
bcc	Body Centered Cubic
BET	Brunauer Emmett Teller
CA	Contact Angle
CNT	Carbon Nanotube
CV	Cyclic Voltammetry
CVD	Chemical Vapor Deposition
J	Current Density
Dc	Direct Current
DCM	Dichloromethane
DFT	Density Functional Theory
DRIFT	Diffused Reflectance Infrared Fourier Transform
DOS	Density of States
DPV	Differential Pulse Voltammetry
DSC	Differential Scanning Calorimetry
DT	Differential Thermogravimetry
EDX or EDS	Energy Dispersive X-Ray Spectroscopy
ESCA	Electron Scanning for Chemical analysis
ET	Electron Transfer
fcc	Faced Centered Cubic
FEG	Field Emission Gun
FESEM	Field Emission Scanning Electron Microscopy
FET	Field-Effect Transistors
FFT	Fast Fourier Transform
FRA	Frequency Response Analyzer
FTIR	Fourier Transform Infrared

FWHM	Full Width at Half Maximum
HOMO	Highest Occupied Molecular Orbital
HRTEM	High-Resolution Transmission Electron Microscopy
LSV	Linear Sweep Voltammetry
LUMO	Lowest Unoccupied Molecular Orbital
MEMS/NEMS	Micro/Nano-Electromechanical Systems
MPCs	Monolayer Protected Nanoclusters
MW	Microwave
MWCNTs	Multi-Walled Carbon Nanotubes
NMR	Nuclear Magnetic Resonance
1-D	One-Dimensional
QDL	Quantized Double Layer Charging
Q-dots	Quantum Dots
RBM	Radial Breathing Mode
SAED	Selected Area Electron Diffraction
SAM	Self-Assembled Monolayer
SCCM	Standard Cubic Centimeter per Minute
SECM	Scanning Electrochemical Microscopy
SWCNTs	Single Walled Carbon Nanotubes
SET	Single-Electron Transistors / Transfer
SMSI	Strong-Metal Support Interaction
SPR	Surface Plasmon Resonance
STM	Scanning Tunneling Microscope
STS	Scanning Tunneling Spectroscopy
TEC	Temperature Expansion Coefficient
TEM	Transmission Electron Microscopy
TG	Thermogravimetry
2-D	Two-Dimensional
3-D	Three-Dimensional
TOF	Turn Over Frequency
TON	Turn Over Number

TTO	Total Turn Over
UV	Ultra-Violet
Uv-vis	Ultra-Violet-Visible
Uv-vis-NIR	Ultra-Violet-Visible- Near infrared
VB	Valence Band
VLS	Vapor-Liquid-Solid
XPS	X-ray Photoelectron Spectroscopy
XRD	X-ray Diffraction
0-D	Zero-Dimensional

CHAPTER 1

Rhodium Nanostructures: A Critical Survey

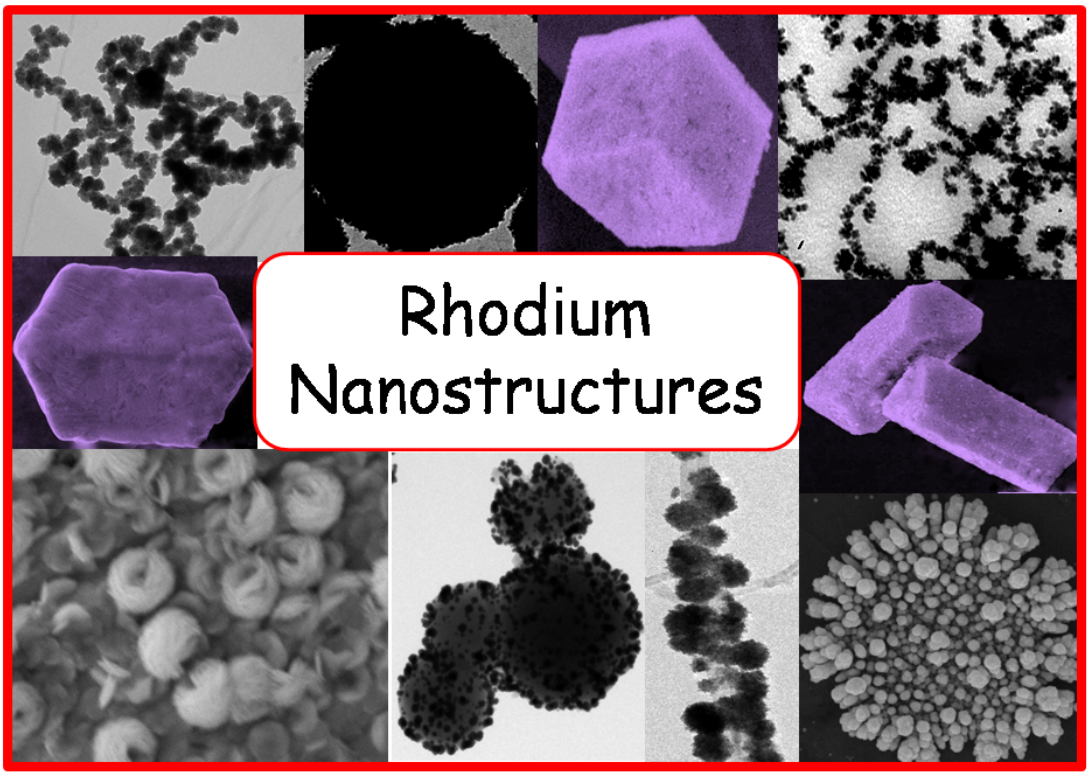

This chapter provides a comprehensive review of the current research activities on high aspect ratio rhodium nanostructures which includes rods, wires and tubes along with many other anisotropic/nonspherical morphologies. The scope for these structures in nanotechnology along with several fundamental issues, related to the origin and evolution of size and shape-dependent properties at the nano scale and their potential applications are also discussed. A brief account of recent endeavours on the synthesis of Rh nanostructures through different modified routes is provided, summarizing the role of all critical factors controlling their dimensionality, stability and reactivity. Potential applications of these Rh based nanostructures in various fields are also discussed with special emphasis on the impact of these nanomaterials as electrocatalysts for fuel cells and also in field emission. Finally after illustrating some of the major advantages and limitations of these materials, the objectives of the present investigation are explained in an attempt to fulfill the existing gaps in literature for this class of low dimensional nanostructures.

1.1. Introduction

In recent years, Nanotechnology has emerged as a new interdisciplinary area with enough promise to solve many complex societal problems like the interlinked constraints of food, water and energy through innovative materials and processes. Its ability to improve the standards of life of people, especially in the developing world is clear from its intimate relationship with the Millennium Development Goals set by United Nations [1]. Public is increasingly aware of the rapid advancement of ***Nanotechnology*** as a means of accomplishing economic growth and its interdisciplinary features encompassing interrelated concepts of chemistry, physics and biology for engineering new applications. Progress in Nanotechnology has revealed numerous examples at the scale of 1-10 nm giving rise to dramatic changes in the physicochemical properties of individual compounds and systems [2].

During the past 10-15 years, progress in nanotechnology has been largely associated with elaboration of new methods for the preparation and control of various nanostructures, unraveling their electronic structure as a function of size and shape followed by design and fabrication of many nanoelectronic devices [3]. This has helped to gain many insights into the reactivity of nanostructures comprising of relatively small number of atoms [4]. Moreover, it is also associated with the synthesis, modification and stabilization of individual nanoparticles and also to their directed self-assembly to more complex nanostructures for useful response. Research in this direction has been triggered by the recent availability of revolutionary instruments and approaches that allow investigation of material properties with subatomic resolution. Strongly connected to such technological advances are the pioneering efforts that have recently revealed new physical and chemical insights of materials at a level intermediate between atomic/molecular and bulk, which are expected to make a significant impact on many potential applications [5]. Remarkable attention has been captured by these nanostructured materials and as a result, their growth has actually been at an unprecedented rate, principally due to their unique and outstanding properties which could be controlled by tuning their morphology.

One of the most successful examples has been provided by the recent advances from the area of micro/nanoelectronics, where "smaller" essentially means enhanced performance ever since the invention of integrated circuits; more components per chip, faster operation, lower cost and less power consumption pointing out eventually to the use of molecules as both passive and active electronic components [6]. Moreover, a wealth of interesting and new phenomena is also associated with these nanostructures with unprecedented examples including quantized or ballistic conductance, coulomb blockade or single electron tunneling and metal-insulator transition [7]. Further, a large number of prospective applications in areas such as optoelectronics, sensors, catalysis, energy and photochemistry could be realized due to the development of many innovative hybrid materials using these advances based on the size and shape dependent behavior. However, each new technology has its potential drawbacks (and may be a threat to the society, according to some people) and it is important that implications of such developments should be understood properly. Similarly, as nanotechnology has created a brighter future, simultaneously it has also generated a general apprehension (at least in some minds) that some of its developments would pose severe risks. Therefore, the opponents of nanotechnology sometimes gain momentum, demanding a complete halt on such research, at least in few places (anti-nanotechnology) while the proponents come up with arguments to stop these efforts [8].

One of the important areas where the impact of nanotechnology is visible is that of materials as this has directed effectively towards the improvement in the functionality of materials by making relatively simple changes to existing technologies. The future of this interdisciplinary field however holds possibilities for extremely complex solutions for producing functional/smart materials [9]. Motivation for this arises actually from nature itself; for example, Lotus leaf and many other biological materials have hierarchical surface structures that prevent dirt and even bacteria from sticking. This "Lotus leaf effect" is related to superhydrophobicity and has attracted tremendous attention due to its wide applications related to the development of mimicking materials for water-repellent and stainless coatings, self-cleaning, anti-fouling application and lab-

on-a-chip devices. These new materials may incorporate nanosensors and nanomachines into their structure and have enabled progress in many areas, including display technologies, drug delivery and related medical applications [10].

1.2. Nanostructure: Influence on Properties

In recent years, various synthetic routes are available for the preparation of a variety of nanostructures with reasonable size and shape selectivity using methods like laser or plasma deposition, chemical/physical vapor deposition, sol-gel or other wet chemical routes and electrodeposition [11]. However, these methods generally result in very tiny (2-10 nm) particles with different sizes and shapes, often in a metastable phase and due to the small sizes and shapes, many of the properties are influenced to a greater extend by quantum size effects. Experimental evidence of the quantum size effects for small particles has been provided by different methods, while the surface induced effect could be verified by the measurement of thermodynamic properties like vapor pressure, specific heat, thermal conductivity and melting point of small metallic particles [12]. Generally, smaller the size, larger is the band gap, since greater is the difference in energy between the valence band and conduction band edges as more energy is needed to excite the electrons and concurrently, more energy is released when they return to their original state [13]. For example, all most all quantum dots (semiconductor nanocrystals) show optical properties as a function of their size and shape by virtue of band-gap engineering. The electronic structure of a nanomaterial critically depends on its size and is drastically different from their bulk or atomic/molecular analogues as shown schematically in Figure 1.1. This change in electronic structure due to their lower dimensionality can be generally defined by the electron movement in a restricted environment such that the particle size is of the order of mean free path i.e. phase coherence length of the electrons at least in one dimension, (commonly known as quantum confinement) resulting into a dramatic change in all properties.

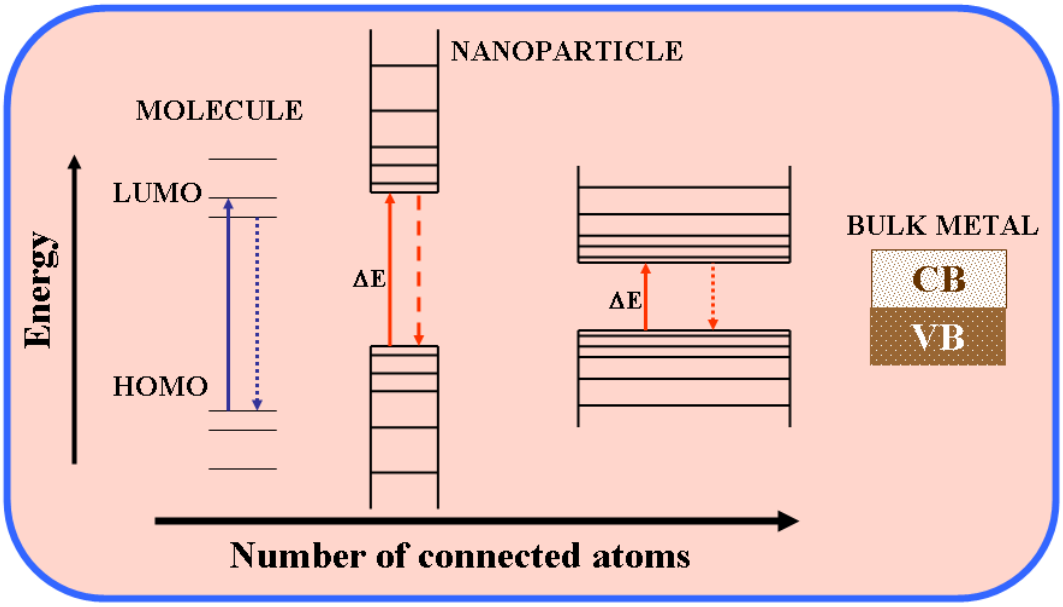

Figure 1.1. Comparative band structures for metallic particles in lower dimensions along with associated HOMO-LUMO structure for respective molecules; scheme adopted from [13].

Especially in the case of metallic nanostructures, there are numerous reasons, why a size reduction can, in principle affect all material properties. These could be understood in terms of different origins; (i) large fraction of surface atoms and hence large surface energy, (ii) quantum confinement and (iii) reduced imperfections. Moreover, these factors can tune all properties including reactivity and strength since as particle size decreases, a greater proportion of atoms are found at the surface compared to those inside. For example, as shown in Figure 1.2, gold nanoparticles with a 30 nm size have 5 % of the atoms on its surface while with 10 nm, it is 20 % and subsequently with 3 nm, their is 50 % [14], which can explain properties like increase in the melting point with increase in size converging finally to the bulk melting point.

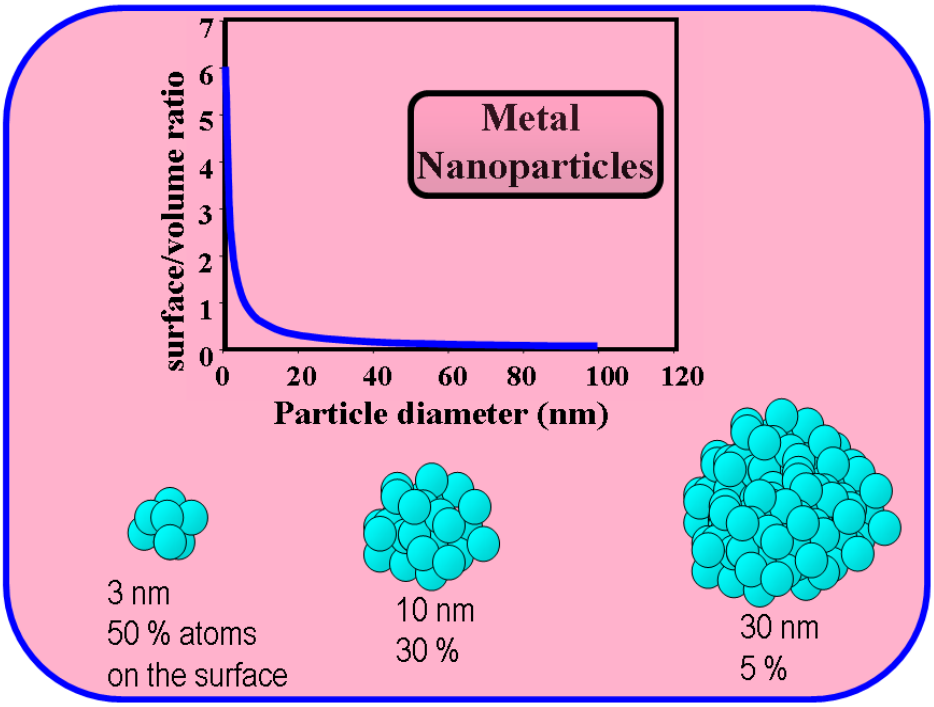

Figure 1.2. A schematic representation of the variation of surface atoms with size for metal (Au) nanoparticles; scheme adopted from [14].

Because of this reduced dimension, the lattice contraction or lattice strain generated due to hydrostatic pressure on the surface induced by the intrinsic surface stress is also important. As most of the atoms are situated on the surface of smaller particles, they have excess free energy and this explains the depression of melting point by minimizing the surface energy [15]. Thus nanoparticles have a much greater surface area per unit mass compared with larger particles. As growth and chemical reactions occur at surfaces, this means that a given mass of material in nano particulate form will be much more reactive than the same mass of material of larger particles. Sometimes they are so reactive that a monolayer or polymer cover is essential to isolate and study them in the laboratory. Such clusters are called monolayer protected clusters (MPCs), like dodecane thiol protected Au nanoclusters.

The emergence of molecularity in the metal-to-molecule transition is signaled by the emergence of an energy gap (see Figure 1.1), which may be detected optically or electrochemically or both. The electrochemical energy gap could be considered as the

difference between electrochemical potentials for the first oxidation and first reduction wave from a parent species. For example, within the family of Au nanoparticles protected by organothiolate ligands, electrochemical energy gaps have been detected for MPCs designated as having core sizes of ~Au_{75}, ~Au_{55}, ~Au_{38}, ~Au_{25} and ~Au_{13} [16]. This progress towards defining the metal-to-molecule transition based on tunable band gap (for Au nanoparticles with organothiolate ligands) is summarized in Figure 1.3. Significantly, three regimes of nanoparticle behavior, from bulk continuum at the left, where no voltammetric features are observable, to quantized double layer charging for Au_{225} and Au_{140}, in the intermediate region to molecule-like on the right could be identified as a function of size.

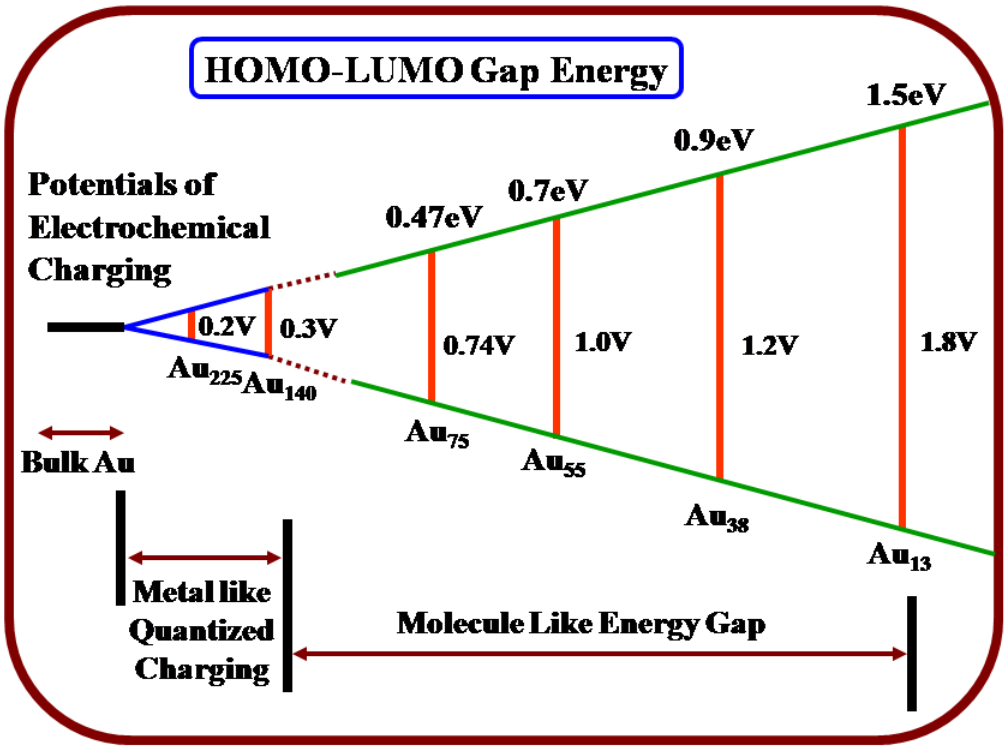

Figure 1.3. A summary of the electrochemical behavior of monolayer protected Au nanoparticles as a function of core size, showing the estimated energy gaps (HOMO-LUMO gaps); scheme adopted from [16].

Another example includes the shifting of optical absorption peak, λ_{max} of metallic nanoparticles by hundreds of nanometers (particle charging energies by hundreds of millivolts) with a change in particle size and shape [17]. Similarly, magnetic properties of

nanostructured materials are also distinctly different from that of bulk materials. For example, ferromagnetism of bulk material disappears and transfers to superparamagnetism in the nanometer scale and similarly mechanical properties of nanomaterials reach their theoretical strength, which is one or two orders of magnitude higher than that of single crystals in the bulk form [18, 19]. The enhancement in mechanical strength is simply due to the reduced probability of both surface and structural defects. In view of these tunable structural properties, enormous improvements have been made, to date, in transition metal nanostructures using ruthenium (Ru), platinum (Pt), palladium (Pd), rhodium (Rh), rhenium (Re) and iridium (Ir), since most of these have their electronic properties comparable to that of normal semiconductors [20].

1.3. Why Nanostructured Rhodium?

Rh is an important metal for many applications, as it has been widely exploited both as homogeneous and heterogeneous catalysts, offering immense scope for developments in green/environmental chemistry. The commonly used application of Rh is in catalytic converters especially for the purification of automobile exhaust gas, where harmful oxidizing gases such as carbon monoxide, sulphur dioxide, nitrous oxide, various hydrocarbons or reducing nitrogen oxide from the engine are converted into less pollutant gases. Interestingly, in 2007 alone, about 81 % of the world production of Rh has been consumed to produce three-way catalytic converters [21]. Moreover, Rh shows several advantages over other platinum group metals for the reduction of nitrogen oxides to nitrogen and oxygen [22]:

$$2\ NOx \rightarrow x\ O_2 + N_2$$

Rh-based catalysts are used in a number of other industrially important processes, for example, in the Monsanto process for the production of acetic acid, in the manufacturing of silicone rubbers and also for reducing benzene to cyclohexane [23]. Apart from this, Rh films are also used in mirror optics, as an alloying agent for hardening and improving the corrosion resistance of structurally similar metals like Pt and Pd etc. More significantly, Rh is especially promising for several other applications

due to its features such as excellent electrical performance, corrosion resistance, chemical inertness, mechanical strength, remarkable thermal stability, lower electron affinity and significant stability towards ion bombardment. Even though, it has all the above mentioned physical and chemical properties, its prohibitively high cost limits the utility for many applications like its use in microelectronics [21].

The genesis of the present work is inspired by the outstanding role of Rh as a multifunctional catalysts in many industrial applications, with the goal to alleviate its use because of the high cost, by taking advantage of nanotechnology. It is well known that the manipulation of the size and shape at the nanoscale can contribute to lowering of the metal usage concomitantly achieving the necessary cost reduction through their high reactivity along with enhanced selectivity [24]. In recent decade, there have been plenty of studies in exploring the control of Rh nanostructures for improving the understanding of basic properties of these materials with respect to their applications. As a result, monometallic and bimetallic Rh nanostructures in supported and unsupported form have been widely exploited as catalysts for a variety of organic transformations. Some specific examples include, hydrogenation reactions, particularly in olefin, alkyne, benzene, ethylene and arenes, along with styrene hydroformylation [25]. Moreover, various shapes of Rh have offered specific surface exposure towards selective planes, for example, Rh {100}, {111} and {110} surfaces and as a result of this, these shapes of Rh nanoparticles can affect both the catalytic reactivity and selectivity [24]. Supported Rh nanoparticles have also been studied to obtain better catalytic properties (their sensitivity and selectivity) by using Rh nanoparticles on SBA-15, multi-walled carbon nanotubes (MWCNTs), Al_2O_3, TiO_2, CeO_2 and multi-functional glasses, ceramics, oxides and fibers [26]. Thus, experimental results strongly suggest that careful control of growth conditions can serve as functional/effective building blocks to fine tune their fundamental properties by emphasizing their prospective applications in catalysis, sensors, photochemistry, biomedical, nanoelectronics, photovoltaic and optoelectronics.

1.4. Synthesis of Rh Nanostructures

The actual behavior of Rh nanostructures critically depends on various experimental and fundamental issues including the ability to control size, dimensionality, composition, defects and concentration gradients [27]. Therefore various synthetic approaches for the fabrication of anisotropic nanostructures depend on careful variations of their parameters. Conveniently used methods for the synthesis of such nanomaterials include solution phase growth, templated and non-templated methods, carbothermal reactions, solid-liquid-solid processes, electrochemical approach, solvothermal process and vapor phase growth (including thermal evaporation, atomic layer deposition, chemical vapor-phase deposition, metal-organic chemical vapor phase deposition) etc. [11]. However, in comparison with zero-dimensional (0D) and two-dimensional (2D) nanostructures, the advancement of one-dimensional (1D) nanostructures with high aspect ratio has been slow until very recently, perhaps, due to the difficulties associated with the synthesis of these nanostructures with well-controlled dimensions, morphology, phase purity and chemical composition. Although high aspect ratio nanostructures can now be fabricated using a number of advanced techniques, further development of these techniques into practical routes on large scale at reasonably low cost, still requires great ingenuity. In this context, chemical, electrochemical as well as chemical vapor deposition routes can provide an alternate strategy for generating high aspect ratio structures in terms of material diversity and cost effective, large volume production [27].

The following section briefly reviews different synthetic strategies for the formation of high aspect ratio Rh nanostructures with special emphasis on 1D nanostructures. In contrast to spherical particles, non-spherical Rh nanoparticles such as rods (short/long), wires, cubes, nanocages, multi-concentric shells, triangular prisms, as well as other more exotic structures such as hollow tubes, even branched nanocrystals have garnered significant research attention in the past few years [28]. They exhibit unique properties which either strongly differ or are more pronounced from those of symmetric/spherical Rh nanoparticles. Their unusual optical and electronic properties, improved mechanical properties and specific surface-enhanced spectroscopies make them

ideal structures for emerging applications in photonics, electronics, optical sensing and imaging, biomedical labeling and sensing, catalysis and electronic devices. Although an exhaustive description of all available reports is difficult, an attempt is carried out to summarize the central contributions in this area. Accordingly, we survey the most common synthetic methods for the controlled synthesis of Rh nanostructures.

1.4.1. Seeded Growth Method

Because of its inherent, highly symmetric fcc structure, it is not easy for Rh to acquire a non-spherical shape. This poses a challenge to achieve anisotropic nanostructures, despite having immense interest because of its extraordinary surface reactivity against their natural tendency to form thermodynamically stable spherical shapes [29]. In this context, it would be of interest to examine, how atoms (and other building blocks) could be rationally assembled into a variety of metastable shapes. Thus, there is a great interest in the development of new methodologies based on bottom-up approaches for the selective synthesis of anisotropic shapes. One of the commonly adopted strategies for achieving shape control is based on the manipulation of growth kinetics with the help of capping molecules that preferentially bind to crystal faces of growing particle, thus introducing anisotropy into the particle geometry along with controlling preferred growth direction [30]. Another interesting strategy and extension of the above approach is the addition of foreign species in the reaction mixture which could significantly alter the growth kinetics of specific crystallographic facets [31]. In the Polyol synthesis, these foreign ions are expected to have a pronounced influence on the nucleation than surfactants or polymers because of their relatively smaller size and increased ability to form complexes with reactive species in solution [32]. Accordingly, Table 1.1 summarizes all available procedures for the preparation of different of Rh nanostructures. A slightly different strategy for the growth of anisotropic structures is through the introduction of defects in seed crystals, which could reduce the symmetry of cubic lattice.

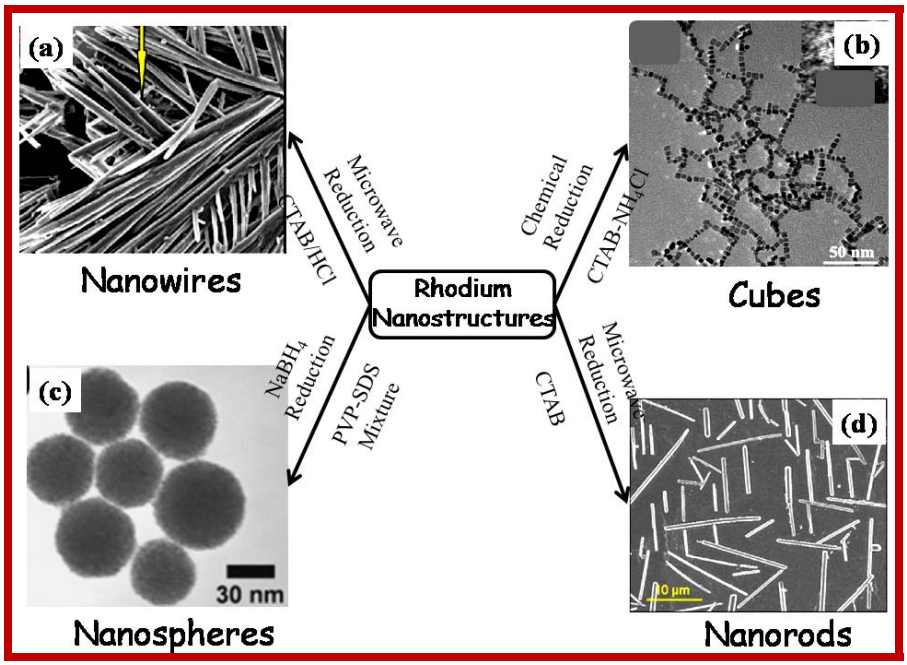

Figure 1.4. Comparison of different routes demonstrating the synthesis of Rh along with their respective micrographs; Figure adopted from [33-35].

Wang and co-workers have demonstrated the tunable shape-evolution of Rh nanostructures in aqueous phase using halide ions as the controlling agents. For example, the TEM image shown in Figure 1.4 (b) suggests highly shape and size selective assembly of Rh cubes on micron level with an average diameter of about 4.8 ± 0.3 nm perhaps due to the specific adsorption of bromide ions on respective planes [34]. A slightly different approach without any external metal ions has been developed by Pal and coworkers for the synthesis of Rh nanowires and nanorods using $RhCl_3$ as the metal precursor and cetyltrimethylammonium bromide (CTAB) as a reducing agent with NH_4ClO_4 a stabilizing agent. Moreover, it has been observed that pH has a remarkable influence on the alteration of aspect ratio resulting into the evolution of nanowires in acidic condition as shown Figure 1.4 (a) and (b) respectively [33]. Apart from these strategies, anisotropic structures are also realized through physical constrictions imposed by structure directing materials which include both hard and soft templates. Some of the key issues and shortcomings involved in these approaches during the synthesis of Rh

nanostructures along with utility of these nanostructures for various applications are also discussed.

1.4.2. Electrochemical Synthesis

Over the past decade, synthesis of nanostructured materials by electrochemical method has received considerable attention because of the ease of controlling even complex morphology such as fractal geometry and dendritic growth. This method is particularly advantageous because the crucial steps in nucleation and growth can be controlled by modulating parameters such as electric field, solvent, ionic strength and concentration of the source. In most of these cases, however, growth occurs under nonequilibrium conditions and, interestingly, a dramatic variation in morphology hence arises under low and high over potentials, respectively. Hence a variety of metals and alloys have been prepared to achieve improved physical and chemical properties [36]. In this respect, electrochemically deposited nanocrystals are quite different from other nanostructures, which are based on consolidated particles. For example, Lewerenz and coworkers have reported the electrochemical deposition of Rh nanostructures onto H-terminated p-Si surfaces by the simultaneous oxidation leading to the formation of nano-dimensioned metal-oxide-semiconductor (MOS) type contacts [37].

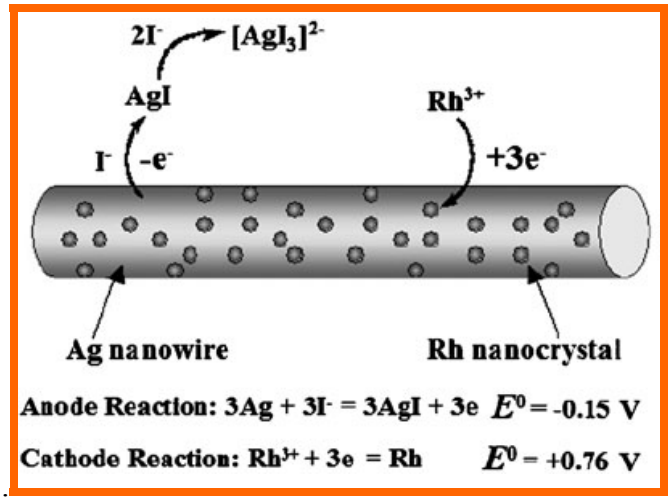

Figure 1.5. Diagrammatic illustration of the typical replacement process between Ag nanowires and Rh^{3+} ions during the formation of Rh nanotubes, Adopted from [49].

Recently, Lu and coworkers have attempted the replacement of Ag^+/Ag pair (0.80 V vs. SHE) with a comparatively lower redox potential (Rh^{3+}/Rh = 0.76 V vs. SHE) for shape selective synthesis of Rh [38]. Here, the replacement occurs between Rh^{3+} and Ag nanowires, quite readily, at room temperature to yield hollow Rh nanotubes with uniform shells and smooth surfaces. The driving force for the formation of Rh nanotubes through probable electron transfer pathway is illustrated in Figure 1.5. In the presence of saturated I^- ion solution, redox potential of Ag species decreases markedly from + 0.80 V (Ag^+/Ag) to - 0.15 V (AgI/Ag), which is much lower than that of the Rh^{3+}/Rh couple, thereby causing the reduction of Rh^{3+} to Rh atoms. Moreover, when iodide, is replaced by Br^- in above explained process, Rh nanotubes with high yield are obtained.

Another way for the synthesis of high aspect ratio nanostructures is by the template-assisted electrochemical deposition, employing either an active or restrictive template. Normally porous alumina or polymeric membranes with highly ordered nanochannel-array are used as cathode in an electrochemical cell and Rh is deposited electrochemically into the pores. Pioneering work carried out by Mohney and co-workers using a template based approach has enabled Rh nanowires followed by their heterostructured to Si nanowires [39]. Significantly, this method of heterostructure synthesis using membrane based templates can be extended for any other combinations of several other metals. Templated technique is also useful for the preparation of free-standing nanowire arrays, which can be used as electrodes to study their electrochemical properties [36]. Interestingly, capillaries of carbon nanotubes can also be used as templates for the growth of metal nanowires; accordingly, nanowires of other metals like Au, Ag, Pd and Pt have been synthesized by this intercalation method [40]. Although several such advances have been made, the template method suffers from disadvantages of very low yield and contamination. However, Ichikawa and co-workers have reported a method for the synthesis of Rh nanowires (diameter 2.5 nm, length 10-50 nm) in pores of FSM-16 by using photoreduction of the FSM-16 followed by bimetallic heterojunctions of nanowires of Pt–Rh [41].

1.4.3. Chemical Vapor Deposition

Chemical Vapor Deposition (CVD) is an extensively studied method for the synthesis of 1D metal nanostructures, involving multiple, reactive intermediates and steps of the nanomaterials depending on the starting compounds using carrier gases to produce a nonvolatile solid that deposits atomistically on a suitably placed substrate at comparatively higher temperatures. This has been commonly used due to its simplicity and ease of control of orientation and selected especially for thin film applications in solid state microelectronics.

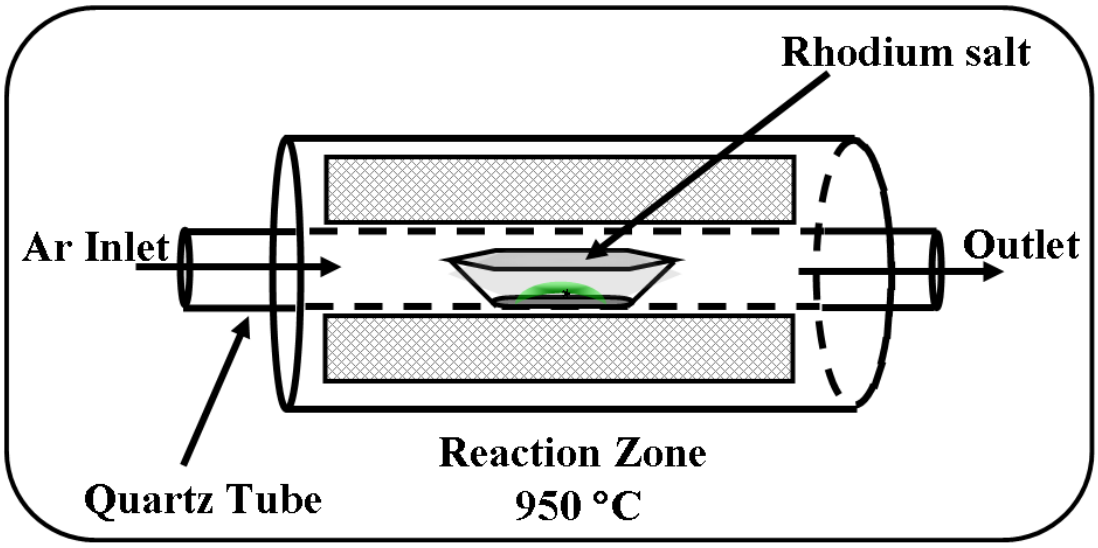

Figure 1.6. Chemical vapor deposition set-up for the synthesis of oriented Rh nanostructures using various organo-metallic precursors in Ar atmosphere for controlled growth.

A variety of CVD reactors have been developed depending upon types of precursor used, deposition conditions and several variants are also available (like plasma and laser deposition) to activate chemical reactions desired for depositing a variety of thin films on different substrates (Figure 1.6.)

1.4.4. Other Methods

The main advantages of above mentioned synthetic strategies are that they are comparatively cheaper and bulk quantity could be produced without any significant efforts. There are several other methods involving molten salts, supercritical solvents, photo-irradiation, laser-ablation and sonochemistry to synthesize size controlled anisotropic nanostructures of Rh and their heterostructures [42]. Further, decomposition or thermolysis of organometallic salts at higher temperatures also produces alkyl-chains-passivated nanostructures [43]. Several single-phase (non-aqueous) methods are also available for the synthesis of nanostructures, where soluble organometallic compounds are reduced with suitable reducing agents in presence of surface passivating molecules [42]. Other advantages of single-phase techniques are the absence of phase-transfer catalysts (may cause surface contamination), ease of separation/purification and flexibility for large scale preparation [44].

Table 1.1.: Different methods for the shape-selective synthesis of Rh nanostructures.

Nanostructures	Method	Reaction Conditions	References
Tripod/tetrapods	Modified Polyol	anhydrous $Na_3[RhCl_6]$ as a precursor in ethylene glycol-polyvinyl pyrollidone system	[45]
Tetrahedron	CVD	decomposition of an organo-metallic compound $[Rh_2\ (CO)_4Cl_2]$ in oleyl amine	[46]
Cubes	Modified Polyol process	ethylene glycol-PVP-TTAB (trimethyl tetradecyl ammonium bromide) system with $RhCl_3$	[47]
Thin film Patterning	Plasma Enhanced CVD	$Rh(CO)_5\ C_5H_7O_2$	[48]
(111) oriented thin film Patterning	Atomic Layer Deposition	$Rh(acac)_3$ and O_2	[49]
Cubes and Multipods	Seed mediated Polyol Method	Rh nanocubes and multipods by reducing $RhCl_3$ in the ethylene glycol-PVP system using the seed growth method	[50]

However, uncapped nanostructures synthesized by wet chemical approaches have limited stability and their high surface energy causes them to agglomerate in

solution/solid state due to Ostwald ripening and other growth modes. However, these clusters can be stabilized electrostatically or sterically and stabilization occurs through the involvement of electrical double-layer consisting organized cations, anions and solvent molecules. Agglomeration of highly charged particles is restricted by coulombic repulsion which decreases exponentially with increasing the interparticle distance. These techniques offer a precise control of the deposition parameters possibly at the level of single atom, along with good film quality. Accordingly, Table 1.1 summarizes the important synthesis methods for achieving anisotropic nanostructures of Rh, in order to compare influence different methods in size/shapes.

1.5. Mechanism of Anisotropic Growth

One of the widely accepted mechanisms for the anisotropic particle growth in liquid media assumes kinetic control of growth rate of various facets of the seed particle by appropriate capping molecules or nucleating agents. For example, according to Xia and co-workers, lowering of the precursor concentration reduces the chemical potential for crystallization and therefore a manipulation of the precursor concentration enables one to decrease the chemical potential to synthesize thermodynamically stable crystals as compared to the kinetically stable ones [51].

The structural stability of nanomaterials depends on the surface energy, which could be understood from the energy minimization process by preferential crystallization of atoms and so, for the case of metallic nanostructures, lower energy {111} facets dominate most of the thermodynamically stable structures [52]. In such a case, in order to achieve anisotropic growth of nanostructures against their thermodynamically stable ones, preferential growth of various facets is necessary. This is usually achieved by the selective binding of capping molecules on various planes. For example, as in the case of Ag and Au, PVP preferentially binds {100} planes rather than {111} and {110} planes, allowing further deposition of metal atoms at vacant planes resulting into cubic and octahedral shapes [53]. The nonspherical/anisotropic (cubic, cuboctahedral and octahedral) shapes are characterized by different surface energies with various

crystallographic planes and an approximate sequence can be given as: $\gamma\{111\} < \gamma\{100\} < \gamma\{110\}$ for fcc structured metal particles [54]. Consequently, main possible directions of nucleation and growth of metal nanoparticles are in the [111], [100] and [110] planes leading to the possibility of faceting [55]. In contrast, polyhedrons of cube, octahedron, cubo-octahedron and tetrahedron have their low-index planes formed in various morphological combinations. Clearly, Rh nanocubes with their good morphologies are single crystals with all {100} faces and cuboctahedron by combination of {111} and {100} tetrahedron and octahedron bounded by all {111} facets. Moreover, these Rh

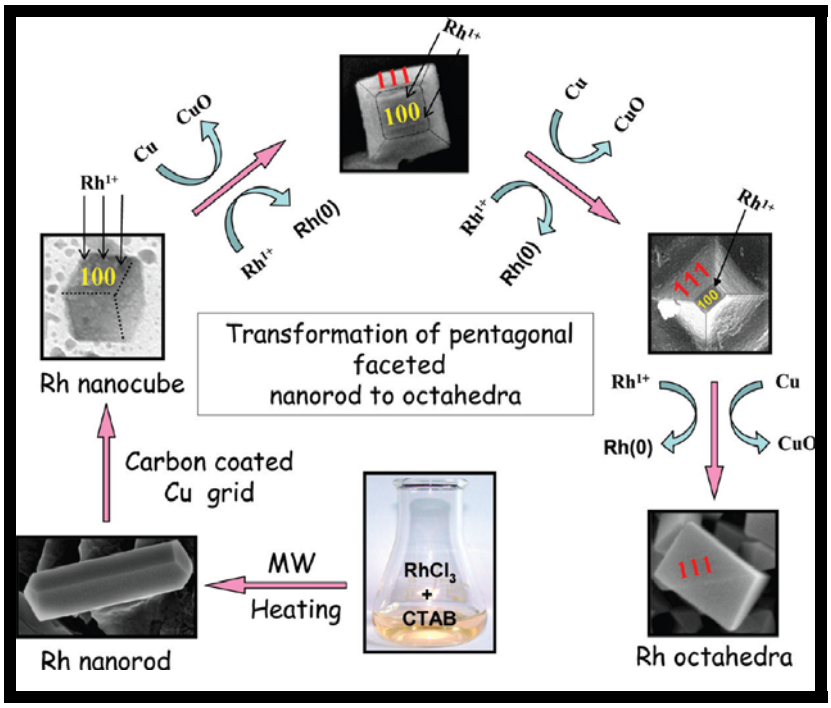

Figure 1.7. Mechanistic pathway showing the transformation of various shapes of Rh through tunable reaction conditions; figure adopted from [33].

{100}, {111} and {110} surfaces offer their activities for potential applications, as in catalysis and electrocatalysis [56]. For example, recently literature explores the shape dependent catalytic reduction of NO and CO on Rh nanopolyhedra unraveling higher activity of single crystalline nanocubes from 230 to 270 °C, due to their exposure of high-index planes [57]. More recently, Pal and coworkers have also reported a remarkable shape-selective synthesis of Rh nanorods using CTAB as the surfactant,

where these rods can be converted into nanocubes with oxidized Rh species specifically adsorbed on (100) facets by the treatment with Cu [33]. Significantly, these controlled oxidized (Rh^+) species are more reactive and their treatment with Cu wire results into the transformation of nanocubes into smaller Rh octahedra as represented schematically in Figure 1.7.

1.6. Properties of Nanostructured Rhodium

As compared to bulk Rh**,** reduced dimensions generate many novel properties and a few examples of such features are discussed in details below.

1.6.1. Optical Properties

The reduction of dimension at nanoscale has a dramatic effect on optical properties of Rh and the size dependence can be generally understood from two different points of view. One is due to increased energy level spacing as the system becomes more confined and the other is related to collective response [surface plasmon resonance (SPR)] [58]. Interestingly, after the landmark report from Gans, SPR of anisotropic nanostructures has attracted tremendous attention towards the understanding of fundamentals of nanostructures [59].

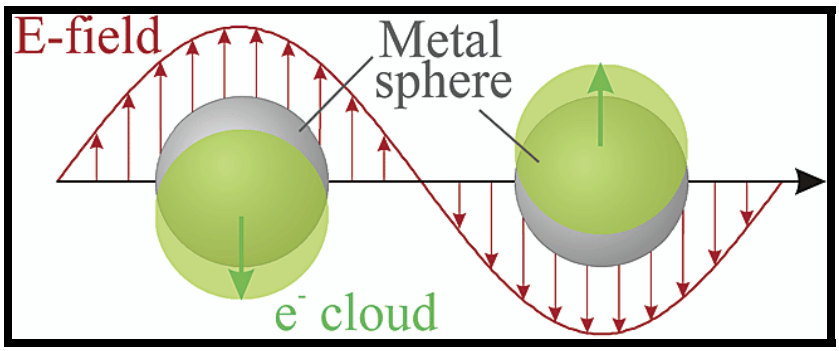

Figure 1.8. Displacement of the conduction electron charge cloud relative to the nuclei of a sphere; scheme adopted from [60].

However, the spherical nanoparticles *per se* could be envisaged to elicit a more uniform response as a result of their plasmonic field enhancement to a perturbation known as dipole surface plasmon resonance (Figure 1.8). The restoring forces due to the

Coulombic attraction of electrons with nuclei oppose displacement of electrons with incoming electric field ultimately leading to the oscillations, frequency of which is strongly influenced by: (i) density of electrons, (ii) the effective electron mass and (iii) the shape and size of the charge distribution. Higher modes of plasmon excitation can also occur, such as quadrupole mode where, half of the electrons moves parallel to the electric field and the other half moves anti-parallel [60].

Conversely, the departure from sphericity due to asymmetry in the field of nanoparticles or the presence of disordered (anisotropic) morphology can have a "diffuse" response, resulting in a splitting of their dipole absorbance in to multiple bands [61]. Significantly, optical properties of Au, Cu and Ag nanostructures have been known for nearly 150 years, culminating in many niche application of their SPR in various fields. In contrast, the optical properties of Rh nanoparticles remain relatively unexplored [62]. Both thin films and spherical nanoparticles of Rh do not exhibit any absorption signal in the visible region as a result of the very small imaginary part of dielectric constant. The location of SPR peak of Rh nanoparticles in the UV region makes them blackish gray in color and it's causes are much more difficult to probe, mainly because of less absorption of light at this wavelength. All these results reflect that the picture of the SPR of Rh is still not clear necessitating more investigations [61, 63].

Accordingly, several approaches have been made for the explanation of light scattering from Rh nanoparticles of arbitrary shape, where extinction is considered as the sum of scattering and absorption. On the basis of discrete dipole approximation (DDA), Xia and coworkers, have proposed a weak and broad SPR signal at ~380 nm for Rh multipods, although, the presence of air shifts the SPR peak towards a shorter wavelength due to the transformation from branched to spherical shape [64]. Indeed, different morphologies of Rh via seeded Polyol route have been reported recently, revealing shape and capping dependent SPR features [45-50]. For example, UV-Vis spectrum of the branched Rh nanocrystals displays an attractive SPR feature, as a weak and broad peak around 380 nm. More recently, Rh nanotubes have also been reported to show interesting broad SPR at 500 nm due to the formation of hollow structures and uniform walls [65].

Most of the SPR observations of Rh nanostructures are in accordance with the Mie theory, which explains the emergence of SPR signal with particle size and shape depending on the dielectric constant of the medium, solvent refractive index, temperature and particle-particle interactions [66]. Further, the effect of core charge has also been investigated for SPR, which shows the accumulation of excess electronic charge causing a blue shift of the SPR position and vice versa. The nature of capping molecule has a dramatic effect on SPR position, which could be selectively used for applications in optical sensors and medical diagnostics. Apart from absorption features of nanostructures, they are also attractive for fluorescence studies. For instance, the fluorophore groups functionalized nanostructures exhibit resonant energy transfer phenomenon, which is of great interest in biophotonics and materials science.

1.6.2. Electrochemical Properties

The tunable size of nanoparticles has been found to reveal several interesting electrochemical properties like quantized charging behavior depending upon the core size or nature of surface passivating molecules. A major emphasis has been placed on the investigation of the double-layer charging properties of smaller nanoparticles (< 3 nm) to understand their electron transfer features [67]. The freely diffusing or surface attached nanoparticles on electrode surface show discrete double layer charging features with respect to one electron, where the capacitance (auto farads; aF) is associated with ionic space charge formed around each nanoparticles in the electrolyte solution, known as quantized double layer (QDL) charging [68]. The QDL phenomenon has been reported for various nanoparticles and several effects, like core size, chain length, nature of monolayer, temperature and magnetic field, have been studied, although this property is not known for larger nanoparticles [69]. For example, Figure 1.9, shows a series of quantized double layer charging events in solution phase voltammetry at room temperature from Rh nanoclusters (4.9 ± 0.2 nm) of approximate composition $Rh_{2057}(TDA)_{321}$. The unusual variation in the FWHM for both cathodic and anodic regions in the differential pulse voltammetry (DPV) might be due to several complex

factors including reorganization or disproportionation of charged clusters coupled with electron transfer processes pertaining to Rh-Rh bond [70]. However, more detailed investigations based on structure-property correlation are really needed for exploring this to device applications.

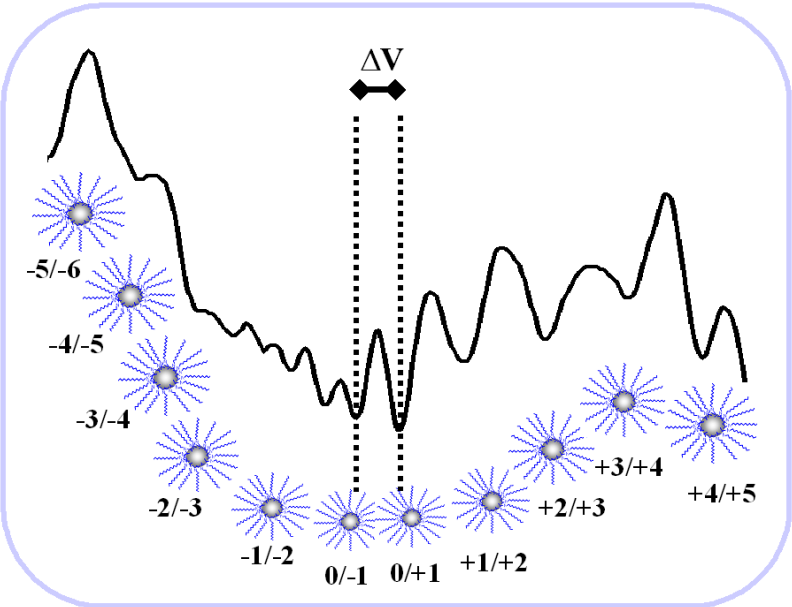

Figure 1.9. Schematic representation of the quantized double layer (QDL) charging behavior showing a series of charging events for Rh nanoparticles (4.9 ± 0.2 nm) of approximate composition Rh_{2057} $(TDA)_{321}$ in solution DPV at room temperature; scheme adopted from [70].

1.6.3. Electronic Properties

The band structure of Rh undergoes a dramatic change due to quantum size effects like other nanomaterial [71]. However, the effects of size and shape towards electron transport in nanostructures is complex, since they are based on distinct mechanisms. These mechanisms can be generally grouped into various categories such as surface scattering including grain boundary scattering, quantized conduction including ballistic transport, Coulomb charging and tunneling, widening of band gap along with reorganization of energy levels [72]. In addition, increased structural perfection during growth kinetics such as reduced impurity, structural defects and dislocations would also affect electrical conductivity of nanostructures [74].

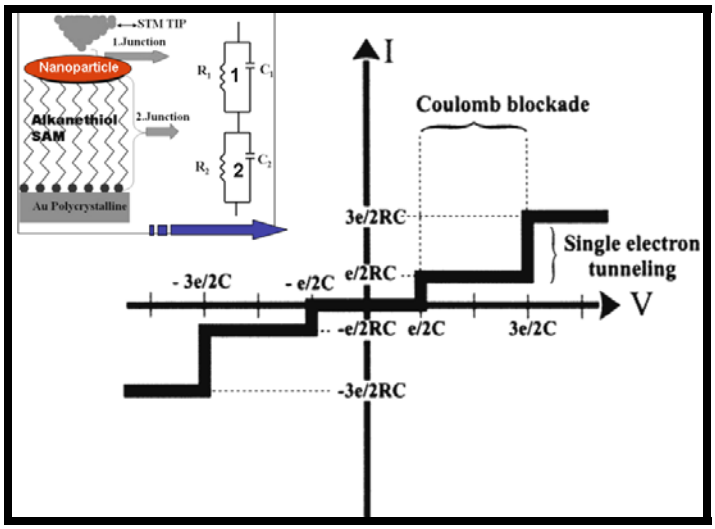

Figure 1.10. The ideal Coulomb blockade phenomenon as depicted in current–voltage (I-V) graph, (Coulomb staircase); inset shows a widely investigated nanoparticles based metal-insulator-nanocluster-insulator-bulk metal (MINIM) system to illustrate such behavior; adopted from [72].

Accordingly, electronic properties of metallic nanoparticles would be promising for constructing electrical devices based on single electron transfer (SET), superior to presently available semiconductor based integrated circuits and information storage devices. Although their typical resistivity value suggests semiconducting behavior, especially if the size is < ~2 nm, the I-V curves show Coulomb blockade behavior that manifests single electron tunneling at room temperature as shown in Figure 1.10. Further, organized/superlattice assemblies of these nanoparticles have unique electronic properties due to their collective tunable interactions although the I-V behavior is strongly affected by the nature of capping molecule, including its length [75].

1.6.4. Emission Properties

The usual theoretical treatment of electron emission from metal into vacuum on application of high electrostatic field is based on the Fowler-Nordheim (F-N) model, which assumes that- (i) temperature of the metal is 0 K (ii) the free electron model is valid, (iii) surface is a smooth plane, and (iv) potential barrier close to the surface in the

vacuum region consists of an image force potential and a potential due to the applied electric field [76].

Accordingly, the applied electric field (F) is defined as F = V/d, where V is the applied voltage and d is the separation (d = 5 mm). However, the actual enhanced field at the apex of the hexagons can be estimated from the equation as follows [76].

$$\beta = -6.8 \times 10^3 \phi^{3/2} / m \quad \text{---------- (1.1)}$$

Where, β is the field enhancement factor, ϕ is the work function of the emitter material in eV. For crystalline surfaces, the work function associated with field emission is the average over the emitter surface, weighted towards the lower work function areas.

The F-N equation has been found to be adequate for describing the field emission from metals. With the advent of various nanostructures, a variety of field emission (cold) cathode materials have been developed to date [77]. These include materials for microfabricated field emitter arrays, diamond and related films, carbon nanotubes, other quasi 1D nanomaterials and printable composite materials. Important parameters include electron affinity, dielectric constant, thermal conductivity, chemical and physical robustness. In addition, cold cathode materials have a wide range of applications such as in flat panel displays, high-power vacuum electronic devices, microwave-generation devices, vacuum microelectronic devices and vacuum nanoelectronic devices [78]. Recently, recognizing the strong possibility that vacuum nanoelectronic devices using quasi 1D nanomaterials such as carbon nanotubes may emit electrons with driving voltages comparable to that of a solid-state device, there is a growing interest in novel applications of such devices [79]. With such exciting opportunities, there is now a flurry of activities to explore applications far beyond those considered for conventional hot cathodes that operate on thermionic emission. In particular, nanotubes and nanowires with sharp tips are promising materials for applications as cold cathode field emission devices [80]. Moreover, the Rh nanostructures also have higher electron emission properties at an ultra low threshold with high current density.

Consequently, a number of anisotropic materials have been found to act as efficient field emission cathodes, since some of these can operate remarkably well below

the intrinsic current limit due to their thermal effects [81]. Enormous improvements have been made, to date, in metal nanostructures using Ru, Pt, Pd, Rh, Re and Ir, since most of these have their work function comparable to that of silicon. Among these, Rh could especially be promising due to its features such as excellent electrical performance, chemical inertness, mechanical strength, remarkable thermal stability, lower electron affinity and significant stability toward ion bombardment [82].

1.6.5. Other Properties

High aspect ratio Rh nanostructures also exhibit several other important properties, such as surface enhanced scattering, fluorescence quenching or enhancement depending on the proximity to the surface [83]. Due to the strong electromagnetic field generated at the surface of metal nanoparticles, chromophores within ~ 5 nm of the surface of metal nanoparticles have their fluorescence quenched, while chromophores at distances of ~10 nm or greater have their fluorescence enhanced up to 100-fold. Anisotropic Rh nanoparticles also exhibit interesting catalytic properties. For example, it has been recently demonstrated that high aspect ratio nanoparticles with more corners and edge atoms have higher catalytic reactivity than similar nanoparticles with fewer corner and edge atoms [24, 25]. In addition to this, anisotropic Rh nanoparticles show significant field enhancement at the surface due to photo-excitation of conduction of electrons [84]. In particular, local field enhancement factor increases many times, when nanoparticles with lower symmetry and/or bi-metallic concentric structures are used. It has been demonstrated that triangular particles with dimensions smaller than 50 nm produce strong field enhancement near their vertices, reaching several hundred times the amplitude of illumination wave. This strong, but extremely localized field, is the central reason for the observation of hot spots and blinking phenomena experimentally in Raman scattering. This technique is promising for the single molecule detection when appropriate nanoparticles are used for the substrate. For example, Xia and coworkers, have explored the SPR properties of Rh multipods and its use as a substrate in SERS displays, which find important use in applications such as *in situ* monitoring of catalytic reactions [64].

The magnetic nanoparticles provide an opportunity for studying the effect of crystal, size, shape and surface state on magnetism. The magnetic moment depends also strongly on nanoparticle/cluster structures [85]. For example, although bulk Rh is magnetically inert, experimental studies for Rh clusters up to 60 atoms and theoretical studies for clusters up to 19 atoms show that Rh clusters could have large magnetic moments [86]. Zitoun and coworkers reported an interesting magnetic behavior of chemically produced bimetallic nanoparticles (Co-Rh) revealing a decrease of the coercive field and a simultaneous increase of the anisotropy field with nanoparticles size [87].

1.7. Applications of Rh Nanostructures

Having completed the discussion on controlled synthesis, growth mechanism and properties of anisotropic metallic nanostructures, we are now in a stage to consider methods to rationally assemble atoms or other building blocks into structures with their controlled dimensions and surface structure for tuning their properties and reactivity. Many potential applications have recently been found for Rh nanostructures in wide areas of material sciences, including catalysts for various organic transformations and electrocatalysts for energy conversion. However, the cost of Rh and Rh based nanomaterials, limits the large scale processing and difficulty of precise control of their assemblies on large scale a significant barrier for realizing some of these applications [88].

Moreover, Rh nanostructures have offered several other applications due to their fascinating properties arising from quantum confinement. Such size-dependent structural changes in Rh especially for one dimensional structures (such as wire, tubes etc.) help in transporting controlled current from one place to another. Similarly, Rh and Rh based heterostructures are also known to be highly sensitive towards H_2, CO, NO, NH_4 for sensing vapors based on their change in resistance ($\Delta R/R_0$) [89].

Plasmonics is an another emerging field in optics, dealing with the so-called surface plasmon of many nanoparticles for extraordinary properties of anisotropic

structures of Rh could be analyzed from a fundamental point of view for numerous technological applications [64]. Apart from these exciting developments in plasmonic, Rh will have a plethora of applications in various other areas.

1.7.1. Electrocatalysis

Electrocatalysis is the relative ability of different electrode materials, under the same conditions to accelerate the rate of a given electrochemical process. The use of nanomaterials as electrocatalysts has a number of important attributes including, a large surface area to volume ratio, high surface concentration (electric field distribution) of corner and edge atoms, low coordination numbers of surface atoms and unique electronic properties (quantum size effects). Moreover, in the case of structure sensitive reactions, these interactions of reactant species vary, depending on the crystallographic plane exposed on their surface. All these factors could be fine-tuned by the size, shape, composition, crystallinity and structure (solid versus hollow), which acquire a great relevance from the application point of view.

Besides the above factors, the presence of high-miller-index crystal faces also influences the electrocatalytic activity. For example, in the case of oxygen reduction reaction (ORR), it has been observed that electrocatalytic performance is higher for flower-like structures of gold compared to other shapes such as pinecone and nanosheets. This enhanced activity of gold flowers is ascribed to the presence of high miller- index crystal faces such as (220) and (331), which exposes their surface irregularities, steps and kinks [90]. Moreover, in the case of CO electro-oxidation on cubooctahedral Rh nanostructures bound by (111) and (100) facets, the transfer of CO molecules from (100) to (111) site takes place, since the latter is a thermodynamically favoured site for CO oxidation [91]. Electrocatalytic performance of nonspherical Rh nanostructures has been investigated for several fuel cell reactions to demonstrate their enhanced electrocatalytic activity. For example, low symmetry Rh (100) plane shows a higher electrocatalytic activity than that of Rh (111) in sulphuric acid towards the oxidation of CO [92].

1.7.2. Catalysis

Rhodium is a very important catalyst for many industrial processes because of its intrinsic ability to catalyze a wide range of heterogeneous reactions. On the other hand, the price of Rh is very high. Therefore, for the sake of maximum utilization of Rh, it is necessary to precisely control the size, shape and crystallographic plane of Rh crystals for exposing the maximum number of atoms to have highest atom efficiency and turnover number. This interaction as observed for normal catalytic reactions strongly depends on the surface properties of the catalyst. In the case of structure sensitive reactions, these interactions of reactant species do vary depending on different crystallographic planes exposed on the surface, and the coverage of intermediates.

High aspect ratio nanomaterials of Rh have important applications in catalysis due to their shape dependent catalytic activity. In particular, they exhibit different catalytic activity on their various crystallographic facets. Many interesting examples are available like the Suzuki coupling reaction, hydride transfer reaction, oxidation of alcohols into organic acids, selective hydrogenation/hydroformylation of unsaturated hydrocarbon compounds and petroleum refining process. In addition to this Rh is also a well-known catalyst for NOx reduction in three-way automobile catalysts. In all these applications, small clusters of Rh are found to be catalytically more reactive than bulk Rh metal as their chemical and electronic properties change with shape and size.

1.7.3. Field Emission Devices

Transition metal based nanostructures are one of the best known field emitters, especially if they have many sharp tips and edges. The smaller the radius of curvature of the tip is, the more is the concentration of the electric field, enabling increased field emission. The sharpness of the tip also means that they emit at especially low voltage, an important factor for building low-power electrical devices that utilize this feature [93]. Significantly, metal nanostructures can carry an astonishingly high current density with extremely high stability. An immediate application of this behavior receiving considerable interest is in field-emission flat-panel displays. Instead of a single electron

gun, as in a traditional cathode ray tube display, in metal nanowire-based displays there is a separate nanowire electron gun for each individual pixel in the display. Their high current density, low turn-on and operating voltages and steady, durable behavior make nanowires very attractive in this application. Other applications utilizing the field-emission characteristics of high aspect ratio metal nanostructures include general types of low-voltage cold-cathode lighting sources, lightning arrestors and electron sources.

1.7.4. Molecular Electronics

In recent years, nano-technology has led to a new way of making electronic devices and many novel devices in the field of information and communication technology, that have appeared recently in many laboratories of the world. One of these nano-devices, single electron tunneling device using small particles in their systems has been successfully prepared and many other devices like high-density memory devices, high-speed low power switching devices, high-sensitive electrometer devices and others are expected to be produced in the near future. Using an organic molecule as a coulomb island electrode, it is possible to use organic electronic devices based on the potential ability of molecules for flexible devices. For example, organic SET devices, using organic and inorganic insulators and ultra-narrow (nano-gap) electrodes have been investigated for the electrical properties of these single electron tunneling devices with or without light irradiation [94].

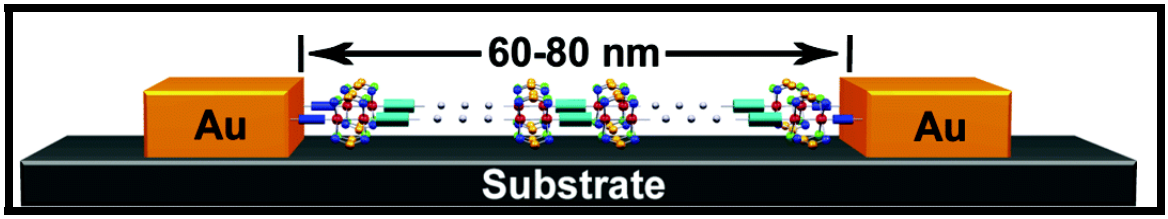

Figure 1.11. Layer-by-layer growth of Rh-Rh bonded supramolecular thin films through mercaptoethylpyridine and its use in fabrication of lateral nanoscale devices; adopted from [95].

Recently, Lin and coworkers have demonstrated layer-by-layer self-assembly of Rh-Rh bonded supramolecules to fabricate lateral nano-electronic devices by using sequential assembly of alternating layers of redox active dirhodium complexes like $[Rh_2(DAniF)_2]_2(O_2CCH_2CO_2)_2$ (DAniF=N, N′-di-p-anisylformamidinate) and conjugated

organic ligands trans-1,2-bis(4-pyridyl)ethylene as schematically shown in Figure 1.11. [95]. Moreover, tailoring the chemistry of templating ligand enables their more effective assembly on desired surfaces. The idea of building more efficient and flexible electronic circuits out of essential building blocks of materials and organic molecules has seen a major revolution during the past few years as one of the key components of nanoelectronics. Their geometry, interconnect design, electrical conductivity and ability to precisely fabricate nanowires, nanotubes as crucial parameters to control the performance of devices in molecular electronics including that of switches. A novel nanoelectronic component recently demonstrated has been a nanoscale transistor that can be switched between "on" and "off" states with a single electron which works efficiently at room temperature [96]. These tiny field-effect transistors (FETs) are individually controllable and can be integrated on a single chip. Prior to this study, nanoparticle FETs could not be turned on and off individually.

Similarly, when an aqueous suspension of Rh nanoparticles is placed in an alternating current between two planar electrodes, the particles assemble into conducting microwires that grown from one electrode to the other. However, the wires are not nanowires as their diameters are few micrometers, and the method represents an easy way to create electrical connections in liquid environments [97]. These wires could be used in wet electronic and bioelectronic circuits including that of chemical sensors. In another key step towards the fabrication of single-molecule electronic devices, researchers have wired a single molecule into an electrical circuit by chemically bonding two molecular ends to metal conductors [98]. The, current-voltage characteristics of the resulting circuit could be studied to reveal many fascinating issues about individual collisions at molecular level. A nanoparticle could be tethered to both the ends of a conjugated organic molecule acting as a molecular wire using the conducting tip of an atomic force microscope to contact the nanoparticle, thus forming a complete circuit [99]. However, there are tip induced artifacts and other contact problems which require low temperature for unraveling single molecular phenomenon without thermal fluctuations [100].

1.8. Conclusion and Perspectives

Anisotropic nanostructures of Rh constitute one of the most fascinating classes of nanomaterials which has attracted immense recent interest. After understanding the significance of high aspect ratio nanostructures and also their different synthetic routes, it is important to ask how the unique properties of these nanostructures could be exploited for various applications. This has been answered by considering their crucial role in the area of electrocatalytic reactions of formaldehyde and formic acid oxidation, relevant for fuel cells. There are also a range of applications for anisotropic nanostructures outside electrocatalysis, including molecular electronics, tunable optical signals, ultra-sensitive chemical and biosensors, micro/nano-electromechanical systems (MEMS/NEMS), optoelectronics, information storage, medical diagnostics and electron gun in various spectroscopic instruments. There are almost unlimited research opportunities in many of these applications of nanotechnology and the future potential is surely bright.

However, there are a number of unsolved issues that remain to be addressed before these materials could reach successful industrial applications. For example, in electrocatalysis, better performance of a catalyst requires the absence of surface passivating agents or foreign species and solid matrices for supports normally used during the synthesis, often via a soft route. More importantly, the nanostructures which are used as catalysts should have high uniformity in size and shape distribution along with plane selectivity on its surface to achieve their higher selectivity and product yield in organic transformations. However, a majority of the cases have the presence of strong surface passivating agents (or foreign species added to trigger the growth) giving rise to difficulties of separations and contamination. Furthermore, there are several other barriers to cross during the research on nanomaterials including many daunting tasks like addressing the environmental concern and societal impact of these materials since very little is known about their long term effects especially how they behave inside living organisms. Disposal and recyclability concerns also need to be addressed vis-a vis applications.

1.9. Motivation, Scope and Organization of the Thesis

The genesis of the present thesis is inspired by many of these interesting issues unfolded during the foregoing critical review related to both fundamental and applied aspects of various Rh nanostructures. This includes the development of new methods for the synthesis of high aspect ratio Rh nanostructures and their assemblies. If such nanostructures are made to organize in a controllable fashion along with their related hybrid structures, they can open up several unprecedented application possibilities. Consequently, it is imperative to study different properties such as electrochemical, electrical, optical, catalytic etc. of these materials for the pursuit of various applications.

1.10. Objectives of the Present Thesis

The foregoing critical review of Rh based nanostructures shows several important methods for their synthesis and applications, although several lacunae are still present impeding for their wide utilization for various applications. For example, most of the nanostructures synthesized by CVD (and other methods as well) contain other unwanted structures along with the desired materials or structures, whose removal is very troublesome. Also, the effect of temperature and other reaction conditions on the preparation methods is rather crucial to design these nanostructures in a desired manner. Since the nanostructures of Rh are very important as a backbone for the fabrication of electronic devices including FETs, electrochemical devices and flat panel displays, it is of immense importance to understand the influence of the reaction conditions on their chemical as well as physical properties. Further, their heterostructures with nanotubes (Rh-CNTs), especially, are extremely important in order to understand the interfacial interactions resulting into the improvement in desired properties. Furthermore, the use of Rh-CNTs as a support in electrocatalysis for various fuel cell reactions along with their use as heterogeneous catalysts for various organic transformations has tremendous utility due to their favorable characteristics such as high surface area, mechanical strength, inert carbon network and chemically tunable topography. Hence, it will be interesting to

explore the catalytic properties of Rh after making their hybrid materials with carbon based materials like carbon nanotubes, carbon nanospheres and graphene, where the effect of substrate along with their co-operative interactions plays an important role. Moreover, this hybrid structures having tunable features would be interesting to explore their behavior towards field emission application. The specific objectives of the work embodied in this thesis are set out in this perspective as follows:

(a) To synthesize anisotropic Rh nanostructures using chemical synthesis with the help of various surface bound molecules;

(b) To explore the electrochemical approach towards the synthesis of different morphology along with their tunable optical features based on their surface structure;

(c) To accomplish the shape-selective synthesis of Rh nanostructures (cubes, pyramids, hexagons) using chemical vapor deposition along with their electrocatalytic studies and their co-relation with surface structure;

(d) To elucidate the enhanced field emission and tunable electrical conductivity studies from these shapes;

(e) To synthesize and characterize the anchoring of monodispersed Rh nanoparticles on MWNTs for tunable field emission;

Hence, the objectives of the present investigation have been formulated to address some of these important challenges related to the synthesis, characterization and possible applications (especially in electrocatalysis and field emission) of high aspect ratio nanostructures of Rh. This system has been selected because of its outstanding role as multifunctional catalysts in many industrial applications and as efficient electrocatalysts in fuel cells. More interestingly, the fabrication of Rh/MWNTs hybrid materials has been discussed along with the results from their promising enhancement in field emission

behavior. These results have been explained in six separate chapters as per the following sequence.

First chapter represents a critical review of synthesis, characterization and various properties of differently shaped nanostructured materials. The electrical, chemical and other physical properties of these high aspect ratio nanostructures have been discussed in relation to their size and shape along with their assembly with emphasis on nanomaterials of Rh. The impact of these materials on nanotechnology for diverse applications such as catalysis, electronic, electrochemical and magnetic device construction, environmental and pollution control has been discussed concisely. Specific objectives of the present study have been elaborated in the end with special relevance for future applications especially for electrocatalytic activity and field emission behavior. Finally, a few of the major existing limitations with respect to synthesis and processing of these high aspect ratio materials are also discussed.

Second chapter deals with a synthesis of highly monodispersed nonspherical Rh nanoparticles along with high aspect ratio (nanochains, nanoneedles and nanorods) nanostructures by using modified colloidal approach with the help of various mono and polyfunctional organic molecules including various amines, acids and polymers. These nanomaterials have been further characterized by techniques including Scanning electron microscopy (SEM), High resolution transmission electron microscopy (HRTEM), X-ray photoelectron spectroscopy (XPS), Thermogravimetry (TG), Raman Spectroscopy, Furrier Transform infrared spectroscopy (FTIR), X-ray diffraction (XRD), DC conductivity and Cyclic Voltammetry (CV). Considering different time scales of various reactions and the diffusion of different reactants and products, a tentative growth mechanism has been proposed in conjunction with possible multidimensional role of organic molecules towards the assembly formation. Finally, electro-catalytic activity of these nanostructures has been discussed towards formic acid oxidation, as an important test reaction for micro-fuel cells.

Third chapter demonstrates the preparation of Rh nanostructures through a galvanic displacement approach using Al substrate as a sacrificial material. The structural

and morphological characterization data from TEM, SEM, Surface plasmon resonance (SPR) and XRD have been discussed followed by electrochemical measurements including CV and I/t kinetics suggesting the formation of Rh nanostructures presumably through the formation of micro-galvanic cells. Further, the role of the applied potential, concentration of Rh source, pH, temperature, presence of capping molecules (PVP) and their effect on the diffusion of reactant (Rh^{3+}) and product (Rh^{0}) species toward and away from the surface of the Al has been elucidated using important experimental data obtained using all these techniques. These Rh nanostructures, significantly exhibit enhanced electrocatalytic activity toward many fuel cell reactions as demonstrated by results obtained using formaldehyde oxidation as a model reaction.

Fourth Chapter demonstrates synthetic strategies for stabilizing different shapes of Rh nanostructures like hexagons, cubes, pyramids with the help of a modified chemical vapor deposition (CVD) method. These nanostructures have been characterized using a host of techniques like SEM, TEM, XRD, XPS and TGA to reveal the similarities and differences with respect to solution phase growth demonstrated in earlier chapters. Further, their electrocatalytic activity has been tested using CV and I/t transient, highlighting their unique shape-dependent reactivity towards formic acid oxidation. A comparison of the electrocatalytic activities of these remarkable structures towards formic acid oxidation as compared to other shapes helps in correlating activity with crystallographic orientation obtained from x-ray diffraction analysis. Further electrical conductivity measurements as a function of temperature for all the as-synthesized nanostructures suggest a metallic behavior. A remarkable field emission behavior from same Rh hexagons have been discussed at the end of this chapter where, the presence of sharp tips of the nanopotrusions with a higher areal density is indicated to be responsible for a stable current density along with their excellent current and mechanical stability toward ions bombardment. The smaller size of emitting area, excellent current density, and stability over a period of more than 3h are promising characteristics for the development of electron sources using these nanomaterials.

Fifth Chapter deals with various synthetic attempts towards the synthesis of high quality carbon nanotubes (CNTs) along with their heterostructures with Rh nanostructures. In one such attempt targeted for the synthesis of heterostructures, Rh nanospheres have been anchored on acid functionalized multi-walled carbon nanotubes (MWNTs) after formation using Al (reducing substrate for Rh ions) followed by their characterization using SEM, TEM, XPS and XRD techniques. Raman spectroscopic studies have also revealed independent evidence for the mechanism of oxidative functionalization followed by effective decoration of Rh nanospheres at the defect sites of the MWNTs. The higher current density at an ultra low applied field indicates the origin of extraordinary emission performance from the co-operative interaction of Rh with MWNTs.

A summary of all the major conclusions of the present study with respect to the shape selective synthesis of Rh nanostructures, their heterostructure formation with CNTs along with their structure-property relationship and effects on various properties like electrocatalytic, SPR and electron transfer are discussed in **chapter six**. One of the key results is the synthesis of highly monodispersed and shape selective Rh nanostructures with tunable reactivity and their presumable mechanism of formation by CVD. In addition, a simple and efficient method of chemical functionalization of MWNTs has been discussed with enhanced water solubility. This could be obtained only by a rapid and efficient generation of an appreciable amount of hydrophilic functional groups using microwave radiation followed by Rh decoration as demonstrated by their further electrochemical, spectroscopic and field emission behaviour. Other related experimental studies also clearly show the usefulness of acid functionalization in synthesizing Rh/MWNTs hybrid materials. The physical properties of these hybrid nanostructures are indeed, different from that of their individual counterparts indicating their intrinsic flexibility for tuning properties based on co-operative interactions between the individual components. However, several limitations such as size and shape selectivity of catalysts, wide distribution of different sizes and their interconversion could restrict their wide spread commercial applications and further work is desired to alleviate some of these

disadvantages. Various other barriers such as long reaction time, tendency of temperature dependent reorganization and reorientation of the capping organic monolayer, and the enhanced sensitivity towards environment also need to be addressed seriously. Despite these limitations, the results of present study are believed to be useful to understand several fundamental phenomena of metal nanostructures for fabricating nanoscale devices in future.

The results presented in the thesis clearly suggest the usefulness of high aspect ratio nanostructures of Rh as a multifunctional nanomaterial for many industrial applications like electrocatalysis, field emission and nanoelectronics in comparison to that of bulk Rh. The possibility of manipulating the electron transfer properties of Rh by shape, size and aspect ratio has been demonstrated in this thesis, which is expected to hopefully resolve several important issues related to fundamental properties of Rh nanostructures.

1.11. References

1. (a) Buentello, F. S.; Persad, D. L.; Court, E. B.; Martin, D. K.; Daar, A. S.; Singer, P. A. *PLoS Medicine* **2005**, *2*, **97**. (b) Kearnes, M.; Grove-White, R.; Macnaghten, P.; Wilsdon, J.; Wynne, B. *Science as Culture. Science* **2006,** *15,* **291**. (c) http://www.informaworld.com (d) http://www.etcgroup.org/ documents/Com8788SpecialPNano (d) Scrinis, G.; Lyons, K. *International Journal of Sociology of Agriculture and Food* **2007**, *15,* **2**.
2. (a) http://www.nanotec.org.uk (b) http://busca.estadao.com (c) http://www.nsti.org/Nanotech2004
3. (a) http://mems.sandia.gov/tech-info/mems-overview.html (b)Melosh,N.; Boukai, A.; Diana, F.; Gerardot, B.; Badolato, A.; Petroff, P.; Heath, J. R. *Science* **2003**, *300*, **112**. (c) Das, S.; Gates, A. J.; Abdu, H. A.; Rose, G. S.; Picconatto, C. A.; Ellenbogen, J. C. *IEEE Trans. on Circuits and Systems I* **2007**, *54*, **11**. (d) Goicoechea, J.; Zamarreñoa, C. R.; Matiasa, I. R.; Arregui, F. J. *Sensors and Actuators B* **2007**, *126,* **41**. (e) Aviram, A.; Ratner, M. A. *Chem. Phys. Lett*. **1974**, *29*, **277**. (g) Aviram, A. *J. Am. Chem. Soc*. **1988**, *110*, **5687**. (f) Jensen, K.; Weldon, J.; Garcia, H.; Zettl A. *Nano Lett*. **2007**, *7*, **3508**. (g) Postma; Henk W. Ch.; Teepen, T.; Yao, Z.; Grifoni, M.; Dekker, C. *Science* **2001,** *293*, **76**. (h) Xiang, J.; Lu, W.; Hu, Y.; Wu, Y.; Yan, H.; Lieber, C. M. *Nature* **2006**, *41*, **489**. (i) Tian, B.; Zheng, X.; Kempa, T. J.; Fang, Y.; Yu, N.; Yu, G.; Huang, J.; Lieber, C. M. *Nature* **2007**, *449*, **885**. (j) LaVan, D. A.; McGuire, T.; Langer, R. *Nat Biotechnol.* **2003**, *21*, **1184**. (k) Grace, D. *Medical Product Manufacturing News* ***2008***, *12*, **22**. (l) Saito, S. *Science* **1997**, *278*, **77**. (m) Cavalcanti, A.; Shirinzadeh, B.; Freitas, R. A.; Hogg, T. *Nanotechnology* **2008**, *19*, 015103. (n) Cheng, M. M. C.; Cuda, G.; Bunimovich, Y. L.; Gaspari, M.; Heath, J. R.; Hill, H. D.; Mirkin, C. A.; Nijdam, A. J.; Terracciano, R.; Thundat, T.; Ferrari, M. *Curr. Opin. Chem. Biol*. **2006**, *10*, **11**. (o) Patolsky, F.; Timko, B. P.; Yu, G.; Fang, Y.; Greytak, A. B.; Zheng, G.; Lieber, C. M. *Science* **2006**, *313*, **1100**. (p) Frist, W. H. *N. Engl. J. Med*. **2005**, *352*, **267**. (q)

Cavalcanti, A.; Shirinzadeh, B.; Zhang, M.; Kretly, L. C. *Sensors* **2008**, *8*, **2932**. (r) Couvreur, P. ; Vauthier, C. *Pharm. Res.* **2006**, *23*, **1417**.

4. (a) Xuan, Y.; Wu, Y. Q.; Shen, T.; Qi, M.; Capano, M. A.; Cooper, J. A.; Ye, P. D. *Appl. Phys. Lett.* **2008**, *92*, **013101**. (b) Lu, W.; Lieber, C. M. *Nature Mater.* **2007**, *6*, **841.** (c) Borghetti, J.; Snider, G. S.; Kuekes, P. J.; Yang, J. J.; Stewart, D. R.; Williams, R. S. *Nature* **2008,** *464*, **873.** (e) Pirovanol, A.; Schuegraf, K. *Nat. Nanotechnol.* **2010**, *5*, **177.**
5. (a) Cao, G. *Nanostructures & Nanomaterials: Synthesis, Properties and Applications*, **2004**, ISBN 186094-415-9 (b) Regan, L.; DeGrado, W. F. *Science* **1988**, *241*, **976**. (c) Kroto, H. W. *Nature* **1985**, *318*, **162**. (d) Iijima, S. *Nature* **1991**, *354*, **56**. (e) Binnig, G.; Rohrer, H. *Rev. Mod. Phys*. **1987**, *59*, **615**. (f) Watzky, M. A.; Finke, R. G. *J. Am. Chem. Soc*. **1997**, *119*, **10382**. (g) Murray, C. B. *J. Am. Chem. Soc.* **1993**, *115*, **8706**. (h) Peng, X. *Nature* **2000**, *404*, **59**. (i) Gates, B. *Adv. Funct. Mater*. **2002**, *12*, **219**. (j) Wagner, R. S.; Ellis, W. C. *Appl. Phys. Lett*. **1964**, *4*, **89**. (k) Trentler, T. J. *Science* **1995**, *270*, **1791**. (l) Morales, A. M.; Lieber, C. M. *Science* **1998**, *279*, **208**. (m) Duan, X.; Leiber, C. M. *Adv. Mater.* **2000**, *12*, **298**. (n) Holmes, J. D. *Science* **2000**, *287*, **1471**. (o) Wu, Y.; Yang, P. *J. Am. Chem. Soc*. **2001**, *123*, **3165**. (p) Yu, H. *Nat. Mater*. **2003**, *2*, **517**. (q) Yu, H. *J. Am. Chem. Soc*. **2003**, *125*, **16168**. (r) Xia, Y. *Adv. Mater*. **2003**, *15*, **353**. (s) Smalley, R. E. *Nanotechnology Energy and People* 23, **2005**. (u) McGhee, M. D.; Coakley, K. M. *Chem. Mater*. **2004**, *16*, **4533**. (v) Shaheen, S. E. *Mater. Res. Bull*. **2005**, *30*, **10**. (w) Hoppe, H.; Sariciftci, N. S. *J. Mater. Res.* **2004**, *19*, **1924**. (x) Nierengarten, J. F. *New. J. Chem*. **2004**, *28*, **1177**. (y) Xue, J. *Appl. Phys. Lett*. **2005**, *86*, **5757**. (z) Strano, M. S. *Nat. Mater*. **2005**, *4*, **86**.
6. (a) Kordesch, K.; Simader. G. *Fuel Cells and Their Application*, VCH, Weinheim, **1996**. (b) Brayner, R. *J. Mol. Catal. A: Chem*. **2002**, *182*, **227**. (c) Liu, C. *J. Mol. Catal. A: Chem*. **2000**, *157*, **253**. (d) Drelinkiewicz, A. J. *Catal*. **1999**, *186*, **123**. (e) Joo, S. H. *Nature* **2001**, *412*, **169**. (f) Yuan, F. *J. New Mater.*

Electrochem. Syst. **2004**, *7*, **311**. (g) Planeix, J. M. *J. Am. Chem. Soc*. **1994**, *116*, **7935**. (h) Zhu, J. *Nano Lett*. **2003**, *3*, **1033**. (j) Takagi, M. *Scripta Mater*. **2001**, *44*, **2145**. (k) Bhattacharya, V.; Chattopadhyay, K. *Scripta Mater*. **2001**, *44*, **1677**. (l) Ferkel, H.; Mordike, B. L. *Mater. Sci. Eng. A* **2001**, *298*, **193**. (m) Dong, S. R. *Mater. Sci. Eng. A* **2001**, *313*, **83**. (n) Kuzumaki, T. K. *Adv. Eng. Mater*. **2000**, *2*, **416**. (o) Xu, C. L. *Carbon* **1999**, *37*, **855**. (p) Ying, D. Y.; Zhang, D. L. *Mater. Sci. Eng. A* **2000**, *286*, **152**. (q) El-Eskandarany; Sherif, M. J. *Alloys Compd.* **1998**, *279*, **263**. (r) Rohatgi, P. K. *Int. Mat. Rev*. **1986**, *31*, **115**. (s) Kawabe, A. *J. Jpn. Inst. Met.* **1999**, **149**. (s) Liu, H. *Mater. Manuf. Processes*. **1997**, *12*, **831**.

7. (a) Friedman, R. S.; McAlpine, M. C.; Ricketts, D. S.; Ham, D.; Lieber, C. M. *Nature* **2005**, *434*, **1085**.
8. (a) Deshpande, V. V.; Bockrath, M.; Glazman, L. I.; Yaco, A. *Nature* **2010**, *464*, **209**. (b) Tkachenko, V. A.; Baksheyev, D. G.; Tkachenko, O. A.; Liang, C. T. *JETP Lett.* **2001**, *74*, **209**.
9. Bhushan, B. (Ed.) *Springer handbook of nanotechnology* **2004**, Spinger-Verlag Berlin Heidelberg New York.
10. (a) Ihn, J. B.; Chang, F. K. *Smart Mater. Struct.* **2004**, *13*, **621**. (b) Liao, W. H. *Smart Mater. Struct*. **2010**, *19*, **120201**. (c) Robert S. Chem. Mater., 1996, 8, 1747.
11. (a) Wang, S.; Jiang, L. *Adv. Mater.* **2007**, *19*, **3423**. (b) Young, T. *Phil. Trans. R. Soc. Lond*. **1805**, *95*, **65**. (c) Wenzel, R. N. *Ind. Eng. Chem*. **1936**, *28*, **988**. (d) Extrand, C. *Langmuir* **2005**, *68*, **2495**. (e) Johnson, R E.; Dettre, R. H. *J. Phys. Chem*. **1964**, *68*, **1744**. (f) Onda, T.; Shibuichi, S.; Satoh, N.; Tsujii, K. *Langmuir* **1996**, *12*, **2125**. (g) Miwa, M.; Nakajima, A.; Fujishima, A.; Hashimoto, K.; Watanabe, T. *Langmuir* **2000**, *16*, **5754**. (h) Shirtcliffe, N. J.; McHale, G.; Newton, M. I.; Perry, C. C. *Langmuir* **2003**, *19*, **5626**. (i) Teare, D.; Spanos, C. G.; Ridley, P.; Kinmond, E. J.; Roucoules, V.; Badyal, J. P. S.; Brewer, S. A.; Coulson, S. *Chem. Mater.* **2002**, *14*, **4566**. (j) Bico, J.; Marzolin,

C.; Quere, D. *Europhys. Lett.* **1999**, *47*, **743**. (k) Extrand, C. *MRS Bulletin* **2008**, **733**. (p) Gao, L. C.; McCarthy, T. J. *Langmuir* **2007**, *23*, **3762**. (l) Chen, W.; Fadeev, A. Y.; Hsieh, M. C.; Oner, D.; Youngblood, J.; McCarthy, T. J. *Langmuir* **1999**, *15*, **3395**. (m) Wang, S. T.; Liu, H.; Jiang, L. *Ann. Rev. Nano Res*. **2006**, *1*, **573**. (n) Lim, H. S.; Kwak, D.; Lee, D. Y.; Lee, S. G.; Cho, K. *J. Am. Chem. Soc.* **2007**, *129*, **4128**. (o) Xue, C. H. *Sci. Technol. Adv. Mater*. **2008**, *9*, **035008**. (p) Xue, C. H. *Sci. Technol. Adv. Mater*. **2008**, *9*, **035001**. (q) Yuan, Z. *Sci. Technol. Adv. Mater*. **2008**, *9*, **045007**. (r) Ressine, A.; Marko-Varga, G.; Laurell, T. *Biotechnol. Ann. Rev.* **2007**, *13*, **149**.

12. (a) Zhen H. L.; Donald G. T. *J. Am. Chem. Soc*. **2008**, *130,* **12698**. (b) Nagarajan, R. *Nanoparticles: Synthesis, Stabilization, Passivation, and Functionalization. ACS Symposium Series* **2008**, *996,* **2.** (c) Drexler, E. *Engines of Creation: The Coming Era of Nanotechnology;* Anchor Press/ Doubleday: New York, **1986**. (d) Drexler, K. E. *Nanosystems: molecular machinery, manufacturing and computation;* John Wiley & Sons: New York, **1992**. (e) Kohler, M.; Fritzsche, W. *Nanotechnology, An Introduction to Nanostructuring Techniques*, Wiley-VCH Verlag GmbH and Co. KgaA, **2004**.
13. (a) West, A. R. *Solid State Chemistry and Its Applications.* **ISBN: 978-0-471-90874-6.** (b) Cottey A. A. *J. Phys. C: Solid State Phys.***1971**, *4,* **1734**
14. http://www.nanowerk.com
15. Schmid, G.; Corain, B. *Eur. J. Inorg. Chem.* **2003**, **3081**.
16. (a) Wolfe, R. L.; Murray, R. W. *Anal. Chem.* **2006**, *78*, **1167**. (b) Stiles, R. L.; Balasubramanian, B.; Feldberg, S. W.; Murray, R. W. *J. Am. Chem. Soc*. **2008**, *130*, **1856**. (c) Kim, Y.G.; Garcia-Martinez, J. C.; Crooks, R. M. *Langmuir* **2005**, *21*, **5485**. (d) Wolfe, R. L.; Balasubramanian, R.; Tracy, J. B.; Murray, R. W. *Langmuir* **2007**, *23,* **2247**. (e) Chen, S.; Sommers, J. M. *J. Phys. Chem. B* **2001**, *105,* **8816**. (f) Murray R. W. *Chem. Rev*. **2008**, *108,* **7**. (g) Thumu, U. B.; Rao, B. N.; Thalappil, P. *J. Am. Chem. Soc*. **2010**, *132*, **16305.**
17. (a) Raether, H. *"Surface plasmons on smooth and rough surfaces and on*

gratings". Springer Verlag, Berlin. ISBN 978-3540173632, **1988**. (b) Stefan Maier, S. "*Plasmonics: Fundamentals and Applications"*. Springer. ISBN 978-0387331508, **2007**. (c) Richard B.M.S.; Tudos, J. A. *"Handbook of Surface Plasmon Resonance"*. RSC publishing. ISBN 978-0-85404-267-8, **2008**.

18. (a) Cullity, B. D.; Graham, C. D. "*Introduction to Magnetic Materials"*. *II*nd Ediation, Wiley-IEEE. ISBN 0471477419, **2008**. (b) Buzea, C.; Pacheco, I.; Robbie, K. *"Nanomaterials and Nanoparticles: Sources and Toxicity"*. Biointerphases 2 (4): MR17–MR71, **2007**.
19. Thilly, L; Lecouturier, F.; Coffe, G.; Peyrade, J. P.; Askenazy, S. *Physica B: Condens. Mat.* **2001**, *648,* **294**.
20. (a) Day, S.; Goswami, J.; Gu, D.; Waard, H.; Marcus, S.; Werkhoven, C.; *Appl. Phys. Lett*. **2004**, 84, **1606**. (b) Park, K.; Parsons, G. *Appl. Phys. Lett*. **2006**, 89, **043111**.
21. (a) Cotton, F. A.; Wilkinson, G. *Advance Inorganic Chemistry*, 4th ed. Wiley, NewYork,**1980**.(b) www.kitco.com ; http://www.kitco.com/charts/ rhodium.html (c) http://www.webelements.com/webelements/ elements/text/Rh/hist.html
22. Brandt, E. P.; Wang, Y.; Grizzle, W. J. *IEEE Transactions On Control Systems Technology,* **1999**, *10,* **120.**
23. Zoeller, J. R.; Agreda, V. H.; Cook, S. L.; Lafferty, N. L.; Polichnowski, S. W.; Pond, D. M. *Catalysis Today* **1992,** *13*, **73**.
24. (a) Myers, C. J.; and, Penn, L. R. *J. Phys. Chem. C* **2007**, *111,* **10597.** (b) Sardar, R.; Funston, M. A.; Mulvaney, P.; Murray, W. R.; *Langmuir* **2009**, 2*5,* ***13840*** *(c) Mo*stafa, *S.*; Behafarid, F.; Croy, J. R.; Ono, L. K.; Li, L.; Yang*,* J. C.; Frenkel**,** A. I.; Cuenya, B. R. *J. Am. Chem. Soc.* **2010**, *132*, **15714**. (d) Njoki, P. N; Jacob, A.; *K*han, B.; Luo, J.; Zhong, C. J. *J. Phys. Chem. B* **2006,** *110,* **22503.** (e) Kruszynska,M.; Borchert, H.; Parisi, J.; Olesiak, J. K *J. Am. Chem. Soc.* **2010**, *132***, 15976**. (f) Niederberger, M. *Acc. Chem. Res.* **2007,** *40,* **793**. (g) Murphy, C. J.; Sau, **T. K.**; Gole, A. M.; Orendorff C. J.; Gao, J.:, Gou, L.; Hunyadi, S. E.; Li, *T. J. Phys. Chem. B* **2005**,109**, 13857**. (h) Narayanan, R.; El-

Sayed, M. A. *Nano Lett.* **2004**, *4,* **1343.** (i) Christopher, P.; Ingram, B. B.; Linic, S. *J. Phys. Chem. C* **2010**, *114*, **9173** (j) Narayanan, R.; El-Sayed, M. **A.** *J. Phys. Chem. B* **2005,** *109* **12663** (k) Zhu, J.; Liu, S.; *Pal*chik, O.; Koltypin, Y.; Gedanken, A. *Langmuir* **2000**, *16,* **6396**. *(l)* Snchez-Snchez, C. M.; Solla-Gulln, J.; Vidal-Iglesias, F. J.; Aldaz, A.; Montiel, V.; Herrero, E. *J. Am. Chem. Soc.* **2010**, *132*, **5622**. (m) Hernández, J.; Solla-Gullón, J**.; H**errero**, E.**; Aldaz, A.; Feliu, J. M. *J. Phys. Chem. C* **2007**, *111*, **14078**. (n) Radi, A.; Pradhan, D.; Sohn, Y.; Leung, K. T. *ACS Nano* **2010,** *4,* **1553. (**o) Chen, M.; Cai, Y.; Yan, Z.; Goodman, D. W. *J. Am. Chem. Soc*. **2006**, *128*, **63*41***. *(p) Grozovsk*i**,** V.; Solla-Gulln, J.; Climent, V.; Herrero, E.; Feliu, J. M. *J. Phys. Chem. C* **2010**, *114,* **13802**. (q) Murphy, C. J.; Gole,A. M.; Stone, J. W.; Sisco, P. N.; Alkilany, A. M.; Goldsmith, E. C.; Baxter, S. C. *Acc. Chem. Res*. **2008**, *41,* **1721**. (r) Okitsu, *K.; Sharyo, K.;* Nishimura, R. *Langmuir* **2009**, *25*, **7786**. (s) Wiley, B.; Herricks, T.; Sun, Y.; Xia, Y. *Nano Lett.* **2004**, *4,* **1733**.

25. (a) Pan, H. B.; Wai, C. M. *J. Phys***.** *Chem.* **C 2009**, *113,* **19782**. (b) Pan, H. B.; Wai, C. M. *J. Phy***s. *C***hem. *C* **2010**, *114,* **11364**. (c) Buil, M. L.; Esteruelas, M. A.*; Niembro*, **S.;** Oliv**n, M**.; Orzechowski, L.; Pelayo, C.; Vallribera, A. *Organometallics* **2010**, *29,* **4375**. (d) Weissermel, K.; Arpe, H.-J. *Industrial Organic Chemistry; VCH: New York,* **1993**. (e) Schulz, J.; Roucoux, A.; Patin, H. *Chem. Commun.* **1999,** *35,* **535**.
26. (a) Barbaro, P.; Bianchini, C.; Santo, V. D.; Meli, A.; Moneti, S.; Pirovano, C.; Psaro, R.; Sordelli, L.; Vizza, F. *Organometallics* **2008**, *27,* **2809**. (b) Poirier, G. E.; Hance, B. K.; White, J. M. *J. Phys. Chem. C* **1993**, *97,* **6500**. (c) Finocchio, E.; Busca, G.; Pio Forzatti, P.; Groppi, G.; Beretta, A. *Langmuir* **2007**, *23,* **10419** (d) Motoyama, Y.; Takasaki, M.; Yoon, S. H.; Mochida, I.; Nagashima, H. *Org. Lett.* **2009**, *11*, **5042**. (e) Izumi, Y.; Konishi, K.; Tsukahara, M.; Obaid, D. M.; Aika, K. *J. Phys. Chem. C* **2007**, *111,* **10073** P. (f) Barinov, D. A.; Gregoratti, L.; Scaini, D.; He, Y. B.; Over, H.; Kiskinova, M. *J. Phys. Chem. C* **2008**, *112,* **9040** (g) Martinez, I. S.; Ewels, C. P.; Ke, X.; Tendeloo, G.

V.; Thiess, S.; Drube, W.; Felten A.; Pireaux, J. J.; Ghijsen, J.; Bittencourt, C. *ACS Nano* **2010**, *4,* **1680**. (h) Ziegelbauer, J. M.; Gatewood, D.; Gull, A. F.; Guinel, M.; Ernst, F.; Ramaker, D. E.; Mukerjee, S. *J. Phys. Chem. C* **2009**, *113,* **6955**. (i) Zhang, W.; Yanagisawa, K.; Kamiya, S.; Shou, T. *Cryst. Growth. Des*. **2009**, *9,* **3765**.

27. (a) Berchmans, S.; Thomas, P. J.; Rao, C. N. R. *J. Phys. Chem. B* **2002**, *106,* **4647**. (b) Lee, D.; Donkers, R. L.; DeSimone, J. M.; Murray, R. W. *J. Am. Chem. Soc*. **2003**, *125,* **1182**. (c) Pillai, Z. S.; Kamat, P. V. *J. Phys. Chem. B* **2004**, *108,* **945**. (d) Chaki, N. K. ; Singh, P. ; Dharmadhikari, C. V. ; Pillai, V. K. *Langmuir* **2004**, *20*, **10208**. (e) Peng, X. *Adv. Mater*. **2003**, *15,* **459**. (f) Schmid, G. Nanoparticles: From Theory to Application; Wiley-VCH: **2004.** (g) Cao, G. Nanostructures and Nanomaterials: Synthesis, Properties and Applications; Imperial College London, **2004**. (h) Peng, S.; Wang, C.; Xie, J.; Sun, S. *J. Am. Chem. Soc*. **2006**, *128*, **10676**. (i) Ganesan, M.; Freemantle, R. G.; Obare, S. O. *Chem. Mater*. **2007**, *19,* **3464**. (j) Kim, M. K.; Jeon, Y. M.; Jeon, W. S.; Kim, H. J.; Hong, S. G.; Park, C. G.; Kim, K. *Chem. Commun*. **2001**, 667. (k) Brust, M.; Walker, M.; Bethell, D.; Schiffrin, D. J.; Whyman, R. J. *Chem. Commun.* **1994**, 801. (l) Egusa, S.; Redmond, P. L.; Scherer, N. F. *J. Phys. Chem. C* **2007**, *111,* **17993**.

28. (a) Yuanab, Q.; Wang, X. *Nanoscale* **2010**, *2,* **2328** (b) Lim, B.; Jiang, M.; Camargo,P. H. C.; Cho, E. C.; Tao, J.; Lu, X.; Zhu, Y.; and Xia, Y. *Science* **2009**, *324,* **1302**. (c) Jana, N. R.; Wang, Z. L.; Sau, T. K.; Pal, T. *Curr. Sci.* **2000**, *79*, **1367**. (d) Hoefelmeyer, J. D.; Niesz, K.; Somorjai, G. A.; Tilley, T. D. *Nano Lett.* **2005**, *5*, **435**. (e) Zettsu, N.; McLellan, J. M.; Wiley, B.; Yin, Y.; Li, Z.; Xia, Y. *Angew. Chem. Int. Ed*. **2006**, *45,* **1288**. (f) Zhang, Y.; Grass, M. E.; Kuhn, J. N.; Tao, F.; Habas, S. E.; Huang, W.; Yang, P.; Somorjai, G. A. *J. Am. Chem. Soc*. **2008**, *130,* **5868**. (g) Mahmoud, M. A.; Tabor, C. E.; El-Sayed, M. A.; Ding, Y.; Wang, Z. L. *J. Am. Chem. Soc*. **2008**, *130*, **4590**. (h) Lim, B.; Jiang, M. J.; Camargo, P. H. C.; Cho, E. C.; Tao, J.; Lu, X. M.; Zhu, Y. M.; Xia,

Y. N. *Science* **2009**, *324*, **1302**.

29. (a) Leontidis, E.; Kleitou, K.; Kyprianidou, T.; Bekiari, V.; Lianos, P. *Langmuir* **2002**, *18*, **3659**. (b) Mahmoud, M. A.; Tabor, C. E.; El-Sayed, M. A.; Ding, Y.; Wang, Z. L. *J. Am. Chem. Soc*. **2008**, *130,* **4590**. (c) Lim, B.; Jiang, M. J.; Camargo, P. H. C.; Cho, E. C.; Tao, J.; Lu, X. M.; Zhu, Y. M.; Xia, Y. N. *Science* **2009**, *324*, **1302**. (d) Xiong, Y.; McLellan, J. M.; Yin, Y.; Xia, Y. *Angew. Chem., Int. Ed.* **2007**, *46,* **790**. (e) Yau, S. L.; Kim, Y. G.; Itaya, K. *J. Am. Chem. Soc*. **1996**, *118,* **7795**.
30. (a) Murphy, C.; Sau, T.; Gole, A.; Orendorff, C. *Mater. Res. Bull.* **2005**, *30,* **349**. (b) Sun, Y.; Gates, B.; Mayers, B.; Xia, Y. *Nano Lett*. **2002**, *2,* **165**. (c) Sun, Y.; Yin, Y.; Mayers, B. T.; Herricks, T.; Xia, Y. *Chem. Mater*. **2002**, *14,* **4736**.
31. Chen, J.; Herricks, T.; Geissler, M.; Xia, Y. *J. Am. Chem. Soc*. **2004**, *126,* **10854**.
32. (a) Elechiguerra, J. L.; Reyes-Gasga, J.; Yacaman, M. J. *J. Mater. Chem*. **2006**, *16,* **3906**. (b) Hulteen, J. C.; Martin, C. R. *J. Mater. Chem*. **1997**, *7,* **1075**. (c) Kline, T. R.; Tian, M.; Wang, J.; Sen, A.; Chan, M. W. H.; Mallouk, T. E. *Inorg. Chem.* **2006**, *45*, **7555**. (d) Luo, Y.; Lee, S. K.; Hofmeister, H.; Steinhart, M.; Gosele, U. *Nano Lett*. **2004**, *4*, **143**. (e) Sehayek, T.; Lahav, M.; Popovitz-Biro, R.; Vaskevich, A.; Rubinstein, I. *Chem. Mater*. **2005**, *17*, **3743**. (f) Jana, N. R.; Gearheart, L.; Murphy, C. J. *J. Phys. Chem. B* **2001**, *105*, **4065**. (g) Yu, Y. Y.; Chang, S. S.; Lee, C. L.; Chris Wang, C. R. *J. Phys. Chem. B* **1997**, *101*, **6661**. (h) Zhang, D.; Qi, L.; Ma, J.; Cheng, H. Chem. Mater. **2001**, *13*, **2753**. (i) Nikoobakht, B.; El-Sayed, M. A. *Chem. Mater*. **2003**, *15*, **1957**.
33. Pradhan, M.; Sarkar, S.; Sinha, A. K.; Basu, M.; Pal, T. *J. Phys. Chem. C* **2010**, *114,* **16129.**
34. Yuan, Q.; Zhou, Z.; Zhuang, J.; Wang, X. *Inorg. Chem*. **2010**, *49,* **5515**
35. Ewers, T. D.; Sra, A. K.; Norris, B. C.; Cable, R. E.; Cheng, C. H.; Shantz, D. F.; Schaak R. E. *Chem. Mater*. **2005**, *17*, **514**
36. (a) Peng, S.; Wang, C.; Xie, J.; Sun, S. *J. Am. Chem. Soc*. **2006**, *128,* **10676**. (b) Pradhan, D.; Leung, K. T. *Langmuir* **2008**, *17,* **9707**. (c) Subhramannia, M.;

Pillai, V. K. *J. Mater. Chem*. **2008**, *18,* **5858**. (d) Skrabalak, S. E.; Chen, J.; Sun, Y.; Lu, X.; Au, L.; Cobley, C. M.; Xia, Y.; *Acc. Chem. Res*. **2008**, *41*, 1587. (e) Singh, A. V.; Bandgar, B. M.; Kasture, M.; Prasad, B. L. V.; Sastry, M. *J. Mater. Chem*. **2005**, *15,* **5115**.

37. Muñoz, A. G.; Skorupska, K.; Lewerenz, H. J. *ChemPhys Chem* **2010**, *11,* **2919.**
38. Bi, Y.; Lu, G. *Chem. Commun*. **2008**, *47,* **6402**
39. Mohammad, A. M.; Abdullah, A. M.; El-Anadouli, B. E.; Mohney , S. E. *Inter. J. Nanomanufacturing* **2009**, *4,* **146**.
40. (a) Govindaraj, A.; Satishkumar, B. C.; Nath, M.; Rao, C. N. R. *Chem. Mater.* **2000**, *12*, **202**. (b) Fullam, S.; Cottel, D.; Rensmo, H.; Fitzmaurice, D. *Adv. Mater*. **2000**, *12,* **1430**.
41. A. Fukuoka, Y. Sakamoto, M. Ichikawa, *J. Am. Chem. Soc*., **2001**, *123,* **3373.**
42. (a) Wai, C.; Ye, X.; Lin, Y. D.; *Nanostructured Materials Synthesized in Supercritical Fluid" Encyclopedia of Nanoscience and Nanotechnology* 6th Volume **2004** (b) Pan, B. H.; Wai, C M. *J. Phys. Chem. C* **2009**, *113,* **19782.** (c) Ferrando, R.; Jellinek, J.; Johnston, R. L. *Chem. Rev*. **2008**, *108*, **845**. (d) Cademartiri, L.; Ozin, G. *Adv. Mater*. **2009**, *21*, **1013**. (e) Zhang, Q.; Ge, J.; Pham, T.; Goebl, J.; Hu, Y.; Lu, Z.; Yin, Y. D. *Angew. Chem., Int. Ed.* **2009**, *48,* **3516**. (f) Dumestre, F.; Chaudret, B.; Amiens, C.; Renaud, P.; Fejes, P. *Science* **2004**, *303*, **821**. (j) Huang, X.; Zhang, H.; Guo, C.; Zhou, Z.; Zheng, N. *Angew. Chem., Int. Ed*. **2009**, *48*, **4808**. (k) Grass, M. E. *Angew. Chem. Int. Ed.* **2008***, 47,* **8893**. (l) Vesselli, E. *Chem Phys Chem* **2004**, *5,* **133**. (m) Maillard, F.; Savinova, R. R.; and Stimming, U. *J. Electroanal. Chem.* **2007**, *599,* **221**.
43. Wilcoxon, J. P.; Abrams, B. L. *Chem. Soc. Rev*., **2006**, 35, **1162.**
44. (a) Green, M.; O'Brien, P. *Chem. Commun*. **2000**, *3***,** **183**. (b) Jana, N. R.; Peng, X. *J. Am. Chem. Soc*. **2003**, *125,* **14280**. (c) Gu, H.; Zheng, R.; Zhang, X.; Xu, B. *J. Am. Chem. Soc.* **2004**, *126*, **5664**. (d) Sharma, J.; Mahima, S.; Kakade, B. A.; Pasricha, R.; Mandale, A. B.; Vijayamohanan, K. *J. Phys. Chem. B* **2004**, *108*, **13280**. (e) Chen, M.; Liu, J. P.; Sun, S. *J. Am. Chem. Soc*. **2004**, *126,* **8394**.

(f) Hiramatsu, H.; Osterloh, F. E. *Chem. Mater*. **2004**, *16*, **2509**. (g) Aslam, M.; Fu, L.; Su, M.; Vijayamohanan, K.; Dravid, V. P. *J. Mater. Chem*. **2004**, *14*, **1795**.

45. Zettsu, N.; McLellan, J. M.; Wiley, B.; Yin, Y.; Li, Z. Y.; Xia, Y. *Angew. Chemi. In. Ed.* **2006**, *118*, **1310**.
46. Park, K. H.; Jang, K.; Kim, H. J.; Son, S. U. *Angew. Chem., Int. Ed.* **2007**, *46*, **1152.**
47. Zhang, Y.; Grass, M. E.; Kuhn, J. N.; Tao, F.; Habas, S. E.; Huang, W.; Yang, P.; Somorjai, G. A. *J. Am. Chem. Soc*. **2008**, *130,* **5868**.
48. Etspiiler, A.; Suhr, H. *Appl. Phys.* **1989**, *373*, **A48**
49. Aaltonen, T.; Ritala, M.; Leskela, M. *Electrochem. Solid-State Lett.,* **2005**, *8,* **99**.
50. Hoefelmeyer, J. D.; Niesz, K.; Somorjai, G. A.; Tilley, T. D. *Nano Lett*. **2005**, *5,* **435**.
51. Sun, Y.; Xia, Y. *Adv. Mater.,* **2004**, *16,* **264**.
52. (a) Marks, L. D. *Rep. Prog. Phys.* **1994**, *57*, **603**. (b) Cleveland, C.; Landman, U., *J. Chem. Phys.* **1991**, *94*, **7376**.
53. (a)Wiley, B.; Sun, Y.; Mayers, B.; Xia, Y. *J. Chem. Eur.* **2005**, *11*, **454**. (b) Liu, M.; Guyot-Sionnest, P. *J. Phys. Chem. B.* **2005**, *109,* **22192**. (c) Gerisher, H.; Tobias, C. W. *In Advances in electrochemistry and electrochemical engineering Eds.* Wiley: New York, **1978**. (d) Herrero, E.; Buller, L. J.; Abruna, H. D., *Chem. Rev.* **2001**, *101*, **1897**. (e) Kolb, D. M.; Przasnyski, M.; Gerischer, H. *J. Electroanal. Chem.*, **1974**, *54,* **25**. (f) Anacker, E. W. *In Cationic Surfactants; Jungermann, Ed.* Marcel Dekker: New York **1970.** (g)Lofton, C.; Sigmund, W. *Adv. Funct. Mater.* **2005**, *15,* **1197**.
54. Wang, Z. L. *J. Phys Chem B.* **2000**, *104,* **1135**.
55. Peng, Z.; Yang, H. *Nanotoday* **2009**, *4,* **143**.
56. Lim, B.; Jiang, M.; Tao, J.; Camargo, P.H.C.; Zhu, Y.; Xia, Y. *Adv. Funct. Mater*. **2009**, *19,***189**.
57. (a) Renzas, J.R.; Huang, W.; SomorJai, G. A. *Catal Lett.* **2009**, *132,* **317**.(b) Tao,

F.; Grass, M. E.; Zhang, Y.; Butcher, D. R.; Renzas, J. R.; Liu, Z.; Chung, J.Y.; Mun, B. S.; Salmeron, M.; SomorJai, G. A. *Science* **2008**, *322,* **932**.

58. (a) Kan, C.; Zhu, J.; Zhu, X., *J. Phys. D: Appl. Phys.* **2008**, *41*, 155304, **1**. (b) Siekkinen, A. R.; McLellan, J. M.; Chen, J.; Xia, Y., *Chem. Phys. Lett.* **2006,** *432,* **491**. (c) El-Sayed, M. A. *Acc. Chem. Res.*, **2001**, *34,* **257.** (c) Hu, M.; Chen, J.; Li, Z.; Au, L.; Hartland, G.V.; Li, X.; Marquez, M.; Xia, Y. *Chem. Soc. Rev.* **2006**, *35*,**1084**.
59. Gans, R., *Ann. Phys*. **1912**, *342*, **881**.
60. Kelly, K. L.; Coronado, E.; Zhao, L. L.; Schatz, G. C. *J. Phys. Chem. B.* **2003**, *107*, **668**.
61. (a) Creighton, J. A.; Eadont, D. G. *Faraday Trans.* **1991,** *87*, **3881**. (b) Ye, J.; Dorpe, P. ; Roy, W.; Lodewijks, K.; Vlaminck, I.; Maes, G.; Borghs, G., *J. Phys. Chem. C.* **2009**, *113*, **3110**.
62. (a) Felidj, N.; Aubard, J.; Levi, G. *J. Chem. Phys.* **1999**, *111,* **1195**. (b) Bohren, C. F.; Huffman, D. R. *Absorption and scattering of light by small particles;* Wiley Interscience: New York, **1983.** (c) Link, S.; El-Sayed, M. A. *J. Phys. Chem. B.* **1999**, *103*, **8410**.
63. Wang, Y.; Russell, S. D.; Shimabukuro, R. L. *J. Appl. Phys.* **2005,** *97,* **023708.**
64. Zettsu, N.; Mclellan, J. M.; Wiley, B.; Yin, Y.; Li, Z.; Xia, Y. *Angew. Chem., Int. Ed.,* **2006**, *45,* **1288**.
65. Yingpu, B.; Gongxuan, L. *Chem. Commun.* **2008**, *47,* **6402.**
66. (a) Draine, B. T.; Flateau, P. J. *User Guide for the Discrete Dipole Approximation* DDSCAT.6.0, http://arxiv.org/abs/astro-ph0309069 (b) Yang, W. H.; Schatz, G. C.; Van Duyne, R. P. *J. Chem. Phys.* **1995**, *103*, **869**. (c) Jensen, T.; Kelly, K. L.; Lazarides, A.; Schatz, G. C. *J. Cluster Sci.* **1999**, *10,* **295**. (d) Kelly, K. L.; Lazarides, A. A.; Schatz, G. C. *Comput. Sci. Eng*. **2001**, *3*, **67**. (e) Bian, R. X.; Dunn, R. C.; Xie, X. S.; Leung, P. T. *Phys. Rev. Lett*. **1995**, *75*, **4772**. (f) Dabbousi, B. O.; Rodriguez-Viejo, J.; Mikulec, F. V.; Heine, J. R.; Mattoussi, H.; Ober, R.; Jensen, K. F.; Bwaendi, M. G. *J. Phys. Chem. B.* **1997**,

101, **9463**. (g) Yang, J.; Fendler, J. H. *J. Phys. Chem.* **1995**, *99*, **5505**. (h) Hao, E.; Schatz, G. C. *J. Chem. Phys.* **2004**, *120*, **357**. (i) Coronado, E.; Schatz, G. C. *J. Chem. Phys.* **2003**, *119*, **3926**. (g) Jensen, T.; Kelly, K. L.; Lazarides, A.; Schatz, G. C. *J. Clust. Sci.* **1999**, *10*, **295**.

67. (a) Henglein, A. In Modern Trends of Colloid Science in Chemistry and Biology; Eicke, H.-F. Eds.; Berkhäuser-Verlag: Basel, Switzerland, 1985. (b) Henglein, A., *J. Phys. Chem*. **1993**, *97*, **5457**. (c) Henglein, A. *Top. Curr. Chem*. **1988**, *141*, **113**. (d) Henglein, A.; Mulvaney, P.; Linnert, T. *Faraday Dis. Chem. Soc*. **1991**, 92, **31**. (e) Henglein, A., *Ber. Bunsen-Ges. Phys. Chem*. **1977**, *81*, **556**. (f) Henglein, A. *Chem. Phys. Lett.* **1989**, *154*, **473**. (g) Tausch-Treml, R.; Henglein, A.; Lilie, Ber; B. *J.Phys. Chem.* **1978**, *82*, **1335**.
68. (a) Rossetti, R.; Nakahara, S.; Brus, L. E. *J. Chem. Phys*. **1983**, *79*, **1086**. (b) Haram, S. K.; Quinn, B. M.; Bard, A. J. *J. Am. Chem*. Soc. **2001**, *123*, **8860**. (c) Ding, Z.; Quinn, B. M.; Haram, S. K.; Pell, L. E.; Korgel, B. A.; Bard, A. J. *Science* **2002**, *296*, **1293**. (d) Chen, S.; Truax, L. A.; Sommers, J. *Chem. Mater.* **2000**, *12*, **3864**. (e) Bae, Y.; Myung, N.; Bard, A. J. *Nano Lett*. **2004**, *4*, **1153**. (f) Kucur, E.; Riegler, J.; Urban, G. A.; Nann, T. *J. Chem. Phys*. **2003**, *119*, **2333**. (g) Poznyak, S. K.; Osipovich, N. P.; Shavel, A.; Talapin, D. V.; Gao, M.; Eychmuller, A.; Gaponik, N. *J. Phys. Chem. B.* **2005**, *109*, **1094**.
69. (a) Gerischer, H.; Tobias, C. Advances in Electrochemistry and Electrochemical Engineering; Eds.; Wiley, New York, **1977,** *10*. (b) Plieth, W. J., *Surf. Sci.* **1985**, *156*, **530**.
70. Kakade, B. A.; Shintri, S. S.; Sathe, B. R.; Halligudi, S. B.; Pillai, V. K. *Adv. Mater.* **2007**, *19*, **272**.
71. Park, K.; Parsons, G. *Appl. Phys. Lett.* **2006,** *89,* **043111**.
72. (a) Chen, S. *J. Phys. Chem. B.* **2000**, *104*, **663**. (b) Pileni, M. P. *J. Phys. Chem. B* **2001**, *104*, **3358**. (c) Whetten, R. L.; Shafigullin, M. N.; Khoury, J. T.; Schaaff, T. G.; Vezmar, I.; Alvarez, M. M.; Wilkinson, A. *Acc. Chem. Res.* **1999**, *32*, **397**. (d) Schmid, G.; Baumle, M.; Greekens, M.; Heim, I.; Osemann, C.; Sawitwoski,

T. *Chem. Soc. Rev*. **1999**, *28*, **179**. (e) Feldheim, D. L. *Nature* **2000**, 408, **45**. (f) Fendler, J. H. *Chem. Mater*. **2001**, *13*, **3196**.

73. (a) Andres, R. P.; Bein, T.; Dorogi, M.; Feng, S.; Henderson, J. I.; Kubiak, C. P.; Mahoney, W.; Osifchin, R. G.; Reifenberger, R. *Science* **1996**, *272*, **1323**. (b) Feldheim, D. L.; Keatig, C. D. *Chem. Soc. Rev*.**1998**, *27*, **1.** (c) Dorogi, M.; Gomez, J.; Osifchin, R.; Andres, R. P.; Reifenberger, R., *Phy. Rev. B* **1995**, *52*, **9071**. (d) Thomas, P. J.; Kulkarni, G. U.; Rao, C. N. R. *Chem. Phys. Lett*. **2000**, *321*, **163**. (e) Harrell, L. E.; Bigioni, T. P.; Cullen, W. G.; Whetten, R. L.; First, P. N. *J. Vac. Sci. Technol*. *B.* **1999**, *17*, **2411**.
74. (a) Remacle, F.; Levine, R. *J. Am. Chem. Soc.* **2000**, 122, **4084**. (b) Lambe, J.; Jaklevic, R. C. *Phy. Rev. Lett*. **1969**, 22, **13`71**. (c) Cavicchi, R. E.; Silsbee, R. H. *Phy. Rev. B* **1988**, 37, **706**.
75. Mott, N. F.; Davis, E. A. *Electronic Processes in Noncrystalline Materials; Clarendon Press:* Oxford, UK, **1971.**
76. Modinos, A. *Field emission, thermionic and secondary electron emission spectroscopy, Plenum Press*, New York (1984).
77. (a) Fang, X.; Bando, Y.; Gautam,U. K.; Ye, C.; Golberg, D. *J. Mater. Chem*. **2008**, *18,* **509**. (b) Xu, N. S.; Huq, S. E. *Mater. Sci. & Eng. Res.* **2005** , *48,* **47**.
78. (a) Li, X. J.; Jiang, W. F. *Nanotechnology* **2007**, *18*, **065203**. (b) Baek, Y.; Song, Y.; Yong, K. *Adv. Mater.* **2006**, *18*, **3105**. (c) Yang, C. J.; Park, J.; Cho, Y. R. *Adv. Eng. Mater*. **2007**, *9*, **88**.(d) Fan, S. S.; Chapline, M. G.; Franklin, N. R.; Tombler, T. W.; Cassell, A. M.; Dai, H. J. *Science* **1999**, *283,* **512**.(e) Wang, W. Z.; Zeng, B. Q.; Yang, J.; Poudel, B.; Huang, J. Y.; Naughton, M. J.; Ren, Z. F. *Adv. Mater.* **2006**, *18*, **3275**. (f) Banerjee, D.; Jo, S. H.; Ren, Z. F. *Adv. Mater*. **2004**, *16*, **2028**. (g) Lai, G. H.; Li, Z. L.; Cheng, L.; Peng, J. B. *J. Mater. Sci. technol*. **2006**, *22*, **677**. (h) Chiu, J. J.; Kei, C. C.; Perng, T. P.; Wang, W. S. *Adv. Mater*. **2003**, *15*, **1361**. (i) Li, C.; Lei, W.; Zhang, X. B.; Wang, J. X.; Sun, X. W.; Tan, S. T. *J. Vac. Sci. Technol. B* **2007**, *25,* **590**. (j) Wei, L.; Zhang, X. B.; Zhu, Z. Y. *J. Vac. Sci. Technol. B* **2007**, *25,* **608**. (k) Milne,W. I.; Teo, K. B. K.;

Amaratunga, G. A. J.; Legagneux, P.; Gangloff, L.; Schnell, J. P.; Semet,V.; Thien Binhc, V.; Groening, O. *J. Mater. Chem*. **2004**, *14*, **933**.(l) Bai, X.; Wang, M. S.; Zhang, G. M.; Yu, J.; Zhang, Z. X.; Guo, D. Z.; Zhao, X. Y.; Xue, Z. Q. *J. Vac. Sci. Technol. B* **2007**, *25*, **561**. (m) Yang,Y. H.; Wang, C. Y.; Chen, U. S.; Hsieh, W. J.; Chang, Y. S.; Shih, H. C. *J. Phys. Chem. C* **2007**, *111*, **1601.**

79. (a) Baek, Y. H.; Yong, K. J. *J. Phys. Chem. C* **2007**, *111*, **1213**. (b) Chang, M. T.; Chou, L. J.; Chueh, Y. L.; Lee, Y.; Hsieh, C.C. H.; Chen, C. D.; Lan, Y. W.; Chen, L. J. *Small* **2007**, *3,* **658**. (b) Li, Y. B.; Bando, Y.; Golberg, D. *Adv. Mater.* **2003**, *15,* **1294**.(c) Zhou, J.; Gong, L.; Deng, S. Z.; Chen, J.; She, J. C.; Xu, N. S.; Yang, R. S.; Wang, Z. L. *Appl. Phys. Lett.* **2005**, *87*, **223108**. (d) Liu, J. G.; Zhang, Z. J.; Zhao, Y.; Su, X.; Liu, S.; Wang, E. G. *Small* **2005**, *1,* **310**. (e) Wu, Q.; Hu, Z.; Wang, X. Z.; Lu, Y. N.; Huo, K. F.; Deng, S. Z.; Xu, N. S.; Shen, B. Zhang, R.; Chen, Y. *J. Mater. Chem*. **2003**, *13,* **2024**. (f) Yin, L. W.; Bando,Y.; Zhu, Y. C.; Li, M. S.; Li, Y. B.; Golberg, D. *Adv. Mater.* **2005**, *17*, **110**.(g) Tang, Y. B.; Cong, H. T.; Cheng, Z. G.; Cheng, H. M. *Appl. Phys. Lett.* **2005**, *86,* **233104**. (h) Shi, S. C.; Chen, C. F.; Chattopadhyay, S.; Chen, K. H.; Chen, L. C. *Appl. Phys. Lett*. **2005**, *87*, **073109**.

80. (a) Chen, Z.; Cao C. B.; Zhu, H. S.; *J. Phys. Chem. C* **2007**, *111*, **1895**. (b) Tang, Y. B.; Cong, H. T.; Cheng, H. M. *Appl. Phys. Lett*. **2006**, *89,* **093113**. (c) Tang, Y. B.; Cong, H. T.; Wang, Z. M.; Cheng, H. M. *Appl. Phys. Lett*. **2006**, *89,* **253112**.(d) Zhao, Q.; Xu, J.; Xu, X. Y.; Wang Z.; Yu, D. P. *Appl. Phys. Lett.* **2004**, *85,* **5331**.(e) He, J. H.; Yang, R. S.; Chueh, Y. L.; Chou, L. J.; Chen, L. J.; Wang, Z. L. *Adv. Mater*. **2006**, *18,* **650**. (f) Tang, Y. B.; Cong, H. T.; Zhao, Z. G.; Cheng, H. M. *Appl. Phys. Lett*. **2005**, *86,* **153104**. (g) Liu, C.; Hu, Z.;Wu, Q.; Wang, X. Z.; Chen, Y.; Lin, W. W.; Sang,H.; Deng, S. Z.; Xu, N. S. *Appl. Surf. Sci.* **2005**, *251,* **220**. (h) Pan, Z. W.; Lai, H. L.; Au, F. C. K.; Duan, X.; Zhou, W.; Shi, W.; Wang, N.; Lee, C. S., Wong, N. B.; Lee, S. T.; Xie, S. S. *Adv. Mater*. **2000**, *12,* **1186**.

81. (a) Deng, S. Z.; Li, Z. B.; Wang, W. L.; Xu, N. S.; Zhou, J.; Zheng, X. G.; Xu,

H. T.; Chen J.; She, J. C. *Appl. Phys. Lett.* **2006**, *89*, **023118**. (b) Shen, G. Z.; Bando, Y.; Ye,C. H.; Liu B. D.; Golberg, D. *Nanotechnology* **2006**, *17*, **3468**. (c) Wu, Z. S.; Deng, S. Z.; Xu, N. S.; Chen, J.; Zhou J.; Chen, J. *Appl. Phys. Lett*. **2002**, *80,* **3829**. d) Zhou, W. M.; Wu, Y. J.; Kong, E. S. W.; Zhu, F.; Hou Z. Y.; Zhang, Y. F. *Appl. Surf. Sci*. **2006**, *253,* **2056**. (e) Tang C. C.; Bando, Y. *Appl. Phys. Lett*. **2003**, *83*, **659**. (f) Ryu, Y. H.; Park, B. T.; Song, Y. H.; Yong, K. J. *J. Cryst. Growth* **2004**, *271*, **99**. (g) Xing, Y. M.; Zhang, J. H. Yang, W. W.; Yu,Y. H.; Song, Z. R.; Lin, X.; Shen, D. S. *Appl. Phys. Lett*. **2004**, *84,* **5461**.

82. (a) Day, S.; Goswami, J.; Waard, V. M.; Werkhoven, C. *Appl. Phys. Lett.* **2004**, *84,* **1606**. (b) Park K.; Parsons, G.; *Appl. Phys. Lett.* **2006,** *89*, **043111**. (c) Rosencrance, S. W.; Burnham, J. S.; Sanders, D. E.; He, C.; Garrison, B. J.; Winograd, N.; Postawa, Z.; De Pristo, A. E. *Phys. Rev. B* **1995**, *52*, **6006.**
83. (a) Ren, B.; Lin, X. F.; Yan J. W.; Mao, B. W.; Tian Z. Q. *J. Phys. Chem. B* **2003,** *107*, **899**. (b) Shibata, S. *Bull. Chem. Soc. Jpn* **1965**, *38*, **1330**. (c) Kim, P. G.; Zhang, P.; Sham, T. K. *Langmuir* **2004,** *20*, **4690**.
84. Zhu, J.; Zach, M. *Current Opinion in Colloid & Interface Science* **2009,** *14,* **260**.
85. Wang, B.; Wang, G.; Ren,Y.; Sun, H.; Chen, X.; Zhao, J. *J. Phys.: Condens. Matter*. **2003**,*15*, **2327.**
86. Wanga, L.; Ge, Q. *Chem. Phys. Lett.* **2002**,*366,* **368**.
87. Zitoun D.; Amiens C.; Chaudret B.; Fromen, M.C.; Lecante, P.; Casanove, M.J.; Respaud, M. *J. Phys. Chem*. **2003** *107,* **6997**.
88. Rhodium.". www.kitco.com. http://www.kitco.com/charts/rhodium.html. 2010.
89. Lin W. G., Sun,S. G.; Zhou,Z. U.; Chen, S. P.; Wang H. C. *J. Phys. Chem. B* **2002**, *106,* **11778**.
90. Yin L.; Gaoquan S. *J. Phys. Chem. B* **2005**, *109,* **1243.**
91. Lin, W. G.; Sun, S. G.; Zhou, Z. Y.; Chen, S. P.; Wang, H. C. *J. Phys. Chem. B* **2002,** *106,* **11778**.
92. Jiang, Q.; Lu, H. M.; Zhao, M. *J. Phys.: Condens. Matter*. **2004**, 16, **521**.
93. Milne, W. I.; Teo, K. K.; Amaratunga, G. J.; Legagneux, P.; Gangloff, L;

Schnell, J. P.; Semet, V.; Binhc, V. T.; Groening, O. *J. Mater Chem*. **2004**, *14*, **33**.

94. Elke S.; Peter R. *New J. Phys.* **2008**, *10*, **065004**.
95. Chun L.; Cherie R. K. *J. Am. Chem. Soc.* **2003**, *125,* **336**.
96. (a) http://www.organicsemiconductors.com, (b) Kwok, K.; Ellenbogen, J. C. *Materials Today* **2002**, *5*, **28.** b) Cassoux, P. *Science* **2001,** *291*, 263. (c) Noel, S.; Hush, Y. *Acad. Sci.* **1006**, *2003,* **1**. (d) Bendikov, M; Wudl, F; Perepichka, D. F. *Chem. Rev.* **2004**, *104*, **4891**.
97. Kevin, D. H.; Simon O. L.; Jacob P. W.; Eric W. K.; Orlin D. V. *Science* **2001**, *294*, **1082**.
98. (a)Aviram, A.; Ratner, M. A. *Chem. Phys. Lett.* **1974,** *29*, **277**. (b) Gimzewski, J. K.; Joachim, C. *Science* **1999**, *283,* **5408**.
99. (a) Service, R. F. *Science* **2003**, *302,* 5645 (b) Kubatkin, S. *Nature* **2003***, 425*, **6959**.
100 Mirkin, C. A.; Ratner, M. A. *Annual Rev. Phys. Chem.* **1992**, *43*, **719**.

CHAPTER 2

High Aspect Ratio Rhodium Nanostructures: Synthesis, Characterization and Tunable Electrocatalytic Activity*

One dimensional assembly of rhodium nanoparticles (5-7 nm mean diameter) has been generated with the help of poly-dentate molecules like hexamethylene tetraamine, tridecyl amine, tartaric and ascorbic acid as effective capping agents. Subsequent characterization by using transmission electron microscopy, scanning electron microscopy, X-ray diffraction and X-ray photoelectron spectroscopy reveals the formation of unique inter-connected network of needles and bundles of nanorods on a larger scale. The structural evolution has been further analyzed with thermogravimetric and Fourier transform infra-red spectroscopic results to demonstrate the importance of controlling critical parameters like concentration of Rh ions, temperature, pH and reaction media to obtain their unique morphological features using polyfunctional molecules. A noteworthy negative shift of the onset potential towards the electrooxidation of formic acid using nanochains, nanoneedles and nanorods compared to that of bulk Rh from cyclic voltammetry along with current densities from current-time transient suggests their potential application as an efficient electrocatalyst for fuel cells. These findings open up new possibilities for tailoring nanostructured electrodes with potential benefits since the development of a better electrocatalyst for many fuel cell reactions continues to be an important challenge.

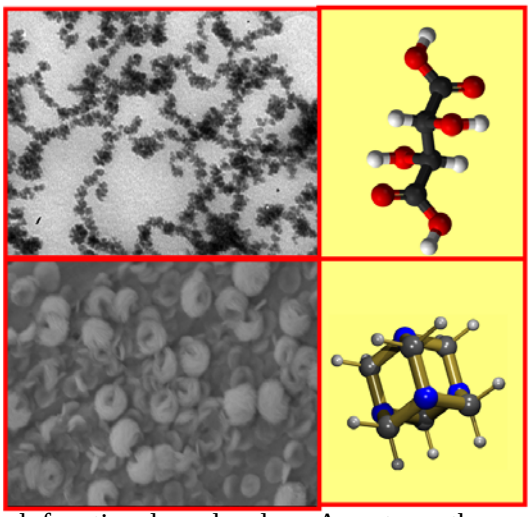

*A part of the work discussed in this chapter has been published in: ***"Energy and Environmental Science,*** *2010 (in press)"*

2.1. Introduction

Synthesis of monodispersed nanoparticles has been a central issue of surface and interfacial electrochemistry with many techno-commercially important applications. Although a large scale synthesis of most of these particles has been achieved in the past, simultaneous control of their shape, surface structure and anisotropy is still a challenge for many of them [1]. Interestingly, as compared to homogeneously structured nanoparticles, anisotropic and interconnected (inter-assembled) nanostructures promise further degrees of freedom towards tuning their structure-function relationship related with the size and shape of each segment as well as the coupling between them [2]. Accordingly, recent literature is replete with various attempts for the coupling of "as-synthesized" metal nanoparticles often with *in situ* assembly of nanostructured colloids, nanoparticle agglomerates, submicron hollow spheres and nanoparticle rings using bi-functional surfactants or analogous polymeric systems [3]. Distinct properties exhibited by 1D (chains, needles, rods, wires and tubes) nanostructures with respect to individual particles dictate their potential applications [4]. For example, such 1D nanostructures of transition metals like Pd, Pt, Rh, Ir and Ru have special importance in areas like oxidation catalysis, fuel cells, solar energy conversion, environmental remediation owing to their excellent activity, tenability and stability [5].

In spite of the high cost, Rh is an attractive metal which needs to be exploited fully for many applications such as fuel cell and electrocatalysis in view of its high tolerance for CO poisoning (inadvertently present in the hydrogen fuel stream or formed as an intermediate contaminant when methanol is used) with respect to Pt and more significantly due to its relatively unknown size-dependent properties [6]. Moreover, it has several unique capabilities like chemical inertness towards mineral acids, specific catalytic activity for a variety of organic transformations [7], especially on single crystals [8], multivalent redox tendency [9] and its uncanny ability to act as supported catalysts on a variety of flat oxide substrates [10]. For a majority of these applications, however, mechanistic details such as the rate dependence of formic acid oxidation on Rh nanoparticles are not well understood and more studies are hence necessary to elucidate

the size and shape-dependent reactivity. This is partly due to the fact that many of these studies have been performed under widely varying experimental conditions and with samples using different synthetic methods.

In the first chapter, we have given a brief review of the synthesis, assembly and various properties of Rh based nanostructures with their morphological details. All preparation methods, including colloidal/chemical, electrochemical and chemical vapor deposition have been discussed in relation to their precise control over selective growth of nanostructures with few major limitations highlighting the importance of maintaining an accurate system profile during the synthesis. However, no experimental details have been given about how to make high aspect ratio Rh nanostructures. Accordingly, in this chapter we describe a facile and straightforward route for the synthesis of high aspect ratio Rh nanostructures including chains, rods and needles using specific capping molecules such as hexamethylene tetraamine (HTA), tridecyl amine (TDA), tartaric (TA) and ascorbic (AA) acids. These 1D nanostructures have been further characterized by various techniques including scanning electron microscopy (SEM), transmission electron microscopy (TEM), X-ray photoelectron spectroscopy (XPS) and thermogravimetry (TG). These nanostructures have also been tested as electrocatalysts for fuel cell reactions using cyclic voltammetry (CV) and I/t transients to show significant enhancement in electrocatalytic activity/performance in comparison with that of bulk Rh. Further a tentative growth mechanism has been proposed to explore the effect of polyfunctionality corresponding to the capping molecules towards the building of 1D morphologies along with tunable activity.

2.2. Experimental Section

2.2.1. Materials

Rhodium chloride ($RhCl_3.3H_2O$) (99.9 %), ascorbic acid (AA), tartaric acid (TA), hexamethylene tetraamine (HTA), tridecyl amine (TDA), sodium borohydride ($NaBH_4$) and commercial Rh foil (bulk Rh) were purchased from Aldrich Chemicals, while AR grade sulphuric acid, formic acid, ethanol and acetone were obtained from Merck. All

reagents were used without any further purification and deionized water (18MΩ) from Milli-Q system was used in all experiments.

2.2.2 Synthesis

Rh nanostructures were synthesized by the reduction of Rh^{3+} ions in presence of polyfunctional (surface passivating) molecules like tartaric acid and ascorbic acid as capping agents. Detailed synthesis of nanochains through the involvement of various steps via nucleation and growth control followed by their self-assembly into aligned nanochains is diagrammatically shown in Figure 2.1 and all relevant reaction conditions are also summarized in Table 2.1.

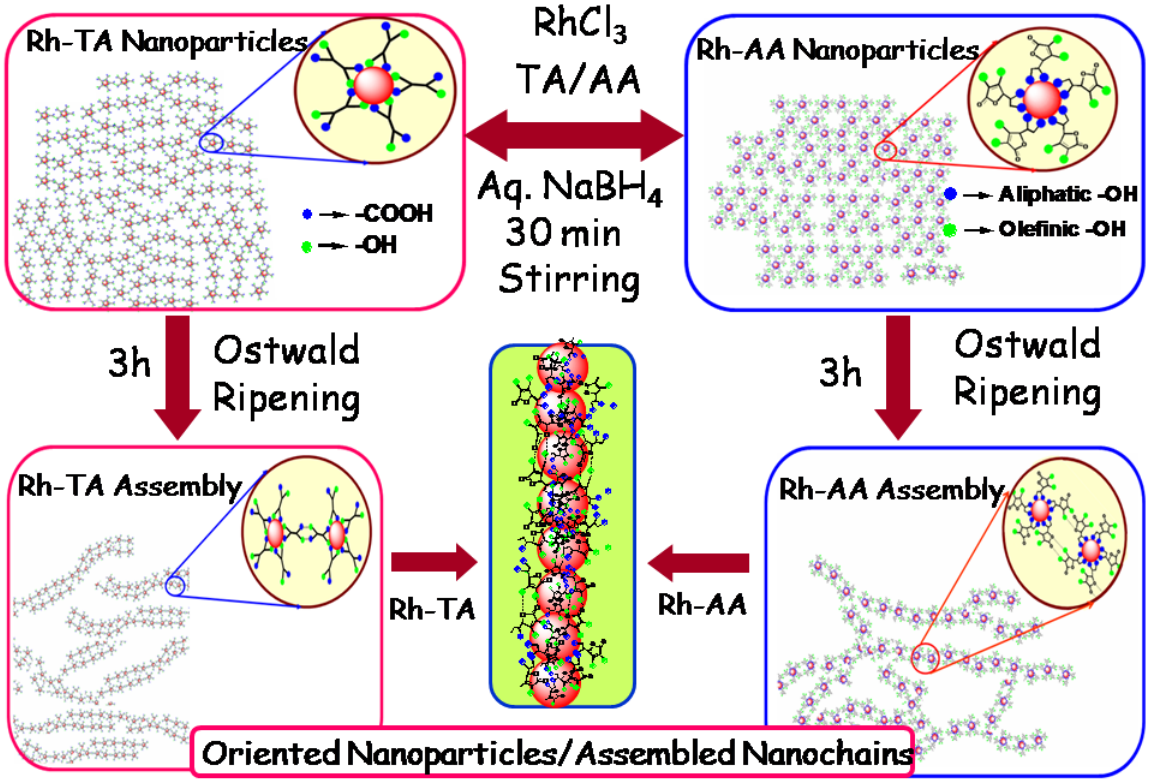

Figure 2.1. Diagrammatic representation of various steps involved during the formation of Rh nanoparticles via nucleation and growth through aggregation followed by their self-assembly into aligned nanochains: TA and AA represent tartaric and ascorbic acid molecules respectively.

Initially, a single phase (aqueous) mixture of Rh^{3+} and TA/AA in 1:2 molar ratio was stirred in an ice bath for 30 min followed by subsequent reduction using drop-wise addition of 0.1 M aqueous $NaBH_4$. The orange red colour of Rh solution became blackish gray indicating the formation of Rh nanoparticles within 30 min. Rh nanochains were synthesized by a further extension of the above experiment for next 3h to effect Ostwald Ripening [11].

Table 2.1. Experimental conditions for the evolution of different Rh morphologies by various poly-functional molecules in 1:2 molar ratio using 1mM rhodium chloride.

No.	Morphology	Nanochains		Nanoneedles	Nanorods
1.	**Symbol**	Rh-AA	Rh-TA	Rh-TDA	Rh-HTA
2.	**Capping Agent**	Ascorbic acid	Tartaric Acid	Tridecyl amine	Hexamethylene tetraamine
3.	**Nucleating agent**	-	-	Rh-AA Nanoparticles	Rh-AA Nanoparticles
4.	**Reaction Medium**	Water	Water	Ethylene Glycol	Ethylene Glycol
5.	**Temperature**	0 °C	0°C	170 °C	170 °C
6.	**Reducing Agent**	$NaBH_4$	$NaBH_4$	-	-
7.	**Reaction Time**	3h	3h	40 min	40 min
8.	**Solvent For purification**	Acetone/ Ethanol	Acetone/ Ethanol	Acetone/ Ethanol	Acetone/ Ethanol

Nanorods and nanoneedles were synthesized by a slightly modified Polyol method using the calculated amount (Table 2.1.) of hexamethylene tetraamine or tridecyl amine as a capping molecule. For the synthesis of high aspect ratio nanostructures (Rh-AA) nanoparticles were used along with TA/TDA capping molecules respectively and $RhCl_3$ was added simultaneously in anhydrous ethylene glycol in the presence of pre-synthesized Rh-AA (~ 5 nm) nanoparticles for nucleation at 170 °C with continuous stirring. Subsequently, these were precipitated using ethanol to remove any unbound capping molecules repeatedly, before further characterization studies.

2.3. Structural and Morphological Characterization

2.3.1. X-ray Diffraction (XRD)

X-ray powder diffraction studies were performed using CuKα (λ = 1.54 Å) radiation on a Philips PW1830 instrument operating at 40 kV and a current of 30 mA at room temperature. Diffraction patterns were collected at a step of 0.02° (2θ) after background subtraction with the help of a linear interpolation method [12]. The samples were prepared as thin films on glass substrates.

2.3.2. Scanning Electron Microscopy (SEM) and Energy Dispersive X-ray (EDX) Analysis

The morphology of these Rh nanostructures was examined using a LEICA Stereoscan 440 scanning electron microscope (SEM). A small amount of the sample was mounted on Cu stubs and micrographs were recorded with a 20 kV tension and 20 pA current with the help of a camera attached on the high resolution recording unit. This SEM instrument was been equipped with Phoenix energy dispersive spectral (EDS) analysis setup to map the elemental analysis.

2.3.3. Transmission Electron Microscopy (TEM)

A selected amount of Rh nanostructured sample was sonicated in ethanol to prepare a homogenous suspension. A drop of this was cast on lacey carbon film-coated Cu micro-grids. After drying, these grids were then used for structural investigation using a transmission electron microscope (TEM) - JEOL model 1200 EX instrument operated at an accelerating voltage of 120 kV attached with selected area electron diffraction (SAED). The images were digitized in the size of 256 × 256 pixels with a pixel size of 0.03994 nm and thus atomically resolved images were possible. These images were stored after digitization and the power spectra were calculated to enable detailed structural analysis in terms of interplanar distances and angle between planes.

2.3.4. X-ray Photoelectron Spectroscopy (XPS)

XPS measurements were carried out on a VG MicroTech ESCA 3000 instrument at a pressure of >1 × 10^{-9} Torr (pass energy of 50 eV, electron takeoff angle 60°, and overall resolution ~1 eV using monochromatic Mg Kα (source, hν = 1253.6 eV). The core level spectra of the C 1s and S 2p orbitals were recorded with an overall instrumental resolution of ~1 eV. The alignment of binding energy was carried out using Au 4f (84 eV) as a reference. The X-ray flux (power 70 W) was kept deliberately low to reduce the beam-induced damage. The spectra were fitted using a combined polynomial and Shirley type background functions [13].

2.3.5. Thermogravimetric Analysis (TGA)

Thermal stability and relative strength of capping/building molecules along with their Rh residues were quantitatively traced out using TG measurements. In order to carry out thermogravimetry (TG), about 2-3 mg of the Rh sample was heated on a TGA Q5000 TA Instruments-Thermal analyzer from 50 °C to 900 °C at a rate of 10 °C/min in air.

2.3.6. Electrochemical Measurements

All the electrochemical measurements were performed on an Autolab PGSTAT30 (ECO CHEMIE) instrument using a standard three electrode cell comprising of Rh nano-chain/ nanoneedles/nanorods modified glassy carbon disc (GC; 3 mm diameter from ECO CHEMIE) as working electrode, Pt foil as counter electrode and Hg/Hg_2SO_4 as a reference electrode in 0.5 M H_2SO_4 at room temperature. The glassy carbon electrode was polished before each experiment with 1.0, 0.05 and 0.03 μm alumina slurry and then sonicated in de-ionized water for 10 min. Calculated amount of nanostructured Rh samples were sonicated for 10 min and drop casted on the active tip of the GC electrode maintaining the same Rh loading on the electrode surface for all measurements. After evaporation under a partial vacuum for 30 min, 10 μL of 0.1 wt % Nafion solution was drop-casted on the electrode surface to cover and stabilize the nanostructures for all

electrochemical studies. Prior to all analysis, the electrolyte was saturated by passing ultra-high purity nitrogen.

2.4. Results and Discussion

2.4.1. Morphological Studies

2.4.1.1. Rhodium Nanochains

Figure 2.2 (a) and (b) shows a comparison of the TEM images of Rh nanoparticles (Rh-TA and Rh-AA) synthesized using polyfunctional molecules like tartaric acid (TA) and ascorbic acid (AA) as capping molecules having size of ~ 7 nm and ~ 5 nm respectively, which distinctly reveal the difference in the size and shape distribution along with their interconnected arrangements.

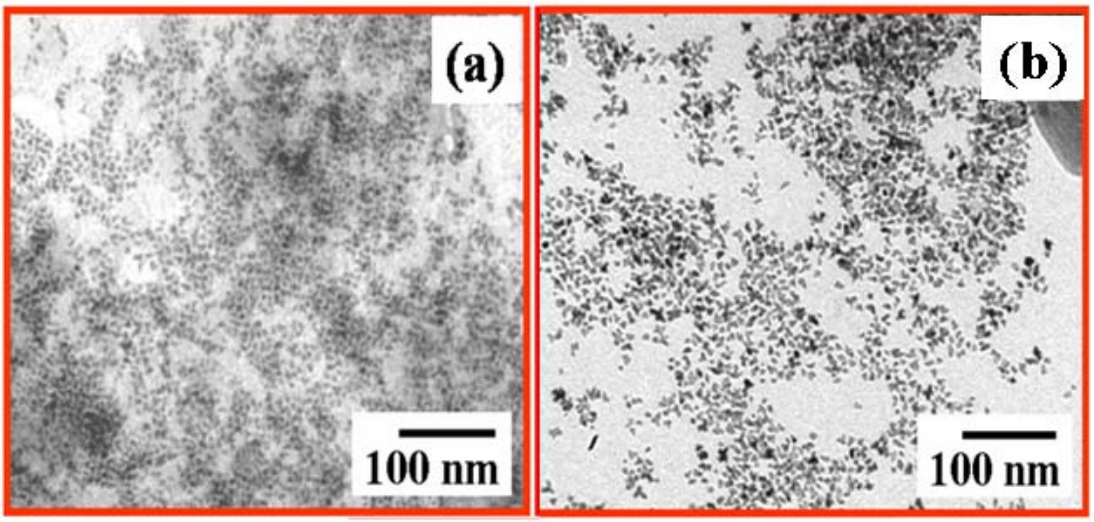

Figure 2.2. TEM image of purified Rh nanoparticles with different capping molecules; (a) Rh-TA and (b) Rh-AA revealing particle sizes of ~7.0 nm and ~5.0 nm respectively.

These particles have nonspherical shapes (anisotropic) which could be due to multiple functional groups that provide surface passivation (TA and AA) along with their flexible connections facilitating inter-particle interactions. However, once we extend the reaction for next 3h, nanoparticles of same size are seen to self-assemble into nanochains at micron levels as shown in TEM images [Figure 2.3 (a) and (b)], for Rh-TA and Rh-AA cases respectively. Moreover, their morphological variation with time leads to a

remarkable networking on a larger scale, instead of coalescence to bigger particles, which can mainly be explained by the nature of polyfunctional capping agents.

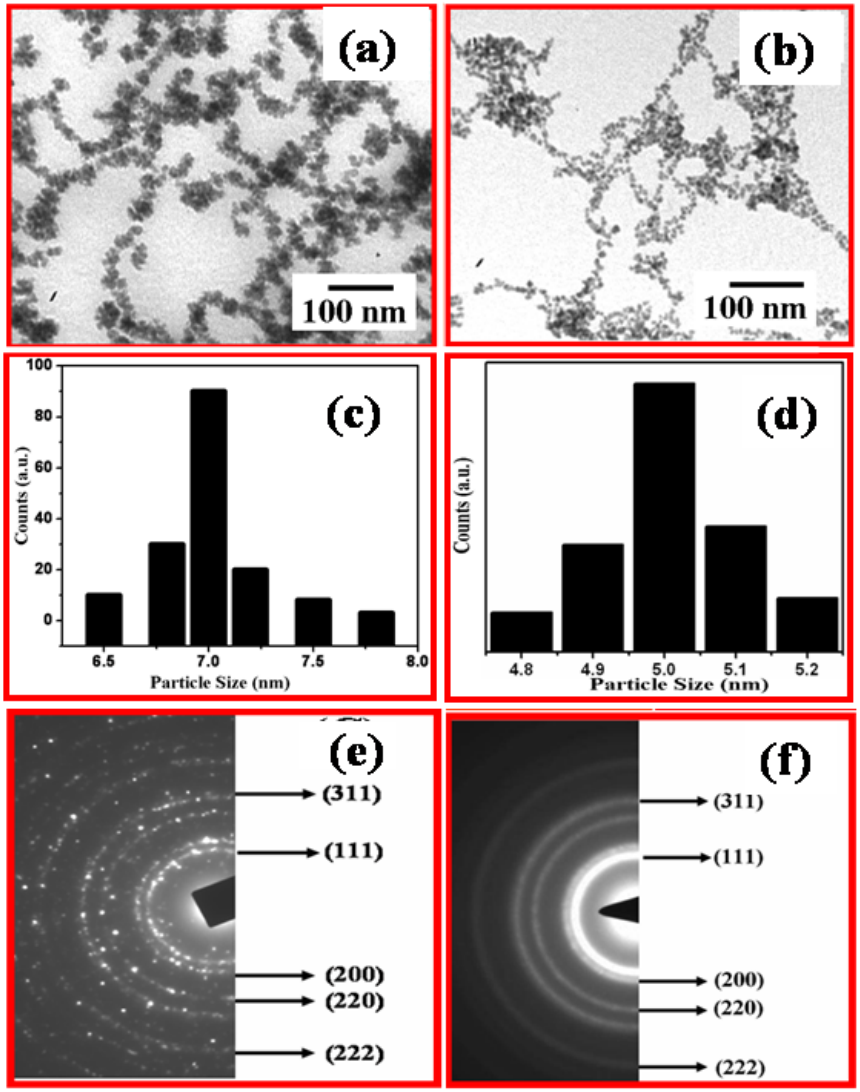

Figure 2.3. A comparison of the TEM images of Rh-TA (a) and Rh-AA (b) nanochains by the interlinking of nanoparticles after 3h having assembly on micron scale; (c) and (d) indicate their particle size distribution with particle mean diameter of 7.0 ± 0.5 nm and 5.0 ± 0.5 nm respectively, while SAED (e) and (f) reveal diffraction pattern corresponding to crystalline Rh (fcc).

After 3h, in both the cases, nearly monodispersed chains of 7.0 ± 0.5 nm and 5.0 ± 0.5 nm respectively for Rh-TA and Rh-AA are formed having a length of several microns. However, a closer observation of these TEM images of nanochains shown in figure 2.3

(a) and (b) indicates significant morphological differences. For example, Rh-AA nanochains show a close packed assembly of smaller Rh nanoparticles compared to those of Rh-TA which could be explained due to the structural variations of TA and AA molecules. A similar large assembly of Au nanoparticles has been reported by Xu and coworkers, using conjugated polymers by a related approach [14]. Further, Thomas and coworkers have demonstrated, the organization of Au nanorods to nanochains by using simple polyfunctional molecules like α, ω-alkanedithiols especially for their tunable optical features through the inter-plasmon coupling [15]. Recently, Chan and co-workers have also reported chains of Ni hollow microspheres through the aggregation of small Ni nanoparticles for tunable magnetic properties by a related approach [16]. Chain formation has been monitored by the size and shape analysis of TEM images at different time scales during the growth process.

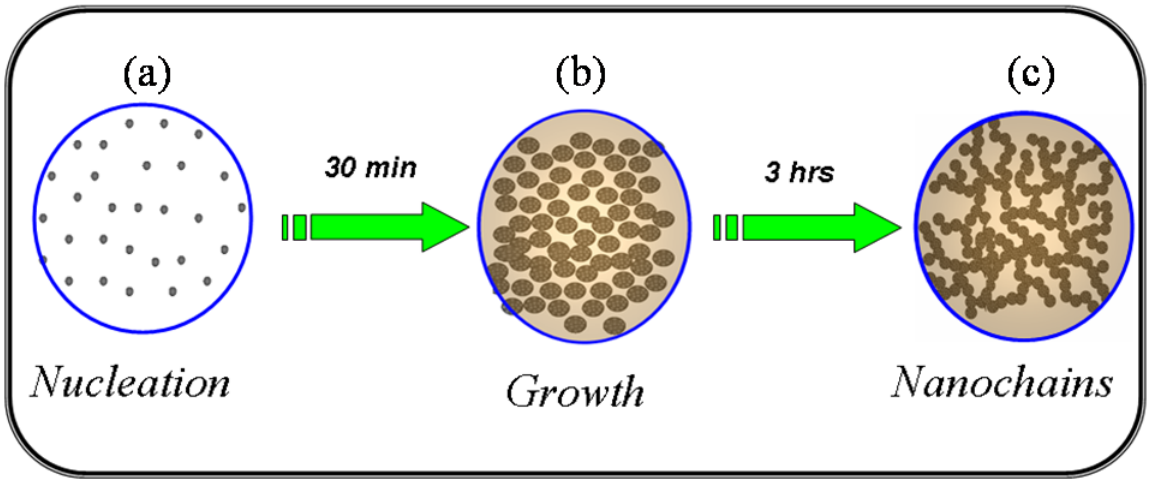

Figure 2.4. A schematic representation of the growth mechanism of Rh nanochains: (a) process of nucleation and (b) growth through aggregation followed by (c) self-assembly into chain formation.

As illustrated in Figure 2.4 (a-c), a schematic representation of a three step model is proposed to explain the growth mechanism along with well-aligned organization of Rh nanochains. In the first step, the primary Rh nanocrystallites nucleate and grow into nearly monodispersed nanoparticles as presented in Figures 2.1 and 2.4 (a), (b) and also in images shown in Figure 2.2 and 2.3 (a) and (b) respectively. Finally, these

nanoparticles reach their equilibrium size and further self-assemble into nanochains through various functional groups of the TA and AA molecules. As a result of this, for a longer reaction time (3h), nanochain formation has been observed instead of their further growth into bigger nanoparticles except perhaps their interlinking. Accordingly, Figure 2.3 (c) and (d) respectively shows a similar size distribution for both Rh-TA and Rh-AA. This tendency of self-assembly into nanochains along with their strong binding energy contribution dominates the thermodynamic driving force from aggregation resulting into nanochain formation. It is clear from the above discussion that polyfunctional molecules play an important role in improving their connectivity and stability. The crystal structures as shown in Figure 2.3 (e) and (f) by representative SAED patterns of Rh-TA and Rh-AA respectively, exhibit dominant reflections corresponding to (111), (200), (220) and (311) planes of the fcc Rh, which is also in complete agreement with the XRD results [17]. However, the SAED rings are not continuous, and the discrete spots, suggest preferential orientation of the Rh nanoparticles in the interconnected network.

2.4.1.2. Rhodium Nanoneedles and Nanorods

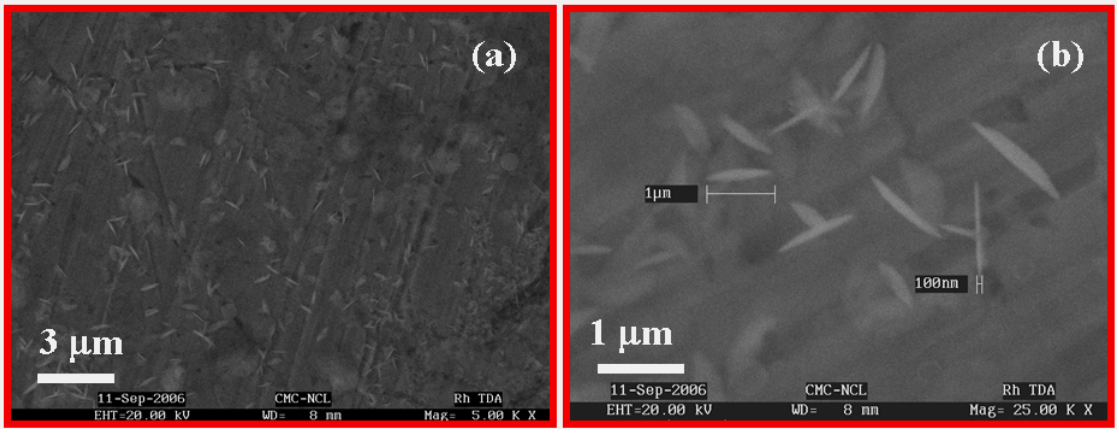

Figure 2.5. A comparison of SEM images of Rh-TDA nanoneedles synthesized using modified Polyol method at ~270 °C at different magnifications (a and b) having lengths of ca. 1µm and thickness of 100 nm.

Figure 2.5, shows a comparison of the SEM images of Rh nanorods synthesized using modified Polyol method at ~270 °C with TDA as the capping agent. More specifically,

low magnification SEM image (a), reveals a uniform distribution of nanoneedles in separated form as shown in (a) with a high yield. The magnified image shown in (b) demonstrates that the length of the nanoneedles are ~1 µm having a thickness of about ~ 100 nm. A close observation of these individual nanoneedles also indicates that in contrast to other 1D nanostructures, both ends of these structures have sharp tips. Further, a comparison of Figure 2.6 (a) and (b) shows SEM images of Rh nanorods as bundles prepared by modified Polyol process with HTA as the capping agent that suggests a high yield with uniform features. For example, low magnification SEM image in (a) reveals high yield of nanorods having diameter ~1 µm and length upto ~1.5 µm with few single nanorods of even 300 nm size as observed in Figure 2.6 (b). This unique morphological feature is significantly different compared to that of other regular nanorods of Au, Ag, Pd and Pt which also show bundles with a loosely interconnected network. The growth of these nanorods due to higher surface energy and large number of additional free functional groups present in HTA is controlled by their inter-wall interactions towards each other that allow coordination with solvents, contributing to the driving force to form bundles [18].

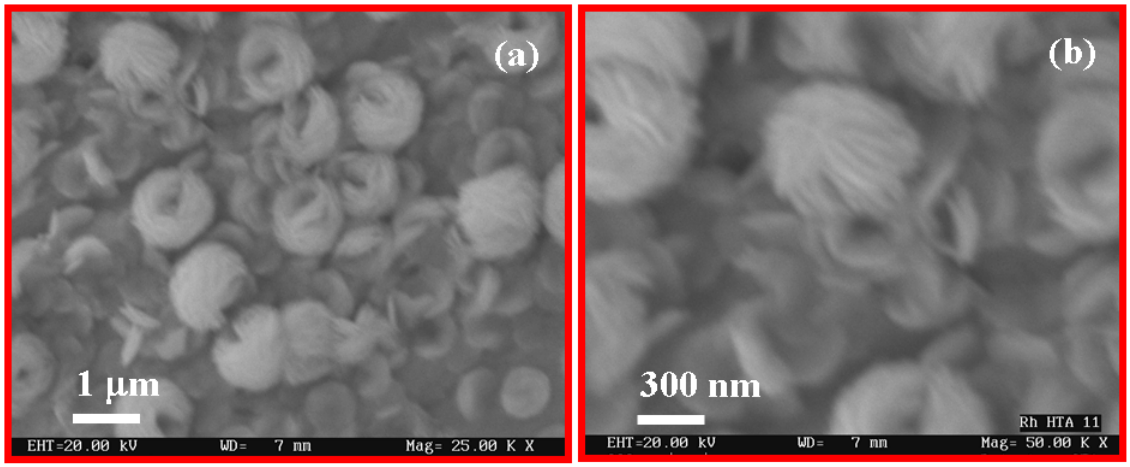

Figure 2.6. SEM images of Rh-HTA nanorod bundles, synthesized using modified Polyol method in ethylene glycol medium at ~260 °C under different magnifications (a) and (b) having the length of ~ 1µm and thickness of ~60 nm.

2.4.2. X-ray Diffraction and Energy Dispersive X-ray Analysis

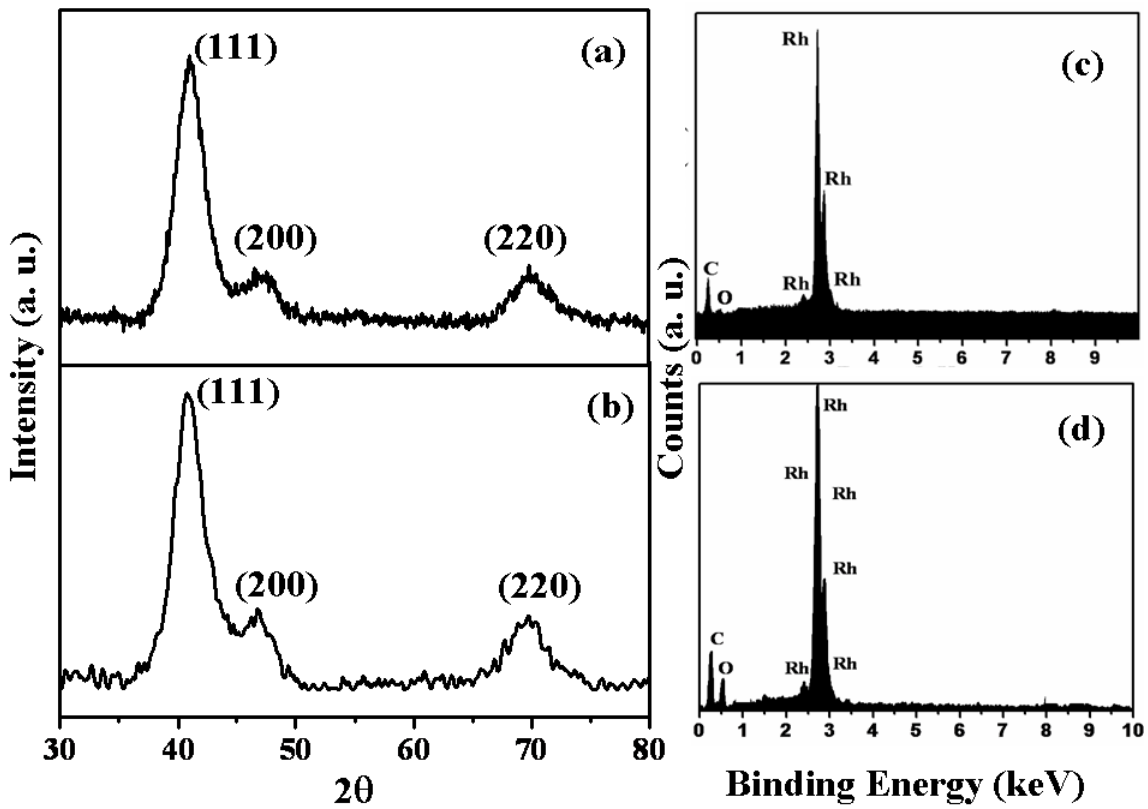

Figure 2.7. X-ray Diffraction patterns of as-synthesized Rh-AA (a) and Rh-TA (b) nanoparticles revealing reflections from (111), (200) and (220) planes, which suggest fcc structure along with EDS profile of as-synthesized Rh-TA (c) and Rh-AA (d) nanoparticles respectively.

Results of X-ray diffraction carried out to investigate the crystallinity and phase purity of these nanostructures and also to evaluate their size distribution are shown in Figure 2.7 (a) and (b), which reveal the fcc structure as known earlier for as synthesized Rh nanoparticles corresponding to that in figure 2.3 (a) and (b) respectively [19]. Crystallite size is calculated from the full width at half maxima (FWHM) of the (111) (43.54º peak; corresponding to d values of 2.25 Å and 2.27 Å) peak using the Debye-Scherrer formula [20],

$$\text{Crystallite Size} = Ks\lambda_X / B\cos\theta \qquad (2.1)$$

Where, Ks is the Scherrer constant (0.9 for spherical particles), λ_X is the wavelength of the X-ray diffraction (1.54 Å for Cu Kα), B is the FWHM of the peak and θ the

diffraction angle [12, 20]. The calculated crystallite sizes are ~ 7 nm and ~ 5 nm for Rh-TA and Rh-AA respectively, which is again in excellent agreement with the corresponding size from TEM images as shown in Figure 2.2 (a) and (b) respectively. This of course, assumes the spherical shape of these particles along with no lattice strain and no peak broadening due to temperature effects.

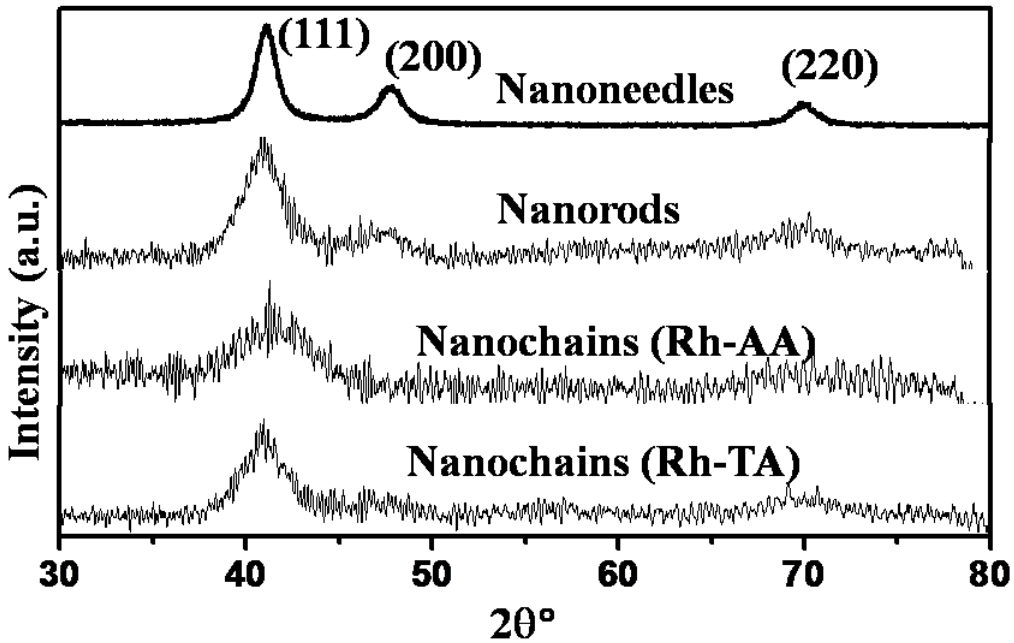

Figure 2.8. Superimposed X-ray Diffraction pattern of as-synthesized nanoneedles, nanorods and nanochains revealing reflections from (111), (200) and (220) planes, which suggest fcc structure.

Moreover, no impurity phases corresponding to rhodium oxide or other reactants has been detected which is also verified by the EDS analysis as shown in Figure 2.7 (c) and (d) respectively. The local chemical composition of Rh-TA/Rh-AA nanoparticles, where signals at 0.26 keV and 0.51 keV correspond to carbon and oxygen from the capping molecules confirm the presence of TA and AA capping respectively, while peaks in the range 2.6-3.2 KeV could be identified as $L_{\beta 1}$ and $L_{\alpha 1}$ emission corresponding to X-ray signals of Rh [21]. The relative change in broadening of (111) peak with morphology changes are clearly evidenced in Figure 2.8, where, a comparison of XRD pattern of nanochains, nanoneedles and nanorods reveals interesting changes.

2.4.3. Thermogravimetric Analysis

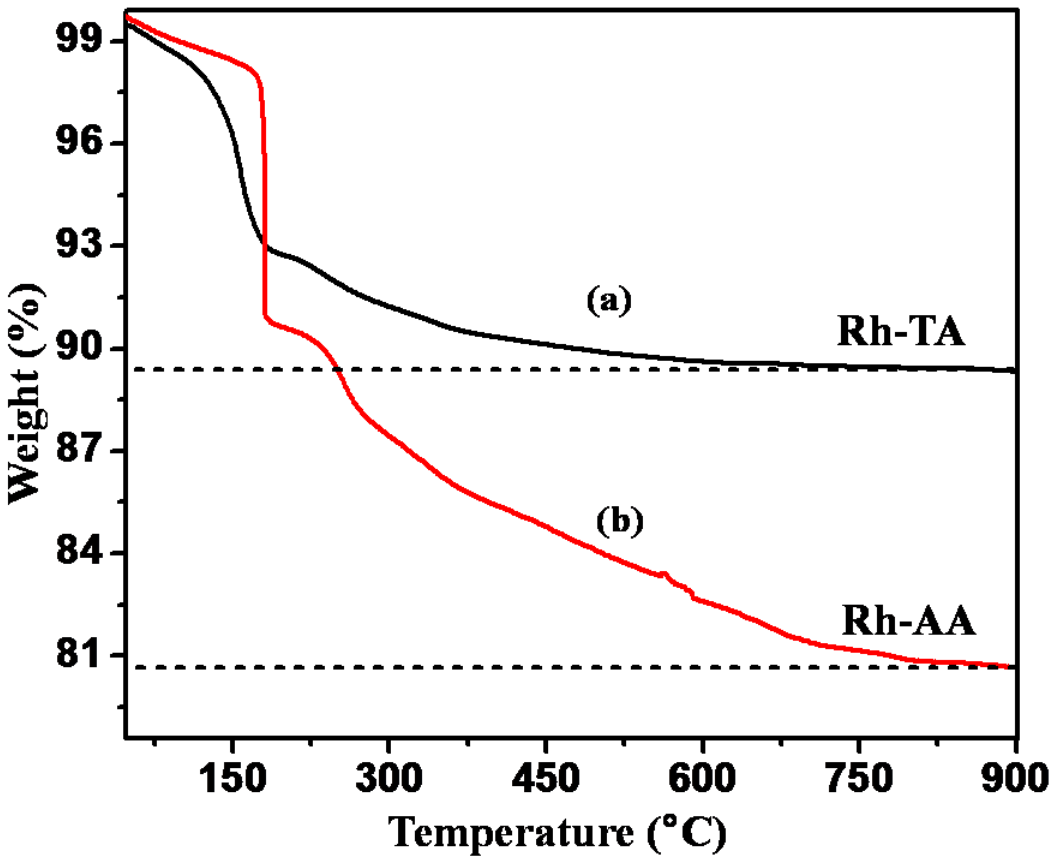

Figure 2.9. Thermogravimetric profiles of (a) Rh-AA and (b) Rh-TA revealing a slow decomposition of AA molecules having (~ 20 % weight loss) than that of TA having ~12 % loss in air respectively.

A comparative analysis of thermogravimetric (TG) properties provides a measure of the strength of the chemical bonding between the Rh surface atoms and the capping molecules from the change in percentage of weight loss corresponding to the decomposition of the capping molecules [22]. Accordingly, Figure 2.9 shows superimposed TGA curves obtained for (a) Rh-AA and (b) Rh-TA nanochains in the temperature range of 50-900 °C under air. Initially, ~12 % weight loss corresponding to the TA takes place in the temperature range of 160-570 °C, while Rh-AA shows only ~20 % weight loss corresponding to the removal of AA in the range of 200-850 ºC. Comparatively higher thermal stability (~300 ºC) of Rh-AA with respect to Rh-TA along

with their slow decrease in weight loss in a wider range could be due to the fundamental structure of AA having a cyclic furan ring with relatively higher thermal stability than that of aliphatic TA along with their own contribution from inter-chain van der Waals interactions. If we assume that these respective decomposition temperatures are indicative of a measure of the strength of the capping molecules to Rh, Figure 2.9 suggests that the -O-Rh bond of Rh-AA is stronger than that between Rh-TA. However, for TA capped Rh nanochains, the overall weight loss (~12 %) is much smaller than that corresponding (20 %) to AA capped Rh nanochains. This is also supported by the appearance of intensity variation of multiple de-convoluted XPS peaks corresponding to Rh, C and O signals, indicating the intriguing geometrical effects of TA/AA molecules towards their stability and assembly formation [23].

2.4.4. Fourier Transform-Infra Red Studies

FT-IR studies also reveal the relative role of capping molecules towards the 1D nanostructure formation. Accordingly, figure 2.10 (a)-(d) shows a comparison of the FTIR spectra of TA and AA before and after capping with Rh. Interestingly, a comparison of these spectra reveals the disappearance of two/four bands in the range of 3300-3600 cm^{-1} for the nanochains (Rh-TA and Rh-AA respectively) which corresponds to the symmetric -O-H stretching of both TA and AA skeleton. The capping molecules are linked through the -O-H groups to the Rh nanoparticles as can be seen from (a) and (d). More importantly, the appearance of additional strong bands in the range of 1350-1650 cm^{-1} in both the cases suggests the involvement of carbonyl and lone pair of oxygen, also for their network formation. Moreover, the appearance of an additional strong band at 900 cm^{-1} in case of Rh-TA and at 500 cm^{-1} in case of Rh-AA is attributed to the presence of Rh-O bond [24]. The rest of the peaks remain common in both the cases corresponding to the capping molecular skeleton. Therefore, it is likely that Rh nanoparticle surfaces in the nano-chain already had a complex like environment because of the poly-dentate nature of TA and AA molecules. This is also supported by the TG

analysis which reveals a slow weight change/loss due to the disparate utilization of poly-functional association of TA and AA towards the assembly formation.

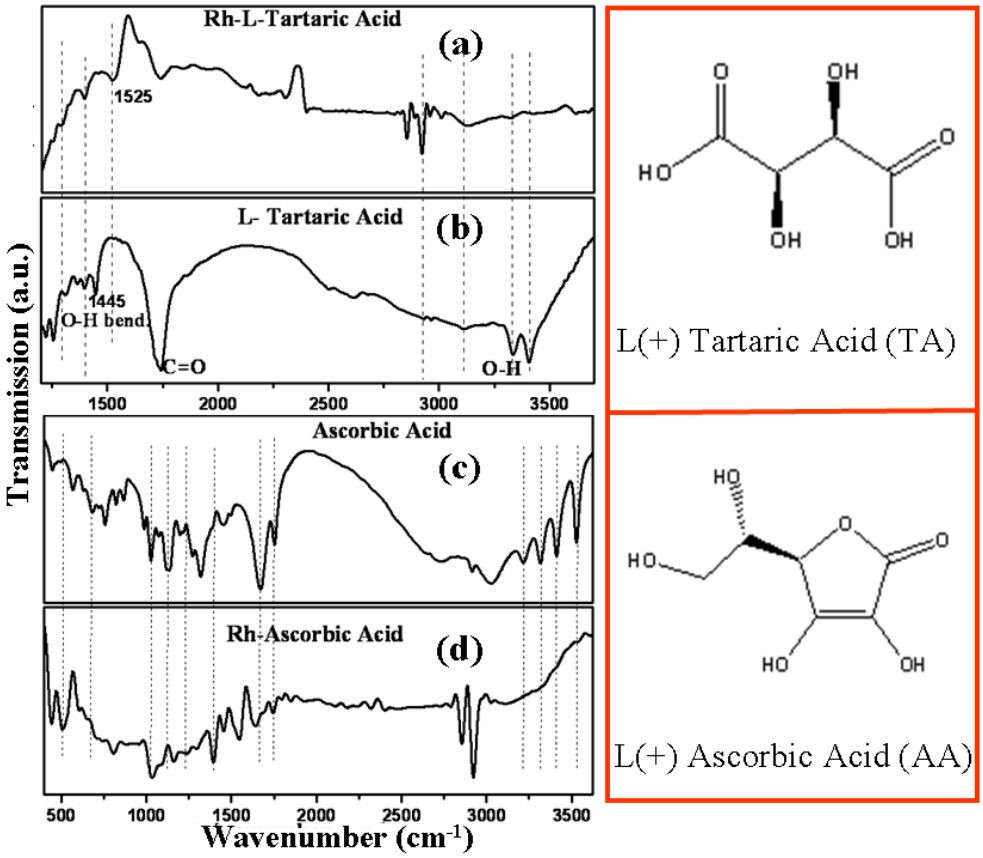

Figure 2.10. Superimposed Fourier transform-infra red spectra of (a) Rh-TA, (b) TA (c) AA and (d) Rh-AA in KBr matrix indicating strong peaks at 900 cm^{-1} and 500 cm^{-1} corresponding to Rh-O linkage of Rh-TA and Rh-AA respectively.

Further, the functional involvement of the passivated TDA molecules on these nanoneedles (Rh-TDA) can be obtained from the FTIR analysis, as shown in Figure 2.11 (a), where the C-H stretching region (2800- 3000 cm^{-1}) is particularly informative about the orientation of methylene chains and Rh-TDA nanoneedles. In addition, Figure 2.11 (a) reveals that the capping agent is intact except for the disappearance of a peak due to –N-H stretching at 3320 cm^{-1} after anchoring to Rh surface. The appearance of an additional strong band at 812 cm^{-1} is attributed to the presence of Rh-N bond [25]. A few sharp bands near 1030 and 1358 cm^{-1}, which are absent in the spectra of TDA, could be

ascribed to the coordinated N species. In addition, a broad band at 2320 cm^{-1} suggests the presence of N as a charged amine species ($-NH^{+}$), indicating the involvement of electrostatic interactions, especially with the nanoparticle surface [26].

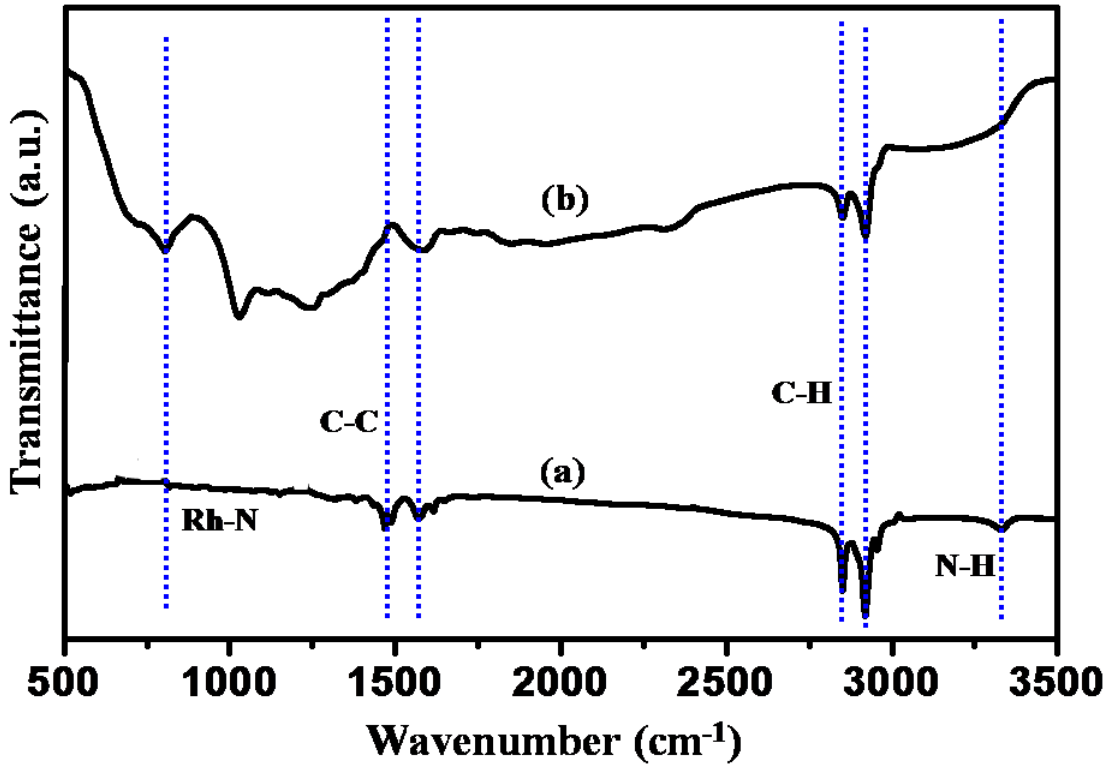

Figure 2.11. Superimposed FTIR spectra of **(a)** TDA and (b) Rh-TDA (nanoneedles) indicating the involvement of tridecylamine for the organization of nanoneedles; a strong peak at 812 cm^{-1} corresponds to Rh-N linkage.

2.4.5. X-Ray Photoelectron Spectroscopy

XPS analysis has been carried out in order to understand the molecular level interactions of the capping (TA, AA, HTA and TDA) molecules on Rh nanochains and these results are in good agreement with that of FTIR, EDS and TG analysis. For example, Fig. 2.12 shows a comparison of the core level spectra of (a) Rh 3d, (b) O 1s and (c) C 1s of Rh-TA nanochains. The peak position, line shape and peak-to-peak separation (~ 4.7 eV) are a standard measures of the Rh oxidation state and the binding energy for Rh 3d doublet (306.1eV and 310.8 eV) is consistent with Rh^{0} oxidation state [Figure 2.12 (a)] [27].

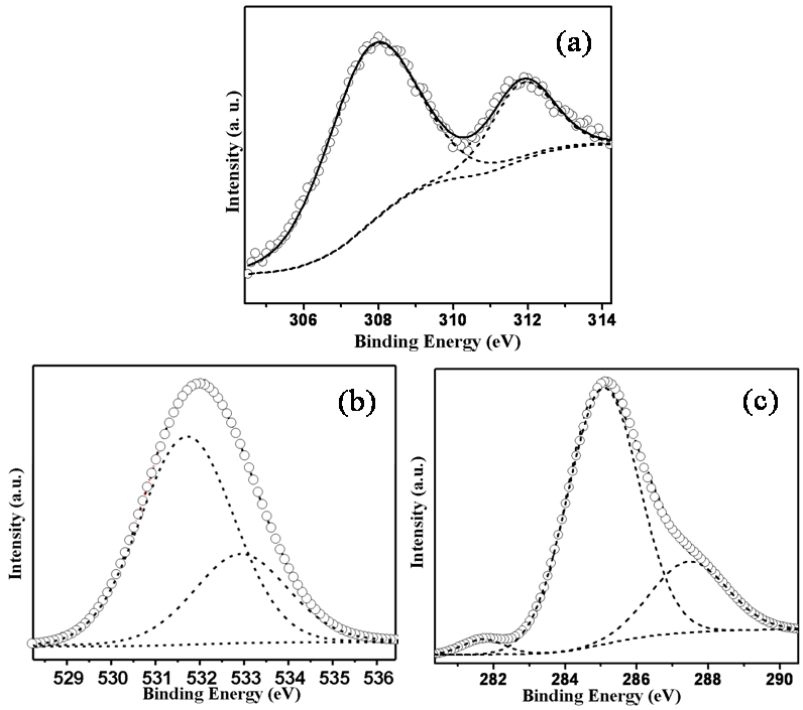

Figure 2.12. XP spectra of Rh-TA nanochains revealing the core level information on the linker capping molecule, (a) Rh 3d (b) O 1s and (c) C 1s signals (experimental data points are shown as circles, resultant fitting curves as continuous lines and individual fitted curves as dashed lines deconvoluted by using Shirley fitting algorithm).

Figure 2.12 (b) shows XP spectra of O1s where the deconvolution of the peak with respect to Gaussian fitting show two distinct peaks at 532.2 eV and 533 eV, corresponding to oxygen species of carbonyl (>C=O) and -O- of all the hydroxyl groups of TA respectively. These perhaps reveal potentially active sites for interconnected organization. Figure 2.12 (c) shows C 1s XP spectra having three distinct peaks at 284.8 eV, 281.7 and 287.5 eV respectively. The peak at 284.8 eV is attributed to the C 1s peak for -C-C- linkage corresponding to TA, while another higher binding energy peak at 287.5 eV is presumably for -C-O linkage corresponding to carbonyl group; another lower binding energy peak at 281.7 eV might be due to overcharged carbon of the carbonyl group after the network formation [28]. Similarly, the XP spectra for other nanostructures have been analyzed based on Shirley fitting and the binding energies of C 1s, Rh 3d, O 1s and N 1s present in Rh nanochains, nanoneedles and nanorods are shown in Table 2.2.

Table 2.2: A Comparison of the binding energy positions of C 1s, Rh 3d, O 1s and N 1s present in Rh nanochains, nanoneedles and nanorods.

Species		**Binding Energies (eV)**			
		Nanochains (Rh-TA)	**Nanochains (Rh-AA)**	**Nanoneedles (Rh-TDA)**	**Nanorods (Rh-HTA)**
C 1s		284.8, 281.7, 287.5	284.5, 286.2	286.5, 285	286.7, 284.9
Rh 3d	**$3d_{5/2}$**	306.1	306.5	305.1	304.8
	$3d_{3/2}$	310.8	311.5	309.7	309.5
O1s		532.2, 533	533.4, 532.8	----------	---------
N1s		---------	----------	398.5	398.8

These XPS results are in good agreement with that of FT-IR studies, which confirm the presence of capping molecule on the surface of Rh nanostructures. Moreover, the use of these molecules render the Rh more active as the tendency for agglomeration is prevented by modifying the Rh surface. In other words, polyfunctional molecules like TA, AA and HTA form self-assembled network of nanoparticles and nanorods through the remaining functionality present on the surface revealing that quantum size effects as confirmed by some of the earlier reports [29]. The control over particle size and dispersity by surface functionalization intended to enhance particle stability and dictate surface chemistry, solubility, the degree of particle interactions and also helps to increase their electrocatalytic performance. All the above results by TEM, XRD, FT-IR, TGA, EDS and XPS clearly show that the structural changes of the passivating organic molecules could be responsible for their morphological evolution.

2.4.6. Electrocatalytic Studies towards Formic Acid Oxidation

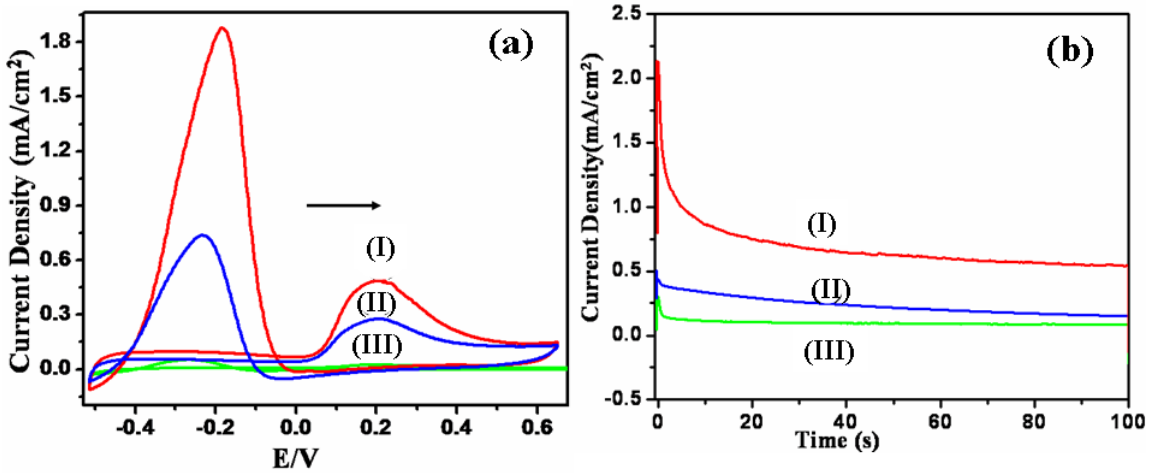

Figure 2.13. (a) Superimposed cyclic voltammograms of (I) Rh-TA, (II) Rh-AA and (III) bulk Rh electrode in a mixture of 0.5 M HCOOH and 0.5 M H_2SO_4 using a Hg/Hg_2SO_4 as reference electrode and Pt foil as a counter electrode at a scan rate of 50 mV/s (second cycle). (b) Superimposed transient current density curves of formic acid oxidation for (I) Rh-TA, (II) Rh-AA and (III) bulk Rh at an applied potential of 0.20 V for 100 s.

Figure 2.13 (a) shows the superimposed cyclic voltammograms (CVs) of Rh in (I) 0.5 M H_2SO_4 and (II) in a mixture of 0.5 M H_2SO_4 and 0.5 M HCOOH solution at a scan rate of 50 mV/s to correlate the potential range of Rh-oxidation and formic acid oxidation respectively. Accordingly, superimposed CVs in (I) 0.5 M H_2SO_4 exhibit a prominent oxidation with an anodic peak at 0.40, 0.20 and 0.23 V corresponding to (I) Rh bulk, (II) Rh-TA and (III) Rh-AA along with a reduction of the oxide species at -0.05, -0.20 and -0.22 V respectively during the reverse cathodic sweep. Furthermore, voltammogram (II) compares the electrochemical features of formic acid oxidation using bulk Rh, Rh-TA and Rh-AA in a mixture of 0.5 M HCOOH and 0.5 M H_2SO_4. When the anodic potential increases during the forward scan, peaks at 0.25, 0.19 and 0.20 V are observed for bulk Rh metal, Rh-TA and Rh-AA respectively corresponding to the oxidation of HCOOH. During the forward scan, formic acid oxidation produces a prominent anodic peak with a current density of 490 and 280 $\mu A/cm^2$ for Rh-TA and Rh-AA respectively, while only 30 $\mu A/cm^2$ is seen for bulk Rh.

Table 2.3. A comparison of the electrocatalytic performance of Rh nanostructures from cyclic voltammetric data for the oxidation of HCOOH (0.5 M) in H_2SO_4 (0.5 M) at 50 mV/s.

No.	Electrocatalyst	Onset Potential (V)	Current Density (mA/cm^2)	Relative Enhancement Factor (η)
1	Bulk Rhodium	0.25	0.030	-
2	Rh-AA (nanochains)	0.21	0.280	1200
3	Rh-TA (nanochains)	0.19	0.490	2000
4	Rh-TDA (nanoneedles)	0.105	0.626	2500
5	Rh-HTA (nanorods)	0.101	1.466	6000

Figure 2.14 (a), shows superimposed cyclic voltammetric response of (I) Rh-HTA, (II) Rh-TDA and (III) bulk Rh towards formic acid oxidation at a typical scan rate of 50 mV/s. When the anodic potential increases during the forward scan, peaks at 0.105 and 0.101 V are observed for Rh-TDA and Rh-HTA respectively corresponding to the oxidation of HCOOH. During the forward scan, formic acid oxidation produces a prominent anodic peak with a current density of 626 and 1466 $\mu A/cm^2$ for Rh-TDA and Rh-HTA respectively.

As discussed earlier, the voltammograms show two oxidation peaks, typical for the transformation of formic acid and/or CO to CO_2. A significant negative shift in the onset potential and high anodic peak current for the formic acid oxidation have been observed on the Rh-HTA as compared to all other nanostructures and bulk Rh that confirms their highest electrocatalytic activity (Table 2.3). This improvement in the activity of nanoneedles is in excellent agreement with morphological results as discussed in more details in the next section.

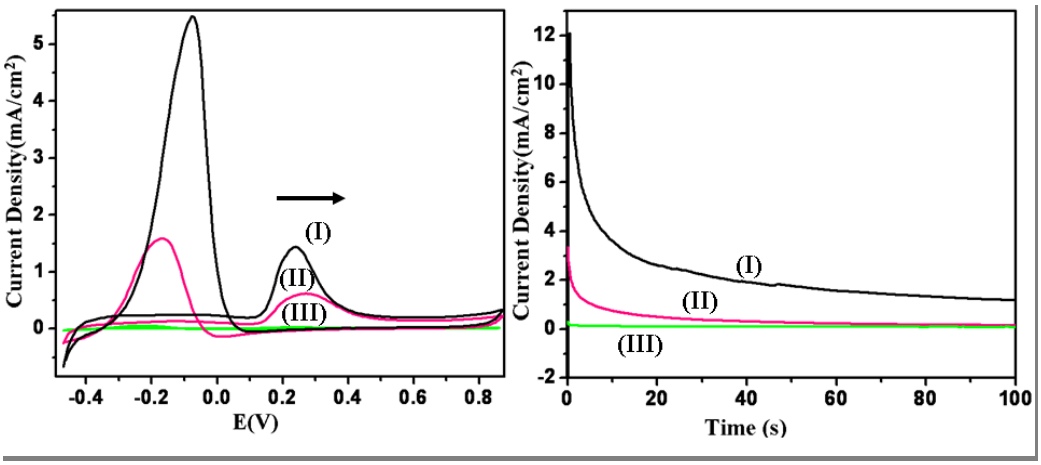

Figure 2.14. (a) Superimposed CVs of (I) Rh-HTA, (II) Rh-TDA and (III) bulk Rh electrode in a mixture of 0.5 M HCOOH and 0.5 M H_2SO_4 using a Hg-Hg_2SO_4 as reference electrode and Pt foil as a counter electrode at a scan rate of 50 mV/s (second cycle). (b) Superimposed transient current density curves of formic acid oxidation for (I) Rh-HTA, (II) Rh-TDA and (III) bulk Rh at an applied potential of 0.20 V for 100 s.

Further this enhanced electrocatalytic activity, confirmed from I-t transients for all three samples also supports the above conclusion. Accordingly, a comparison of data in Figures 2.13 (b) and 2.14 (b) shows that transient current density at room temperature after normalizing with respect to the electroactive Rh surface area for formic acid oxidation at 0.20 V (corresponding to the potential selected from the CV) on all the nanostructures are much higher than that on bulk Rh. Interestingly, the current density shows a decreasing trend, in the order of Rh-HTA> Rh-TDA> Rh-TA >Rh-AA >>> bulk Rh as also summarized in Table 2.3. The enhancement factor R, which is defined as the ratio of the current density measured on Rh nanoparticles versus that acquired on commercial Rh, ranges up to 6000 % for Rh-HTA and 1200 % for Rh-AA respectively [31]. Moreover, these 1D nanostructures are stable even after electrochemical measurements indicating that the morphology is potential-independent, which is unaffected by intermediate reactive species generated during the formic acid oxidation.

2.5. Structure-Property Correlation

The electrocatalytic activity of these 1D nanostructures could be explained on the basis of their morphology and tunable properties. The electrooxidation of HCOOH is very subtle and greatly sensitive to the surface structure, leading to a dramatic variation of the rate with size, shape and nature of Rh morphologies [31]. Accordingly, comparative studies on electrocatalytic performance of different 1D Rh nanostructures towards the electrooxidation of formic acid are carried out to explore its validity for micro fuel cell applications. The irreversible electrooxidation of HCOOH to CO_2 on Rh surface could be written as,

$$HCOOH \rightarrow CO_2 + 2H^+ + 2e^- \quad \text{.....} \quad (2.2)$$

$$E_0 = -0.25\ V\ vs\ NHE$$

The electrooxidation of HCOOH to CO_2 on Rh surface proceeds *via* a dual path mechanism, which involves a reactive intermediate (main path, dehydrogenation) leading to CO_2 evolution and adsorbed CO as a poisoning species (parallel path, dehydration) as shown schematically in pathway steps (1-3) [30]. Hence, all the noticeable current can be attributed to the oxidation of formic acid and/or CO to CO_2. The first anodic peak is due to the oxidation of HCOOH to CO_2 [step (1)] on surface sites that remain unblocked by CO whereas the second anodic peak corresponds to the oxidation of surface adsorbed CO [peak current slightly increases on cycling due to steps (2) and (3)]. During the cathodic sweep, a peak is observed after the partial reduction of irreversibly formed surface oxides, which interestingly, represents the actual catalytic activity of the Rh surface.

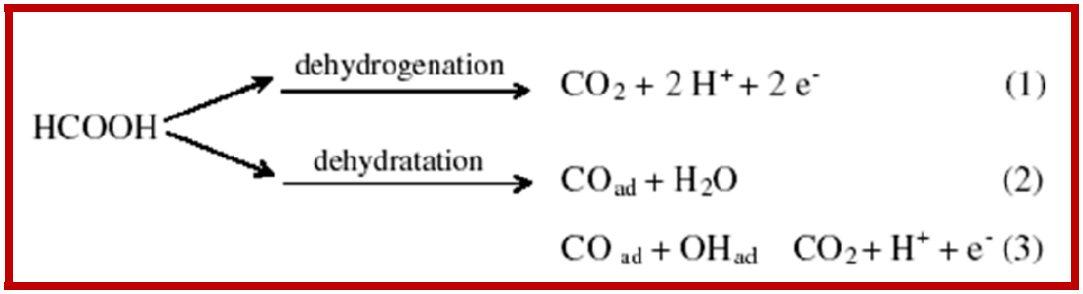

A plausible explanation for the growth of interconnected nanochains may be offered on the basis of a kinetically controlled mechanism since the particle surface

becomes more stable *via* the deactivation of larger facets by the capping molecules including HTA, TDA, TA and AA, necessitating a comparatively longer time for the growth of nanochains, nanorods, and nanoneedles from nanoparticles. For example, extendable assembly of these nanoparticles is formed upon stirring, especially in the presence of capped TA/AA having free functional groups leading to the nanochain formation as illustrated (Oswalds Ripening) in Figure 2.1. Interestingly, even after the formation of Rh nanochains (Figure 2.2 and 2.3), the average diameter does not change, suggesting no predominant effect of stirring on the anisotropic growth modes, perhaps due to qualitative conformational changes in their capped polyfunctional molecules finally leading to their assembly [18]. This is a clear evidence for our assertion that nanochains are formed by the interlinking of nanoparticles on the basis of polyfunctional nature of the capping molecule. Recently, Zhou et al. have reported a similar strategy for the synthesis of Ni/Ni_3C nanochains (size ~25.4 nm) by using a mixture of trioctylphosphine oxide (TOPO) and poly vinyl pyrollidone (PVP) with a bigger size and poly-dispersity, perhaps due to the weaker binding nature of the capping molecules (PVP and TOPO) [32]. Another supportive reason for the network formation can be drawn by the relative metal-binding ability of both -OH and >C=O groups. The adjacent Rh nanoparticles are interconnected either by hydrogen bonding through the direct coupling between -OH and >C=O groups or by covalent bonding (see Figure 2.1) as evident from the combined results TEM, TG, FTIR and XPS analysis. Further, the role of -OH and >C=O as surface passivating agents as well as linkers for the chain formation is inferred from their highly branched interconnected nanochains.

In this way, the surface bound capping molecules TA and AA moieties provide more stability and controllable chemical properties to these nanoparticles. Moreover, the use of TA and AA render Rh nanostructures more active as the tendency for agglomeration is prevented by modifying Rh surface geometrically/electronically through their assembly formation. In other words, TA and AA form self-assembled mono/multilayers on the surface providing stability at nano size distribution (5-7 nm) revealing quantum size effects as confirmed by some of our earlier reports of excellent

catalytic activity and single electron performance [7-10]. As colloidal nanoparticles, their surface passivation by organic capping molecules does not block all the active sites, especially when polydentate molecules like HTA, TA and AA are used. The control over particle size and dispersity by surface functionalization, intended to enhance particle stability, dictate surface chemistry, solubility and the degree of particle interactions that also helps to increase their electrocatalytic performance.

2.6. Conclusions

Interconnected Rh nanostructures have been successfully prepared at room temperature by a simple solution phase approach and their structural evolution has been analyzed by thermogravimetric and Fourier transform infra-red spectroscopic results to demonstrate the importance of controlling critical experimental parameters using polyfunctional molecules. A negative shift of the onset potential from cyclic voltammetry and analysis of current time transient towards formic acid oxidation suggest their potential applications as efficient electrocatalysts in fuel cells. These findings open up new possibilities for tailoring nanostructured electrodes with potential benefits since the development of a better electrocatalyst for many fuel cell reactions continues to be an important challenge. The redox behavior of all these 1D nanostructures further opens up their unique ability to manipulate the surface properties.

2.7. References

1. Steele, B. C. H. *Nature* **1999,** *400,* **619.**
2. Caswell, K. K.; Wilson, J. N.; Bunz, U. H. F.; Murphy, C. J. *J. Am. Chem. Soc.* **2003,** *125,* **13914.**
3. (a) Polavarapu, L.; Xu, Q. H. *Nanotechnology* **2008,** *19,* **075601.** (b) Nikhi, J. R.; Peng, X. G. *J. Am. Chem. Soc.* **2003,** *125,* 14280**.** (b) Sardar, R.; Shumaker-Parry, J. S. *Nano Lett.* **2008,** *8,* **731.** (c) Lin, S.; Li, M.; Dujardin, E.; Girard, C.; Mann, S. *Adv. Mater.* **2005,** *17,* **2553**. (d) Liu, Z. P.; Li, S.; Yang, Y.; Peng, S.; Hu, Z. K.; Qian, Y. T. *Adv. Mater.* **2003,** *15,* **1946.**
4. (a) Liu, C.; Guo, L.; Wang, R.; Deng, Y.; Xu, H.; Yang, S. *Chem. Comm.* **2004, 2726**. (b) Huang, L. S.; Wright, S.; Yang, S. G.; Shen, D. Z.; Gu, B. X.; Du, Y. W. *J. Phys. Chem. B* **2004**, *108*, **19901**. (c) Kohno H.; Takeda, S. *J. Surf. Sci. Nanotechnol.* **2005**, *3*, **131**.
5. (a) Doyle M.; Rajendran, G. *Handbook of Fuel Cells Fundamentals, Technology and Applications;* John Wiley & Sons: Chichester, U. K. **2003**, *3*, 30, **351**. (b) http://www.fueleconomy.gov/feg/fcv_pem.html, (c) Service, R. F. *Science,* **2007**, *315*, **172**.
6. (a) Mndez, E.; Rodrguez, J.; Arvalo, M. C.; Pastor, E. *Langmuir* **2002**, *18*, **763**. (b) Wieckowski, A.; Savinova E. R.; Vayenas, C. G. *Catalysis and Electrocatalysis at Nanoparticle Surfaces*, Marcel Dekker, Inc., New York, **2003**.
7. (a) Weissermel, K.; Arpe, H. J. *Industrial Organic Chemistry*, VCH, New York, **1993**. (b) Schulz, J.; Roucoux, A.; Patin, H. *Chem. Commun*. **1999**, **535**. (c) Motoyama, Y.; Takasaki, M.; Yoon, S. H.; Mochida, I.; Nagashima. H. *Org. Lett*. **2009**, *11*, **5042**. (d) Ziegelbauer, J. M.; Gatewood, D.; Gull, Andrea F. Maxime, J. F.; Guinel.; Ernst, F.; Ramaker, D. E. Mukerjee, S. *J. Phys. Chem. C* **2009**, *113*, **6955**.
8. Lam-Wing H.; Weaver, M. J. *J. Phys. Chem. C* **1989**, *93*, **7218**.

9. Kakade, B. A.; Shintri, S. S.; Sathe, B. R.; Halligudi S. B.; Pillai, V. K. *Adv. Mater*. **2007**, *19*, **272**.

10 (a) Galletti, C.; Specchia, S.; Saracco, G.; Specchia, V. *Ind. Eng. Chem. Res*. **2008**, *47*, **5304**. (b) Galletti, C.; Fiorot, S.; Specchia, S.; Saracco, G.; Specchia, V. *Top. Catal.* **2007**, *145*, **15**.

11 (a) Porter, L. A.; Ribbe, Jr., A. E.; Buriak, J. M. *Nano. Lett*. **2003,** *3*, **1043**. (b) Huang, J.; Cao, Y.; Wang, M.; Huang, C.; Deng, Z.; Tong, H.; Liu, Z. *J. Phy. Chem. C* **2010,** *114*, **14748**. (c) Wang, X.; Peng, Q.; Li, Y. *Acc. Chem. Res*. **2007** *40*, **635**. (d) Choi, J. W.; McDonough, J.; Jeong, S.; Yoo, J. S.; Chan, C. K.; Cui Y. *Nano Lett*. **2010**, *10*, **1409**. (e) Saunders, A. E.; Popov, I.; Banin, U. *J. Phy. Chem. B* **2006,** *110*, **25421**. (f) Wang, X.; Xi, G.; Liu, Y.; Qian, Y. *Cry. Growth Des*. **2008**, *8*, **1406**. (g) Cheng, B.; Shi, W.; Russell Tanner, J. M.; Zhang, L.; Samulski, E. T. *Inorg. Chem.* **2006**, *45*, **1208**. (h) Chen, J.; Xing, X.; Watson, A.; Wang, W.; Yu, R.; Deng, J.; Yan, L.; Sun, C.; Chen. X. *Chem. Mater.* **2007**, *19*, **3598**. (i) Rørvik, P. M.; Grande, T.; Einarsrud, M. A. *Cry. Growth Des.* **2009**, *9*, **1979**.

12 (a) Culllity, B. D.; Stock, S. R. *Elements of X-ray Diffraction, 3rd Edition,* Englewood Cliffs, N. J: Prince-Hall, **2001**. (b) West, A. R. *Solid State Chemistry and Its Applications* ISBN: 978-0-471-90874-6, **1991**. Kittel, C. *Introduction to Solid State Physics* (Wiley: New York, **2004**). (c) Rosenberg, H. M. *The Solid State* (Oxford University Press: Oxford, **1995**). (d) Hoddeson, L.; Braun, E.; Teichmann, J.; Weart, S. *Out of the Crystal Maze. Chapters from the History of Solid State Physics*, *ed.* (Oxford: Oxford University Press, **1992**). (e) Omar, M. A. *Elementary Solid State Physics,* **1993** Vth Ediation. (f) Motl, N. E.; Ewusi-Annan, E.; Sines, I. T.; Jensen, L.; Schaak R. E. *J. Phy. Chem. C* **2010**, *114*, **19263.** (g) Azurdia, J. A.; Marchal, J.; Shea, P.; Sun, H.; Pan, X. Q.; Laine, R. M. *Chem. Mater*. **2006**, *18*, **731**.

13 (a) Hegde, M. S.; Madras, G.; Patil, K. C. *Acc. Chem. Res.* **2009**, *42*, **704.** (b) Vegh, J. *J. Elect. Spectroscopy Related Phenomena* **2006**, *151*, **159.**

14 Polavarapu, L.; Xu, Q. H. *Langmuir* **2008**, *24,* **10608**.

15 Joseph, S. T. S.; Ipe, B. I.; Pramod, P.; George Thomas K. *J. Phys. Chem. B* **2006**, *110* , **150.**

16 Wang, N.; Cao, X.; Kong, D.; Chen, W. Guo, L. Chen C. *J. Phys. Chem. C* **2008**, *112*, **6613**.

17 (a) Hoefelmeyer, J. D.; Niesz, K.; Somorjai, G. A.; Tilley, T. D. *Nano Lett*. **2005**, *5*, **435**. (b) Ewers, T. D.; Sra, A. K.; Norris, B. C.; Cable, R. E.; Cheng, C.; Shantz, D. F.; Schaak, R. E. *Chem. Mater*. **2005**, *17*, **514**.

18 (a) Lim, B.; Xia, Y. *Angew. Chem. Int. Ed.* **2007,** *46,* **9279** (b) Zhu, X.; Wang, L.; Lin, J.; Zhang, L. *ACS Nano* **2010**, *4*, **4979.** (c) Baranov, D.; Fiore, A.; Huis, M. V. Giannini, C.; Falqui, A.; Lafont, U.; Zandbergen, H.; Zanella, M.; Cingolani, R.; Manna, L. *Nano Lett*. **2010** *20,* **104878.**

19 (a) Humphrey, S. M.; Grass, M. E.; Habas, S. E.; Niesz, K.; Somorjai, G. A.; Tilley, T. D. *Nano Lett*. **2007**, *7*, **785.** (b) Kundu, S.; Wang, K.; Liang, H. *J. Phys. Chem. C* **2009**, *113*, **18570**. (c) Ewers, T. D.; Sra, A. K.; Norris, B. C.; Cable, R. E.; Cheng, C. H.; Shantz, D. F.; Schaak, R. E. *Chem. Mater*. **2005**, *17*, **514.** (d) Yuan, Q.; Zhou, Z.; Zhuang, J.; Wang, X. *Inorg. Chem*. **2010**, *49*, **5515.** (e) Wang, Y.; Ren, J.; Deng, K.; Gui, L.; Tang, Y. *Chem. Mater*. **2000**, *12*, **1622.** (f) Yuan, Q.; Zhou, Z.; Zhuang, J.; Wang, Xun *Inorg. Chem*. **2010**, *49*, **5515.** (g) Wang, Y.; Ren, J.; Deng, K.; Gui, L.; Tang, Y. *Chem. Mater.* **2000**, *12*, **1622.** (h) Zhang, Y.; Grass, M. E.; Habas, S. E.; Tao, F.; Zhang, T.; Yang, P.; Somorjai G. A. *J. Phys. Chem. C* **2007**, *111*, **12243**.

20 Scherrer, P.; Gesell, G. N.; Patterson, A. *Phys. Rev.* **1918**, *56,* **978**.

21 (a) Jacinto, M. J.; Kiyohara, P. K.; Masunaga, S. H.; Jardim, R. F.; Rossi, L. M. *Appl. Cat. A: Gen.* **2008,** *338*, **52.** (b) Pan, H. B.; Wai, C. M. *J. Phys. Chem. C* **2010**, *114*, **11364.**

22 Terril, R. H.; Postlethwaite, T. A.; Chen, C. H.; Poon, C. D.; Terzis, A.; Chen, A.; Hutchison, J. E.; Clark, M. R.; Wignall, G.; Londono, J. D.; Superfine, R.; Falvo, M.; Johnson Jr., C. S.; Samulski, E. T.; Murray, R. W. *J. Am. Chem. Soc*.

1995, *117*, **12537.**

23 (a) Han, Y. K.; Oh, S. G.; Shin, S. I.; Joung, W. D.; Yi, S. C.; Cho, C. G. *Coll. Surf. B: Bio.* **2002**, *24*, **33.** (b) Rumpler, M.; Woesz1, A.; Dunlop, J. W. C.; Van Dongen, J. T.; Fratzl, P. *J. R. Soc. Interface* **2008,** *5*, **1173.**

24 Shido, T.; Okazaki, T.; Ichikawa, M. *Cat. Lett*. **1993**, *20*, **37.**

25 Pinchas, S.; Laulicht, I. *Infrared Spectra of Labeled Compounds*, Academic Press: London, **1971**; Chapter 9. *NIST Vibrational Spectroscopy Database* via. Internet: http://srdata.nist.gov/vb .

26 Frolov, V. M.; Shuikina, L. P.; Turisbekova, K. K.; Bondarenko G. N. *Catal. (Eng. Trans.)* **1994**, *35*, **800**.

27 (a) http://srdata.nist.gov/xps/elm_in_comp_res (b) Weng-Sieh, Z.; Gronsky, R.; Bell, A. T. *J. Catal.* **1997,** *170,* **62**. (c) Rubel, M.; Pszonicka, M.; Palczewska, W. *J. Mater. Sci*. **1985**, *20*, **3639**.

28 *X-ray Photoelectron Spectroscopy Database NIST Standard Reference Database 20, Version 3.5* http://srdata.nist.gov/xps.

29 (a) Wang, Z.; Levy, R.; Fernig, D. G.; Brust, M. *Bioconjugate Chem*. **2005**, *16*, **497**. (b) Mirkin, C. A.; Letsinger, R. L.; Mucic, R. C.; Storhoff, J. J. *Nature* **1996**, *382*, **607.** (c) Alivisatos, A. P.; Johnsson, K. P.; Peng, X.; Wilson, T. E.; Loweth, C. J.; Bruchez, M. P. Jr.; Schultz, P. G. *Nature* **1996**, *382*, **609**. (d) Mucic, R. C.; Storhoff, J. J.; Mirkin, C. A.; Letsinger, R. L. *J. Am. Chem. Soc.* **1998**, *120*, **12674**. (e) Loweth, C. J.; Caldwell, W. B.; Peng, X.; Alivisatos, A. P.; Schultz, P. G. *Angew. Chem. Int. Ed.* **1999**, *38*, **1808**. (f) Storhoff, J. J.; Mirkin, C. A. *Chem. Rev.* **1999**, *99*, **1849**. (g) Mann, S.; Shenton, W.; Li, M.; Connolly, S.; Fitzmaurice, D. *Adv. Mater*. **2000**, *12*, **147**. (h) Taton, T. A.; Mirkin, C. A.; Letsinger, R. L. *Science* **2000**, *289*, **1757**. (i) Niemeyer, C. M. *Angew. Chem. Int. Ed.* **2001**, *40*, **4128**. (j) Zanchet, D.; Micheel, C. M.; Parak, W. J.; Gerion, D.; Alivisatos, A. P. *Nano Lett*. **2001**, *1*, **32**. (k) Sastry, M.; Rao, M.; Ganesh, K. N. *Acc. Chem. Res.* **2002**, *35*, **847**. (l) Niemeyer, M.; Ceyhan, B.; Hazarika, P. *Angew. Chem. Int. Ed*. **2003**, *42*, **5766**. (m) Fu, A.; Micheel, C. M.;

Cha, J.; Chang, H.; Yang, H.; Alivisatos, A. P. *J. Am. Chem. Soc.* **2004**, *126*, **10832**. (n) Li, M.; Mann, S. *J. Mater. Chem.* **2004**, *14*, **2260**. (o) Gourishankar, A.; Shukla, S.; Ganesh, K. N.; Sastry, M. *J. Am. Chem. Soc.* **2004**, *126*, **13186**. (p) Wessels, J. M.; Nothofer, H. G.; Ford, W. E.; Von Wrochem, F.; Scholz, F.; Vossmeyer, T.; Schroedter, A.; Weller, H.; Yasuda, A. *J. Am. Chem. Soc.* **2004**, *126*, **3349**. (q) Kanaras, A. G.; Wang, Z.; Bates, A. D.; Cosstick, R.; Brust, M. *Angew. Chem. Int. Ed* **2003,** *42*, **191**. (r) Wang, Z.; Kanaras, A. G.; Bates, A. D.; Cosstick, R.; Brust, M. J. *Mater. Chem.* **2004**, *14*, **578**. (s) Niazov, T.; Pavlov, V.; Xiao, Y.; Gill, R.; Willner, I. *Nano Lett.* **2004**, *4*, **1683**. (t) Turkevich, J.; Stevenson, P. C.; Hillier, J. *Discuss. Faraday Soc.* **1951**, *11*, **55**.

30 (a) Lam-Wing, H.; Weaver, M. J. *J. Phys. Chem*. **1989**, *93*, **7218**. (b) Matsuda, H.; Avabe, Y. Z. *Electrochem. Comm.* **1955**, *59*, **494**. (c) Brett, C. M. A.; Brett, A. M. O. *Electrochemistry: Principles, Methods and Application*s; Oxford University Press **1993**.

31 Tian, N.; Zhou, Z. Y.; Sun, S. G.; Ding, Y.; Wang, Z. L. *Science*, **2007**, *316*, **732**.

32 Zhou, W.; Zheng, K.; He, L.; Wang, R.; Guo, L.; Chen, C.; Han X.; Zhang, Z. *Nano Lett.* **2008**, *8*, **1147**.

CHAPTER 3

Evolution of Rhodium Nanostructures through Micro-Galvanic Cells*

This chapter describes the shape-selective morphological evolution of nanostructured Rh by a galvanic displacement reaction using Al in aqueous Rh (III) chloride at 298 K. Nanospheres obtained in this manner have size of ~200 nm assembled by individual nanoparticles of around 2.9 ± 0.4 nm diameter. Considering the role of Al substrate and diffusion of reactant and product species towards and away from the surface, a tentative mechanism for the formation of microgalvanic cells has been proposed. Further, investigations towards manipulating the surface

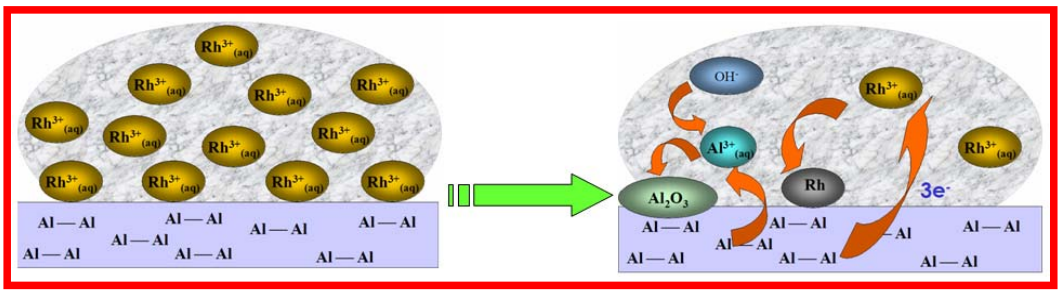

to tune plasmonic emission reveal morphology-dependent optical features of Rh nanostructures. The emergence of surface plasmon peaks at 375 and 474 nm respectively, is ascribed to truncated and smooth surface of nanospheres in contrast to the absence of surface plasmon for bulk Rh (0) in the visible range. Interestingly, the difference in growth in the presence of poly vinyl pyrollidone (PVP) during galvanic reactions, indicates a control over the surface structure (surface tension) between Rh and Al substrate. Small sized, faceted domains are responsible for the promising characteristics of these Rh nanostructures which might be especially useful for catalytic, field emission and magnetic applications. This chapter ends with a discussion about the electrocatalytic activity towards many fuel cell reactions as demonstrated by HCOOH oxidation.

---

*A part of the work discussed in this chapter has been published in: "***Appl. Phys. Letts.*** 96, 233101, **2010** and another part in ***J. Phys. Chem. C*** 113, 9616, **2009**"

3.1. Introduction

Synthesis of metallic nanostructures followed by their assembly on a desired surface in large scale especially using bottoms-up approach is essential for many of their successful applications in various fields with profound implications on understanding their collective behavior [1]. Several recent developments have enabled important applications in electronics, sensing, catalysis and electrochemistry due to their fascinating properties, primarily determined by their size, shape, composition and structure [2]. Indeed, this has been successfully accomplished to achieve different size, controlled shape and their self-organization at nanolevel for metals like Ag, Au, Pd and Pt using solution chemistry [3]. However, these colloidal nanostructures dispersed in liquids cannot be used directly for many applications including heterogeneous catalysis and also for device fabrication, especially because of the challenges in separation and recycling aspects. Furthermore, it is very difficult to control the size, composition and their self-organization [4]. One way to overcome these problems is by using electrochemical tools to precisely control the crystal growth and to design high quality metal and metal oxide nanostructures [5].

Consequently, the growth of nanostructures by electrochemical methods has received considerable attention as the presence of electric field could offer enormous help in controlling even complex morphologies such as fractal geometry and dendritic growth. This method is particularly advantageous because crucial steps such as nucleation and further growth can be regulated by modulating appropriate physical parameters like concentration, number of surface active sites on Al surface, temperature, pH and electric field. In most of these cases, however, growth has occurred under non-equilibrium conditions and interestingly, a dramatic variation in morphology has been observed either at low or high overpotentials. For example, recently Pt and RuO_2 mesostructures prepared using porous alumina template have shown interesting potential-dependent morphological evolution for their tunable electrochemical and electrical performance [6]. Similarly, such a slow evolution of Rh nanostructures under equilibrium conditions could be effected by the simple approach of galvanic exchange, offering a unique way to control the morphology by choosing a suitable redox couple and this approach has been

applied successfully to achieve different shapes (viz. cubes, rods, wires and core-shell nanostructures) of Au, Ag, Pd, Pt and their alloys [7]. This approach is particularly attractive for preparing nanostructures with well-controlled dimensions and moreover, due to their simplicity (no need of sophisticated equipments), cost effectiveness and high throughput. However, some of these nanostructures are contaminated by impurities of *in-situ* generated side products and there are also concerns on their variable composition and morphological dispersion [8].

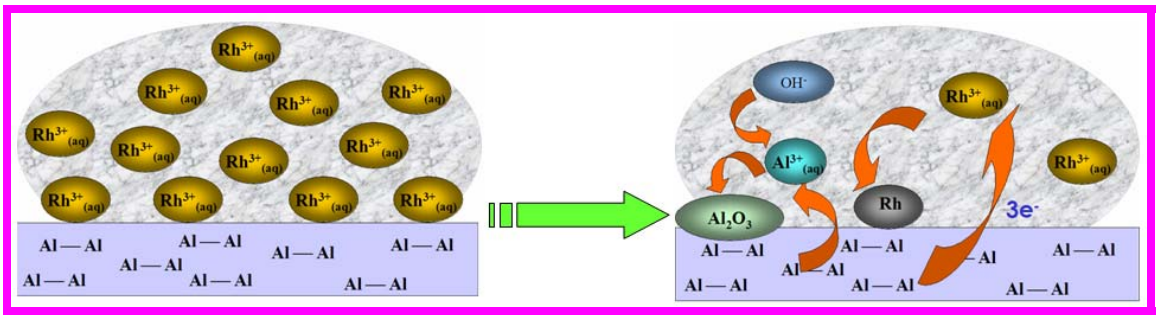

Figure 3.1. A schematic illustration of the galvanic displacement reaction between Al substrate and Rh ions in solution; the reaction can continue as long as ions could diffuse to cause electron transfer through the surface film.

Although a detailed mechanism of galvanic displacement is not well understood, an accurate control of key parameters is possible by applying the concepts of corrosion from the mixed potential theory [9]. In this case, redox exchange proceeds as long as the oxidized Al^{3+} ions continue to permeate through the metal film into the solution or until a thick dielectric layer of hydroxide forms, thereby preventing further mass transfer as shown in Figure 3.1. Accordingly, Al loses electrons ($E°_{Al^{3+}/Al}$ = -1.66 V vs. SHE) and goes into the solution as solvated Al^{3+} ions, while Rh^{3+} ions in the solution accept these electrons ($E°_{Rh^{3+}/Rh}$= 2.3 V vs. SHE) to form Rh on the surface of Al by the following displacement reaction,

$$RhCl_{3\,(aq)} + Al_{(s)} \rightarrow Rh^{0}_{(s)} + Al^{3+}_{(aq)} + 3Cl^{-}_{(aq)}$$

[$E°_{cell}$ = 3.96 V vs. SHE; ΔG = -270 kcal/mole at Standard Temperature and Pressure (STP)]

Some Rh (III) ions could also get reduced in solution to form aggregated spheres on a larger scale. Interestingly, the open-circuit potential (OCP; 0.99 V) shows a significant decrease with time, perhaps due to a decrease in Rh ion concentration, with concomitant film formation on Al surface which also confirms the above reaction. It is well known that chloride ions do cause pitting corrosion on Al surface and these localized pits can facilitate the formation of microgalvanic cells [10]. However, many questions like *in situ* optical response, morphological evolution, thermodynamic aspects and the growth mechanism have been left unanswered due to the difficulty of controlling the size. One way to achieve high quality, one dimensional (1D) nanostructures, is by using solution-phase techniques, via preferential capping mechanisms. It is believed that molecular capping agents play a significant role in the kinetic control of the nanocrystal growth by preferentially adsorbing to specific crystal faces, thus inhibiting growth of those surfaces. Evidence for this selective capping mechanism has been recently demonstrated by the formation of Ag nanowires using PVP as a capping agent. One possible explanation is that PVP selectively binds to the {100} facets of silver while maintaining {111} facets to grow further. Because of this unusual ability of PVP towards facet selective capping/binding, we have employed that to our microgalvanic approach to modulate Rh ion diffusion towards substrate followed by their reduction. Therefore, this hybrid approach is expected to offer many benefits towards the synthesis of 1D Rh nanostructures.

In the preceding chapter, we have discussed the role of polyfunctional molecules towards the evolution of shape-selective interconnected and 1D nanostructures of Rh using external reducing agents for the reduction of Rh^{3+} ions followed by their tunable electrocatalytic activities. The present chapter extends these studies by using a new approach to achieve facet-selective Rh nanostructures via galvanic displacement based on the potential difference between Al and Rh ions and also by changing external parameters like pH, concentration of Rh ions, temperature and time of exposure. On the basis of morphological evolution and electrochemical studies, we also propose a tentative growth mechanism for their structural evolution through micro-galvanic cell formation,

explaining novel optical features and a correlation with growth kinetics on the basis of *in situ* UV-visible and time-dependent XRD studies. These Rh nanostructures are of potential relevance to many applications like single electron devices, electrocatalysts in fuel cells [11], photo-electrochemical cells and catalysis of a variety of organic reactions [12] (hydrogenation, hydroformylation, hydride transformation etc.) as demonstrated by their enhanced electrocatalytic properties towards formaldehyde oxidation.

3.2. Experimental Section

3.2.1. Materials

Rhodium chloride (99%), potassium chloride, potassium bromide and poly vinyl pyrollidone (PVP) were obtained from Aldrich, whereas aluminum foil (99.9% pure), acetone, ethanol, formaldehyde and sodium sulphate AR grade were from Merck.

3.2.2. Synthesis of Rhodium Nanostructures by Galvanic Displacement

For the synthesis of Rh nanostructures; galvanic displacement was carried out by immersing an Al foil (thickness 75 μm after etching in 1M NaOH for few minutes to remove the surface oxide layer) in aqueous 1 mM $RhCl_3$. In a typical synthetic procedure, an Al foil of bilateral surface area of 2 cm^2, was first cleaned by sonication in 50 % nitric acid for 2 min. (to remove the native oxide layer from surface) followed by vigorous rinsing with deionized water (~18 MΩ.cm) and finally the residual i.e., adsorbed organic impurities were removed by washing with ethanol and dried with nitrogen. This foil was then immersed in 100 mL of aqueous 1 mM $RhCl_3$ solution at room temperature. Potential-dependent (based on peak potential estimated from cyclic voltammetry) morphological evolution was carried out using a similar strategy by controlling other experimental parameters such as concentration, temperature, time of immersion and exposed aluminum area. Subsequently, the micro-galvanic cells grown on aluminum surface were analyzed by removing the Rh nanostructures using ultra-sonication in deionized water.

The effect of capping molecules on the morphological evolution of nanostructured Rh was further demonstrated by a modified galvanic displacement approach, using PVP as the stabilizer, for the building of nanorods. In a typical procedure, similar experiments were carried out using the above procedure in the presence of PVP at appropriate Rh: PVP ratio (1:5 both solutions in mM). The material grown on the surface of aluminum were collected, washed first with 1M NaOH to remove the impurities of alumina embedded into the nanostructures, followed by deionized water and finally with ethanol to remove the impurities like chloride ions and excess of $RhCl_3$. This purified material was further characterized by transmission electron microscopy (TEM), scanning electron microscopy (SEM), X-ray diffraction (XRD), X-ray photoelectron spectroscopy (XPS) and thermogravimetric analysis (TGA).

3.3. Structural and Morphological Characterization

3.3.1. Cyclic voltammetry

Cyclic voltammetric measurements were performed using an Autolab PGSTAT30 (ECO CHEMIE) instrument, using pure Al substrate as the working electrode and a platinum foil/wire as the reference and counter electrodes respectively in an aqueous solution of 1 mM $RhCl_3$ in 0.5 M Na_2SO_4.. Cyclic voltammetric studies were carried out both with and without $RhCl_3$ solution using Al and/or Pt working electrodes in 0.5 M Na_2SO_4. After verifying the thermodynamic parameters like redox potentials from cyclic voltammetry, chrono-amperometry was carried out at fixed potentials (anodic and cathodic) to investigate the growth mechanism of nanostructures through galvanic displacement reactions. Nanostructures obtained at these controlled potentials were collected and washed with 0.1 M NaOH to remove the impurities of alumina followed by deionized water till pH became neutral, followed by a final washing with ethanol by repeated centrifugation (5000 rpm). These purified samples were used for XPS, SEM analysis and electrocatalytic studies. Experimental details of other characterization details like FT-IR (DRIFT mode), SEM, HRTEM, XPS and TGA have been already described in section 2.3 of chapter 2.

3.3.2. Electrocatalytic Studies

Electrocatalytic activities of Rh nanostructures were obtained from cyclic voltammetry using a standard three-electrode cell on an Autolab PGSTAT30 (Eco chemie) instrument. As per the procedure discussed in chapter 2 (section 2.3.7), a calculated amount of Rh sample was dropcasted on the electrode surface for electrocatalytic studies. A Pt foil and a Pt wire were used as the counter and reference electrodes respectively. Formaldehyde (HCHO) oxidation was carried out using a solution of 0.5 M NaOH and 0.5 M HCHO at room temperature; all the voltammograms were measured at a sweep rate of 50 mV/s. All the potentials here presented with respect to (Hg-HgO and Hg-Hg_2SO_4) as the reference electrodes respectively.

3.4. Results and Discussions

3.4.1. Scanning Electron Microscopic Studies

3.4.1.1. Time dependent Morphological Evolution

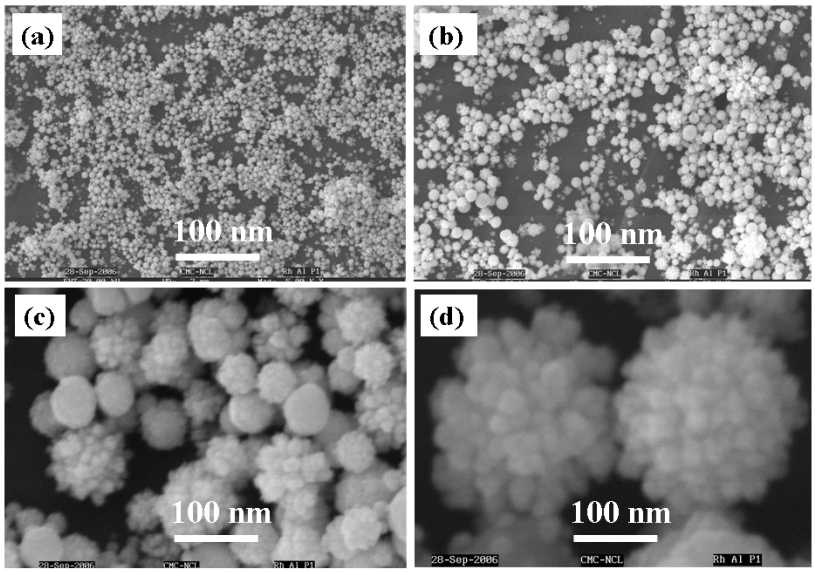

Figure 3.2. Scanning electron micrographs of Rh nanostructures grown on Al surface at the same magnifications after (a) 5 min. (b) 10 min. (c) 20 min. and (d) 40 min. from 1 mM $RhCl_3$ solution at room temperature.

In order to explore the time-dependent morphological evolution of Rh nanostructures, scanning electron micrographic images at various stages have been analyzed for subtle changes. Accordingly, Figure 3.2 shows a comparison of SEM images of Rh nanostructures formed on the surface of pretreated Al surface at for different time intervals like 5, 10, 20 and 40 min. The images clearly depict high coverage of nanospheres of ca. 20 nm size immediately after 5 min. The particle distribution on Al surface from figure 3.2(a) indicates that some of the initial nanoparticles could act as nucleating centers for further growth. The presence of hetero-sites on Al surface [sites, where Rh ad-ion initially had got reduced as Rh (0)] and the limited nucleation density are considered as critical parameters promoting both the instantaneous growth and the evolution of morphology. Interestingly, it is clear from the SEM images shown in Figure 3.2 (a)-(c) that, the average diameter of spherical particle varies as 20, 35 and 75 nm after 5, 10 and 20 min respectively. Assuming the shape to be invariant, there is only a minor size variation with time along with a concomitant interlinking of these nanospheres forming a hierarchical assembly. Consequently, Figure 3.2(d) reveals a typical SEM image of as synthesised Rh nanostructures after 40 min exhibiting nanospheres with an average diameter of ~150 nm, consisting nanospheres of ~30 nm size on its surface having their incomplete growth.

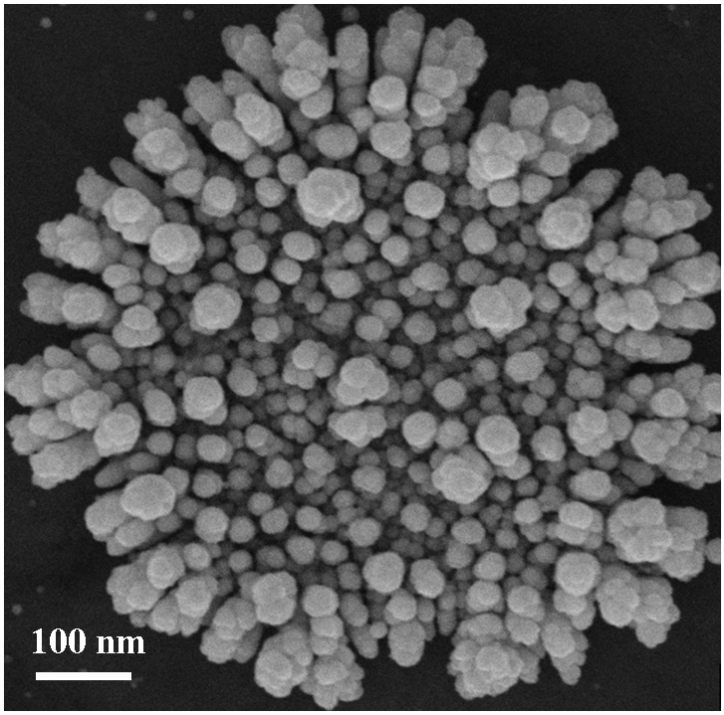

Figure 3.3. Representative scanning electron micrographic image of Rh nanoassemblies on Al surface at room temperature for 80 min revealing one directional growth.

Interestingly, these small nanospheres seem to form the foundation for further 1D growth at longer time (~ 80 min) as shown in SEM image (Figure 3.3). Therefore, their further growth has generated three dimensional flowerlike assemblies having lower symmetry and these morphological changes with time do agree well with structural changes observed from XRD analysis shown in Figure 3.9. Although these structures have no regular shape, every branch grows along the forward direction and all the arms appear to have a common origin with varying lengths of about 10 to 100 μm.

3.4.1.2. Potential Dependent Morphological Evolution

Figure 3.4 shows representative series of scanning electron micrographs of Rh nanostructures formed under identical experimental conditions at three fixed potentials of -1.10, 0.99 (open circuit potential; OCP) and 1.42 V vs Hg-Hg_2SO_4 respectively. These potentials are selected on the basis of CV using 1 mM $RhCl_3$ solution in 0.5 M Na_2SO_4 as

the supporting electrolyte using Al substrate as a working electrode. Cyclic voltammogram for 1 mM $RhCl_3$ in 0.5 M Na_2SO_4 solution gives a cathodic peak at -1.10 V, indicating that, in the presence of Al, charge transfer facilitates Rh (0) formation. The rate of growth however, is controlled by the mass transfer rate of Rh^{3+} to the growing Rh nuclei centered on the Al substrate surface.

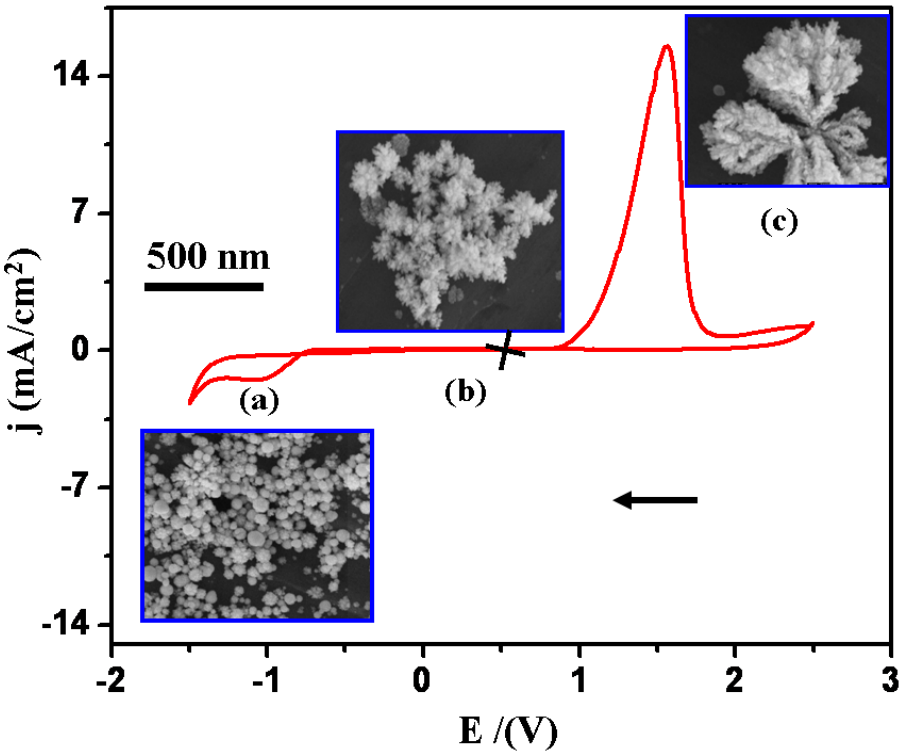

Figure 3.4. Cyclic voltammogram for a mixture of 1 mM $RhCl_3$ and 0.5 M Na_2SO_4 aqueous solution on Al substrate as a working electrode at 50 mV/s; inset shows SEM images of corresponding nanostructures prepared at different peak potentials; (a) -1.10 V, (b) OCP, 0.99 V and (c) 1.42 V respectively.

Indeed, Rh starts depositing from 0.99 V (OCP indicated in CV Figure 3.4) onwards and causes different morphology depending on the potential even up to -1.40 V, where hydrogen evolution becomes rampant. This is the primary reason for causing Rh^{3+} diffusion slower with respect to H^+ ions and this higher concentration of H^+ ions at the interface could be responsible for the formation of a large number of active sites for the reduction of Rh^{3+} ions on Al surface leading to their growth. Furthermore, it reveals a

chain like pattern, which could be attributed to the presence of lower inter-nuclei distance and presumably their higher surface energy. Crossover between anodic and cathodic current curves during the reverse potential sweep (-0.50 V to 0.90 V) arises perhaps due to the change in nucleation processes on the Al surface. In comparison, during the anodic scan, a sharp peak is seen at 1.42 V due to Rh dissolution, with concomitant oxide formation. Further, in the successive stages due to the effect of the overlap between diffusional fields around the growing nuclei, one can expect the development of local concentration changes and a potential distribution. These overlapped zones of reduced concentration (in between the nuclei) result into a diminished nucleation rate controlling their growth, orthogonal to the plane as shown in Figure 3.4(c).

3.4.1.3. Effect of Polyvinyl Pyrollidone

Figure 3.5 shows the SEM image of Rh nanorods synthesized by the same galvanic displacement approach in the presence of PVP. Interestingly, in the presence of a very small amount of PVP (5 mM), the morphology changes from nanospheres (as shown in Figure 3.2) to bundles of nanorods having 1-1.5 μm length and ~200 nm diameter.

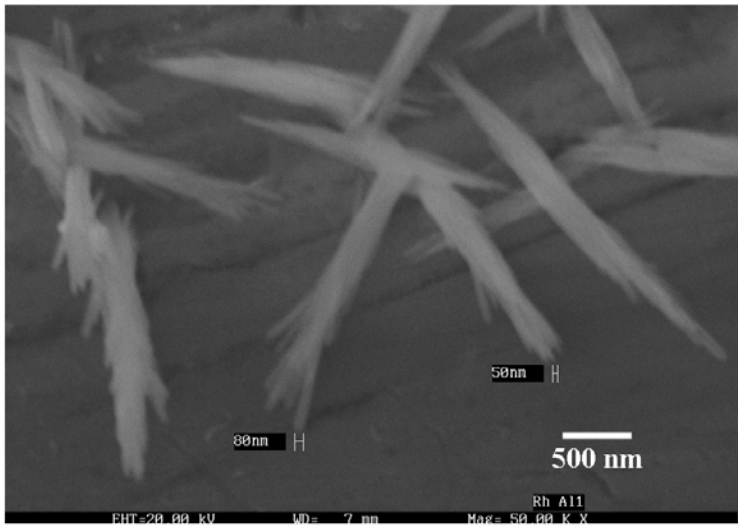

Figure 3.5. Scanning electron micrographs of "as synthesized" Rh nanorod bundles, in the presence of (1:5) Rh^{3+}: PVP ratio in mM concentration.

However, each bundle has many nanorods of ~40 nm diameter. Significantly, this extraordinary one dimensional growth of the Rh in presence of PVP could be due to the blocking of other Al sites present on the surface during nucleation. The diffusion of Rh ions towards limited number of nucleating sites present on Al surface (unblocked by PVP) is believed to be responsible for the formation of nanorods instead of 3D nanostructures.

3.4.2. Transmission Electron Microscopic Analysis

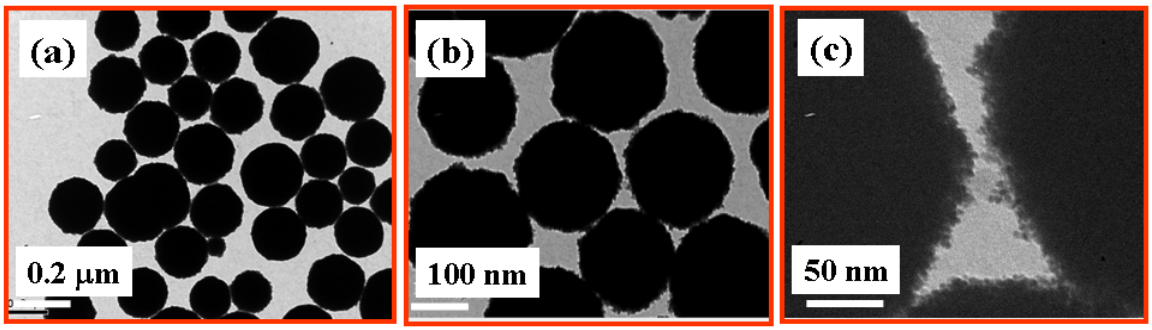

Figure 3.6. Bright field transmission electron micrographs of Rh nanostructures at different magnifications; (a) and (b) Rh nanospheres (~200 nm) made up of smaller particles having size 2-3 nm along with (c) of high magnification TEM image of two half nanospheres grown after 5 min. to reveal surface roughness.

Figure 3.6(a) and (b) shows a comparison of the TEM images of colloidal Rh nanostructures synthesised at OCP (0.99 V) taken after 5 min. These images clearly indicate an average diameter of ~200 nm having a polydispersity of ~10 %. However, outer surface of some of them are shown to have an irregular surface due to their uncontrolled growth as evident from high magnification TEM image of a single truncated Rh nanosphere with much hair like protrusions as illustrated in Figure 3.6 (c). HR-TEM images in Figure 3.7 a and b clearly indicate that these aggregates are made up of nanoparticles having their tendency for organization due to the high surface energy. The size distribution and regular arrangement are evident from a comparison of the TEM images of these particles. For example, a high population of uniformly sized particles with an average size of 2.9 ± 0.4 nm along with their statistical distribution (Gaussian), as

shown in Figure 3.7 (c), is obtained as a result of the analysis of more than 100 spherical particles, verified from four different samples.

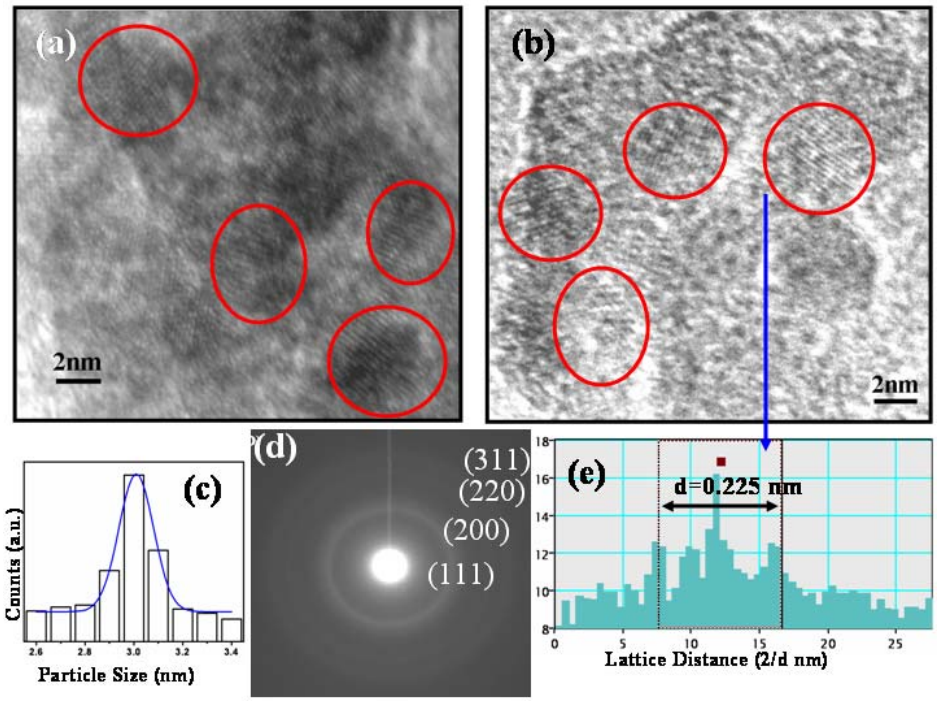

Figure 3.7. (a-b) High resolution transmission electron micrographs of Rh nanoparticles prepared by galvanic displacement reaction on Al, revealing a uniform distribution of Rh nanoparticles into spheres of size ~200 nm; with lattice fringes of (111) plane; (c) histogram indicating an average size of 2.9 ±0.4 nm; (d) SAED pattern revealing rings corresponding to crystalline Rh with fcc pattern and (e) profile of lattice fringes of Rh (111) encircled in (b), clearly exhibiting a distance of 0.225 nm.

Finally, selected area electron diffraction (SAED) pattern shows the crystalline nature of Rh nanostructures exhibiting dominant reflections corresponding to (111), (200), (220) and (311) planes as indicated in Figure 3.7 (d). More specifically, Figure 3.7 (e) shows the profile of lattice fringes of Rh (111) encircled in (b), exhibiting a distance of 0.225 nm which is comparable with the earlier reported value of 0.220 nm for similar sized Rh nanoparticles synthesized by various approaches [13].

3.4.3. *In situ* Optical Studies

Figure 3.8 illustrates the emergence of surface plasmon peaks at around 375 and 474 nm respectively as a result of the difference in the surface roughness of these nanospheres, as evident from the TEM images of respective single nanospheres. Indeed, Somorjai's and Tilley's groups have reported different morphologies of as-synthesized Rh nanostructures using seeded Polyol route revealing surface plasmon absorbance due to shape, size and capping dependent features [14]. Moreover, McLellan *et al.* have also reported a similar surface plasmon resonance of sharp and truncated Ag nanocubes ranging from 60-100 nm having a blue shift in SPR bands along with the possibility of *in situ* sharpening of their edges [15]. Interestingly with time, the intensity of both peaks (absorbance) increases to reach a critical value before its further reduction due to coalescence. The increase in the absorbance of the solution associated with both the peaks upto 10 min may be attributed to the fact that initially the number of nucleating sites are presumably more available for reduction facilitating the formation of more nanospheres. However, after 80 min, the absorption spectrum becomes relatively featureless, revealing a broad band peak along with an overall low absorbance over the visible region, which is consistent with the black colour of the aggregates (and with the structure and morphology). Further decrease in intensity with reaction time observed in this case may be due to the change in the rate of reduction of Rh ions and a concomitant increase in the particle size leading finally to the formation of an aggregated structure.

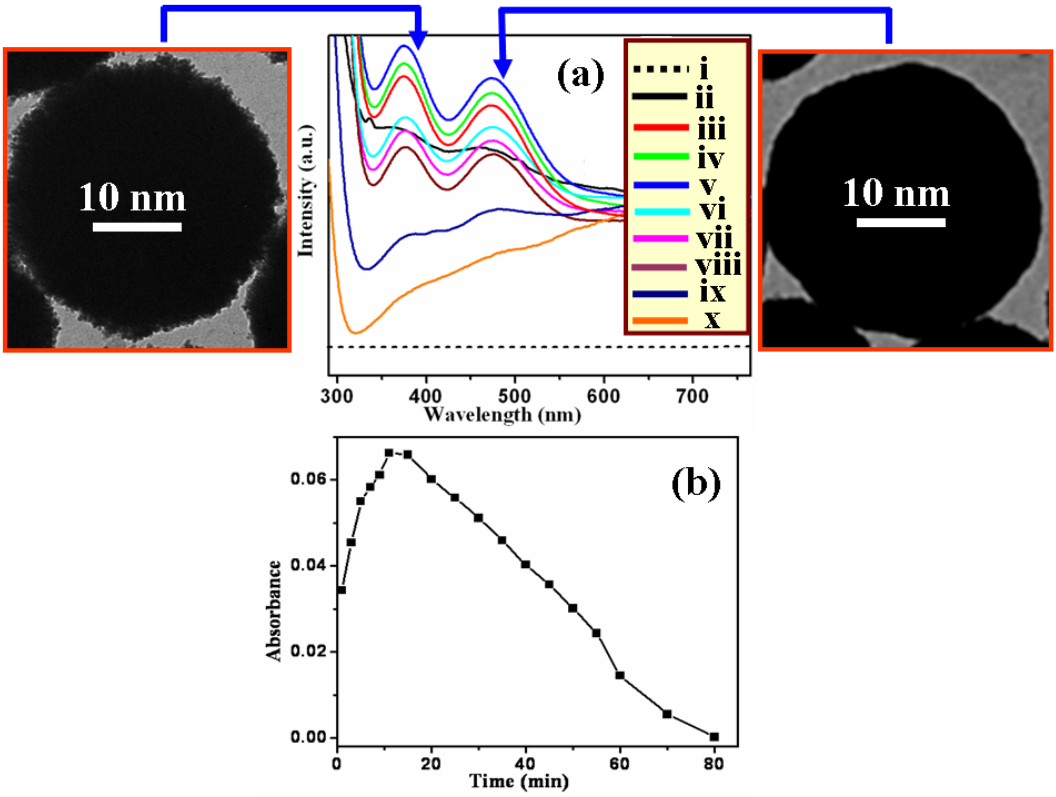

Figure 3.8. (a) Superimposed *in situ* UV-Vis spectra at different stages of the reaction indicating response at 375 nm and 474 nm corresponding to truncated and smooth surfaces respectively [plot numbers i-x stands for scans taken after each 5 min. of time interval] and (b) the variation of the intensity of peak corresponding to 375 nm as a function of time

Additionally, there is an interesting decrease in the rate of reduction of Rh ions with time as more aggregation of these nanoparticles on the heteroactive sites on Al surface occurs. This clearly confirms that the presence of hetero-nuclear sites is necessary for the spontaneous electrochemical displacement. This demonstration of optical tuning indicates that such surface sensitive nanostructures of Rh may find additional use in optical sensing and related SERS applications.

3.4.4. X-ray Diffraction Analysis

In order to investigate the structural evolution with time, XRD studies have been carried out for these Rh samples, which give insights into subtle changes in the organization of these nanostructures. The growth of nanostructures in principle, starts from the lowest

energy sites leading to a progressive displacement to the highest energy sites as a function of time. Accordingly, the entire diffraction profile shown in Figure 3.9 could be indexed to (111), (200), (220) and (311) planes of Rh which confirms the formation of fcc structure [13, 16].

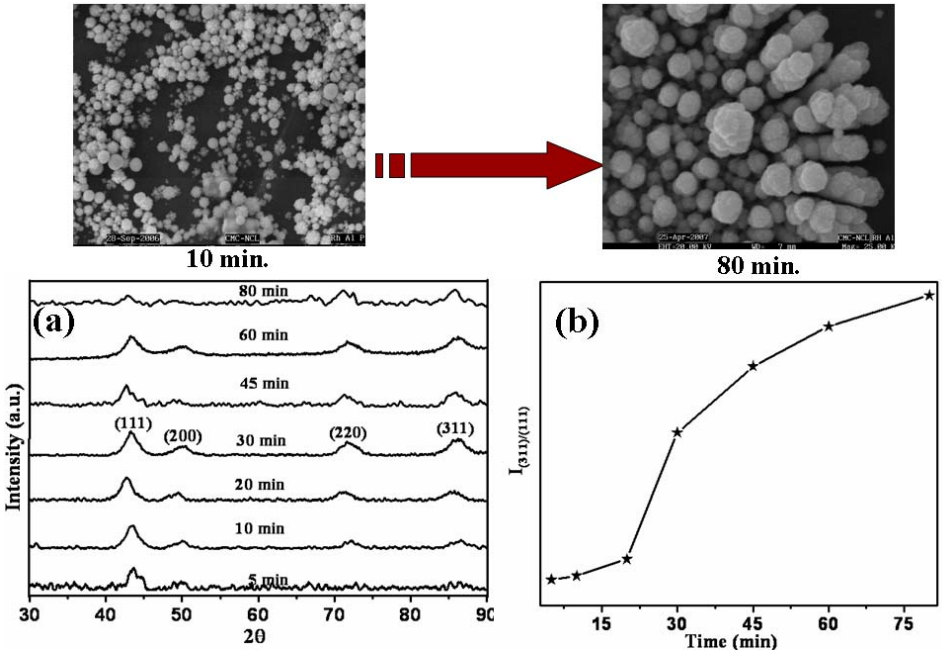

Figure 3.9. (a) Variation of X-ray diffraction pattern for Rh nanospheres having a direct correlation with the morphological evolution, collected at different stages between 5 to 80 min. and (b) variation of the comparative intensity ratios of (311): (111) peaks with time.

The above observation indicates a general model of growth, whereby initially fast reduction of Rh ions favours epitaxial growth into a thermodynamically favorable (111) low energy crystal face, resulting in the minimization of the overall surface energy [17]. Interestingly, the rate of growth, initially in (311) plane is indeed less; although there is an increase with time indicating the competition between thermodynamic and kinetic factors of the galvanic displacement reaction. For example, typically at 5 min, the reaction is dominated by non-equilibrium conditions so that the growth of nanoparticles occurs at the thermodynamically favorable low energy (111) plane. With time, however, these Rh nanospheres become truncated, shifting to a branched surface above 40 min and

finally to nanorods via accelerated additional growth along the (311) (although it is a thermodynamically unstable facet, these nanostructures have been formed due to kinetically driven process) direction. A slight variation in the position and intensity with respect to bulk pattern perhaps arises due to the lattice miss-match during kinetically controlled crystal growth. Crystallite size of these particles is about 2.5 nm calculated by using Scherrer formula, as inferred from the FWHM of the 43.54º peak (corresponding to a d- value of 2.252 Å), which is in excellent agreement (c.a. 2.9 ± 0.4 nm) with the corresponding size from TEM images (Figures. 3.6 and 3.7). Alternatively, growth after longer time (~ 80 min) shown in Figure 3.3. can be explained by a mechanism of oriented attachment, where super-saturation of Rh ions on initially nucleated Rh nanospheres causes steric hindrance between attached aggregates resulting in the formation of a new order, driven by the rate of adsorption at (311) versus (111) face which is kinetically controlled under these nonequilibrium conditions.

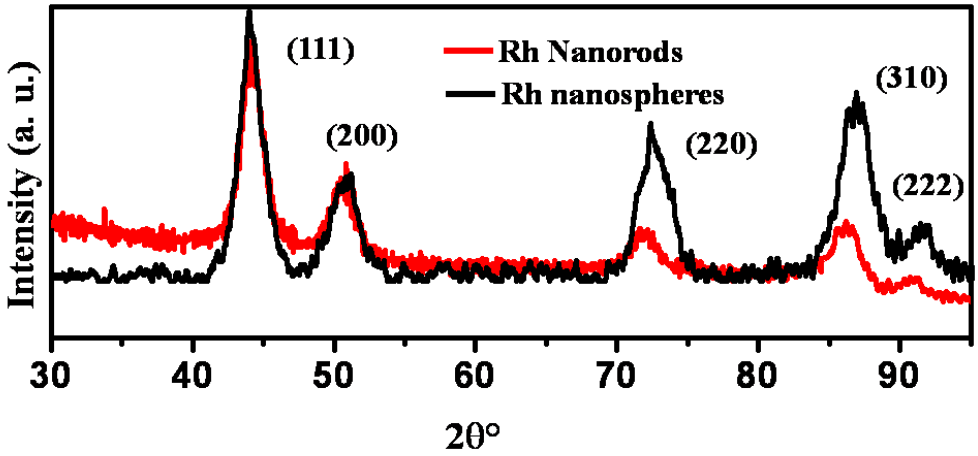

Figure 3.10. Superimposed X-ray diffraction patterns for Rh nanospheres (black) and Rh nanorod bundles (red) synthesized using the galvanic approach at room temperature.

Figure 3.10, depicts the superimposed XRD patterns of Rh nanostructure especially nanospheres (Figure 3.2b) and nanorod bundles (Figure 3.5) with characteristic Rh peaks, indexed to a fcc lattice having (111), (200), (220), (310) and (222) planes. A comparison of the relative intensities of peaks corresponding to Rh-PVP with Rh

nanospheres synthesized by the same approach indicates the existence of a morphology/shape dependent preferential growth in different planes. Moreover, these morphology variations along with specific crystallographic facet could be tailored for both selectivity and reactivity towards catalytic reactions. For example, the enhanced activity of gold nanoflowers is ascribed to the presence of high index crystal faces such as (220) and (331), which exposes surface irregularities, steps and kinks [18]. Similarly, in our case also, Rh nanospheres synthesized by galvanic displacement approach reveal a comparatively higher intensity of crystal faces like (220) and (331) with respect to nanorods using PVP as a capping agent.

3.4.5. Fourier Transform-Infra Red Studies

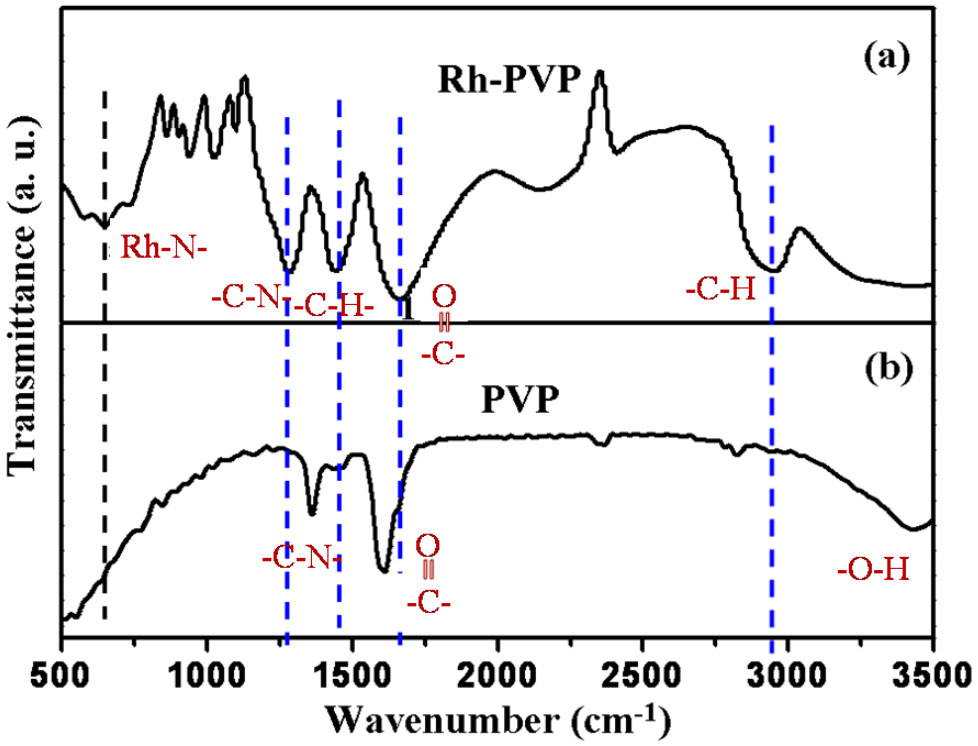

Figure 3.11. Superimposed Fourier transform infra-red spectra of (a) Rh-PVP nanostructures (nanorods) along with that for (b) only PVP to highlight the involvement of PVP in building Rh nanostructures.

In order to understand the role of PVP and their local molecular environment involved in the building of nanorods, FTIR studies have been conducted after making thin pellets with dry KBr. Accordingly, Figure 3.11 reveals the superimposed FTIR spectra of (a) PVP capped Rh nanostructures and (b) of only PVP indicating that the capping molecules do interact with Rh nanostructures. Common peaks at 2805 cm^{-1} and 1450 cm^{-1} give information about the orientation of methylene chains along with the symmetric/asymmetric stretching and bending of the C–H of bound PVP on Rh surface, respectively. Moreover, a strong doublet in the region 1350-1380 cm^{-1} corresponds to the C-N symmetric and asymmetric stretching [19]. Out of these two, only one peak corresponding to C-N stretching has been shifted to lower side, which could be due to the interaction of PVP molecules with Rh. Moreover, the blue shift in the frequency for carbonyl from ~1660 cm^{-1} to 1700 cm^{-1}, merged into the band corresponding to vinyl group in the region of 1620-1660 cm^{-1}, give indirect evidence for the involvement of carbonyl group in the bonding of Rh nanorods [20]. The appearance of an additional band at 550 cm^{-1} in case of Rh-PVP nanostructures is also attributed to the presence of Rh-N interaction [21].

3.4.6. Thermogravimetric Analysis

Superimposed thermo-gravimetric profiles of freshly prepared bare Rh nanostructures (Figure 3.2 b) along with that of PVP capped Rh nanorods (Figure 3.5) is shown in Figure 3.12. Profile (a) for bare nanostructure (Rh nanospheres; without PVP) reveals a low temperature (below 50 °C) decomposition corresponding to volatile impurities, followed by a no weight loss upto 800 °C corresponding to the formation of pure metallic Rh. In comparison, thermal profile for (b) Rh nanorods (Rh/PVP) [Figure 3.12] shows a three step weight loss. In the first step (150-214 °C) a broad region (weight loss upto 0.15 %) is seen attributed to the loss of adsorbed volatile solvent impurities including adsorbed water molecules. In the second step (220-365 °C) a sharp weight loss is seen at 342 °C upto 1.42 %, which could be assigned to the thermal desorption of loosely bound PVP molecules, while in the third step (360-830 °C) could be (4 % wt

loss) due to the decomposition of remaining PVP molecules [22]. All the results including that of EDS and XPS strongly support this observation and ~6 % of PVP is attached to the surface of Rh nanostructures.

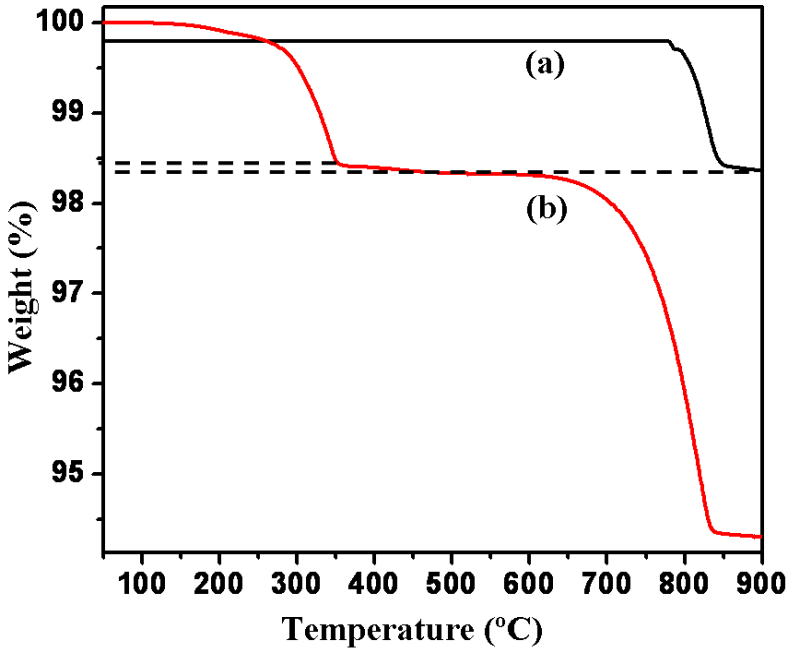

Figure 3.12. Superimposed thermogravimetric profiles of freshly prepared Rh nanostructures, Rh nanospheres and Rh nanorods using Galvanic displacement approach in the (a) absence of PVP (nanospheres) and (b) presence of PVP (nanorods) performed at a heating rate of 10 ºC/min in air.

3.4.7. Cyclic Voltammetry

In order to understand the mechanism of potential-dependent morphological evolution, we have carried out cyclic voltammetric measurements using different combinations of electrodes and electrolytes. Figure 3.13 (a) shows superimposed cyclic voltammograms of Al substrate and/or Pt electrode in the presence/absence of Rh^{3+} ion solution. Accordingly, cyclic voltammogram (I) i.e., a Pt disc as a working electrode in a mixture of 1 mM $RhCl_3$ and 0.5 M Na_2SO_4 solution and (II) Al in blank 0.5 M Na_2SO_4 solution are essentially featureless. In sharp contrast to (I) and (II), voltammogram (III), i.e., Al substrate in a mixture of 1 mM $RhCl_3$ and 0.5 M Na_2SO_4 solution with Al as a working electrode gives a cathodic peak at -1.10 V, indicating that, only in the presence of Al,

charge transfer occurs facilitating Rh(0) formation. During the cathodic scan a peak seen at -1.10 V could be ascribed to the reduction of Rh^{3+} to Rh^0 at the Al surface which can act as nucleating sites for further morphological evolution. This Rh nucleation has been further confirmed by the appearance of new peak during the next anodic sweep. Moreover, during the anodic sweep in the presence of Rh ions another parallel oxidation reaction (Al into Al^{3+}) has occurred and it gives additional electrons for the further reduction of Rh^{3+} ions on Al surface. Thus the anodic peak appeared at ~1.40 V, could be attributed to the combined electron transfer corresponding to Al oxidation followed by Rh reduction (Figure 2.13 a, III). Moreover, these newly generated Al^{3+} ions and Rh^0 at this higher anodic potential is responsible for alloying-dealloying. Significantly, these structural changes at the interface makes different/electron transfer and results in splitting of this sharp oxidation peak into two peaks as shown in Figure 3.13(b). As dealloying occurs, the imbalanced reaction stoichiometry minimizes the total surface energy, enabling the structure to grow in all possible directions into fractal geometry [23].

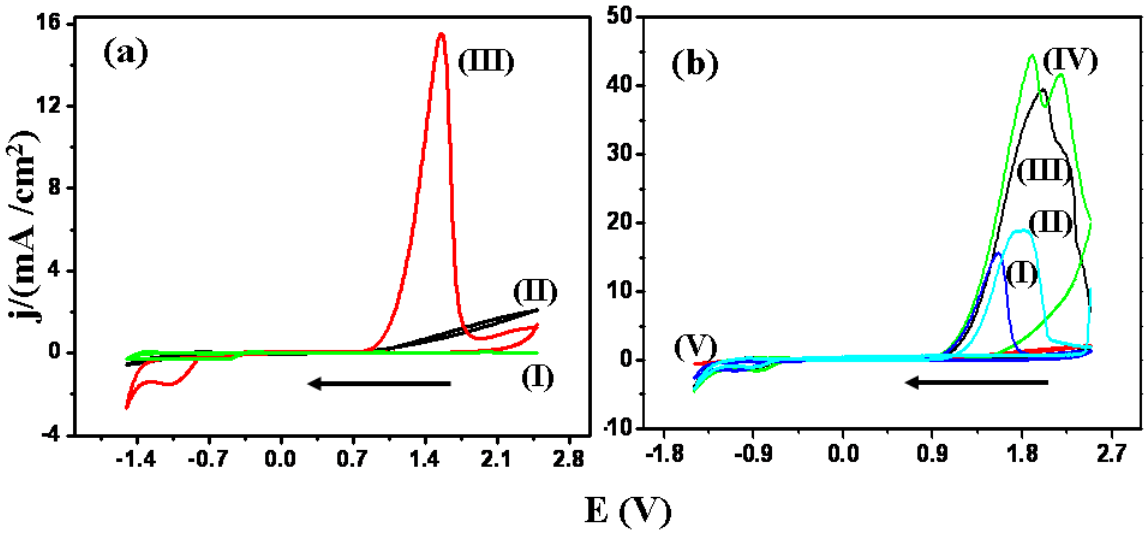

Figure 3.13. (a) Superimposed cyclic voltammograms for (I) Pt electrode in a mixture of 1 mM $RhCl_3$ and 0.5 M Na_2SO_4 solution, (II) Al electrode in 0.5 M Na_2SO_4 solution, (III) Al electrode in a mixture of 1 mM $RhCl_3$ and 0.5 M Na_2SO_4 solution at 50 mV/s; (b) curve (I-IV) correspond to first to fourth cycles and (V) for the blank 0.5 M Na_2SO_4 on Al substrate as a working electrode.

Electrochemical studies on such type of galvanic reactions have been reported in literature to separate out the effect of mass transfer from the substrate and reaction

kinetics for metals like Ni, Zn and Cu, but not on Al [24]. The role of PVP molecules towards the surface modification and stabilization of Rh nanorods has been investigated by cyclic voltammetry using the same amount of PVP in aqueous Rh ion solution. Accordingly, Figure 3.14 shows superimposed cyclic voltammograms for the galvanic displacement of Al by Rh ions on Al electrode from aqueous (a) 1 mM $RhCl_3$ in 0.5 M H_2SO_4 solution and (b) in (1:5) $RhCl_3$: PVP in 0.5 M H_2SO_4 solution at 50 mV/s using Hg-Hg_2SO_4 as the reference and a Pt foil as the counter electrodes respectively.

On the basis of the earlier conclusion and also the schematic representation shown in Figure 3.1, the reduction of Rh^{3+} to Rh^0 has been presented in conjunction with the oxidation of Al to Al^{3+}. The most striking difference between the two cyclic voltammograms is the overpotential difference for Rh deposition on Al surface with and without PVP. As per the earlier reports, the reductive deposition of Rh can occur at potentials negative with respect to the Nernst potential while bulk Rh could oxidize at potentials more positive to this potential [25]. The equilibrium potential for Rh^{3+}/Rh value is 0.04 V (vs SCE) in 1 mM $RhCl_3$ although interestingly on the Al substrate, Rh^{3+} could get deposited under reduced overpotential to the presence of Al_2O_3 barrier associated with Al substrate [26]. Conversely, in the presence of PVP, Rh could be deposited by underpotential deposition. Nucleation of Rh on Al, starts at about -0.23 V (vs SCE), which is also seen to be lower compared to that in the absence of PVP. This observation is also in complete agreement with other systems reported by Li and coworkers, where, the underpotential deposition/reduction of Cu ions has been seen with sufficiently large thiol coverage similar to PVP on the electrode surface [27].

Figure 3.14 shows one of the revealing features as a prominent shift in the anodic peak (~ 900 mV) for Al dissolution. The most important reason for this large shift towards negative potential in the presence of PVP is due to the electrostatic interaction between Rh and the polymeric PVP molecules facilitating reduction at the interface between Rh and Al. Moreover, the lower current density in the presence of PVP could be explained due to a resistance for the Rh^{3+} ions to penetrate the PVP layer through pinholes ("penetration mechanism") on the Al surface [28]. However, during the diffusion of Rh

ions towards Al substrate, some of these Rh ions might carry PVP molecules, along with them to cause a channel like flow resulting into one dimensional growth as shown in Figure 3.5.

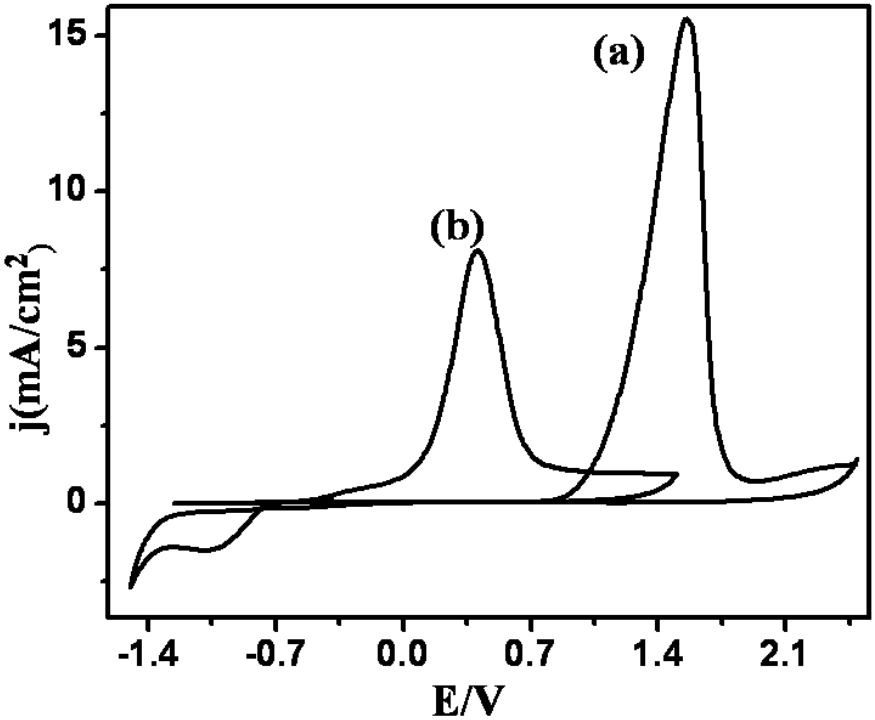

Figure 3.14. Superimposed cyclic voltammograms of Al substrate as an electrode immersed in (a) aqueous 1 mM $RhCl_3$ in 0.5 M H_2SO_4 solution and (b) (1:5) $RhCl_3$: PVP in 0.5 M H_2SO_4 solution at 50 mV/s using Pt foil as a counter and Hg-Hg_2SO_4 as reference electrodes respectively.

According to this model, a small microscopic deviation in the surface structure of Al can have a large effect on the morphological change. Hence, adhesion between Rh nanoparticles and Al substrate has strong effect towards the effective patterning of 3D nanostructures of Rh. In case of Rh-PVP system the adhesion during nucleation is however poor, which is also independent of the amount of Rh and the surface roughness of Al. This could be due to the independent polymer wrapping on the surface of Rh nanorods making them free from all Al substrate interactions. The same effect has been observed when Al substrate is kept vertically in the solution so that the nanorods tend to move downward under gravity.

3.4.8. Microgalvanic Cells

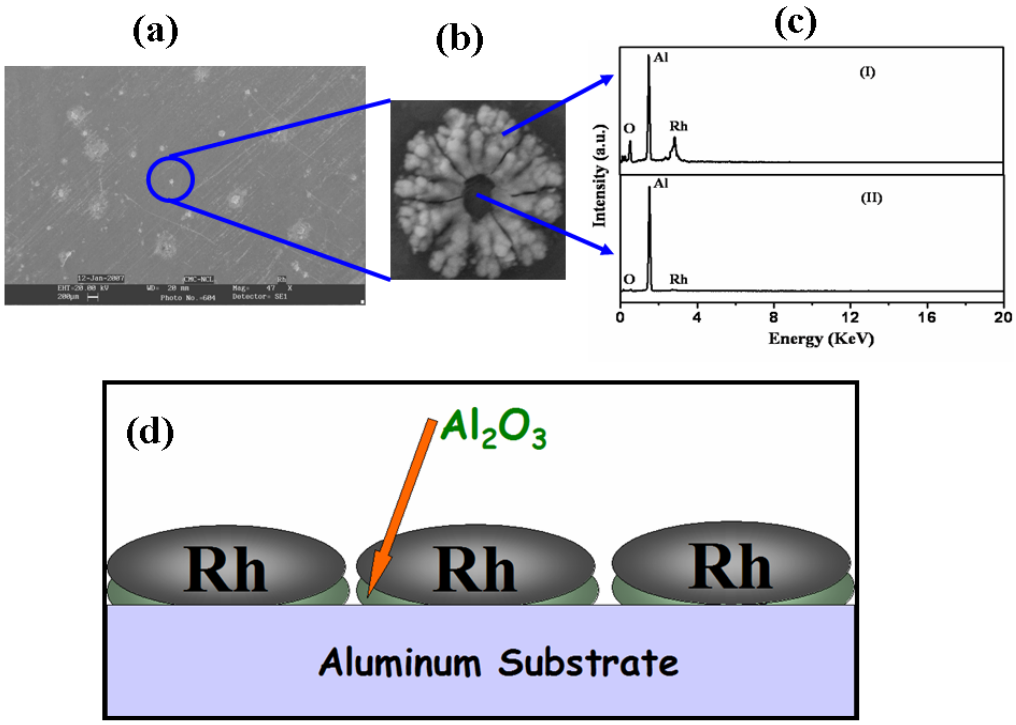

Figure 3.15. A schematic representation of microgalvanic cell formation on Al substrate; (a) low (b) high magnification SEM images of Al substrate after the removal of Rh nanostructures by ultrasonication; (c) spot energy-dispersive spectral (EDS) analysis of region (I) on alumina formed on the border and (II) pure Al cavity which is ready for further displacement; (d) nucleation and growth of Rh nanostructures on Al substrate and the evolution of microgalvanic cells.

Figure 3.15(a) shows a typical low magnification SEM image of Al substrate after sonication for 30 min. to remove the nanostructures, which clearly indicates the formation of a large number (aerial density ~100/cm^2) of micro galvanic cells on their surface. High magnification SEM image of a region after removal of Rh nanostructures as shown in Figure 3.15(b) highlight spherical (thicker) region (about 1.5 µm with central metallic cavity of ca. 1 µm) available for further galvanic reaction. Elemental analysis carried out both inside and outside the domain as shown in Figure 3.15 (c) confirms the local chemical composition. For example, region (I) shows that the peripheral surface is made up of Al hydroxide, while the superficial surface of the galvanic cell has an Al:O

ratio as 30.8: 30 indicating alumina (Al_2O_3) formation at the edge of the hole which further supports the model of simultaneous reduction and oxidation on the metal surface. Furthermore, the additional peak at 3.8 keV in spectra (I) corresponds to Rh which may be trapped by *in situ* grown oxide/hydroxide during the course of the reaction. The central region (II), on the other hand, shows pure Al which is responsible for further reduction of Rh ions from the solution. A schematic representation of nucleation followed by growth on Al through the control over 3D due to alumina formation shown in Figure 3.15(d) demonstrates further growth through the evolution of a large number of microgalvanic cells.

3.4.9. Electrocatalytic Activity towards Formaldehyde Oxidation

Electrochemical oxidation of organic molecules, including methanol, formaldehyde and formic acid, on Pt and Pt alloy electrodes has received great interest due to their importance as anode reactions in fuel cells [29]. Although formaldehyde is toxic and not very suitable for commercial fuel cells, its oxidation is important for a complete understanding of the methanol oxidation mechanism because formaldehyde is produced by the partial oxidation of methanol and also because these are linked with CO poisoning on the electrode surface [30]. Despite the high cost, Rh has been extensively investigated as an electrocatalyst for fuel cells and nanostructured Rh in particular has shown several unique features.

All the structures are electrocatalytically active for formaldehyde oxidation as the rates at the bare GC electrode and on bulk Rh are much lower than that of the Rh nanostructures. The peak current densities are 0.52, 0.41 and 0.25 mA/cm^2 for the reaction on Rh nanospheres, Rh nanorods and bulk Rh as electrocatalysts, respectively (Figure 3.16 a). More specifically, the electrocatalytic activity of the Rh nanospheres is nearly 2 times higher than that of nanorods synthesised by the same galvanic route and both these are significantly higher compared to that of bulk Rh. The improved activity of the Rh nanospheres might be due to their high surface area and preferential crystal facets in high indexing plane, which is in good agreement with results from XRD analysis as

shown in figure 3.10. For example, as reported previously by Rhee and co-workers for Rh, low symmetric plane Rh (100) shows higher electrocatalytic activity than high symmetric Rh (111) for a model electrochemical reaction of perchlorate reduction [31].

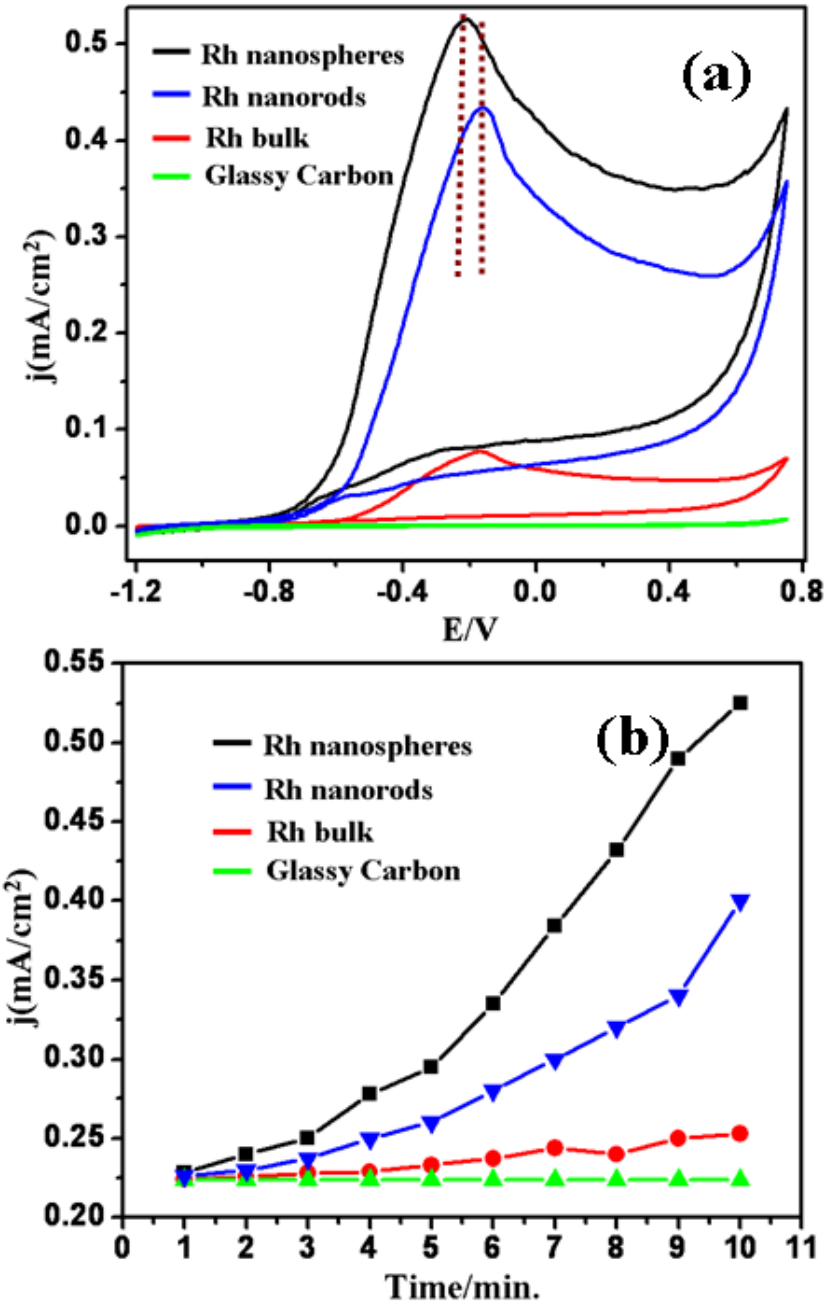

Figure 3.16. (a) Superimposed cyclic voltammograms of formaldehyde oxidation in a mixture of 0.5 M NaOH and 0.5 M HCHO solution (first cycle) on Rh nanospheres, nanorods and bulk Rh coated on a glassy carbon working electrode at 50 mV/s (b) Respective electrocatalytic activity in

terms of variation in current density with time/cycle number [from first 10 cycles] under similar conditions at a peak potential of -0.20 V corresponding of HCOOH oxidation.

Furthermore, these Rh nanostructures have an anisotropic morphology with their growth in asymmetric plane that can improve the mass transport for electrocatalytic reactions leading to more effective catalyst utilization [32].

The present approach for the formation of different morphologies of Rh nanostructures has many intrinsic benefits because of the possibility of tuning the potential changes using molecules like PVP, offering excellent flexibility. In addition, the present approach also helps to generate anisotropic structures by the assistance of controlling the redox properties of the solution and substrate by using other passivating molecules. The higher cost and limited availability of Rh, however, pose several limitations for a complete exploitation in fuel cell technology and hence recent efforts are concentrated on the replacement of Rh and Pt with non-noble metals, nitrogen doped CNTs for retaining similar activity.

3.5. Conclusions

This chapter demonstrates various experimental details of the fabrication and growth mechanism of Rh nanostructures through the evolution of microgalvanic cells, in order to illustrate the critical importance of controlling some of the major factors affecting their surface reactivity. The experimental methodology for controlling Rh morphologies has been described with Al as a sacrificial substrate along with variation in the procedure for the fabrication of hierarchically designed Rh structures. Kinetic studies using *in situ* UV-visible spectroscopy suggest that these nanospheres are surprisingly uniform, possessing spontaneous order over several length scales along with interesting morphology dependent performance. The approach developed in this chapter could serve as an efficient and reliable route for the synthesis of high aspect ratio Rh nanostructures such as nanorods, nanowires and also of other shapes. Although this facile methodology provides an elegant control over surface morphology, this requires a careful modulation of growth parameters such as metal ion concentration, pH, ionic strength, temperature and exposure

time. Future studies are required to focus more on incorporating this method into micro- and nano-lithographic channels to enable site selective catalytic properties. This would ensure more interesting utilization of these nanostructures as important building blocks in complex applications like nanoscale electrical contacts for interfacing a range of different organic and biomolecules, single electron transfer studies, photo-electrochemical and catalytic applications of Rh surfaces. These findings are expected to offer potential benefits in various areas including the designing of electrodes for microfuel cells and chemical sensors.

3.7. References

1. (a) Dong, A.; Chen, J.; Vora, P. M.; Kikkawa, J. M.; Murray, C. B. *Nature* **2010**, *466,* **474**. (b) Parkin, S. P.; Hayashi, M.; Thomas, L. *Science* **2008,** *11,* **320.** (c) Huang, Y.; Duan, X.; Wei, Q.; Lieber, C. M. *Science* **2001,** *1,* **630**. (d) Andersen, E. S.; Dong, M.; Nielsen, M. M.; Jahn, K.; Subramani, R.; Mamdouh, W.; Golas, M. M.; Sander, B.; Stark, H.; Oliveira, L. P. *Nature* **2009,** *459,* **73**. (e) Forgan, R. S.; Friedman, D. C.; Stern, C. L.; Bruns, C. J.; Stoddart, J. F. *Chem. Commun.* **2010,** *46,* **5861**. (f) Taylor-Pashow, K.; Rocca, J. D.; Huxford, R. C.; Lin, W.; *Chem. Commun.* **2010,** *46,* **5832**. (g) Wang, Y.; Neyman, A.; Arkhangelsky, E.; Gitis, V.; Meshi, L.; Weinstock, I. A. *J. Am. Chem. Soc.* **2009,** *131*, **17412**. (h) Kim, J.; Lee, J. *Nano Lett.* **2009,** *9,* **4564**. (i) Daniel, M.; Tsvetkova, I. B.; Quinkert, Z. T.; Murali, A.; De, M.; Rotello, V. M.; Kao, C. C.; Dragnea, B. *ACS Nano* **2010,** *4*, **3853**.
2. (a) Brataas, A. *Nature* **2008,** *452,* **419**. (b) Ray, P. C. *Chem. Rev.* **2010** *110,* **5332**. (b) Ghosh, S.; Pal, T. *Chem. Rev.* **2007,** *107,* **4797**. (c) Roucoux, A.; Schulz, J.; Patin, H. *Chem. Rev.* **2002**, *102,* **3757**. (d) Lin, Y.; Wang, J.; Liu, G.; Wu, H.; Wai, C. M.; Lin, Y. *Biosensors & Bioelectronics* **2008,** *23,* **1659.** (e) Mallik, K.; Mandal, M.; Pradhan, N.; Pal, T. *Nano Lett.* **2001,** *1,* **319.** (f) Armand, M.; Tarascon, J. M. *Nature* **2008,** *451*, **652**. (g) Robert, F. *Service Science* **2008,** *321,* **1036**. (h) Ley, T. J.; Hamilton, B. H. *Science* **2008,** *322*, **1472.**
3. (a) Ahmadi, T. S.; Wang, Z. L.; Green, T. C.; Henglein, A.; El-Sayed, M. A. *Science* **1996**, *272*, **1924.** (b) Srivastava, S.; Kotov, N. A. *Acc. Chem. Res.* **2008,** *41*, **1831**. (c) Zhao, W.; Chiuman, W.; Lam, J.; McManus, S. A.; Chen, W.; Cui, Y.; Pelton, R.; Brook, M. A.; Li, Y.; *J. Am. Chem. Soc.* **2008,** *130*, **3610**. (d) Chandrasekharan, N.; Kamat, P. V. *Nano Lett.* **2001,** *1*, **67**. (e) Kamat, P. V.; Huehn, R.; Nicolaescu, R. *Nanotechnology and the Environment Chapter 20* **2004,** *890,* **163.** [ACS Symposium Series]. (f) Saha, A.; Basiruddin, S. K.;

Sarkar, R.; Pradhan, N.; Jana, N. R. *J. Phys. Chem. C* **2009,** *113*, **18492**.

4. (a) Schmid, G. *Nanoparticles: From Theory to Application; Wiley-VCH:* **2004.** (b) Cao, G. *Nanostructures and Nanomaterials: Synthesis, Properties and Applications; Imperial College London*, **2004**. (c) Peng, S.; Wang, C.; Xie, J.; Sun, S. *J. Am. Chem. Soc.* **2006,** *128,* **10676**. (d) Fendler, J. H.; Meldrum, F. C. *Adv Mater.* **2004,** *7*, **607**. (e) Ana, K.; Hyeon, T. *Nanotoday* **2009,** *4,* **359.** Subramanian, R.; Denney, P. E.; Singh, J.; Otooni, M. *J. Mater. Sci.* **2008,** *33,* **1998**. (f) Daniel, M. C.; Astruc, D. *Chem. Rev.* **2004,** *104*, **293**. (g) Cui, Y.; Lieber, C. M. *Science* **2001**, *291*, **5505**.
5. (a) Pradhan, D.; Leung, K. T. *Langmuir* **2008**, *17*, **9707**. (b) Zeng, H.; Xu, X.; Bando, Y.; Gautam, U. K.; Zhai, T.; Fang, X.; Liu, B.; Golberg, D. *Adv. Funct. Mater.* **2009**, *19*, **3165**. (c) Pradhan, D.; Sindhwani, S.; Leung, K. T. *Nanoscale Res Lett*. **2010, 11671**. (d) Pradhan, D.; Sindhwani, S.; Leung, K. T. *J. Phys. Chem. C* **2009**, *113,* **15788**. (e) Pradhan, D.; Leung, K. T. *J. Mater. Chem.* **2009**, *19*, **4902**. (f) Qian, L.; Yang, X. *Talanta* **2008,** *74,* **1649**. (g) Xiao, R.; Cho, S.; Liu, R.; Lee, S. B. *J. Am. Chem. Soc.* **2007**, *129*, **4483**. (h) Hsu, K. H.; Schultz, P. L.; Ferreira, P. M.; Fang, N. X. *Nano Lett.* **2007**, *7*, **446**. (i) Yang, B.; Wu, Y.; Zong, B.; Shen, Z. *Nano Lett.* **2002,** *2*, **751**. (j) Hamedi, M.; Herland, A.; Karlsson, R. H.; Inganäs, O. *Nano Lett.* **2008,** *8*, **1736**.
6. (a) Subhramannia, M.; Balan, B. K.; Sathe, B. R.; Mulla, I. S.; Pillai, V. K. *J. Phys. Chem. C* **2007**, *111*, **16593.** (b) Subhramannia, M.; Ramaiyan, K.; Pillai, V. K. *Langmuir* **2008**, *24*, **3576.** (c) Subhramannia, M.; Kannan, R.; Aslam, M.; Pillai, V. K. *J. Electroanal. Chem.* **2009,** *627*, **58**. (d) Subhramannia, M.; Kannan, R.; Komath, I.; Aslam, M.; Pillai, V. K. *Chem. Mater.* **2008,** *20,* **601.** (e) Subhramannia, M.; Pillai, V. K. *J. Mater. Chem.* **2008,** *18,* **5858**.
7. (a) Singh, A. V.; Bandgar, B. M.; Kasture, M.; Prasad B. L. V.; Sastry, M. *J. Mater. Chem.* **2005**, *15*, **5115.** (b) Peng, Z.; You, H.; Wu, J.; Yang, H. *Nano Lett.* **2010**, *10*, **1492**. (c) Shpaisman, N.; Givan, U.; Patolsky, F. *ACS Nano*, **2010**, *4*, **1901**. (d) Joshi, R. K.; Yoshimura, M.; Chiu, C. C.; Tung, F. K.; Tanaka, K. U.

J. Phys. Chem. C **2008**, *112*, **1857**. (e) Huang, H.; Ma, H.; Zhang, X.; Yong, F.; Feng, X.; Pan, W.; Wang, X.; Wang, Y.; Chen, S. *J. Phys. Chem. B* **2005**, *109*, **19823.** (f) Yu, Y.; Shi, Y.; Chen, C. H.; Wang, C. *J. Phys. Chem. C* **2008**, *112*, **4176.**

8. (a) Skrabalak, S. E.; Chen, J.; Sun, Y.; Lu, X.; Au, L.; Cobley, C. M.; Xia, Y. *Acc. Chem. Res*. **2008**, *41*, **1587.** (b) Zeng, J.; Zhang, Q.; Chen J.; Xia Y. *Nano Lett.* **2010**, *10*, **30.** (c) Mulvihill, M. J.; Ling, X. Y.; Henzie, J.; Yang P. *J. Am. Chem. Soc*. **2010**, *132*, **268**. (d) Xiao, Z. L.; Han, C. Y.; Kwok, W. K.; Wang, H. H.; Welp, U.; Wang, J.; Crabtree, G. W. *J. Am. Chem. Soc*. **2004**, *126*, **2316.** (e) Murray, B. J.; Li, Q.; Newbweg, J. T.; Menke, E. J.; Hemminger, J. C.; Penner, R. M. *Nano Lett*. **2005**, *5*, **2319**. (f) Choi, K. S.; McFarland, E. W.; Stucky, G. D. *Adv. Mater*. **2003**, *15*, **2018.**
9. (a) Fontana, M. G.; Greene, N. D. *Corrosion Engineering*, Mc Groaw-Hill. Inc. **1978**. (b) Sayed, S. Y.; Wang, F.; Malac, M.; Meldrum, A.; Egerton, R. F.; Buriak, J. M. *ACS Nano* **2009**, *3*, **2809.** (c) Brevnov, D. A.; Olson, T. S.; Lopez, G. P.; Atanassov, P. *J. Phys. Chem. B* **2004**, *108*, **17531.** (d) Gao, D.; He, R.; Carraro, C.; Howe, R. T.; Yang, P.; Maboudian, R. *J. Am. Chem. Soc*. **2005**, *127*, **4574.** (e) Cahen, D.; Chernyak, L. *Adv. Mater*. **1997**, *9*, **861.** (f) Lin, Z. H.; Lin, M. H.; Chang, H. T. *Chem. A Eur. J.* **2009**, *15*, **4656.** (g) Aherne, M. D.; Gara, M.; Kelly, J. M.; Gunko, Y. K. *Adv. Funct. Mater*. **2010**, *20*, **1329.** (h) Bansal, V.; Jani, H.; Du Plessis, J.; Coloe, P. J.; Bhargava, S. K. *Adv. Mater*. **2008**, *20*, **717.**
10 (a) Baumgartner, M.; Kaesche, H. *Mater. Corr.* **1991**, *42*, **158**. (b) Liu, Y.; Laurino, A.; Hashimoto, T.; Zhou, X.; Skeldon, P.; Thompson, G. E.; Scamans, G. M.; Blanc, C.; Rainforth, W. M.; Frolish, M. F. *Surf. Interface Anal.* **2009**, *42*, **185**.
11 (a) Liu, K.; Chien, C. L.; Searson P. C.; Yu-Zhang, K. *Appl. Phys. Lett*. **1998**, *10*, **1426**. (b) Juodkazyte, J.; Juodkazis, K. *Electroanalysis* **2004**, **1622**. (c) Finocchio, E.; Busca, G.; Forzatti, P.; Groppi, G.; Beretta, A. *Langmuir*, **2007**,

23, **10419**. (d) Grass, M. E.; Joo, S. H.; Zhang, Y.; Somorjai G. A. *J. Phys. Chem. C* **2009**, *113*, **8616**.

12 (a) Weissermel, K.; Arpe, H. J. *Industrial Organic Chemistry*, VCH, New York, **1993**. (b) Schulz, J.; Roucoux, A.; Patin, H. *Chem. Commun*. **1999**, **535**. (c) Motoyama, Y.; Takasaki, M.; Yoon, S. H.; Mochida, I.; Nagashima, H. *Org. Lett*. **2009**, 11, **5042**. (d) Ziegelbauer, J. M.; Gatewood, D.; Gull, A. F.; Guinel, M. J. F.; Ernst, F.; Ramaker, D. E.; Mukerjee, S. *J. Phys. Chem. C* **2009**, *113*, **6955**.

13 (a) Kakade. B. A.; Sahoo, S.; Halligudi, S. B.; Pillai, V. K. *J. Phys. Chem. C*. **2008**, *112*, **13317.** (b) Kakade B. A.; Shintri S. S.; Sathe B. R.; Halligudi S. B.; Pillai, V. K. *Adv. Mater*. **2008**, *19*, **272**. (c) Yuan, Q.; Zhou, Z.; Zhuang, J.; Wang, X. *Inorg. Chem.* **2010**, *49*, **5515**. (d) Wang, Y.; Ren, J.; Deng, K.; Gui, L.; Tang, Yo. *Chem. Mater*. **2000**, *12*, **1622**. (e) Zhang, Y.; Grass, M. E.; Habas, S. E.; Tao, F.; Zhang, T.; Yang, P.; Somorjai, G. A. *J. Phys. Chem. C* **2007**, *111*, **12243**.

14 Hoefelmeyer, J. D.; Niesz, K.; Somorjai, G. A.; Tilley, T. D. *Nano Lett*. **2005**, *5*, **435**.

15 McLellan, M.; Siekkinen, A. Chen, J.; Xia, Y. *Chem. Phys. Lett*. **2006**, *427*,**122**.

16 (a) Humphrey, S. M.; Grass, M. E.; Habas, S. E.; Niesz, K.; Somorjai, G. A.; Tilley, T. D. *Nano Lett.* **2007**, *7*, **785**. (b) Kundu, S.; Wang, K.; Liang, H. *J. Phy. Chem. C*, **2009**, *113*, **18570**. (c) Ewers, T. D.; Sra, A. K.; Norris, B. C.; Cable, R. E.; Cheng, C. H.; Shantz, D. F.; Schaak, R. E. *Chem. Mater*. **2005**, *17*, **514**. (d) Yuan, Q.; Zhou, Z.; Zhuang, J.; Wang, X. *Inorg. Chem*. **2010**, *49*, **5515**. (e) Wang, Y.; Ren, J.; Deng, K.; Gui, L.; Tang, Y. *Chem. Mater*. **2000**, *12*, **1622**. (f) Yingpu, G. L. *Chem. Commun*. **2008**, **6402**.

17 (a) Rycenga, M.; Hou, K. K.; Cobley, C. M.; Schwartz, A. G.; Camargo, P. H. C.; Xia, Y. *Phys. Chem. Chem. Phys.* **2009**, *11*, **5903**. (b) Zeng, J.; Zhang, Q.; Chen, J.; Xia, Y. *Nano Lett.* **2010**, *10*, **30**.

18 (a) Shekhawat, G. S.; Dravid, V. P. *Science* **2005,** *310*, **89.** (b) Tsuji, M.;

Matsuo, R.; Jiang, P.; Miyamae, N.; Ueyama, D.; Nishio, M.; Hikino, S.; Kumagae, H.; Kamarudin, S. N.; Tang X. L. *Crys Growth Des* **2008**, *8*, **2528.** (c) Sarkar, A.; Mukherjee, T.; Kapoor, S. *J. Phys. Chem. C* **2008**, *112*, **3334**.

19 (a) Harwood, L. M.; Moody, C. J. *Experimental Organic Chemistry: Principles and Practice*. Wiley-Blackwell, **1989** ISBN 0632020172. (b) White, R.; Lau, W. S. *Chromatography/Fourier Transform Infrared Spectroscopy and its Applications,* **1999**. (c) Hamm, P.; Lim, M. H.; Hochstrasser, R. M. *Infrared characterization for Microelectronics* ISBN: 9810223528. **1998**. (d) Mukamel, S. *A. Rev. Phys. and Chem.* **1999**, *51*, **691.** (e) *Infrared Spectroscopy for Organic Chemists Web Resources:* http://www.dq.fct.unl.pt/qoa/jas/ir.html

20 (a) Sionkowska, A. *Eur. Poly. J.* **2003**, *39*, **2135**. (b) Demirci, S.; Alaslan, A.; Caykara, T. *Appl. Surf. Sci.* **2009**, *255*, **5979**. (c) Lu, X.; Zhao, Y.; Wang, C.; Wei, Y. *Macromol. Rapid Commun*. **2005**, *26*, **1325**. (d) Kong, Q.; Chen, X.; Yao, J.; Xue, D. *Nanotechnology* **2005**, 16, **164**.

21 (a) Shido, T.; Okazaki, T.; Ichikawa, M. *Cat. Lett.* **1993**, *20*, **37**. (b) Pinchas, S.; Laulicht, I. *Infrared Spectra of Labeled Compounds*, Academic Press: London, **1971**; Chapter 9. *NIST Vibrational Spectroscopy Database:* http://srdata.nist.gov/vb.

22 (a) Yao, K. X.; Zeng, H. C. *J. Phys. Chem. C* **2007**, *111*, **13301.** (b) Lee, H.; Choi1, S. H.; Jo, S. M.; Kim, D. Y.; Kwak, S.; Cha, M. W.; Kim, I. D.; Jang, S. Y. *J. Phys. D: Appl. Phys*. **2009**, *42*, **125409.** (c) Kim, J. M.; Joh, H. I.; Jo, S. M.; Ahn, D. J.; Ha, H. Y.; Hong, S. A.; Kim, S. K. *Electro. Acta* **2010**, *55*, **4827.**

23 Skrabalak, S. E.; Chen, J.; Sun, Y.; Lu, X.; Au, L.; Cobley, C. M.; Xia, Y. *Acc. Chem. Res.* **2008,** *41*,**1587.**

24 (a) Krichevski, O.; Markovich, G. *Langmuir*, **2007**, *23*, **1496**. (b) Song, H. M.; Wei, Q.; Ong, Q. K.; Wei, A. *ACS Nano* **2010**, *4*, **5163**. (c) Sau, T. K.; Rogach, A. L. *Adv. Mater*. **2010**, *22*, **1781**. (d) Liu, Q.; Lai, L.; Huang, H.; Sun, J.; Shang, T.; Zhou, Q.; Xu, Z. *Chinese J. Chem.* **2010**, *28*, **537**. (e) He, J. L.; Wu, Z. S.; Hu, P.; Wang, S. P.; Shen, G. L.; Yu, R. Q. *The Analyst* **2010**, *135*, **570.** (f) Liao,

H. G.; Jiang, Y. X.; Zhou, Z. Y.; Chen, S. P.; Sun, S. G. *Angew. Chem*. **2008**, *120*, **9240**. (g) Liao, H. G.; Jiang, Y. X.; Zhou, Z. Y.; Chen, S. P.; Sun, S. G. *Angew. Chem. Int. Ed*. **2008**, *47*, **9100**. (h) Pazos-Prez, N.; Baranov, D.; Irsen, S.; Hilgendorff, M.; Liz-Marzn, L. M.; Giersig, M. *Langmuir* **2008**, *24*, **9855.** (i) Yu, K.; Kelly, K. L.; Sakai, N.; Tatsuma, T. *Langmuir* **2008**, *24*, **5849**. (j) Qin, Y.; Song, Y.; Sun, N.; Zhao, N.; Li, M.; Qi, L. *Chem. Mater*. **2008**, *20*, **3965.** (k) Sun, Y.; Yan, H.; Wiederrecht, G. P. *J. Phys. Chem. C* **2008**, *112*, **8928.** (l) Hansen, C. R.; Westerlund, F.; Moth-Poulsen, K.; Ravindranath, R.; Valiyaveettil, S.; Bjornholm, T. *Langmuir* **2008**, *24*, **3905**. (m) Zhao, N.; Wei, Y.; Sun, N.; Chen, Q.; Bai, J.; Zhou, L.; Qin, Y.; Li, M.; Qi, L. *Langmuir* **2008**, 24, **991**. (n) Kumar, P. S.; Pastoriza-Santos, I.; Rodriguez-Gonzalez, B.; De Abajo, F. J. G.; Liz-Marzan, L. M. *Nanotechnology* **2008**, *19*, **015606**. (o) Nehl, C. L.; Hafner, J. H. *J. Mater. Chem*. **2008**, *18*, **2415**. (p) Sun, Y.; Wiederrecht, G. P. *Small* **2007**, *3*, **1964**. (q) Sun, Y. *Chem. Mater.* **2007**, *19*, **5845**.

25 (a) Quinn, B. M.; Dekker, C.; Lemay, S. G. *J. Am. Chem. Soc*. **2005**, *127*, **6146**. (b) Yarden, T. S.; Joselevich, E. *Nano Lett.* **2010**, *10*, **4742**. (c) Doane, T. L.; Cheng, Y.; Babar, A.; Hill, R. J.; Burda, C. *J. Am. Chem. Soc.* **2010,** *132*, **15624**. (d) Wang, L.; Bo, X.; Bai, J.; Zhu, L.; Guo, L. *Electroanalysis* **2010**, *22*, **2536**. (e) Liang, Y.; Schwab, M. G.; Zhi, L.; Mugnaioli, E.; Kolb, U.; Feng, X.; Mllen, K. *J. Am. Chem. Soc.* **2010**, *132*, **15030.** (f) Zhang, G.; Sun, S.; Li, R.; Sun, X. *Chem. A Eur. J.* **2010**, *16*, **10630.** (g) Dudin, P. V.; Unwin, P. R.; Macpherson, J. V. *J. Phys. Chem. C* **2010**, *114*, **13241.** (h) Ghosh, S.; Retna Raj, C. *J. Phys. Chem. C* **2010,** *114*, **10843**. (i) Peng, X.; Sfeir, M. Y.; Zhang, F.; Misewich, J. A.; Wong, S. S. *J. Phys. Chem. C* **2010**, *114*, **8766.** (j) Yang, L.; Luo, S.; Su, F.; Xiao, Y.; Chen, Y.; Cai, Q. *J. Phys. Chem. C* **2010**, *114*, **7694.** (k) Ritz, B.; Heller, H.; Myalitsin, A.; Kornowski, A.; Martin-Martinez, F. J.; Melchor, S.; Dobado, J. A.; Jurez, B. H.; Weller, H.; Klinke, C. *ACS Nano* **2010**, *4*, **2438.** (l) Guo, S.; Dong, S.; Wang, E. *Adv. Mater.* **2010**, *22*, **1269**. (m) Yang, W.; Ratinac, K. R.; Ringer, S. P.; Thordarson, P.; Gooding, J. J.; Braet, F. *Angew. Chem. Int.*

Ed. **2010**, *49*, **2114**. (n) Yang, W.; Ratinac, K. R.; Ringer, S. P.; Thordarson, P.; Gooding, J. J.; Braet, F. *Angew. Chem.* **2010**, *122*, **2160.** (o) Eder, D. *Chem. Rev.* **2010**, *110*, **1348.** (p) Kauffman, D. R.; Sorescu, D. C.; Schofield, D. P.; Allen, B. L.; Jordan, K. D.; Star, A. *Nano Lett.* **2010**, *10*, **958**. (q) Yu, P.; Qian, Q.; Lin, Y.; Mao, L. *J. Phys. Chem. C* **2010**, *114*, **3575**. (r) Fu, N.; Li, Z.; Myalitsin, A.; Scolari, M.; Weitz, R. T.; Burghard, M.; Mews, A. *Small* **2010**, *6*, **376**. (s) Lim, H.; Song, H. J.; Lee, Y.; Shin H. J.; Choi, H. C. *Langmuir* **2010**, *26*, **1464**. (t) Zhai, X.; Gao, Z. *Anal. Sci.* **2010**, *26*, **343.** (u) Zhuo, Y.; Yuan, R.; Chai, Y. Q.; Hong, C. L. *The Analyst* **2010**, *135*, **2036**. (v) Yu, P.; Qian, Q.; Wang, X.; Cheng, H.; Ohsaka, T.; Mao, L. *J. Mater. Chem*. **2010**, *20*, **5820**.

26 (a) Penner, R. M. *J. Phys. Chem B* **2002,** *106,* **3339**. (b) Bayati, M.; Abad, J. M.; Nichols, R. J.; Schiffrin, D. J. *J. Phys. Chem. C* **2010**, *114*, **18439**. (c) Soreta, T. R. Soreta, Strutwolf, J.; Henry, O.; Sullivan, C. K. *Langmuir* **2010**, *26*, **12293**. (d) Wang, Q.; Zheng, J. *Microchimica Acta* **2010**, *169*, 361. (e) Weng, H.; Wu, C.; Chen, C.; Ho, C.; Ding, S. *Maters Sci: Maters in Med.* **2010,** *21*, **1511**. (f) Yang, Z.; Chu, H.; Jin, Z.; Zhou, W.; Li, Y. *Chinese Science Bulletin* **2010**, *55*, **921**. (g) Luo, Z.; Somers, L. A.; Dan, Y.; Thomas, L.; Kybert, N. J.; Mele, E. J.; Charlie, J. A. T. *Nano Lett.* **2010,** *10*, **777**. (h) Sajanlal, P. R.; Pradeep, T. *Langmuir* **2010,** *26*, **456**. (i) Mubeen, S.; Zhang, T.; Chartuprayoon, N.; Rheem, Y.; Mulchandani, A.; Myung, N. V.; Deshusses, M. A. *Anal. Chem.* **2010**, *82*, **250**. (j) Sun, Y. *Nanoscale* **2010**, *2*, **1626**. (k) Allanore, A.; Feng, J.; Lavelaine, H.; Ogle, K. *J. Electro. Soc.* **2010,** *157*, **24**. (l) Olson, T. S.; Rincn, R. A.; Brevnov, D. A.; Atanassov, P. *Electro. Solid-State Letts.* **2010**, *13* **11**. (m) Sajanlal, P. R.; Subramaniam, C.; Sasanpour, P.; Rashidian, B.; Pradeep, T. *J. Mater. Chem.* **2010**, *20,* **2108**. (n) Pai, Y.; Lin, G. *J. Electro. Soc.* **2010**, *157*.

27 Li, S.; Crooks, R. M. *J. Electro. Soc.* **1991**, *138*, **23**.

28 Sedahmed, G. H.; Shemilt, L. W. *J. App. Electro.* **2002,** *14,* **123**.

29 (a) Mrozek, M. F.; Luo, H.; Weaver, M. J. *Langmuir* **2000,** *16,* **8463**. (b) Miki, A.; Ye, S.; Osawa, M. *Chem. Commun.* **2002**, **1500**. (c) Kelley, S.C.; Deluga, G.

A.; Smyrl, W. H. *Solid-State Lett.* **2000**, *3,* **407**. (d) Lu, G.-Q.; Crown, A.; Wieckowski, A. *J. Phys. Chem. B* **1999**, *103,* **9700**.

30 (a) Herricks, T.; Chen, J. Y.; Xia, Y. *Nano Lett.* **2004,** *4,* **2367**. (b) Teng, X.; Yang, H. *Nano Lett.* **2005**, *5,* **885.** (c) Maksimuk, S.; Teng, X.; Yang, H. *Phys. Chem. Chem. Phys.* **2006,** *8,* **4660**. (d) Tian, N.; Zhou, Z. Y.; Sun, S. G.; Ding, Y.; Wang, Z. L. *Science* **2007**, *316,* **732.** (e) Kawasaki, H.; Yonezawa, T.; Watanabe, T.; Arakawa, R. *J. Phys. Chem. C* **2007**, *111,* **16278**.

31 Rhee, C. K.; Wasberg, M.; Zelenay, P.; Wieckowski, A. *Cat. Lett.* **1991,** *10,* **149.**

32 (a) Somorjai, G. A. *Chemistry in Two Dimensions: Surfaces; Cornell University Press: Ithaca,* **1981**. (b) Hoshi, N.; Kawatani, S.; Kudo, M.; Hori, Y. *J. Electroanal. Chem.***1999**, *467*, **67**. (c) Banholzer, W. F.; Wasel, R. I. *J. Catal.* **1984**, *85*, **127**. (d) Blakely, D. W.; Somorjai, G. A. *Surf. Sci.* **1977,** *65,* **419**. (e) Lin, W. G.; Sun, S. G.; Zhou, Z. Y.; Chen, S. P.; Wang, H. C. *J. Phys. Chem. B* **2002**, *106,* **11778**.

CHAPTER 4

Shape Controlled Synthesis of Rhodium Nanostructures by Chemical Vapor Deposition: Applications in Electrocatalysis and Field Emission*

Shape selective synthesis of Rh nanostructures has been demonstrated with the help of a single step chemical vapor deposition, where different shapes like cubes, pyramids and hexagons have been obtained as a function of temperature. Subsequently, their electrocatalytic activity has been studied using cyclic voltammetry, revealing unique shape-dependant performance towards formic acid oxidation. Significantly better sensitivity of cubes as compared to other shapes has been correlated with the results of X-ray diffraction and X-ray photoelectron spectroscopic analysis. At the end of this chapter, field emission properties of these various Rh shapes have also been studied. An ultra low threshold field of 0.72 V/μm is repeatedly observed to generate a current density of 4 x 10^{-3} μA/cm^2 for hexagonal Rh nanostructures, although the current density becomes 40 μA/cm^2 at an applied field of 1.76 V/μm. A higher value of field enhancement factor (9325) observed might be due to the origin of electron emission from sharp corners and edges of the hexagonal nanostructures. The unusual current stability and resistance to ion bombardment during the electron emission could be due to several complex factors including surface stress, stability towards the self-diffusion of Rh atoms at high field coupled with electron transfer processes pertaining to strong Rh-Rh bonds.

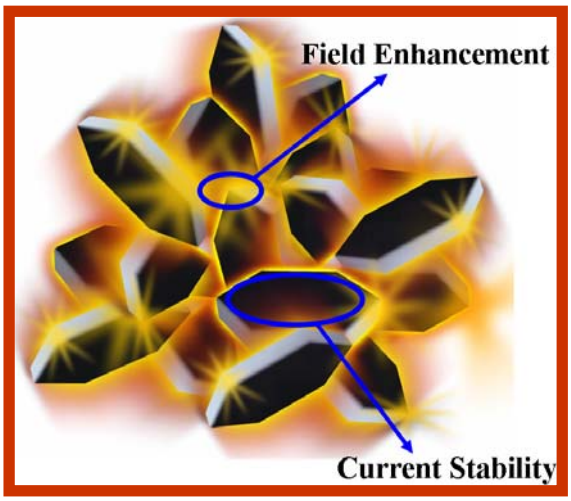

*A part of the work discussed in this chapter has been published in ***"Appl. Phys. Letts.*** 92 253106, **2008** "

4.1. Introduction

Synthesis of nanostructures with controllable size and shape is a critical goal in numerous areas of nanotechnology considering their implications for a variety of applications like fuel cells, solar energy conversion and environmental remediation. Moreover, the manipulation of size and shape has strong impact in controlling the reactivity for many of these applications and also for the development of high-throughput electronic and electrochemical devices, like those based on field emission and energy generation. Accordingly, nanostructured transition metal based catalysts like Pd, Pt, Rh, Ir and Ru have been studied extensively because of their excellent activity, selectivity and stability. Rh could especially be a promising field emission material pertaining to its features like outstanding electrical performance, chemical inertness, mechanical strength, remarkable thermal stability, lower electron affinity and better stability towards ion-bombardment [1]. In addition, one of the interesting ways to pick up the finest performance towards electrocatalytic activity is to achieve their preferential growth in particular facets. For example, low symmetric (100) plane of Rh is known to show higher electrocatalytic activity than the high symmetric Rh (111) in acidic medium owing to different adsorption rate of anions on these facets [2]. Hence, it is important to study anisotropic nanostructures of Rh for many applications including field emission and catalysis because of their surface heterogeneity.

Recently, several advanced synthetic approaches for the fabrication of metallic nanostructures have been reported with subtle precision including both template-based and non-template-based methods [3-5]. Variants of solution-based techniques, carbothermal reactions [6], solid liquid solid processes [7], solvothermal processes [8] and vapor phase growth (including thermal evaporation, chemical vapor-phase deposition, metal-organic chemical vapor phase deposition, arc discharge and laser ablation) have been widely used to achieve synthesis of various nanostructures of Rh with a narrow size distribution, although their selectivity and their correlation with respective shapes have rarely been explored [9-10]. Moreover, these as-synthesized nanostructures which are dispersed in liquids cannot be used directly for many

applications like heterogeneous catalysis and nano-device (electrode) fabrication, especially because of the challenges, due to the presence of surface stabilizer, their separation, purification and recycling aspects [11]. Apart from this, the presence of external capping molecules on the surface of nanostructures may alter their behavior on electrode surface, which in turn could hamper some of their activity. Hence, there is a need to develop suitable methods which avoid any kind of capping agents along with a proper control over the plane selectivity as this could impact many applications like fuel cell catalysis and biosensors [12].

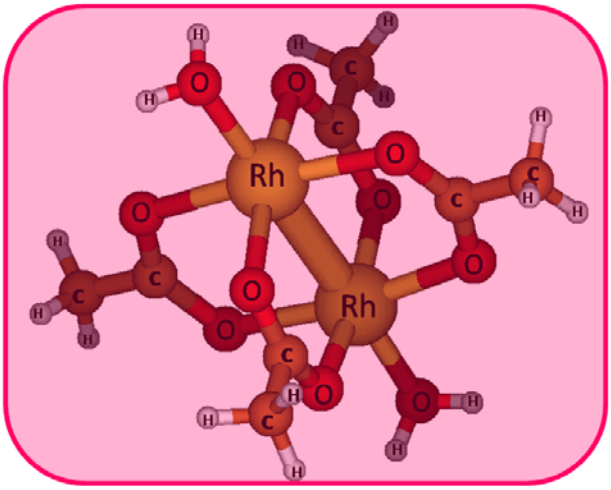

Figure 4.1. Fundamental cage like structure of rhodium acetate having strained Rh-Rh bond in acetate network; adopted from [13].

In the previous two chapters (chapters 2 and 3), we have described the morphological evolution of Rh nanostructures by colloidal and electrochemical synthetic approaches. In contrast to this, in this chapter, we discuss chemical vapor deposition (CVD), to overcome the issue related to the shape selective synthesis of Rh nanomaterials. This has also been inspired by its simplicity, lower cost, scale-up potential and its flexibility towards tuning surface structure [14]. We also report a comparison of the electrocatalytic activity of different shaped Rh nanostructures, prepared through modified chemical vapor deposition using rhodium acetate as a precursor, since, it has an octahedral coordination geometry, having monoclinic crystal structure with a Rh-Rh quadrupole bond with in a tetrahedral organic cage (Figure 4.1). This peculiar cage like

structure is considered to be mainly responsible for the formation of Rh nanostructures followed by their reorganization due to the temperature modulation resulting into different shape evolution. As compared with commercial Rh, these 'as-synthesized' Rh nanostructures give lower onset potential and higher current density for formic acid oxidation. A comparison of the electrocatalytic studies of these structures illustrates improved performance of cubes compared to that of pyramids and hexagons. We have also demonstrated their metallic behavior based on electrical conductivity measurements as a function of temperature. Finally, the field emission properties of Rh hexagonal nanostructures have been discussed from the application point of view. They show excellent current stability and remarkable enhancement in the field emission behavior and the results are explained using the effect of surface heterogeneity.

4.2. Experimental Section

4.2.1. Materials:

Rhodium acetate (99.9%) and Rh foil (bulk Rh) were purchased from Aldrich Chemicals, while AR grade sulphuric acid, formic acid, ethanol and acetone from Merck. All reagents were used without further purification and deionized water (18 MΩ) from Milli-Q system was used in all experiments.

4.2.2. Chemical Vapor Deposition (CVD) set up

Different shapes of Rh nanostructures were synthesized by a modified CVD using rhodium acetate as a source of Rh, having a cage like structure with a strong Rh-Rh bond [13]. The experimental setup consisted of a horizontal high-temperature tubular furnace with a quartz tube (90 cm in length, 22 mm in diameter) attached with a gas flow meter. The Rh precursor was placed in a polycrystalline alumina boat at the center of the furnace, where 500 - 950 °C was maintained by heating at a rate of 5 °C/min along with passing argon at a flow rate of 250 sccm (Figure 1.6). After the completion of the reaction, the furnace was naturally cooled down to room temperature in argon atmosphere.

Similar controlled experiments with different Rh precursors like rhodium chloride, rhodium nitrate and other organo-rhodium precursors revealed that the use of rhodium acetate with Rh–Rh bond (having a dimeric cage like structure) is indispensable for the unique shape evolution. The same kind of morphological evolution was reported in the case of Cu by Bellini et al., where elongated nanotubes of metallic Cu were formed due to the fundamental dimeric and open tetragonal structure of copper (II) acetate precursor [15]. Optimum yields of various Rh shapes were obtained at different temperatures keeping the reaction time as constant (i.e., 3h) based on the initial experiments. Rh nanostructures obtained under such conditions were subsequently characterized by techniques including SEM, EDS, TEM and XRD.

4.3. Materials Characterization

4.3.1. Electrocatalytic Studies

All electrochemical measurements were performed on an Autolab PGSTAT30 (ECO CHEMIE) instrument using a standard three electrode cell comprising of Rh nanostructure modified glassy carbon disc as the working electrode, Pt foil as counter electrode and Hg/Hg_2SO_4 as the reference electrode in 0.5 M H_2SO_4 at room temperature as discussed in section 2.3.6.

4.3.2. Conductivity Measurements

Electrical conductivity of Rh nanostructure was measured using a KEITHLY 220 Programmable current source and KEITHLY 181 Nano-voltmeter coupled with an OXFORD Intelligent temperature controller ITC-4. Thin pellets of samples were made by using the same amount of Rh nanostructures by applying equipressure through a hydraulic press and four probe electrical conductivity was measured in the range of 298-473 K.

4.3.3. Field Emission Set-up

Field emission measurements (FEM) on Rh hexagon sample were carried out in a planar diode configuration under a vacuum of 1×10^{-9} mbar with the help of a sputter ion pump and a titanium sublimation pump. The current-voltage (I-V) characteristics were recorded using a high voltage power supply (0-40 kV, Spellman, USA) and pico-ammeter (Keithley 614) at room temperature. Fowler-Nordheim (F-N) plots were obtained from the recorded I-V data by keeping the cathode-anode separation at ~10 mm for all the samples. All field emission experiments were repeated at least thrice under identical conditions. Accordingly, the cathode (nanostructured Rh hexagons deposited on a Si substrate) was held at a distance of ~10 mm from the transparent anode screen in a high vacuum chamber as shown in the schematic of the conventional FEM configuration (Figure 4.2).

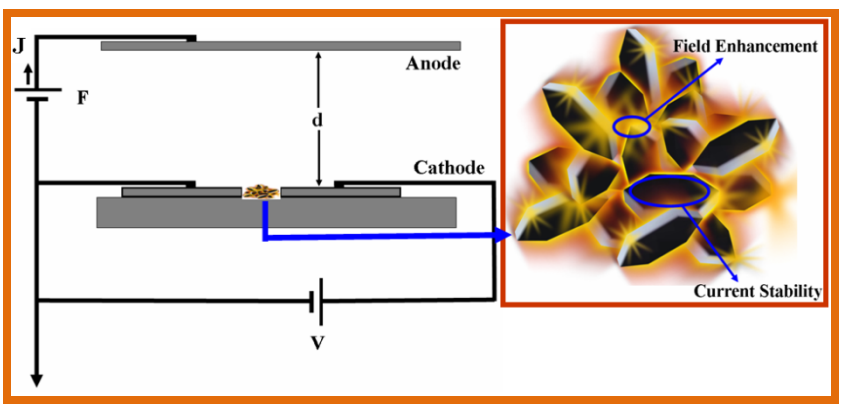

Figure 4.2. Schematic of the conventional FEM configuration; the emitter (cathode) in the form of Rh hexagons is placed inside an evacuated chamber, in front of an anode (typically 5 to 7 cm apart), whereas, F is the applied electric field, V is the applied voltage and the separation (d) is 5 mm between emitter cathode and anode screen.

In the conventional FEM configuration, the emitter (cathode), in the form of a fine needle with a tip radius of ~ 10^{-4} cm was placed inside an evacuated chamber, in front of an anode screen, typically 5 to 7 cm apart. In such a configuration, it is possible to enhance the range of applied electric field to overcome the drawback of arc formation observed in the close-proximity (C-P) configuration. Other characterization details like

XRD, SEM, TEM, HRTEM, EDS, and XPS have already been discussed in Chapter 2, section, 2.3).

4.4. Results and Discussion

4.4.1. X-ray Diffraction

Figure 4.3. depicts a comparison of the XRD patterns of cubes, pyramids and hexagons, where, all samples reveal five prominent reflections corresponding to (111), (200), (220), (311) and (222) suggesting the presence of single phase face-centered cubic (fcc) structure with high crystallinity. Also, all XRD patterns reveal no change in the peak position for all three morphologies/nanostructures as compared to that of size tunable nanocrystals of Rh as reported recently by Somorjai and coworkers [16].

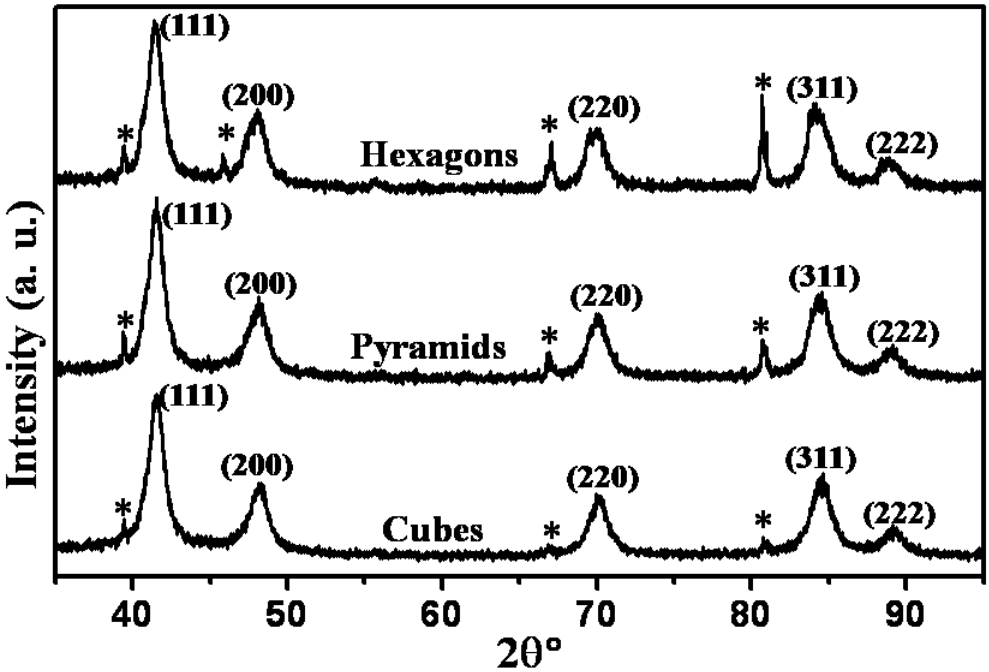

Figure 4.3. Comparison of XRD patterns of cubes, pyramids and hexagons revealing reflections from (111), (200), (220), (311) and (222) planes corresponding to the fcc Rh using Cu Kα (1.54Å) radiation; ∗Peaks corresponding to exposed Pt substrate.

A close examination of the XRD pattern of these structures shows interesting change in the peak area ratio (here we have considered the peak area and not the peak

intensity, since the normalized numbers are more effective) with morphology. For example, a comparison of the intensity ratio of $A_{(111)}/A_{(220)}$ reveals that the area ratio is higher for cubes whereas it is lower for hexagons. This change in orientation with morphology could be responsible for their improved electrocatalytic performance; peaks indicated by * are associated with the planes from the Pt substrate.

4.4.2. Scanning Electron Microscopy and Energy Dispersive X-ray Analysis

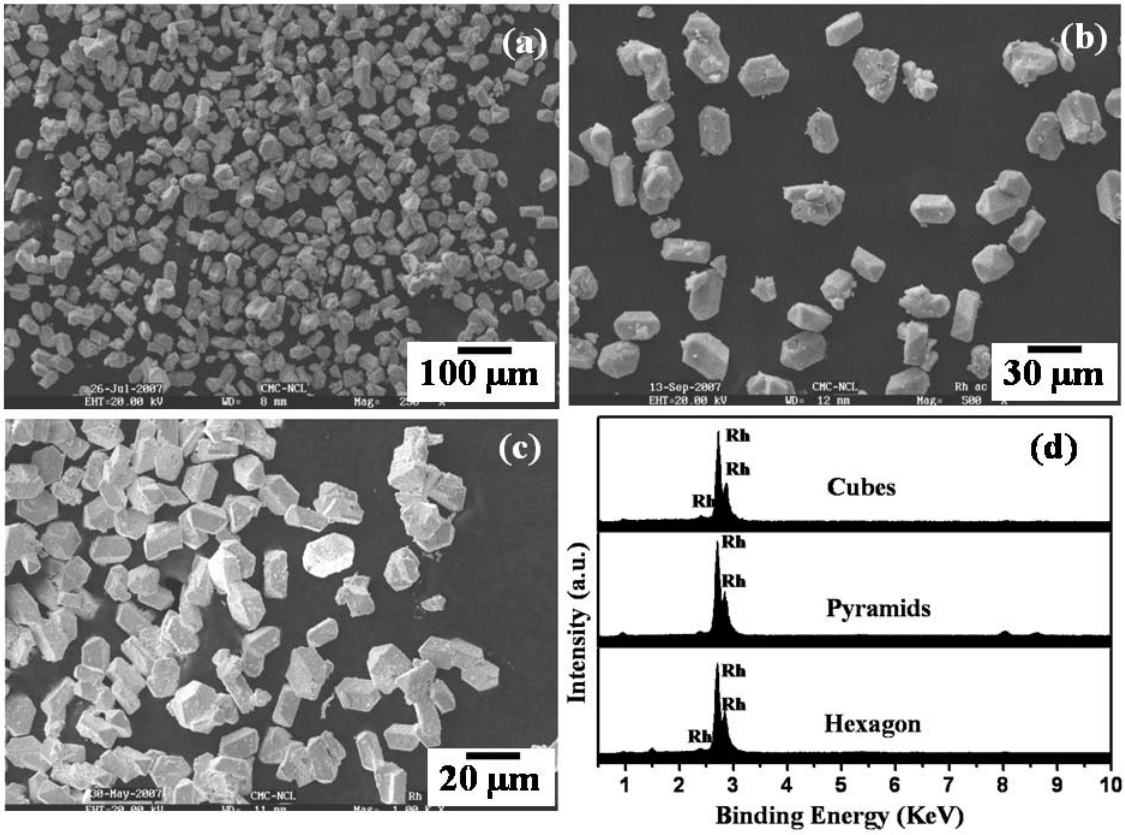

Figure 4.4. Scanning electron micrographs of (a) Cubes, (b) Pyramids, (c) Hexagons along with (d) their EDS profile for all shapes synthesized at different temperatures.

Scanning electron microscopy is an effective tool to unravel the topographical features of various nanostructures. Accordingly, Figure 4.4(a-c) shows comparison of representative SEM images of Rh cubes, pyramids and hexagons synthesized at 600 °C, 750 °C and 950 °C respectively. Interestingly, the images clearly illustrate that there is a remarkable

evolution of different shape along with decrease in their size with respect to the reaction temperature and this might be considered from the fundamental tetrahedral dimeric structure of rhodium acetate. At the temperature of 600 °C, cubes are observed with sharp corners having elongation along one dimension as shown in Figure 4.4(a).

Most of them are found to be located flat with another end at the backside. The base of the cube is thin with varied dimensions suggesting that the growth process is to be initiated from the base, from both sides and growing further, leading a pyramid like geometry at the end. Moreover, the steps/kinks at the edge of the structure suggest the growth mechanism to be started from the edge of cubic structure that is formed prior to the pyramidal structure. A careful observation of the single Rh cube reveals the presence of nanoscale porous features including cracks and kinks that might be responsible for their better performance towards formic acid oxidation.

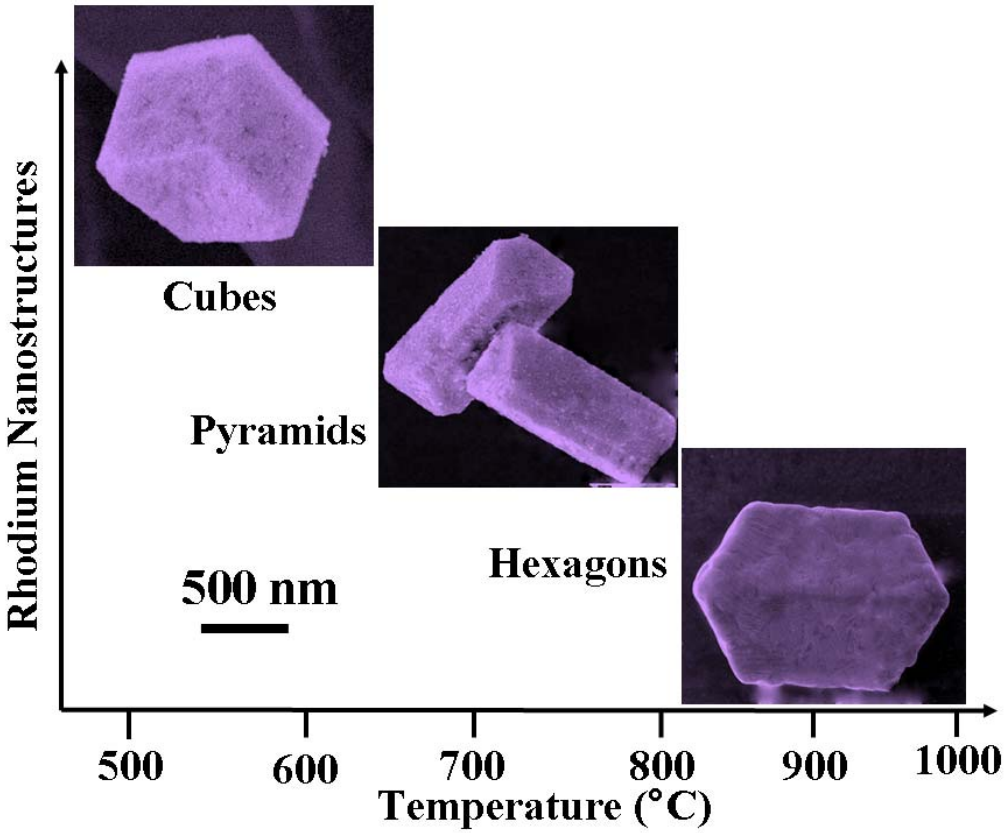

Figure 4.5. Temperature-dependent shape evolution of Rh nanostructures during synthesis by chemical vapor deposition.

Furthermore, above 750 °C, these cubes grow one dimensionally to result rod like geometry indicating that the pyramidal rod structures are likely to be formed in the beginning. However, being a dynamic system, these structures grow further to attain stable morphology with traces of short pyramids. These pyramids are subsequently converted into perfect hexagons between 900-950 °C at similar conditions with a statistical edge length of ~6 μm and thickness of ~0.5 μm for these hexagonal structures as can be seen from the magnified single hexagon. Accordingly, these studies demonstrate the significance of increase in the reaction temperature governing the auxiliary growth and shape transition during the growth. Figure 4.4. shows, a temperature-shape evolution profile of Rh indicating a reduction in the size of these nanostructures nearly about 10 times with increase in the reaction temperature. This could be due to the organization of atoms with temperature and this is also in good agreement with comparatively systematic increase in FWHM of peaks from XRD studies. Further, EDS analysis shown in Figure 4.4 (d) also confirms their pure metallic form for cubes, pyramids and hexagons, whereas peaks at 2.68 keV and 2.89 keV could be identified as the $L_{\beta 1}$ and $L\alpha_1$ emission X-ray signals of Rh respectively. This indicates the presence of single phase metallic nanostructures of Rh as in good agreement with results from the XRD studies (Figure 4.3).

4.4.3. X-ray Photoelectron Spectroscopy

Analysis of the electronic state of the as-synthesized Rh nanostructures is also of particular importance to understand their growth kinetics along with their surface structure/compositions and hence XPS studies have been carried out for all these structures. Accordingly, Figure 4.6 shows the deconvoluted Rh 3d and O 1s signals for all the structures of Rh. The peak position, line shape and peak to peak separation (≈ 4.7 eV) are standard measures of the Rh oxidation state. Significantly, Figure 4.6 (a, c and e) shows separate Rh $3d_{5/2}$ and Rh $3d_{3/2}$ signals for these structures. The peak to peak

separation (3d peaks) for cubes is 4.68 eV while for pyramids and hexagons, this is 4.65 and 4.64 eV respectively, which are standard measures of the Rh oxidation state [17]. All the binding energy positions of the elements are listed in Table 4.1, which implies the presence of Rh (0) in all these structures.

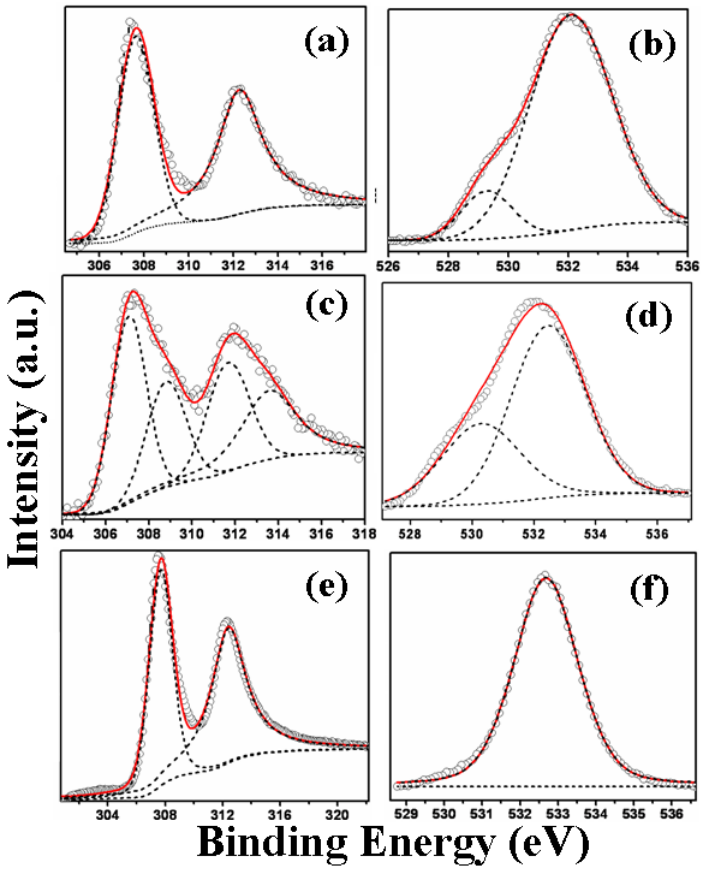

Figure 4.6. Deconvoluted X-ray photoelectron (XP) spectra for Rh 3d and O 1s signals of Rh nanostructures; cubes (a and b), pyramids (c and d) and hexagons (e and f) respectively (experimental data points are shown as circle, resultant fitting curves as red colored continuous lines and individual fitted curves as dashed lines deconvoluted by using Shirley fitting algorithm).

Interestingly, in the case of pyramidal structures as shown in figure 4.6 (c), two different couple are observed after deconvolution having binding energy values corresponding to metallic Rh along with some amount of surface oxide (RhO_2). This is in accordance with reported values and also in good agreement with results from TGA, where, nearly 10 % weight increase from ~500 °C to ~850 °C is observed as shown in

Figure 4.6 and as per the proposed decomposition pathway. While on the other hand, as shown in Figure 4.5 (b, d and e) and as per the corresponding to XPS signals of O 1s core level, all the samples show signals in the range of 531-532 eV analogous to physically adsorbed oxygen molecules on the nanostructure surface, while in the case of cubes and pyramids, an unavoidable surface oxide signal is observed after the deconvolution of lower binding energy, which matches well with the binding energy of RhO_2 [17]. Moreover, the intensity variation of signals for the deconvoluted peaks indicates that cubes have lower surface contamination of oxide as compared to that of pyramids, which is again in excellent agreement with the results of TGA. During the synthesis, the organic cage decomposes and supplies oxygen for the formation of *in situ* surface oxide at respective temperatures, especially in case of Rh pyramids and at some extent for cubes. Accordingly, XP spectra for other shapes have been analyzed based on Shirley fitting and the binding energies of Rh 3d and O 1s signals for all the shapes as shown in Table 4.1.

Table 4.1. Comparison of binding energies of Rh 3d and O 1s for various shapes of the Rh nanostructures.

Sr. No.	Shapes	Rh 3d (eV)		O 1s (eV)
		$3d_{5/2}$	$3d_{3/2}$	
1.	**Cubes**	307.8	312.3	529,5, 531.4
2.	**Pyramids**	307.5,308.9	312.2,313.7	529.3,532.1
3.	**Hexagons**	307.6	312.1	531.8

Thus, a comparison of the binding energy values of Rh 3d and O 1s for all the shapes along with their intensities indicates an *in situ* generated reactive species with surface undergoing oxidation followed by reduction. For example, the presence of *in situ* generated molecules like CO (a reducing molecule) reduces the surface oxide, finally causing Rh (0) hexagons. These results are also in agreement with the electrical conductivity measurements.

4.4.4. Thermogravimetric Analysis

The structural transformation of Rh nanostructures along with their surface oxidation/reduction reaction during the growth has been investigated by thermogravimetric measurements. Accordingly, Figure 4.7 (a) shows thermogravimetric (TG) curve of $Rh(CH_3COO)_2.2H_2O$ in nitrogen atmosphere having two well defined weight loss steps. Evidences from the literature [18] clearly show that the first stage at 90-200 °C is mainly related to the dehydration leading to the formation of $Rh_2(CH_3COO)_4$ and the weight loss at this stage is ca. 0.73 % which approximately matches to the theoretical value corresponding to the loss of two water molecules. The mechanism of formation of Rh(0) by the decomposition of rhodium acetate at 300-450 °C, at a comparatively lower temperature in nitrogen atmosphere is due to the evolved CO, which reduces the Rh-O bond *in situ*, which is reported for other systems [19]. Accordingly, a gradual weight loss of ca. 50 % up to 510 °C observed for pure rhodium acetate could be attributed to the decomposition of organic framework from Rh and the evolution of pure metallic cubic shape by the disproportionation reaction. This is followed by a steady increase in the weight at about 590 °C upto ca. 9 %, corresponding to RhO_2 formation, which is in good agreement with results from XPS studies as shown in Figure 4.6.

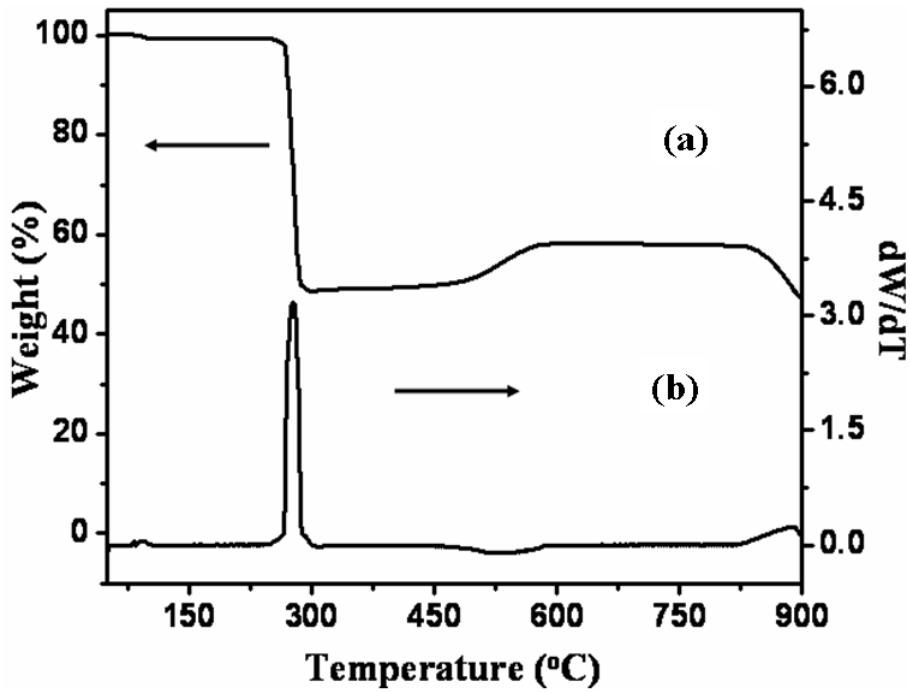

Figure 4.7. (a) Thermogravimetric (TG) curves for the decomposition of Rh $(CH_3COO)_2$. 2 H_2O at a heating rate of 10 °C/min upto 900 °C under a dynamic (10 mL/min) nitrogen atmosphere. (b) dW/dT (differential TG curve) as a function of temperature.

However, above 825 °C, there is a gradual decrease in the weight loss due to the formation of Rh_2O_3 (i.e. decrease in the Rh:O ratio), which is consistent with the results of similar studies with other metal acetate systems [15]. The probable acetate decomposition pathway and intermediate formation as a function of temperature on the basis of TGA, XPS and X-ray diffraction studies is presented below:

Reaction Pathway:

Stage I;

$$(CH_3COO)_4\,Rh_2.2H_2O \rightarrow 2\,(CH_3COO)_2Rh + 2\,H_2O$$

(50-200 °C)

Stage II;

$$2\,(CH_3COO)_2\,Rh \rightarrow Rh_2O_3 + 4\,CH_3COCH_3 \rightarrow 4\,CO + 4\,CH_3\text{-}CH_3\uparrow$$

$$4\,CH_3COCH_3 \rightarrow 4\,CO + 4\,CH_3\text{-}CH_3\uparrow$$

$$Rh_2O_3 + 3\,CO \rightarrow 2\,Rh + 3CO_2\uparrow$$

(300-450 °C)

Stage III;

Surface Rh + *in situ* ½ $O_2 \rightarrow RhO_2$

(525-800 °C)

Stage IV;

$6\ RhO_2 \rightarrow 2\ Rh_2O_3 + 2\ Rh + 3O_2\uparrow$

$2\ Rh_2O_3 \rightarrow 4\ Rh + 3\ O_2\uparrow$

(800-900 °C)

The above mechanism is also relevant to the combustion, pyrolysis and oxidation reactions of metal acetates and other organometallic precursors for generating various nanostructures of Cu, Pt, Au and Ag as a function of temperature [14, 15]. Moreover, many TG decomposition studies of metal acetates like Au, Pd, and Cu acetate suggest that acetic acid is a dominant by-product and its decomposition yields a pure metal at the end [21]. Further evaluation of the relationship between the average crystallite size of the nanostructures with probable precursors and intermediates generated *in situ*, helps to understand the morphological evolution, similar to that in the case of Cu from Cu acetate having a nearly similar decomposition pathway [15].

4.4.5. Electrocatalytic Studies

4.4.5.1. Cyclic Voltammetry and Current Transients

In order to explore the electrocatalytic properties of these Rh nanostructures and their correlation with morphology and structural aspects, we have further investigated their utility for the electro-oxidation of formic acid, which is a surface sensitive reaction relevant for fuel cell technology. The superimposed cyclic voltammograms of formic acid oxidation on different Rh nanostructures at 50 mV/s in a mixture of 0.5 M H_2SO_4 and 0.5 M HCOOH is shown in Figure 4. 8(a). All voltammograms reveal characteristic features of formic acid oxidation and for comparison, we have also included the response of commercial Rh metal which is also in good agreement with that in earlier reports [20, 21].

Accordingly, the oxidation of formic acid using Rh cube gives two peaks in the positive side, corresponding to formic acid oxidation with current densities of 1.65 and

4.55 mA/cm^2 at 0.25 and 0.70 V respectively. In the negative side, a HCOOH oxidation peak with a current density of 0.85 mA/cm^2 is found at 0.05 V, right after the appearance of a reduction peak at 0.18 V. It has been widely accepted that formic acid is oxidized to CO_2 via a dual path mechanism, which involves a reactive intermediate (main path, dehydrogenation) and adsorbed CO as the poisoning species (parallel path, dehydration), as reported earlier for other metals [21]. Hence, it is apparent that all the noticeable current concerning with HCOOH decomposition can be attributed to the oxidation of formic acid and/or CO to CO_2. The first anodic peak is due to the oxidation of HCOOH to CO_2 on surface sites that remain unblocked by CO, whereas the second anodic peak corresponds to the oxidation of surface adsorbed CO. In view of this, one can see that the current density of HCOOH oxidation for the cube is higher than that from other shapes (pyramids and hexagons) including that from bulk Rh wire, although the peak potential in case of cubes (+0.41 V) is more positive than that from Rh wire (+0.24 V); other shapes show their onset potential in between these two values.

Further comparison can be made by taking the ratio for the current density of the first anodic peak (J_{CO2}) to that of the cathodic peak (J_{CO}), which has been used to evaluate the catalyst tolerance to CO poisoning [22]. From Figure 4.8 (a), the J_{CO2}/J_{CO} (Ja/Jc) ratio for cube is ca. 2.57, whereas for commercial Rh wire this is 0.497, suggesting the enhanced CO tolerance of the Rh nanostructures as compared to that of commercial ones. This could be attributed to the orientation of crystallographic planes in Rh during the growth. The data for other nanostructures has been cited in Table 4.2. Interestingly, a close examination of the ratio of area under the first and second anodic peak reveals that charge consumed due to the oxidation of HCOOH to CO_2 is higher compared to that for CO to CO_2. We have calculated this ratio for different shapes of Rh which follow the order; cubes > pyramids > hexagons > commercial Rh.

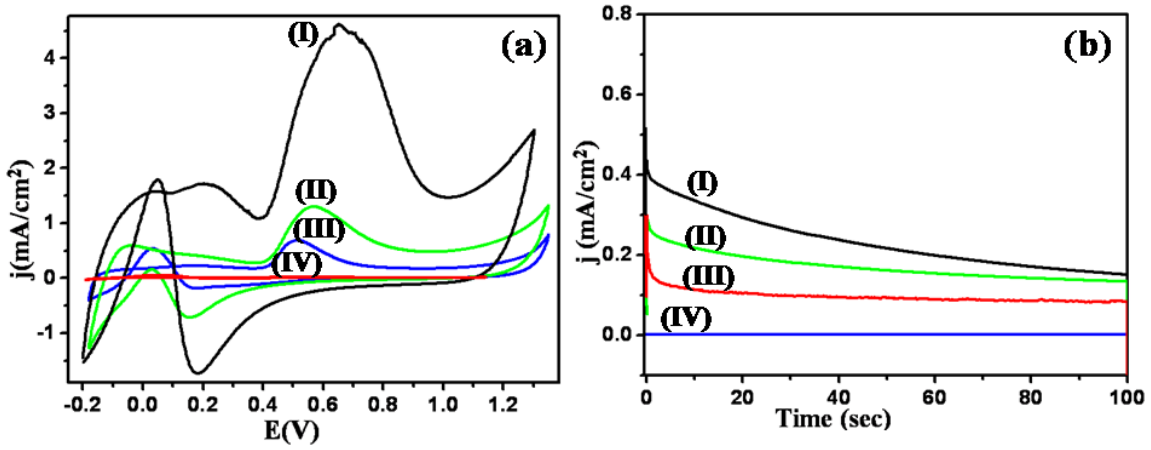

Figure 4.8. (a) Cyclic Voltammetric response of Rh nanostructures - (I) cubes, (II) pyramids (III), hexagons and (IV) commercial Rh-towards formic acid oxidation at 50 mV/s in 0.5 M HCOOH and 0.5 M H_2SO_4; (b) Comparison of current density-time plots for HCOOH oxidation at 30 °C at 0.44 V for (I) cubes (II) pyramids (III), hexagons and (IV) commercial Rh for 100 s.

Further, Figure 4.8(b) shows a comparison of the current-time transients for formic acid oxidation at 0.44 V (potential selected based on cyclic voltammograms) for all Rh nanostructures i.e. cubes, pyramids, hexagons and also for commercial Rh at room temperature after normalizing the current with respect to the electroactive Rh surface area (A_{Rh}) calculated from hydrogen desorption from cyclic voltammograms. Interestingly, the current density of Rh cubes is significantly higher compared to that of other structures and the order is as follows: cubes > pyramids > hexagons > commercial Rh. The enhancement factor R, which is defined as the ratio of the current density measured on Rh cubes versus that acquired on commercial Rh, ranges up to 20,000 % whereas for Rh pyramids and Rh hexagons versus commercial Rh it is up to 17,500 % and 11,000 %, depending upon the electrode potential. Moreover, similar studies in case of various morphologies of Pd and Pt reveal variations in electrocatalytic activities on the basis of their tunable onset potentials and current densities [23]. Thus, compared with the case of commercial Rh (wire), these Rh nanostructures with different shapes show a lower onset potential and a higher peak current density for formic acid oxidation, confirming the caveat of shape-dependant reactivity.

4.4.5.2. Structure-Reactivity Correlation

As shown above, compared to commercial Rh, our Rh nanostructures undoubtedly show significantly less CO poisoning. In addition, the peak during the cathodic sweep corresponding to the real catalytic activity of the Rh surface almost retraces the first anodic peak as can be seen from the voltammograms, which clearly confirms less CO adsorption. Interestingly, a comparison of the peak currents of these different electrodes reveals the same order, exactly like that of the anodic peaks. Hence, it is clear that for formic acid oxidation, Rh cubes show better catalytic activity compared to that of other shapes of Rh.

Table 4.2. Morphology-structure-reactivity correlation of different Rh nanostructures on the basis of electrocatalytic activity towards formic acid oxidation along with a comparison of the four probe electrical conductivity values.

Morphology	**A(111)/A(220)**	**JCO_2/JCO**	**Enhancement factor (%)**	**Conductivity (kS/cm^2)**
Cubes	6.052	2.57	20,000	2.27
Pyramids	7.204	2.04	17,500	4.78
Hexagons	9.752	1.30	11,000	6.25
Commercial Rh wire	0.506	0.497	----------	10.04

It is well-known that, the catalytic properties of metal nanoparticles depend strongly on their size, shape and surface composition, among which the shape of a nanoparticle is perhaps, more important to determine its surface atomic arrangement and coordination [24]. The origin of these shape dependent electrocatalytic activity is mainly due to the variation of surface structure. Moreover, as for face-centered cubic (fcc) metals (Pt, Pd, Rh and Ir) the high index planes, with at least one index being greater than unity are generally more reactive due to their open structure [25]. These open structure planes have higher density of atomic steps and kinks; atoms present in such planes have lower coordination numbers. These low coordinated atoms can easily interact with reactant molecules, which serve as active sites for breaking chemical bonds. For example, in case

of Pt, (210) surface possesses an extremely high catalytic activity for electro-oxidation of formic acid and also for electro-reduction of CO_2 and the (410) plane exhibits unusual activity for catalytic decomposition of NO [26]. In addition to this, these high index planes like Pt (210) have very high density of atomic steps, exhibiting higher thermal and chemical stability under both reducing and oxidizing conditions, even at elevated temperature [27]. Moreover, it is also reported that, low symmetry Rh (100) plane shows higher electrocatalytic activity than that of Rh (111) in CO oxidation through adsorption owing to different adsorption rate of CO on these facets [28].

Further, a close examination of the peak area ratio of $Rh_{(111)}/Rh_{(220)}$ shows the order: cubes < pyramids < hexagons < commercial Rh (Table 4.2). Thus cubes show higher activity towards formic acid oxidation compared to that of pyramids, hexagons and commercial Rh. This is in good agreement with above discussed reports on the electrocatalytic activity towards formic acid. We conclude that one of the possible reasons for the varying reactivity of different shapes of Rh nanostructures is due to the difference in the peak area ratio of various crystallographic planes present in the sample, which needs to be verified by carrying out Rietveld refinement [29]. Electrocatalytic activity decreases from cubes to hexagons partially due to the rearrangement of surface atoms during the synthesis at high temperature in such a way, by increasing their coordination. Moreover, this enhanced activity of unsymmetrical/low coordinated atoms of Rh present on the surface has not been affected by the surface oxide contamination observed by XPS analysis as shown in Figure 4.6. and presented in Table 4.1. As a result, from cubes to hexagons, the decrease in density of atoms present in the high index plane (220) increases the ratio of $A_{(111)}/A_{(220)}$ and decreases their electrocatalytic activity towards formic acid oxidation.

4.4.6. Conductivity Measurements

In order to explore the conductivity of these Rh morphologies and to correlate to structure/geometry, we have also carried out four probe measurements. Accordingly, Figure 4.9 shows a comparison of conductivity values of Rh cube, pyramids and

hexagons. The conductivity differences in the nanostructures can be attributed to their morphological changes associated with the atom reconstruction, surface roughness and modulation along with their size reduction through particle-particle contacts. Due to the decrease in the surface kinks and steps with temperature from cubes to hexagons, the electrical conductivity increases dramatically as shown in Figure 4.9.

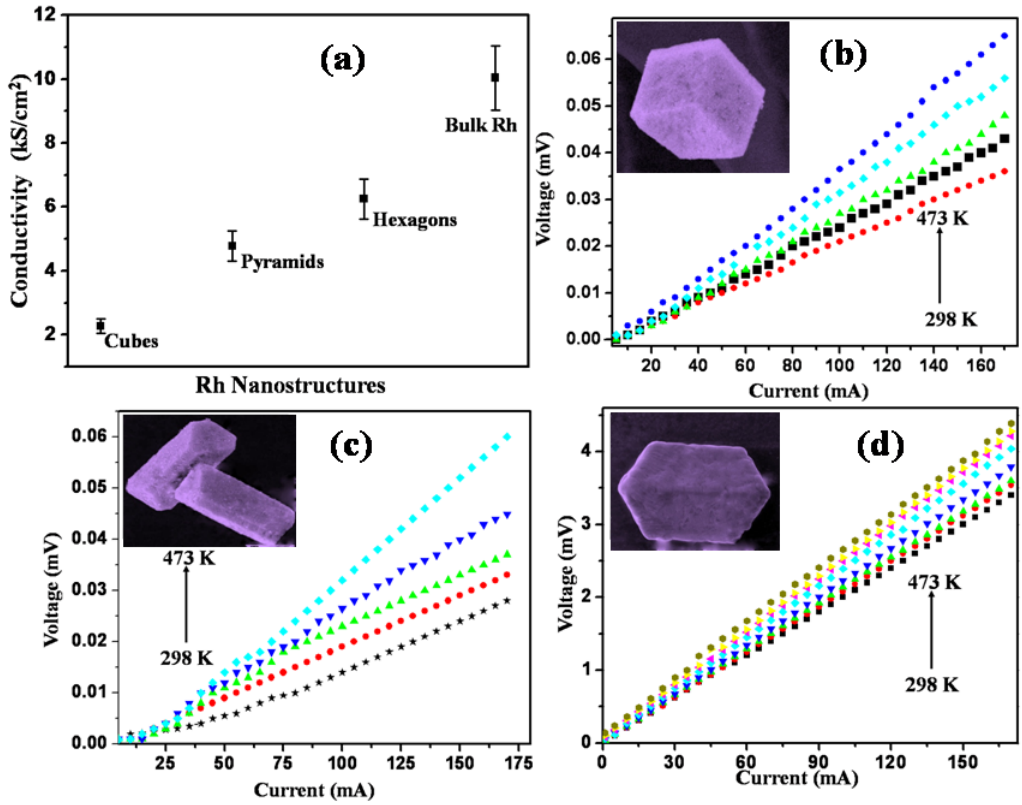

Figure 4.9. (a) Four-probe electrical conductivity values measured at room temperature for cubes, pyramids, hexagons and commercial Rh showing a linear variation with morphologies; temperature dependent I-V measurements have been carried out in the presence of argon for equiamount pellets of (b) cubes, (c) pyramids and (d) hexagons in the range of 298-473K.

4.4.7. Field Emission Studies

Having demonstrated the unique morphological features of nanostructured hexagons due to their sharp edges/tips along with nanoscale surface protrusions, we proceed further to investigate their field emission effects. The field emission is mainly controlled by the potential barrier for the electron tunneling from the interface between the hexagonal Rh nanostructures and the cathodic substrate. However, it has to be clear from the work

function of Rh obtained by atomic layer deposition (ALD), which is higher by ~100-200 meV than that of metals like Pt and Re although the work function of Rh seems to be somewhat unfavorable towards its use for field emission [30].

Accordingly, Figure 4.10(a) shows, typical emission current density-applied field (J-E) characteristics for the diode configuration, where an onset field of 0.6 V/μm, requiring an emission current of 1 nA (corresponding to the current density of 4 x 10^{-3} μA/cm^2) is reproducibly observed. With increase in the applied field, the emission current density rapidly increases, finally reaching upto 40 μA/cm^2 at 1.76 V/μm. Kim and coworkers have reported a similar enhanced field emission for metallic tungsten nanowires, where an applied field of 5 V/μm has generated an emission current density of 0.1 mA/cm^2 [31].

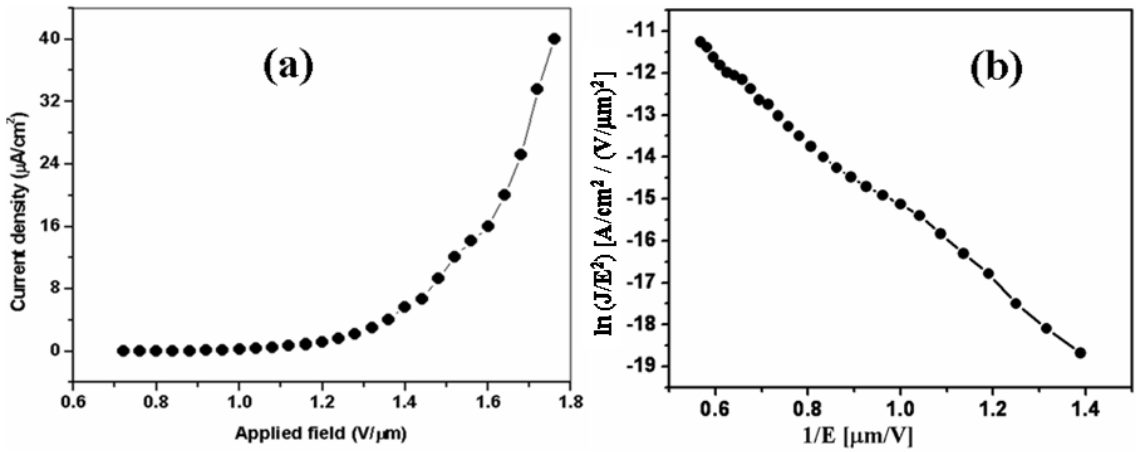

Figure 4.10. Field emission data in the form of (a) current density-applied field (J-E) characteristics of Rh hexagons and (b) Fowler-Nordheim (F-N) plot for Rh hexagons showing typical metallic behavior of the emitter.

Figure 4.10(b), shows Fowler-Nordheim (F-N) plot, where a straight line behavior indicates that the emission from the Rh hexagons follows a quantum mechanical tunneling process, similar to that reported for metallic emitters [32]. In the present studies, the applied electric field (F) is defined as F = V/d, where V is the applied voltage and d is the separation (d = 5 mm) (see schematic shown in Figure 4.2). However, the actual enhanced field at the apex of the hexagons can be estimated from the equation as follows [33].

$$\beta = -6.8 \times 10^3 \phi^{3/2} / m \quad \text{---------- (1)}$$

Where, β is the field enhancement factor, ϕ is the work function of the emitter material in eV. For crystalline surfaces, the work function associated with field emission is the average over the emitter surface, weighted towards the lower work function areas. Recently, Park and coworkers have reported the work function of Rh as 5.25 eV on silica substrate [34]. Higher value of calculated field enhancement factor β (9325) is attributed to the presence of sharp edges/tips of nanostructured hexagonal Rh as seen in Figure 4.4(c) and Figure 4.5.

These significant and specific nanoscale (protrusions) features of the emitters could be responsible for lowering the threshold leading to a final increase in the resultant field emission current. Chen and coworkers have reported a similar enhancement due to active nanoprotrusions on amorphous diamond films facilitating their enhancement in field emission [35]. In comparison, our hexagons are much bigger in size and the areal density is about 100 times smaller perhaps, due to the use of single crystalline Si substrates.

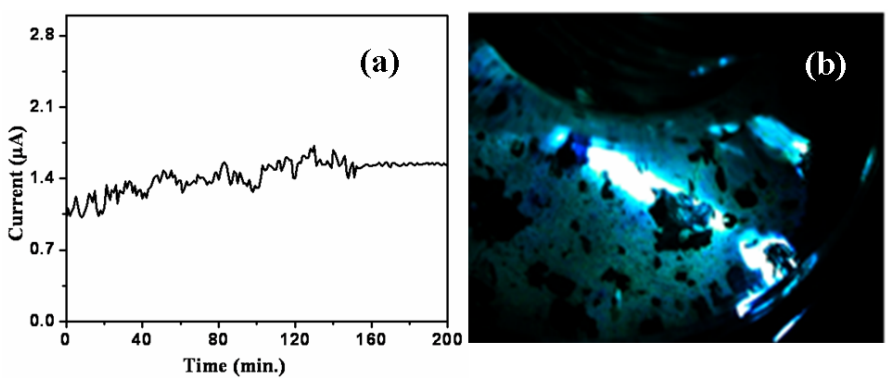

Figure 4.11. (a) I-t transients of Rh hexagons suggesting reasonable stability over a certain period of time (3.5 h). (b) Field emission micrograph of the same; bright spots on the screen represent emission at an applied potential of 10 kV from the protrusions on the emitter surface.

Current stability during field emission is one of the decisive parameters in the context of practical applications of cold cathodes. The current stability of Rh/Si has been investigated at a pre-set current of 1 μA (corresponding to the current density of 4 x 10^{-3} μA/cm^2), over a duration of more than three hours. Accordingly, Figure 4.11(a) shows

the current-time (I-t) plot for this pre-set current value at a base pressure of 1 x 10^{-9} mbar. The Rh hexagons exhibit a remarkable current stability for repeated performance without any obvious signs of degradation, making an initial excursion to ~1.5 μA. Further, a good current stability with current fluctuations within ± 15% of the average value is seen over a period of more than the 3h. The I-t plot shows similar stability after repetitive measurements suggesting lack of any degradation of the emission current during the long-term operation. The observed current fluctuations in the form of spikes could however, be attributed to the adsorption/desorption of the residual gas molecules at the grain boundaries on the emitter surface. Moreover, self-diffusion of atoms at the tip in the presence of high electric field is also expected to contribute to these fluctuations. Accordingly, a comparison of the field emission properties of commonly employed metallic and metal oxide nanostructures along with a brief description of the corresponding synthetic methods is presented in Table 4.3 in order to highlight the importance of the low threshold value for our Rh hexagonal emitter.

Table 4.3. Comparison of the field-emission performance of some recently reported nanostructures with that of our Rh hexagons.

Sr. No.	Emitter Nanostructures	Synthesis method	Turn-on field	Field-enhancement factor (β)	Current Stability	Ref.
1.	ZnO nanowires	Vapor Phase Growth	6 V/μm at 0.1 μA/cm^2	847	2h	36
2.	Ge cone arrays	Electron beam Evaporation	15 V/ μm at 1 mA	560	-	37
3.	SnO_2 nanorods	Thermal Evaporation Method	2.3-4.5 V/ μm at 1 μA/cm^2	1796	2h	38
4.	***Rh Hexagons***	***Chemical Vapor Deposition***	***0.72 V/μm at 4×10^{-3} μA/cm^2***	***9325***	***≥ 3h***	**Present Work**
5.	AlN nano tips	Chemical Vapor Deposition	10.8 V/μm at 10 mA/cm^2	367 and 317	-	39
6.	Strontium oxide coated CNTs	Magnetron Sputter Deposition	4.4 V/μm at 1.96 mA/cm^2	467	-	40

Therefore, such materials are important in the fabrication of field emission devices, requiring stable emission for extended operation. Moreover, the surface morphology of the Rh hexagons on Si substrate by SEM after the field emission measurements shows no severe deterioration even after a long-term operation. This signifies that the Rh hexagons are mechanically robust and have strong resistance towards ion bombardment during the electron emission. The observed field emission pattern comprises of bright and symmetric oval shaped emission spots having higher image stability, as revealed in Figure 4.11 (b).

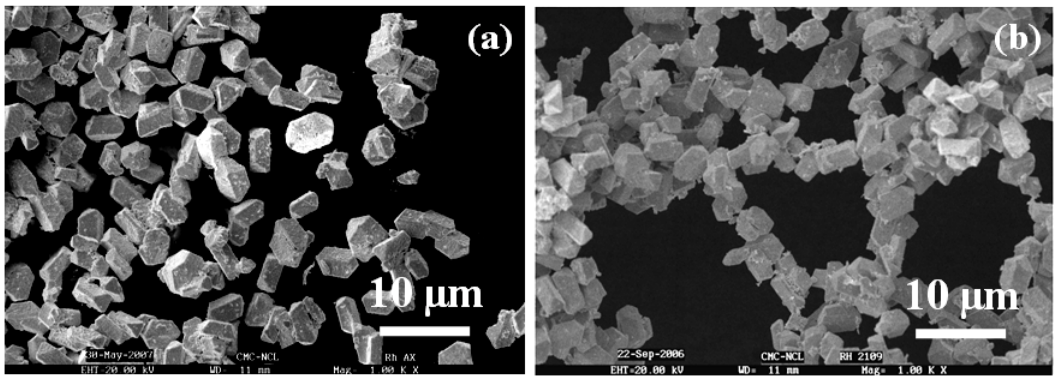

Figure 4.12. SEM image of Rh hexagons before (a) and after (b) field emission measurements.

Figure 4.12 shows a comparative surface morphology of Rh hexagons on Si substrate by SEM both before (a) and after (b) the field emission measurements. There is no obvious deterioration even after a typical long-term operation (few hours) indicating the excellent mechanical stability of these Rh hexagons against ion bombardment along with no field induced mechanical stresses. This excellent current stability would be an asset for sustained performance of the emitters.

4.5. Conclusions

Shape selective synthesis of nanostructured Rh has been demonstrated by a simple chemical vapor deposition using rhodium acetate as a precursor. Different shapes of Rh like hexagons, cubes, pyramids as a function of temperature have been characterized using a host of techniques like scanning electron microscopy, transmission electron microscopy, X-ray diffraction, X-ray photoelectron spectroscopy, thermo gravimetric

analysis and cyclic voltammetry. A comparison of the electrocatalytic activity of these structures illustrates improved performance of cubes in comparison with other structures towards formic acid oxidation. Thus, present results demonstrate the importance of a precise control of morphology and their potential benefits, especially for fuel cell applications since designing a better electrocatalyst for many fuel cell reactions continues to be an important challenge. Further, electrical conductivity measurements as a function of temperature for all the as-synthesized nanostructures suggest a metallic behavior. We have also tested these nanostructured Rh for their remarkable field emission behavior. The presence of sharp tips (100 nm) along with their nano-protrusions with an areal density of 106 /cm^2 is believed to be responsible for a stable current density of 40 μA/cm^2 that is drawn from the emitter at 1.76 V/μm. Post field-emission SEM study shows no significant change in emitter surface morphology indicating excellent mechanical stability of these Rh hexagons against ion bombardment along with no field-induced mechanical stresses, facilitating excellent pre-set current stability.

4.6. References

1. (a) Shintani, R.; Hayashi T. *Nature Protocols* **2007**, *2*, **2903**. (b) Witherspoon, T. C.; Mcfall, W. D.; Lewis, F. A. *Nat. Phys. Sci.* **1973**, *242,* 44. (c) Prestridge, E. B.; Yates, D. J. C. *Nature* **1971**, *234*, 345. (d) Bernskoetter, W. H.; Schauer, C. K.; Goldberg, K. I.; Brookhart, M. *Science* **2009**, *326*, **553.** (e) Maxwell, J. L.; Brown, K. C.; Bartley, D. W.; Kodadek, T. *Science* **1992**, *256,* **1544**. (f) Kundu, S.; Wang, K.; Liang, H. *J. Phys. Chem. C* **2009**, *113*, **18570**. (g) Bianchini, C.; Meli, A.; Patinec,V.; Sernau,V.; Vizza, F. *J. Am. Chem. Soc.* **1997,** *119*, **4945.** (h) Pan, H.; Wai C. M. *J. Phys. Chem. C* **2010,** *114*, **11364.** (i) Hata, H.; Kobayashi, Y.; Bojan, V.; Youngblood, W. J.; Mallouk, T. E. *Nano Lett.* **2008,** *8*, **794.** (j) Hua, G.; Zhou, Z.; Guo,Y.; Hou, H.; Shao, S. *Electrochem. Commun.* **2010***, 12*, **422**. (k) Edwards, H. J.; Hargrave, J. D.; Penrose, S. D.; Frost, C. G. *Chem. Soc. Rev.* **2010**, *39,* **2093**. (l) Kondoh, A.; Jamison, T. F. *Chem. Commun.*, **2010,** *46*, **907.** (m) David, M.; Vincent, N. G.; Lind, S.; Andre B. C. *Chem. Commun.,* **2010**, *46,* **910**. (n) Hoefelmeyer, J. D.; Liu, H.; Somorjai, G. A.; Tilley, T. D. *J. Colloid and Inter Sci.* **2007,** *309*, **86**.
2. (a) Jiang, Q.; Lu, H. M.; Zhao, M. *J. Phys.: Condens. Matter.* **2004**, *16*, **521** and reference therein. (b) Gerney, B. A.; Richter, L. J.; Villarrubia, J. S.; Ho, W. *J. Chem. Phys.* **1987**, *87,* **6710**. (c) Leung, L. W.; He, J. W.; Goodman, D. W. *J. Chem. Phys.* **1990,** *93,* **8328.** (d)Weimer, J. J.; Loboda-Cackovic, J.; Block, J. H. *J. Vac. Sci. Technol., A* **1990**, *8,* **2543.**
3. (a) Homberger, M.; Simon, U. *Phil Trans R Soc A* **2010**, *368*, **1405**. (b) Jana, N. R.; Gearheart, L.; Murphy, C. J. *Adv. Mater.* **2001**, *13,* **1389.** (c) Black, C. T.; Murray, C. B.; Sandstrom, R. L.; Sun, S. *Science* **2000**, *290,* **1131**. (d) Puntes, V. F.; Krishnan, K. M.; Alivisatos, A. P. *Science* **2001,** *291*, **2115**. (e) Gambardella, P.; Rusponi, S.; Veronese, M.; Dhesi, S. S.; Grazioli, C.; Dallmeyer, A.; Cabria, I.; Zeller, R.; Dederichs, P. H.; Kern, K. *Science* **2001**, *300,* **1130**.
4. (a) Martin, C. R. *Chem. Mater.* **1996,** *8,* **1739.** (b) Hulteen, J. C.; Martin, C. R. *J.*

Mater. Chem. **1997,** *7,* **1075.** (c) Davis, M. E. *Nature* **2002**, *417,* **813.** (d) Schuth, F. *Chem. Mater.* **2001,** *13,* **3184**. (e) Hurst, S. J.; Payne, E. K.; Qin, L.; Mirkin, C. A. *Angew. Chem. Int. Ed.* **2006,** *45*, **2672**. (f) Nielsch, K.; Muller, F.; Li, A. P.; Gosele, U. *Adv. Mater.* **2000**, *12,* **582**. (g) Schmid, G. *J. Mater. Chem*. **2002**, *12*, **1231**. (h) Luo, Y.; Lee, S. K.; Hofmeister, H.; Steinhart, M., Gosele, U. *Nano Lett.* **2004**, *4*, **143**. (i) Martin, C. R. *Science* **1994**, *266*, **1961**. (j) Zhang, D.; Qi, L.; Ma, J.; Cheng, H. *Chem. Mater.* **2001**, *13*, **2753**. (k) Nikoobakht, B.; El-Sayed, M. A. *Chem. Mater.* **2003,** *15,* **1957**. (l) Zhao, G. S. *J. Mater. Chem.* **2006,** *16*, **623**.

5. (a) Dai, H.; Wong, E. W.; Lu, Y. Z.; Fan, S.; Lieber, C. M. *Nature* **1995**, *375,* **769.** (b) Liu, H.; Biegelsen, D. K.; Johnson, N. M.; Pnoce, F. A.; Pease, R. F. W. *J. Vac. Sci. Technol. B* **1993,** *11*, **2532**.
6. (a) Zhang, H.; Zuo, M.; Tan, S.; Li, G.; Zhang, S.; Hou, J. *J. Phys. Chem. B* **2005**, *109*, **10653**. (b) Zhao, H.; Lei, M.; Yang, X.; Jian, J.; Chen, X. *J. Am. Chem. Soc.* **2005**, *127*, **15722.**
7. (a) Trentler, T. J.; Hickman, K. M.; Geol, S. C.; Viano, A. M.; Gibbons, P. C.; Buhro, W. E. *Science* **1995,** *270,* **1791**. (b) Markowitz, P. D.; Zach, M. P.; Gibbons, P. C.; Penner, R. M.; Buhro, W. E. *J. Am. Chem. Soc*. **2001,** *123*, **4502**. (c) Lourie, O. R.; Jones, C. R.; Bartlett, B. M.; Gibbons, P. C.; Ruoff, R. S.; Buhro, W. E. *Chem. Mater.* **2000,** *12*, **1808.**
8. (a) Heath, J. R.; LeGoues, F. K. *Chem. Phys. Lett.* **1993,** *208,* **263.** (b) Li, Y.-D.; Duan, X. F.; Qian, Y. T.; Yang, L.; Ji, M. R.; Li, C. W. *J. Am. Chem. Soc.* **1997**, *119*, **7869**.
9. (a) Wagner, R. S.; Ellis, W. C. *Appl. Phys. Lett.* **1964,** *89*, **1753975**. (b) Lu, Y.; Zhong, J. *Todd Steiner. ed. Semiconductor Nanostructures for Optoelectronic Applications* **(2004).** (c) Huang, M. H.; Wu, Y; Feick, H; Tran, N.; Weber, E.; Yang, P. *Adv. Mater.* **2001,** *13*, **113**. (d) Wang, J. *Nonequilibrium Nondissipative Thermodynamics: With Application to Low-pressure Diamond Synthesis. Berlin: Springer Verlag.* **2002**. (e) Bhushan, B. *Springer Handbook of Nanotechnology.*

Berlin: Spinger-Verlag. **2002.**

10. (a) Wang, Y.; Ren, J.; Deng, K.; Gui, L.; Tang Y. *Chem. Mater.* **2000**, *12*, **1622.** (b) Zhang, Y.; Grass, M. E.; Habas, S. E.; Tao, F.; Zhang, T Yang, P.; Somorjai, G. A. *J. Phys. Chem. C* **2007**, *111*, **12243.** (c) Hoefelmeyer, J. D.; Niesz, K.; Somorjai, G. A.; Tilley, T. D. *Nano Lett.* **2005**, *5*, **435.**
11. (a) Schmid, G. *Nanoparticles: From Theory to Application; Wiley- VCH: New York,* **2004**. (b) Cao, G. *Nanostructures and Nanomaterials: Synthesis, Properties and Applications; Imperial College: London,* **2004.** (c) Peng, S.; Wang, C.; Xie, J.; Sun, S. *J. Am. Chem. Soc.* **2006,** *128,* **10676.**
12. (a) Arico, A. S.; Bruce, P.; Scrosati, B.; Tarascon, J.; van Schalkwijk, W. *Nature Maters.* **2005,** *4*, **366**. (b) Greeley, J.; Jaramillo, T. F.; Bonde, J.; Jens, C.; Nørskov, K. *Nature Maters*. **2006**, *5*, **909**. (c) Strasser, P.; Koh, S.; Anniyev, T.; Greeley, J.; More, K.; Yu, C.; Liu, Z.; Kaya, S.; Nordlund, D.; Ogasawara, H. *Nature Chem.* **2010**, *2*, **454**. (d) Strmcnik, D.; Kodama, K.; van der Vliet, D.; Greeley, J.; Stamenkovic, V. R.; Markovic, N. M. *Nature Chem.* **2009,** *1,* **466**. (e) Atkinson, A.; Barnett, S.; Gorte, R. J.; Irvine, J. T. S.; McEvoy, A. J.; Mogensen, M.; Singhal, S. C.; Vohs, J. *Nature Maters.* **2004**, *3,* **17**. (f) Rostamikia, G.; Janik, M. J. *Electrochem. Acta* **2010**, *55*, **1175**. (g) Rosca, V.; Duca, M.; T. de Groot, M.; Marc, T.; Koper, M. *Chem. Rev.* **2009,** *109*, **2209**. (h) Xu, C.; Wang, L.; Mu, X.; Ding, Y. *Langmuir* **2010**, *26*, **7437**. (i) Wang, C.; Peng, B.; Xie, H.; Zhang, H.; Shi, F.; Cai, W. *J. Phys. Chem. C* **2009,** *113*, **13841**. (j) He, Q.; Mukerjee, S.; Shyam, B.; Ramaker, D.; Parres-Esclapez, S.; Illan-Gomez, M. J.; Bueno-Lopez, A. *J. Power Sources* **2009**, *193*, **408**. (k) Chen, J.; Lim, B.; Lee, E. P. ; Xia, Y. *Nano Today* **2009**, *4*, **81**.
13. (a) Rosencrance, S. W.; Burnham, J. S.; Sanders, D. E.; He, C.; Garrison, B. J., Winograd, N.; Postawa, Z.; De Pristo, A. E. *Phys. Rev. B* **1995,** *52,* **8**.
    (b) http://www.webelements.com/webelements/elements/text/Rh/hist.html. (c) Griffith, W. P. *CRC handbook of chemistry and physics: a ready-reference book of chemical and physical data. Boca Raton: CRC Press.* **2003**. (d) Hulett, G. A.;

Berger, H. W. *J. Am. Chem. Soc*. **1904,** *26*, **1512**. (e) Kushner, J. B. *"Modern rhodium plating". Metals and Alloys,* **1940,** *11*, **137**. (f) Amatayakul, W. *J. Clean. Product.* **2001** *9*, **395**. (g) Heck, R. *Appl. Cata. A: Gen*. **2001,** *221*, **443**. (h) Heck, R. *Chem. Eng. J.* **2001,** *82*, **149**. (i) Lide, D. R. (ed.), Holden, N. *CRC Handbook of Chemistry and Physics, 85th Edition CRC Press. Boca Raton, Florida* **2005**.

14. (a) Aktary, M.; Lee, C. E.; Xing, Y.; Bergens, S. H.; McDermott, M. T. *Langmuir* **2000**, *16*, **5837**. (b) Schropp, R. E.; Stannowski, B. I.; Brockhoff, A. M.; van Veenendaal, P. A.; Rath, J. K. *Mater. Phys. Mech.* **2002.** *1,* **73.** (c) *Fundamentals of Chemical Vapor Deposition, by Time Domain CVD, Inc* *http://timedomaincvd.com/CVD_Fundamentals/Fundamentals_of_CVD.html* (d) *Springer Handbook of Nanotechnology, Bharat Bushan (Ed.) Springer-Verlag Berlin Heidelberg, New York* **2004.** (e) Wang, G.; Hsieh, C.; Tsai, D.; Chen, R.; Huang, Y. *J. Mater. Chem.* **2004,** *14,* **3503**.
15. Bellini, J. V.; Machado, R.; Marelli, M. R.; Kiminami, R. H. G. A *Maters. Res.* **2002**, *5,* **453**.
16. (a) Hoefelmeyer, J. D. Niesz, K.; Somorjai, G. A.; Tilley, D. T. *Nano Lett.* **2005**, *5*, **435**. (b) Kundu, S.; Wang, K.; Liang, H.; *J. Phys. Chem. C* **2009**, *113*, **18570**. (c) Zhang, Y.; Grass, M. E.; Kuhn, J. N.; Tao, F.; Habas, S. E. Huang, W.; Yang P.; Somorjai, G. A. *J. Am. Chem. Soc.* **2008,** *130*, **5868**. (d) Ewers, R. D. Sra, A. K. Norris, B. C.; Cable, R. E.; Cheng, C.; Shantz, D. F.; Schaak, R. E. *Chem. Mater.* **2005**, *17*, **514**. (e) Yuan, Q.; Zhou, Z.; Zhuang, J.; Wang, X. *Inorg. Chem.* **2010**, *49*, **5515**. (f) Humphrey, S. M.; Grass, M. E.; Habas, S. E.; Niesz, K.; Somorjai, G. A.; Tilley, D. T. *Nano Lett.* **2007**, *7*,**785**.
17. Wanger, C. D.; Moulder, J. F.; Devis, L.E.; Riggs, W. M. *Handbook of XPS (Eden Prairie, MN Parkin Elmer); National Institute of Standards and Technology (NIST), United States of America, X-ray Photoelectron spectroscopy (XPS) data-base* **1995**, http://www.nist.gov/index.html.
18. Banholzer, W. F.; Wasel, R. I. *J. Catal.* **1984,** *85,* **127**.

19. (a) Fouad, N. E. Mohamed, M. A. Zaki, M. I. Knozinger, H. *J. Anal. and Appl. Pyrolysis* **2000,** *53,* **185.** (b) Lee, S. J.; Han, S.W.; Choi, H. J.; Kim, K. *J. Phys. Chem. B* **2002,** *106,* **2892.**
20. (a) Mrozek, M. F.; Luo, H.; Weaver; M. J. *Langmuir,* **2000,** *16*, **8463.** (b) Sobkowskia, J.; Zelenaya, P. *J. Electroanal. Chem.* **1978,** *91,* **309.**
21. (a) Miki, A.; Ye, S.; Osawa, M. *Chem. Commun.* **2002, 1500.** (b) Kelley, S. C.; Deluga, G. A.; Smyrl, W. H. *Solid-State Lett.* **2000,** *3,* **407.** (c) Lu, G.-Q.; Crown, A.; Wieckowski, A. *J. Phys. Chem. B* **1999,** *103,* **9700.**
22. Lu, G. Q.; Crown, A.; Wieckowski, A. *J. Phys. Chem. B* **1999,** *103,* **9700** and references therein**.**
23. (a) Subhramannia, M.; Ramaiyan, K.; Aslam, M.; Pillai, V. K. *J. Electroanal. Chem.* **2009,** *627,* **58.** (b) Subhramannia, M.; Pillai, V. K. *J. Maters. Chem.* **2008,** *18,* **5858.**
24. (a) Tian, N.; Zhou, Z.; Sun, S. *J. Phys. Chem. C* **2008,** *112,* **19801.** (b) Somorjai, G. A.; Blakely, D. W. *Nature* **1975**, *258,* **580.**
25. Somorjai, G. A. *Chemistry in Two Dimensions: Surfaces*; *Cornell University Press: Ithaca*, **1981.**
26. (a) Hoshi, N.; Kawatani, S.; Kudo, M.; Hori, Y. *J. Electroanal. Chem.***1999,** *467,* **67**. (b) Banholzer, W. F.; Wasel, R. I. *J. Catal.* **1984,** *85,* **127.**
27. Blakely, D. W.; Somorjai, G. A. *Surf. Sci.* **1977**, *65,* **419.**
28. Lin, W. G.; Sun, S. G.; Zhou, Z. Y.; Chen, S. P.; Wang, H.C. *J. Phys. Chem. B,* **2002,** *106,* **11778**.
29. (a) Rietveld, H. M. *J. Appl. Cryst.* **1969,** *2*, **65.** (b) McCusker, L. B.; Von Dreele, R. B.; Cox, D. E.; Louer, D.; Scardi, P. *J. Appl. Cryst.***1999**, *32,* **36.**
30. (a) Park, J.; Parsons, G. *Appl. Phys. Lett.* **2006,** *89*, **043111**. (b) Aaltonen, T.; Ritala, M.; Leskela, M. *Electrochem. Solid-State Lett.* **2005,** *8*, **99.**
31. Kim, S.; Baik, J.; Yu, H.; Kim, K.; Tak, Y.; Lee, J. *Appl. Phys. Lett.* **2005,** *18,* **072105.**
32. Fowler, R. Nordheim, L. *Proc. R. Soc. London, Ser. A* **1928,** *119,* **173.**

33. Gomer, R. *Field emission and field ionization, American Vacuum Society Classics, AIP, Woodbury, New York,* **1993.**
34. Park, K.; Parsons, G. *Appl. Phys. Lett.* **2006,** *89,* **043111.**
35. Chen, J.; Deng, S.; Chen, J.; Xu, N.; Huq, S. *Appl. Phys. Lett.* **2002,** *80,* **4030.**
36. Lee, C.; Lee, T.; Lyu, S.; Zhang, Y.; Ruh, H.; Lee, H. *Appl. Phys. Lett.* **2004,** *81,* **3648.**
37. Wan, Q.; Wang, T.; Feng, T.; Liu, X.; Lin, C. *Appl. Phys. Lett.* **2002,** *81,* **3281.**
38. Zhao, L.; Pang, Q.; Cai, Y.; Wang, N.; Ge, W.; Wang, J.; Yang, S. *J. Phys. D: Appl. Phys.* **2007,** *40,* **3587.**
39. Chen, Z. Cao, C.; Zhu, H. *J. Phys. Chem. C* **2007**, *111,* **1895.**
40. Jin, F.; Liu, Y.; Day, C.; Little, S. *Carbon* **2007,** *45,* **587.**

CHAPTER 5

Rhodium-Carbon Nanotube Heterostructures for Field Emission Applications*

This chapter deals with our attempts towards the synthesis of carbon nanotubes by chemical vapor deposition followed by the formation of their heterostructures with Rh nanospheres. Rh

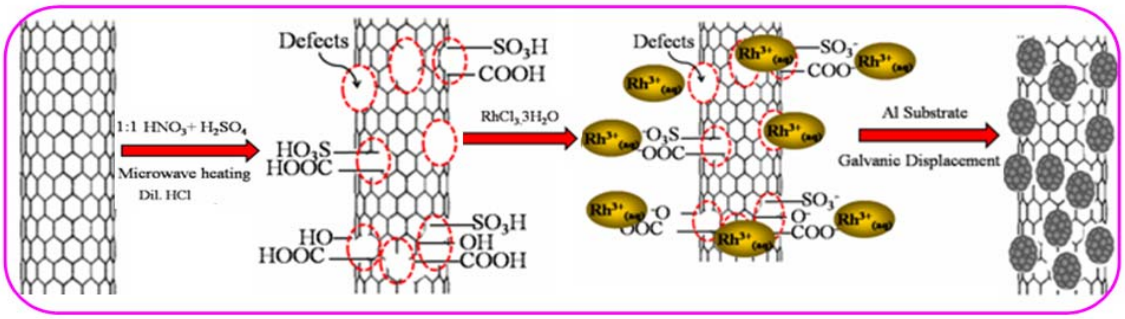

nanospheres decorated on the surface of acid functionalized carbon nanotubes by a galvanic displacement approach using Al (substrate) reveal remarkable field emission behavior of enhanced current density (170 μA/cm^2) generating at an ultra low threshold (300 V/μm). This high current density at low applied field indicates the origin of extraordinary emission from the co-operative interaction of Rh heterostructures with carbon nanotubes. The present process for the synthesis of hybrid materials can easily be scaled up for the development of miniaturized devices like field emission transistors, electron guns and single electron transistors.

*A part of the work discussed in this chapter has been published in***,** ***"Chem. Comm***.46, 5671, **2010** "

5.1. Introduction

Metal nanostructures of tunable size and shape have been the central focus of research due to their unusual electronic, optical and magnetic properties that are often different from their bulk counterparts [1]. Exploitation of the electronic structure of these materials at the nanoscale has strong implications on the development of high-throughput electronic devices [2]. Moreover, carbon-based materials such as diamond, carbon nanotubes (CNTs), carbon nanofibers (CNFs), carbon nanospheres (CNSs) and graphenes are more favorable in terms of their better stability and mechanical strength [3]. Among these, CNTs and graphene do possess unique structural, electronic, mechanical and optical properties and hence they are actively sought as an effective component of a variety of devices including field-effect transistors (FETs), Li-ion batteries, light-emitting diodes (LEDs) and also as a catalyst supports in fuel cells [4]. These properties can be further tuned by making their hybrid structures with inorganic materials like metals or metal oxides. Additionally, higher surface area, mechanical strength and thermal stability of these materials suggest a host of wide-ranging, potential applications in heterogeneous catalysis, field emitters, high-strength engineering fibers, sensors, actuators, composites, tips for scanning probe microscopy, gas storage media and next generation molecular electronic devices [5].

A number of different strategies have therefore been put forward for the fabrication of CNT based metal nanostructures. Current methods of binding nanocrystals to CNTs often make use of small organic bridging molecules via covalent interaction (i.e. organic or biomolecular linkers) to improve the adhesion between the nanostructures and CNTs or through noncovalent interactions [6]. This will not only complicates the process but also results in indirect and poor contact between the different phases. Indeed, the consequential increase in the barrier for electron transport can adversely affect the material performance in emission applications [7]. Another approach involves the direct deposition of nanoparticles onto the surface of CNTs, either through the synthesis of nanoparticles *in situ* using reducing agents or using electrodeposition with CNTs as

templates [8]. Consequently, enormous improvements have been made, in the preparation of metal/CNT heterostructures using silver (Ag), platinum (Pt), nickel (Ni), palladium (Pd), rhodium (Rh) and gold (Au), despite the poor durability issues for some of these heterostructures [8, 9]. Among these, Rh/CNTs could especially be promising due to its central features such as excellent electrical performance, chemical inertness, mechanical strength, remarkable thermal stability, lower electron affinity and significant stability towards ion bombardment [10]. Despite their importance in various fields like lighting, display, efficient emitters and in energy technology (like fuel cells, solar cells), no report on the solution phase synthesis of Rh heterostructure on acid functionalized CNTs, is available. An approach based on galvanic displacement of Al by Rh ions on the basis of the difference in redox potential is very attractive due to its simplicity and ease of control. It is well known that carbon nanotubes are good emitters [11] and more importantly, its desirable properties can be further enhanced by making use of the electronic properties (work function and the nature of density of states) of Rh by making heterostructures with CNTs, since some of these can function remarkably well (at lower applied voltages) i.e., below the intrinsic current limit due to thermal effects [12].

In the previous chapter (i.e. chapter 4), we have discussed the shape selective synthesis of Rh nanostructures using chemical vapor deposition followed by a discussion of their enhanced field emission from hexagonal nanostructures mainly because of the special features from tips and edges. In comparison, in this chapter, we demonstrate enhanced field emission from Rh nanospheres decorated on multiwalled carbon nanotubes (MWCNTs), compared to emission from both Rh nanospheres and acid functionalized MWCNTs. An ultra-low threshold field of 300 V/μm has been observed to generate a comparatively higher current density of 170 $\mu A/cm^2$, for Rh-decorated MWCNTs while Rh nanospheres and acid functionalized MWCNTs display substantially less value of 54 $\mu A/cm^2$ and 32 $\mu A/cm^2$ respectively under similar experimental conditions. Higher current density at this ultra-low threshold field indicates that the origin of extraordinary electron emission performance is from the co-operative interactions between Rh nanospheres and MWCNTs. Further tuning of the size and distribution could

offer several promising characteristics, specially required for the development of high performance electron sources. The smaller size and active area of the carbon nanotubes along with the possibility of modulating their co-operative interaction promises remarkable characteristics for the development of devices like electron guns and futuristic display devices. Moreover, these materials and heterostructures can easily be scaled up by tuning the extent of functionalization on carbon nanotubes, which would be useful for commercial applications.

5.2. Experimental Section

5.2.1. Materials

Multi-walled carbon nanotubes (MWCNTs) were prepared by a CVD method using naphthalene (99.9 %) as the source of carbon at 950 °C with the help of a two step furnace as explained below. Naphthalene was selected because of its attractive features like ease of sublimation, the presence of fused aromatic benzene ring, availability, and crystalline nature. Si wafer (111) from Aldrich and Al substrate (thickness 75 μm, purity 99.99%), ethylene glycol, iso-propanol, acetone, sulphuric acid, nitric acid and hydrochloric acid from Merck (AR grade) were used as received; deionized water (18 MΩ) from Milli-Q system was used for all experiments.

5.2.2. Synthesis of Multi-walled Carbon Nanotubes (MWCNTs)

For the synthesis of MWCNTs, an in-house fabricated CVD set-up, capable of attaining 1200 °C comprising of a dual zone furnace was used. In the beginning, a stream of Ar was passed through the quartz tube (inner diameter 34 mm) at a flow rate of 500 sccm (standard cubic centimeter per minute) to drive out all residual gases and impurities till both the zones could achieve their respective temperatures (pre-heater zone; 200 °C, main zone; 950 °C) as shown in Figure 5.1. Subsequently, a powder of naphthalene approximately (~1 gm) was kept in the first zone maintaining ~180-200 °C to ensure its complete sublimation.

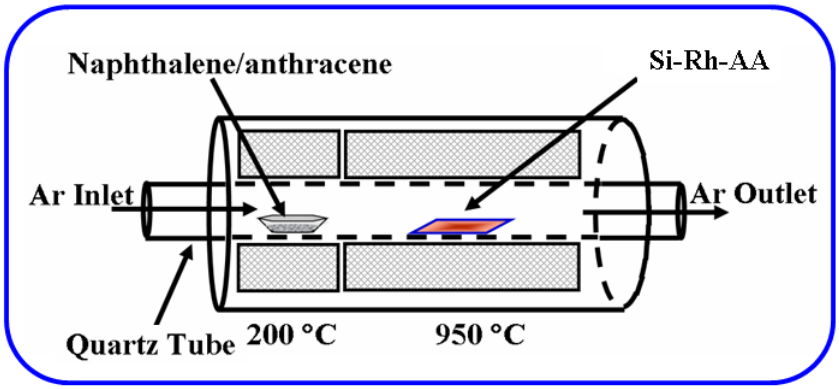

Figure 5.1. Experimental set-up used for CVD illustrating various components including dual-zone heating arrangements for the synthesis of MWCNTs; Rh-AA nanoparticle decorated on Si wafer (111) was used as substrate for nucleation purpose.

In each experiment, Si (2 x 2 cm^2, Aldrich) substrates decorated by Rh nanoparticles (Chapter 2, Section 2.2.2, Rh-AA, size of ~ 5 nm) were kept at the centre of the second zone. Special care was taken during the experiment, so that once the temperature of the second zone was at 950 °C (decomposition of naphthalene), the sublimed molecules of naphthalene (~200 °C) could pass directly into the main zone by means of a mixture with argon as a carrier gas with an optimized flow rate of 250 sccm. The temperature of the pre-heater zone was maintained at the respective value by heating at 5 °C/mins in order to carry out the complete reaction, i.e., complete sublimation with the full utilization of the precursor. The furnace was cooled naturally and the material grown on Si substrate at the center was collected for further studies including morphological and structural characterization.

5.2.3. Functionalization of Multi-walled Carbon Nanotubes

200 mg of as-synthesised MWCNTs (diameter: 20 ± 5 nm) were carboxylated using microwave (MW) treatment in an acid mixture of H_2SO_4 98 % and HNO_3 78 % (1:1) for 4 min at a power of 60 % of the total 700 W (separated by 60s off-time interval). The unfiltered residue was again dispersed in 2 M HCl and sonicated for 30 min to develop –COOH groups rather than $–COO^-$, which perhaps otherwise could have

hindered their further functionalization. The mixture was then filtered through a Polytetrafluoroethylene (PTFE) membrane (pore size of 200 nm) and the carbon residue was washed thoroughly with deionized water, until the pH of the filtrate became neutral. These acidified MWCNTs were then dried at 80 °C in air for 5 h and used for further studies.

5.2.4. Synthesis of Rh Nanospheres Decorated Carbon Nanotubes (Rh/MWCNTs)

Functionalized MWCNTs (10 mg) having a solubility of 0.1 mg/mL was mixed with 500 mL of 1 mM aq. $RhCl_3$ and ultrasonicated (33 kHz) for 30 min to make a homogeneous dispersion. A similar procedure as explained earlier (in chapter 3, section 3.2.2) for the preparation of nanospheres was carried out for the decoration of the Rh on MWCNTs by electroless reduction of Rh ions in the presence of acid functionalized MWCNTs using Al as an active reducing substrate. A schematic representation of various associated processes is illustrated in simple steps in Figure 5.2.

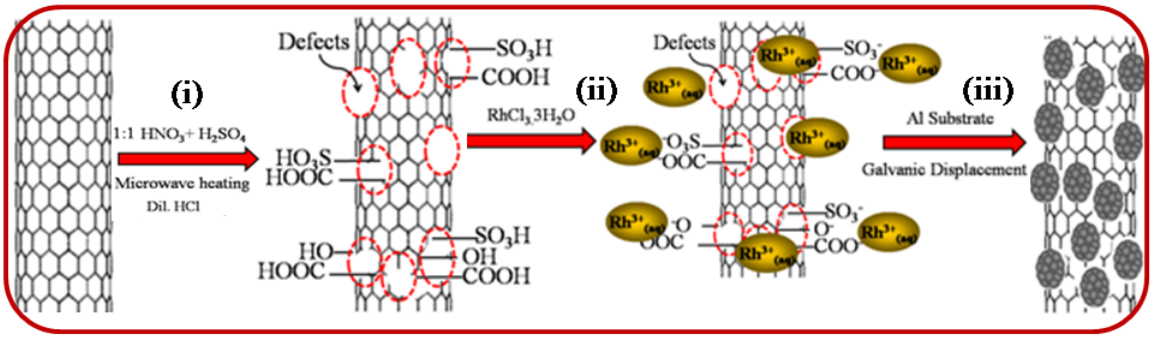

Figure 5.2. A schematic representation of the assembling procedure for the decoration of Rh nanospheres on acid functionalized MWCNTs; steps (i), (ii) and (iii) indicte chemical steps of acid treatment, Rh ion anchoring, followed by the reduction using Al substrate on MWCNTs respectiviely.

The color of the solution changed slowly from initial blackish orange to complete black after the exposure of Al indicating complete adsorption of Rh^{3+} and subsequent reduction on functionalized/defect sites of the MWCNTs. Preferential adsorption of Rh^{3+} ions on side walls was observed, which could be due to more defect sites and an interaction with active $-COO^-$ groups on the side walls of MWCNTs. After 10 min of

the reaction time, Al substrate was removed from the reaction mixture. This solution was filtered first to remove the unreduced Rh^{3+} ions followed by washing using 1 M NaOH to remove the Al releated impurities and at the end by deionized water. This was further characterized using several techniques like scanning electron microscopy (SEM), electron dispersive X-ray analysis (EDX), High resolution transmission electron microscopy (HR-TEM), X-ray diffraction (XRD), X-photoelectron spectroscopy (XPS), Fourier transform infrared spectroscopy (FTIR; DRIFT mode) and thermogravimetric analysis (TGA).

5.3. Structural and Morphological Characterization

5.3.1. Raman Spectroscopy

Raman analysis of various nanotube samples was performed on a JASCO confocal Raman spectrometer using 532 nm green laser (NRS 1500 W) in order to obtain the effect of functionalization. Other characterization details like XRD, SEM, TEM, HRTEM, EDS and XPS have already been described in Chapter 2 (section 2.3), and the details of field emission studies have been explained in chapter 4 (section 2.3).

5.4. Results and Discussion

5.4.1. Scanning Electron Microscopy and Energy Dispersive X-ray Analysis

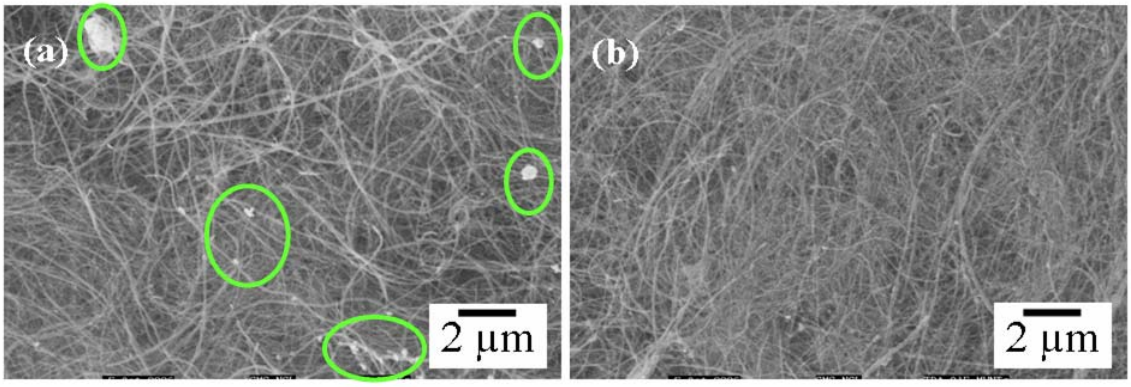

Figure 5.3. Comparative scanning electron micrographic images of MWNTs having size of ~20 nm diameter and length in several microns; (a) pristine MWNTs with agglomerated amorphous carbon (green circles) and (b) MWCNTs after acid treatment.

Figure 5.3, exhibits a comparison of the SEM images of (a) pristine MWCNTs and (b) acid treated MWCNTs revealing their higher quality (i.e., monodispersity in aspect ratio) after functionalization. Importantly, the MWCNTs are found to be unperturbed with respect to their length, suggesting that the cutting of nanotubes had not occurred during the microwave irradiation, despite the use of harsh experimental conditions. Moreover, Figure 5.3 (b) also reveals that the acid treated MWCNTs are slightly aligned relatively parallel to each other perhaps due to the strong intertubular interactions arising (electrostatic) presumably from the presence of newly created surface functional groups. However, this kind of an interaction is absent in case of pristine MWCNTs as evident from Figure 5.3 (a), since the intrinsically hydrophobic surface of MWCNTs (with sp^2 graphene stacking) results into total random orientation. Interestingly, no change in its diameter (despite several sp^3 defects sites) is observed after microwave treatment, which could be due to the higher structural stability attributed to several graphitic layers. However, single walled nanotubes are known to undergo dimensional changes and the creates of many topological defects (stone-Wales) with acid treatment.

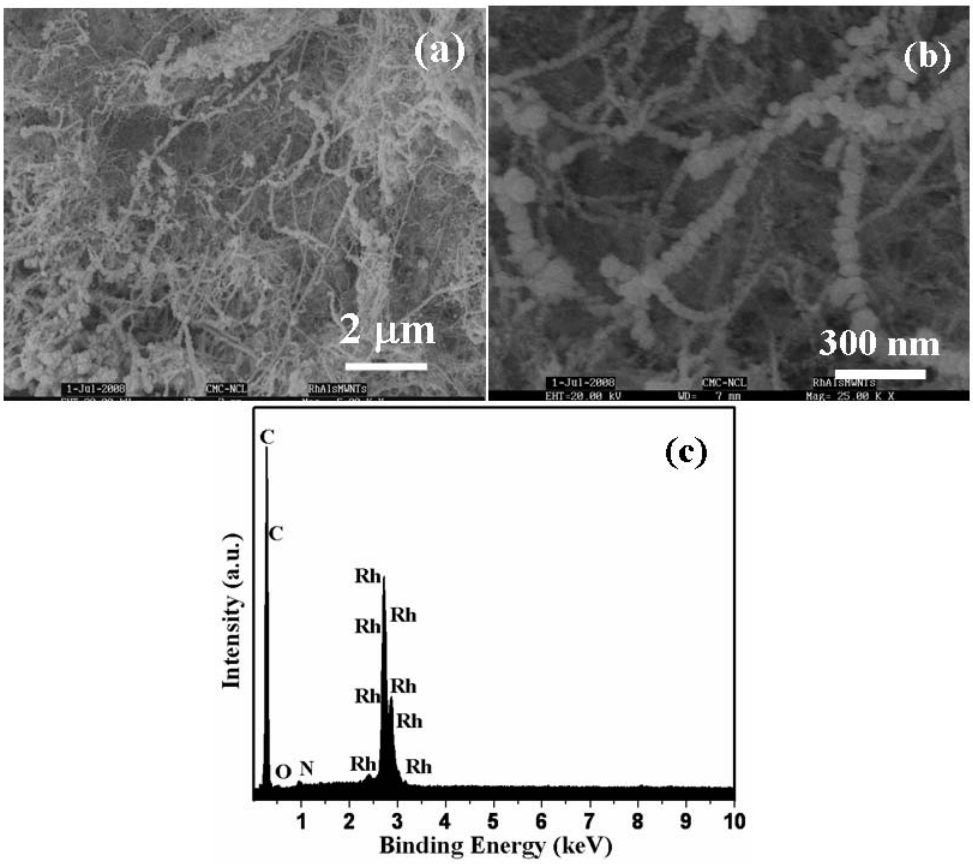

Figure 5. 4. (a and b) scanning electron micrographic images at different magnifications of Rh/MWCNTs prepared using the galvanic displacement approach and (c) elemental composition as obtained from spot energy dispersive spectral analysis.

On the other hand, a comparison of SEM images in Figure 5.4 (a and b) shows Rh nanospheres decorated on the surface of acid functionalized MWCNTs) at different magnifications providing direct evidence for Rh coverage. Interestingly, a high density of coalesced Rh nanospheres (~150 nm size) into an assembly of necklace like morphology could be clearly seen throughout the MWCNT side-walls. Electron dispersive X-ray (EDX) analysis confirms the local chemical composition of Rh/MWCNT heterostructures, where distinct peaks at 2.68 keV and 2.89 keV could be identified as the $L\beta_1$ and $L\alpha_1$ emission X-ray signals of Rh respectively and peaks at 0.26 keV, 0.51 keV and 0.98 keV corresponding to C, O and N from the acid functionalized MWCNTs as shown in Figure 5.4 (c). Moreover, in case of bare Rh only X-ray signals corresponding

to Rh and O are observed (not shown here). This is also in good agreement with the results from XRD and TGA analysis.

5.4.2. Transmission Electron Microscopy and Selected Area Electron Diffraction

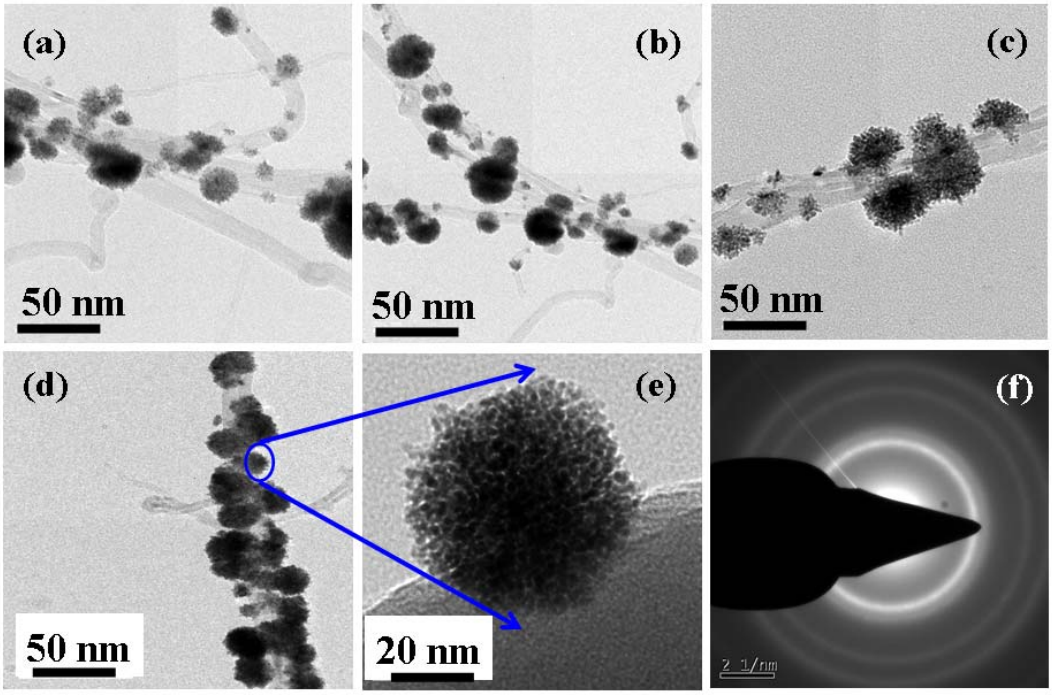

Figure 5.5. (a-d) Low resolution transmission electron micrographic images of Rh/MWCNTs heterostructure and (e) high resolution TEM image of single Rh nanospheres on MWCNT surface, showing the aggregation of small nanoparticles with average diameter of ~2.3 nm; (f) selected area electron diffraction pattern reveals rings corresponding to the crystalline Rh with fcc pattern.

The successful attachment of Rh nanospheres to MWCNTs surface is also revealed by high resolution transmission electron microscopy (HR-TEM) images as shown in Figure 5.5 (a-e). The unique morphological features (when compared to other regular spheres) include their central thicker core and rougher, comparatively less dense outer surface region having a diameter of ~150 nm. A control experiment carried out under similar experimental conditions without carbon nanotubes clearly indicates that the Rh nanospheres are with irregular surface morphology, despite having the same average diameter of ~150 nm (section 3). However, the spacing is the same for assembled

nanoparticles (~2.3 nm) with a good monodisperion as can be seen in the TEM image of Figure 5.5(e). Significantly, this suggest the reduction of Rh atoms on defect/oxidized sites of the MWCNTs, instead of that in solution and on the surface of the Al substrate, perhaps could be due to the initial replacement of H^+ of the acidic functionalities of nanotubes with Rh^{3+} ions. Further, Al substrate oxidation (dissolution) forming a Galvanic couple causes these Rh ions to undergo reduction on this already well-stabilized carbon nanotube platform so that these nanoparticles with extremely high surface energy are formed through spherical growth (as schematic shown in Figure 5.2). This hetero-structure assembly is believed to be responsible for their enhanced field emission, despite having higher size due to the assembly of smaller particles.

5.4.3. X-ray Diffraction

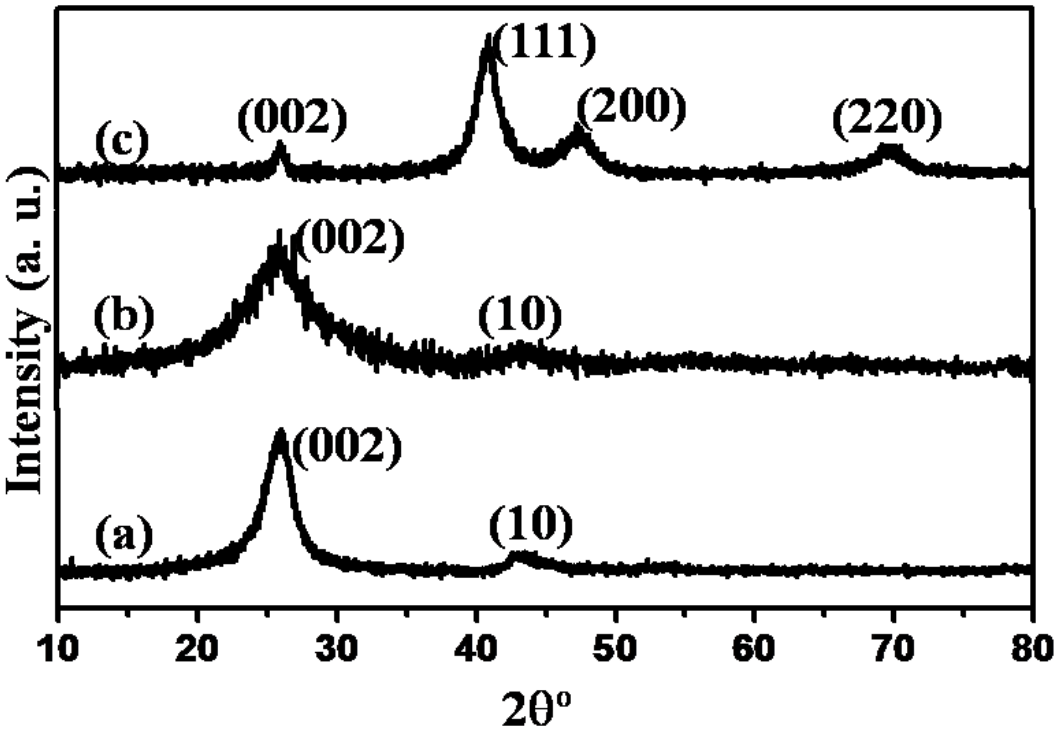

Figure 5. 6. Superimposed X-ray diffraction for (a) as synthesized MWCNTs, (b) acid treated MWCNTs showing inter-planar (002), turbostratic (10) reflections corresponding to graphene stacking of MWCNTs and (c) Rh-MWCNTs showing mixed reflections including (002), (111), (200) and (220) planes.

A comparison of superimposed powder XRD as shown in Figure 5.6 reveals a high degree of crystallinity in cases of (a) pristine MWCNTs, (b) acid treated MWCNTs and (c) Rh-MWCNTs, which provides valuable information on their change in crystallization with surface functionalization and finally their heterostructure formation with unique size distribution of Rh nanoparticles. Accordingly, all the carbon based samples [(a), (b) and (c)] exhibit strong peaks at around 2θ values of 26.6° and 42° that could be attributed to (002) and turbostratic (10) reflections analogous to graphene stacking of MWCNTs [13]. Moreover, pattern (c) corresponding to Rh-MWCNT hetero-structure exhibits additional strong diffractions at around 40°, 46° and 68° which can be indexed as Rh (111), (200) and (220) reflections, suggesting the single phase fcc crystal structure of Rh(0) [10, 14]. The crystallite size of Rh in case of 'as-prepared' Rh-MWCNTs (c) is found to be ~2.45 nm as inferred from the FWHM of 40° peak (corresponding to a *d* value of 2.27 Å), which is in excellent agreement with the size from high resolution TEM images as shown in Figure 5.5 (e).

5.4.4. Fourier Transform Infra-Red Analysis

Structural information on the local molecular environment and hence sp^3 defect sites due to the functional groups on CNTs can be obtained from FTIR analysis. Accordingly, Figure 5.7. shows superimposed FTIR spectra for (a) pristine MWCNTs (b) acid treated MWCNTs and (c) Rh decorated MWCNTs, where the common bands C-H (2800-3000 cm^{-1}) and C=C (1525 cm^{-1}) are particularly informative about the nature of graphitic carbon from the MWCNT network. Moreover, it also gives a clear evidence for the presence of sp^3 defects after functionalization of MWCNT surface followed by their final surface modification through Rh decoration.

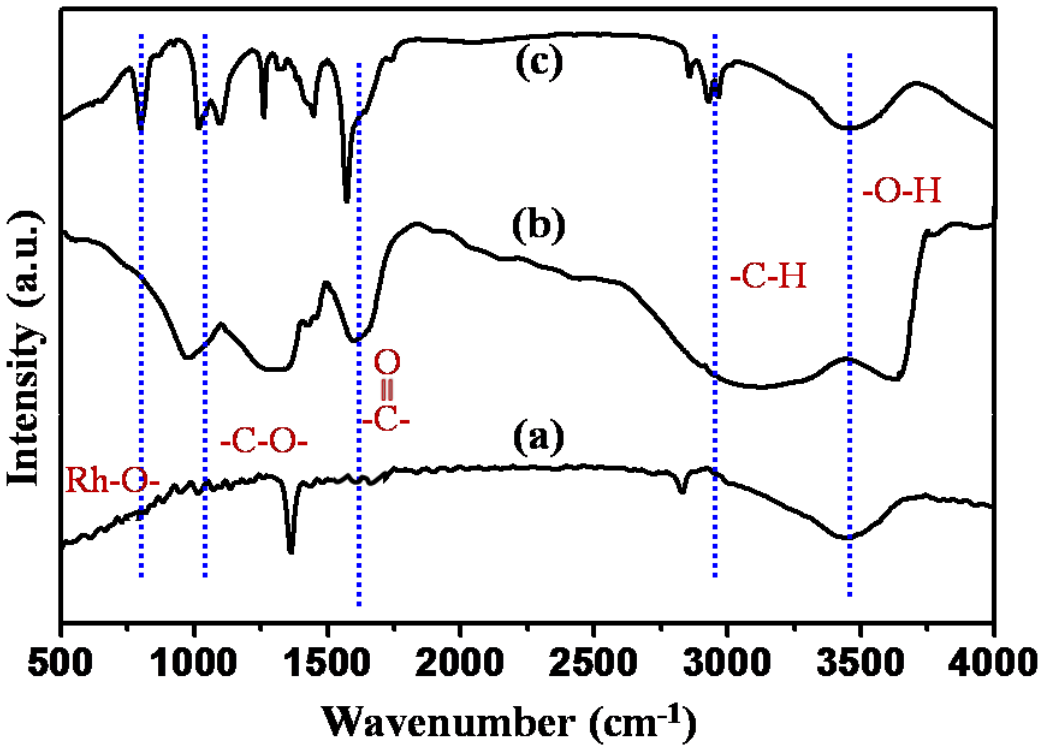

Figure 5.7. A comparison of Fourier transform-infra red spectra of (a) pristine MWCNTs, (b) acid treated MWCNTs and (c) Rh decorated MWCNTs; all spectra have been taken after making pellets using KBr.

Another common and broad band in the high frequency region, at 3480 cm^{-1} corresponding to the free -O-H bonds is invariant with surface modification, although a slight shift (at 3660 cm^{-1}) in the case of acid treated MWCNTs (b) is observed which could be attributed to intermolecular bonding (H-bonding) among various functional groups on sidewalls [15]. The fundamental bands corresponding to C=O (broad; in the range of 1680-1850 cm^{-1}) might be attributed to $-COO^-$ groups while the -O-H (phenolic; 1150 cm^{-1}) band observed for both acid treated and Rh decorated MWCNT heterostructures is common [(b) and (c)], except in the case of pristine MWCNTs (a). Normally the peak at 1600 cm^{-1} is a distinct features of $-COO^-$ group; however in the case of (c), this downward shift is perhaps due to the charge transfer interactions of $–COO^-$ with Rh. Moreover, the appearance of an additional strong band at 800 cm^{-1} in the case of Rh-MWCNTs is attributed to the presence of a Rh-O bond [16].

5.4.5. Thermogravimetric Analysis

Figure 5.8 shows superimposed thermal profiles for acid treated MWCNTs (a) and Rh-MWCNT heterostructures (b) revealing a slight initial and more or less similar weight loss till 300 °C, which is expected for both the samples, due to the loss of residual water, surface adsorbed oxygen and functional groups present on the acid treated MWCNTs and Rh-MWCNTs heterostructures respectively.

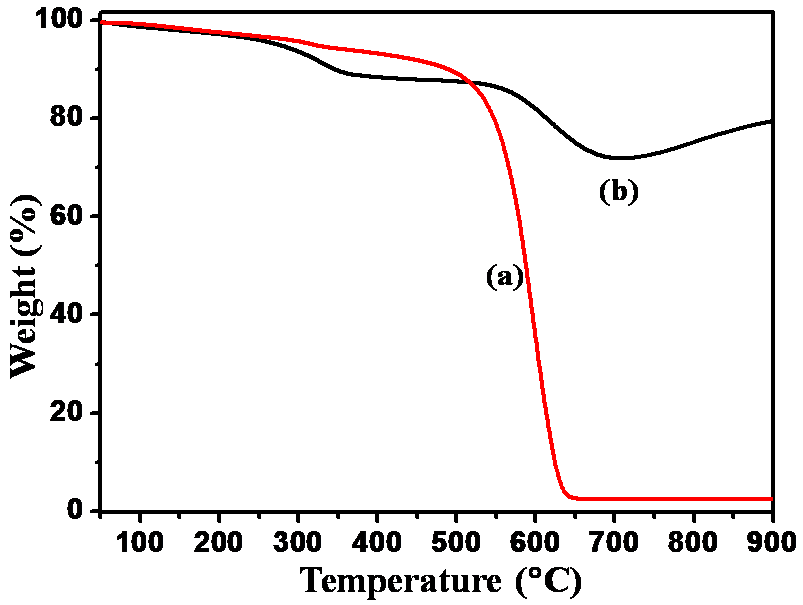

Figure 5.8. Superimposed thermogravimetric (TG) analysis of (a) acid treated MWCNTs and (b) Rh-MWCNTs performed in air at 10 °C/min.

However, a sharp and distinct weight loss step (a) in the range of 550 ^{o}C to 650 ^{o}C in case of acid treated MWCNTs (single stage ~ 99.45 %) suggests clear evidence for the absence of amorphous carbon content after acid treatment. The observed decomposition temperature of carbon is still presumably lower than that of the reported decomposition temperature of MWCNTs (700 ^{o}C) [17-18]. Rh-MWCNTs (b) in comparison, shows clearly two-stage weight loss, since the presence of Rh can facilitate oxidation and a faster decomposition above 300 °C of the Rh decorated surface as expected followed by the other parts of the tubes. As the level of Rh dispersion is significantly higher on Rh-MWCNTs, the oxidation of carbon assisted by Rh is faster in this system and accordingly

the TGA profile displays a quick weight loss region followed by a tail of the gradual decomposition. Finally, from the remaining residue after 730 °C, the amount of Rh in Rh-MWCNTs heterostructures is quantified to be 70 wt% which is also in good agreement with the results of XRD, EDX and XPS studies as explained earlier.

5.4.6. X-ray Photoelectron Spectroscopy

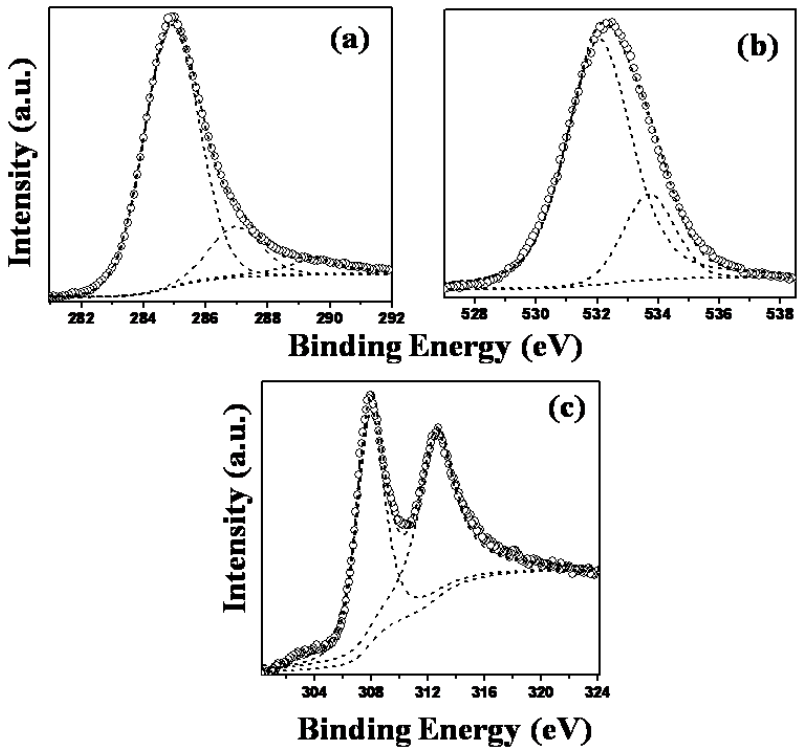

Figure 5.9. X-ray photoelectron spectra of (a) C 1s, (b) O 1s and (c) Rh 3d core levels for Rh-MWCNTs, which show three environments for carbon due to a range of functionalization steps along with Rh decoration (experimental data points are shown as circle, resultant fitting curves as continuous lines and individual fitted curves as dashed lines deconvulated by using Shirley fitting algorithm).

The presence of surface functionalities on the carbon based materials (acid treated MWCNTs and Rh-MWCNTs) along with as-synthesized MWCNTs is confirmed by XPS analysis and the corresponding binding energies for C 1s, O 1s and Rh 3d core levels are presented in Table 5.1. Accordingly, Figure 5.9 (a) shows the XP spectrum of as-synthesized hybrid material where, the C 1s spectrum has been deconvulated to three

peaks; a major peak at 284.5 eV is assigned to C-C bonds, while two minor contributions at 287.1 eV and 288.3 eV respectively, could be attributed to the carbon atoms attached to oxygen atoms in two different environments such as -C-OH and –COOH [19-20]. Minor contributions from three different oxygen functionalities as compared to the major C-C peak also supplement the results of the thermogravimetric studies (only 15 % weight loss), revealing the presence of oxygenated functional groups generated during the synthesis. The oxygen spectrum also gives two peaks (Figure 5.9 b), after a similar fitting procedure: a peak at the binding energy of 531.6 eV corresponds to the double bonded oxygen (like >C=O group) while another peak at 534.6 eV could be attributed to the presence of adsorbed moisture and oxygen.

Table 5.1: A Comparison of the binding energies of C 1s, Rh 3d and O 1s present in MWCNTs, acid treated MWCNTs and Rh-MWCNTs heterostructures.

Sr. No.	**Nanostructures**	**C 1s**	**O 1s**	**Rh 3d**		**Interactions**
				3d $_{5/2}$	**3d$_{3/2}$**	
1.	Pristine MWCNTs	284.6 286.8	531.4 536.1	-	-	C-C, C-O
2.	Acid-treated MWCNTs	284.6 286.8 290.1	533.7 534.8	-	-	C-C, C-OH, C-COOH, C-SO_3H
3.	Rh-MWCNTs	284.7 287.1 288.3	531.6 534.6	307.7	312.2	C-C, C-O, C-O-Rh,

Binding energy values for Rh 3d doublet at 307.7 eV and 312.2 eV with line shape and peak to peak separation (4.5 eV) are consistent with Rh^0 oxidation state. However, a slight negative shift in the binding energy of 3d peak is attributed to the attachment of Rh nanospheres on MWCNTs support, where a charge transfer can occur from the electron rich carbon nanotube support to the Rh [21]. Similarly, the XP spectra for pristine MWCNTs and acid treated MWCNTs have been analyzed based on Shirley fitting and the binding energies of C1s and O1s for all emitter samples have been documented in Table 5.1. A comparison of the binding energy values of O1s for all

samples along with their intensities clearly suggests the functional differences on the surface of MWCNTs. These comparative XP results thus reveal almost a similar chemical environment for oxygen and carbon, although their surface properties could cause a dramatic change in their electronic structure after anchoring Rh.

5.4.7. Raman Spectroscopy

Raman spectroscopy has also been employed to strengthen our interpretation of efficient acid functionalization followed by the decoration of Rh nanospheres on the surface of MWCNTs. Accordingly, Figure 5.10 (a) presents a comparison of the Raman spectra of the pristine, acid treated and Rh nanospheres decorated MWCNTs, each of them consisting of two characteristic bands.

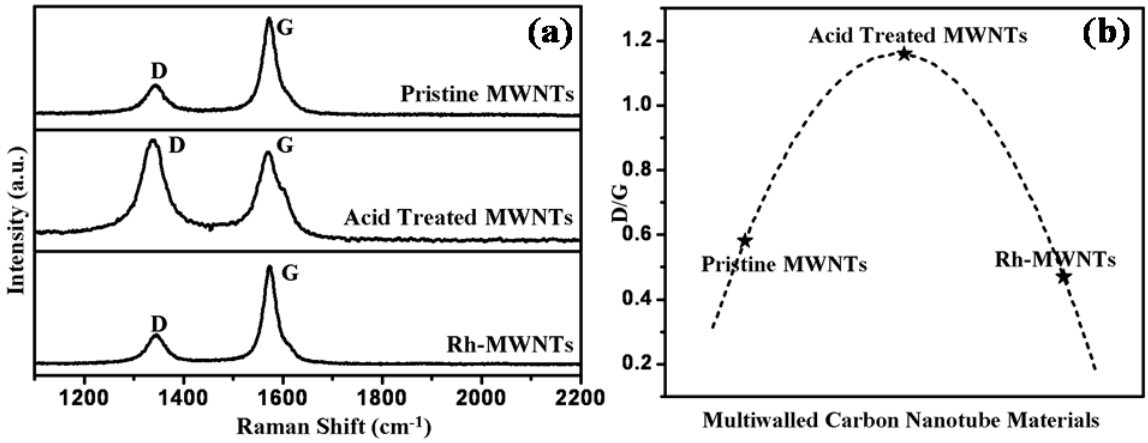

Figure 5.10. (a) Comparative Raman spectra of the pristine, acid treated and Rh nanospheres decorated MWCNTs, and (b) variation in intensity ratio of D to G band of MWCNTs with oxidation and the subsequent decoration with Rh nanospheres.

Bands at 1320 cm^{-1} (for pristine), 1327 cm^{-1} (for oxidized) and 1332 cm^{-1} (for Rh nanospheres-decorated MWCNTs) all correspond to the D band, which is caused by the induction of significant defects or disorder in the CNT surfaces [22]. In comparison, the G band corresponding to the crystallite graphitic structure is obtained at 1578 cm^{-1} (pristine), 1581 cm^{-1} (oxidized) and 1583 cm^{-1} (Rh nanospheres decorated MWCNTs) respectively. The D and G peaks have been analyzed for the intensity ratio (I_D/I_G) to quantify the surface oxidation process along with their concomitant topographic effects.

Accordingly, Figure 5.10 (b) shows the I_D/I_G values for the pristine, acid functionalized and Rh nanosphere decorated carbon nanotubes. The surface oxidized carbon nanotubes have a higher I_D/I_G ratio than that for the pristine carbon nanotubes, which is indicative of oxidative functionalization although further oxidation causes a continuous increase in the number of defective sites, which presumably increases the reactivity of the MWCNTs [23].

The distribution of defect sites on the nanotube lattice is due to the breaking of some of the walls of the MWCNTs by oxidation (schematic shown in Figure 5.2). These defects include the conversion of sp^2-hybridized to sp^3-hybridized carbon during the oxidation process, with the creation of carboxylic and hydroxyl groups. In particular, the I_D/I_G ratio decreases significantly after forming the heterostructures. This suggests that the defect sites generated on the MWCNTs surface during oxidation can be passivated by the Rh decoration, along with a slight red shift of both D and G bands. The increase in I_D/I_G ratio (Figure 5.10 b) together with shifting of G and D bands (Figure 5.10 a) is seem to be related to the strong bond between surface oxidized carbon (carbon defects) and surface Rh-atoms. This also indicates a valency satisfaction (dangling bonds) of surface carbon (from CNTs) by some of the surface Rh atomic electrons present in the clusters similar to self assembled monolayers or monolayer protected clusters, leading to a regular packing of atoms at the interface. These speculations could also be supported by an appreciable suppression of a shoulder of G band (clearly seen in acid treated MWCNTs) after Rh decoration.

5.4.8. Field Emission Studies

Having demonstrated the unique morphological features of these nanostructured Rh/MWCNTs and their co-operative effects between Rh nanospheres and MWCNTs as compared to that of "as-synthesized" Rh nanostructures (Chapter 3, Rh nanospheres) by the same approach and also that of acid functionalized MWCNTs, we now extend our discussion further to illustrate their effect on field emission. Accordingly, Figure 5.11 shows a typical superimposed emission current density Vs applied electric field plot for

the diode configuration of (a) Rh nanospheres decorated carbon nanotubes, (b) Rh nanospheres and (c) acid functionalized MWCNTs respectively.

Both the turn-on-field and the higher current density of the Rh/MWCNTs indicate that the field emission from the Rh nanospheres decorated on MWCNTs is enhanced considerably, where an onset field of 260 V/μm, requiring an emission current of 6.5 nA (corresponding to the current density of 2.5 x 10^{-3} μA/cm^2) is reproducibly observed. The emission current density of the Rh decorated MWCNTs measured at 450 V/μm is seen to improve from 32 μA/cm^2 (acid functionalized MWCNTs) to 54 μA/cm^2 (Rh nanospheres) to finally 68 μA/cm^2. In addition, turn-on field decreases from 340 V/μm (acid treated MWCNTs) to 270 V/μm (Rh/MWCNTs) (shown in Table 5.2.), which could be due to the co-operative effects, explained earlier.

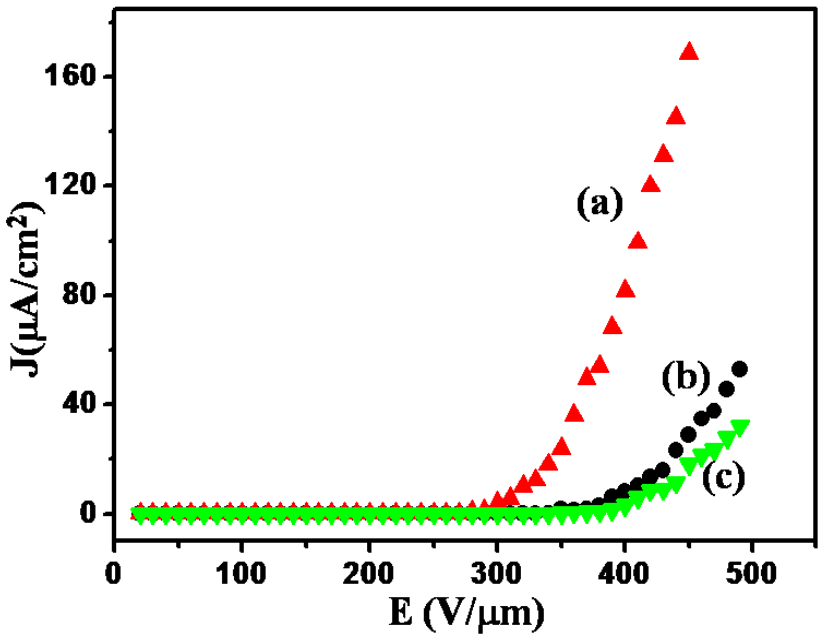

Figure 5.11. Field emission (J-E) characteristics for (a) Rh-MWCNTs, (b) Rh nanospheres and (c) acid functionalized MWCNTs mounted on Si, revealing typical metallic behaviour.

The enhanced emission properties can be explained on the basis of reduced turn-on-field and improvement in emission current density related to the Rh nanospheres anchored on CNTs. The functionalization of CNTs using Rh nanoclusters presumably

decreases the local work function of the field emitters enabling an increase in the density of states (DOS) near the Fermi level of CNTs surface due to the co-operative nature of the electronic interactions from Rh. However, only moderate field emission is observed from acid functionalized MWCNTs as compared to that of other two emitters (Rh decorated MWCNTs and Rh nanospheres). This may be due to the fact that many defect sites created by the acid treatment contain many oxygen functional groups along with the destruction of regular graphitic structure on the surface, which automatically reduces the emission current density. Accordingly, a comparison of the Field-emission performance of our emitter materials along with the list of some recently reported nanostructures is shown in Table 5.2. For example, higher current density at an ultra-low field with a higher field enhancement factor for the Rh-MWNTs than that of the Rh nanospheres, acid functionalized MWNTs and Rh hexagons could be explained based on the comparative results for other reported emitters.

Table 5.2. Comparison of the Field-emission performance of our heterostructures with some recently reported nanostructures.

Sr. No.	Emitter Nanostructures	Synthesis method	Turn-on field	Field-enhancement factor (β)	Reference
1.	Rh/MWCNTs	Galvanic Displacement with Al	168 μA/cm^2 at 450 V/μm	9820	Present work
2.	Rh nanospheres	Galvanic Displacement with Al	54 μA/cm^2 at 490 V/μm	1880	Present work
3.	Acid functionalized MWCNTs	Chemical Vapour Deposition	32 μA/cm^2 at 490 V/μm	1070	Present work
4.	Rh Hexagons	Chemical Vapor Deposition	4×10^{-3}μA/cm^2 at 0.72 V/μm	9325	24
5.	Er/MWCNTs	Chemical Vapor Deposition	3.4 mA/cm^2 at 1.8 V/μm	2543	25
6.	SiC/Si Heterostructures	High temperature carbon implantation into Si	2.6 V/μm at 1μA/cm^2	-	26

5.5. Conclusions

This chapter presents a method for synthesizing unique hetero-junctions of Rh-MWCNTs (size ca. 2.3 nm) on acid functionalized MWCNTs surface (~150 nm) with enhanced field emission behavior. The synthesis consists of acid functionalization of MWCNTs followed by a simple ion exchange, for replacing the proton of acid functionalities by Rh^{3+} ions and subsequent reduction of these ions by a galvanic approach. An ultra-low threshold field of 300 V/μm is observed to generate an emission current density of 170 $\mu A/cm^2$, which is an appreciably large value as compared to that of individual Rh-nanospheres (54 $\mu A/cm^2$) and functionalized MWCNTs (32 $\mu A/cm^2$). Our process can easily be scaled up using larger Al substrates and by tuning the extent of functionalization on MWCNTs which would be useful in microelectronics and also for field emission displays. Moreover, our process can easily be tuned to control the extent of functionalization on carbon nanospheres which would be useful in the development of miniaturized devices for commercial applications. The smaller size of emitting area along with the possibility of modulating their co-operative interaction promises remarkable characteristics for development of futuristic field of microelectronics and emission based devices.

5.6. References

1. Smith, A. M.; Mohs, A. M.; Nie, S. *Nat Nanotechnol.* **2009**, *4,* **56.**
2. Stewart, M. E.; Anderton, C. R.; Thompson, L. B.; Maria, J.; Gray, S. K.; Rogers, J. A.; Nuzzo, R. G. *Chem. Rev.* **2008,** *108*, **494.**
3. (a) Iijima, S. *Nature* **1991**, *354,* **56**. (b) Wildgoose, G. G.; Banks, C. E.; Compton, R. G. *Small* **2006,** *2,* **182**. (c) Lin, Y.; Taylor, S.; Li, H.; Shiral Fernando, K. A.; Qu, L.; Wang, W.; Gu, L.; Zhou, B.; Sun, Y. P. *J. Mater. Chem.* **2004,** *14,* **527.**

4. (a) Tans, S. J.; Devoret, M. H.; Dai, H. J.; Thess, A.; Smalley, R. E.; Geerligs, L. J.; Dekker, C. *Nature* **1997**, *386,* **474.** (b) Chen, J.; Perebeinos, V.; Freitag, M.; Tsang, J.; Fu, Q.; Liu, J.; Avouris, P. *Science* **2005,** *310,* **1171.** (c) Wang, C.; Waje, M.; Wang, X.; Tang, J. M.; Haddon, R. C.; Yan, Y. S. *Nano Lett.* **2004,** *4,* **345.**
5. Bachtold, A.; Hadley, P.; Nakanishi, T.; Dekker, C. *Science* **2001**, *294,* **1317**. (b) Lordi, V.; Yao, N.; Wei, J. *Chem. Mater.* **2001,** *13,* **733.** (c) Planeix, J. M.; Coustel, N.; Coq, B.; Brotons, V.; Kumbhar, P. S.; Dutartre, R.; Geneste, P.; Bernier P.; Ajayan, P. M. *J. Am. Chem. Soc.* **1994,** *116,* **7935**. (d) Baughman, R. H.; Cui, C. X.; Zakhidov, A. A.; Iqbal, Z.; Barisci, J. N.; Spinks, G. M.; Wallace, G. G.; Mazzoldi, A.; De Rossi, D.; Rinzler, A. G.; Jaschinski, O.; Roth, S.; Kertesz, M. *Science* **1999,** *284,* **1340**. (e) Baughman, R. H.; Zakhidov, A. A.; de Heer, W. A. *Science* **2002,** *297,* **787.** (f) Fan, S.; Chapline, M. G.; Franklin, N. R.; Tombler, T. W.; Cassell, A. M.; Dai, H. *Science* **1999,** *283,* **512.** (g) Zhao, Q.; Gan, Z. H.; Zhuang, Q. K. *Electroanalysis* **2002**, *14,* **1609.** (h) Kong, J.; Franklin, N. R.; Zhou, C. W.; Chapline, M. G.; Peng, S.; Cho, K. J.; Dai, H. *Science* **2000,** *287,* **622.** (i) Yang, C.-M.; Kanoh, H.; Kaneko, K.; Yudasaka, M.; Iijima, S. *J. Phys. Chem. B* **2002,** *106,* **8994.** (j) Wong, S. S.; Joselevich, E.; Woolley, A. T.; Cheung, C. L.; Lieber, C. M. *Nature* **1998,** *394,* **52.** (h) Saito, R.; Dresselhaus, G.; Dresselhaus, N. *Physical Properties of Carbon Nanotubes, Imperial College, London,* **1998**.
6. (a) Banerjee, S.; Wong, S. S. *Nano Lett.* **2002,** *2,* **195**. (b) Cho, N.; Choudhury, K. R.; Thapa, R. B.; Sahoo, Y.; Ohulchanskyy, T.; Cartwright, A. N.; Lee, K. S.; Prasad, P. N. *Adv. Mater.* **2007,** *19,* **232.** (c) Moghaddam, M. J.; Taylor, S.; Gao, M.; Huang, S. M.; Dai, L. M.; McCall, M. J. *Nano Lett.* **2004,** *4,* **89**.
7. (a) Akdim, B.; Kim, S. N.; Naik, R. R.; Maruyama, B.; Pender, M. J.; Pachter, R. *Nanotechnology* **2009**, *20,* **355705**. (b) Peng, X.; Chen, J.; Misewich, J. A.; Wong, S. S. *Chem. Soc. Rev.* **2009,** *38,* **1076.**

8. (a) Choi, H. C.; Shim, M.; Bangsaruntip, S.; Dai, H. J. *J. Am. Chem. Soc.* **2002,** *124,* **9058.** (b) Kong, B. S.; Jung, D. H.; Oh, S. K.; Han, C. S.; Jung, H. T. *J. Phys. Chem. C* **2007,** *111,* **8377.** (c) Qu, L. T.; Dai, L. M. *J. Am. Chem. Soc.* **2005,** *127,* **10806**. (d) Qu, L. T.; Dai, L. M.; Osawa, E. *J. Am. Chem. Soc.* **2006,** *128,* **5523.** (e) Lee, Y.; Song, H. J.; Shin, H. S.; Shin, H. J.; Choi, H. C. *Small* **2005,** *1, 975.* (f) Gao, C.; Li, W. W.; Jin, Y. Z.; Kong, H. *Nanotechnology* **2006,** *17,* **2882.** (g) Cao, J. Y.; Du, C.; Wang, S. C. C.; Mercier, P.; Zhang, X. G.; Yang, H.; Akins, D. L. *Electrochem. Commun* **2007,** *9,* **735.** (h) Lu, X.; Imae, T. *J. Phys. Chem. C* **2007,** *111,* **2416**. (i) Banerjee, S.; Wong, S. S. *Chem. Commun.* **2004, 1866.** (j) Banerjee, S.; Wong, S. S. *J. Am. Chem. Soc.* **2003,** *125,* **10342.** (k) Robel, I.; Bunker, B. A.; Kamat, P. V. *Adv. Mater,* **2005,** *17,* **2458.**
9. (a) Yoon, B.; Wai, C. *J. Am. Chem. Soc.* **2005,** *127,* **17174**. (b) Klinke, A.; Delvigne, E.; Barth, J. V.; Kern, K. *J. Phys. Chem. B* **2005,** *109,* **21677. (c)** Fan, Y.; Burghard, M.; Kern, K. *Adv. Mater.* **2002,** *14,* **130.**
10 (a) Ye, X. R.; Lin, Y. H.; Wang, C. M.; Engelhard, M. H.; Wang, Y.; Wai, C. M. *J. Mater. Chem.* **2004,** *14,* **908**. (b) Rosencrance, S. W.; Burnham, J. S.; Sanders, D. E.; He, C.; Garrison, B. J.; Winograd, N.; Postawa, Z.; De Pristo, A. E. *Phys. Rev. B* **1995,** *52,* **6006.** (c) Giordano, R.; Serp, P.; Kalck, P.; Kihn, Y.; Schreiber, J.; Marhic, C.; Duvail, J. L. *Eur. J. Inorg. Chem.* **2003, 610.** (d) Tzitzios, V.; Georgakilas, V.; Oikonomou, E.; Karakassides, M.; Petridis, D. *Carbon* **2006,** *44,* **848.** (e) Star, A.; Joshi, V.; Skarupo, S.; Thomas, D.; Gabriel, J. P. *J. Phys. Chem. B* **2006,** *110,* **21014**.
11 (a) De Jonge, N.; Lamy, Y.; Schoots, K.; Oosterkamp, T. *Nature* **2002,** *420,* **393.** (b) de Heer, W. A.; Chatelain, A.; Ugarte, D. *Science* **1995,** *270,* **1179**. (c) Sharma, R. B.; Late, D. J.; Joag, D. S.; Govindaraj, A.; Rao, C. N. R. *Chem. Phys. Lett.* **2006,** *428*, **102.**

12 (a) Rakhi, R. B.; Reddy, A. L.; Shaijumon, M. M.; Sethupathi, K.; Ramaprabhu, S. *J. Nanoparticle Res.* **2008,** *10*, **179**. (b) Liu, A.; Kim, K. S.; Baek, J.; Cho, Y.; Han, S.; Kim, S. W. *Carbon* **2009**, *47,* **1158**. (c) Jeong, T.; Heo, J.; Lee, J.; Lee, S.; Kim, W.; Lee, H.; Park, S.; Kim, J. M.; Oh, T.; Park, C.; Yoo, J.; Gong, B.; Lee, N.; Yu, S. G. *Appl. Phys. Letts.* **2005**, *87*, **063112**.

13 (a) Bhardwaj, T.; Antic, A.; Pavan, B.; Barone, V.; Fahlman, B. D. *J. Am. Chem. Soc.* **2010,** *132*, **12556**. (b) Rao, C. V.; Cabrera, C. R.; Ishikawa, Y. *J. Phys. Chem. Lett.* **2010,** *18*, **2622**. (c) Kauffman, D. R.; Sorescu, D. C.; Schofield, D. P.; Allen, B. L.; Jordan, K. D.; Star, A. *Nano Lett.* **2010,** *10*, **958**.

14 (a) Ziegelbauer, J. M.; Gatewood, D.; Gull, A. F.; Guinel, M. J.; Ernst, F.; Ramaker, D. E.; Mukerjee, S. *J. Phys. Chem. C* **2009,** *113,* **6955**. (b) Zahmakiran, M.; Zkar, S. *Inorg. Chem.* **2009,** *48*, **8955**.

15 (a) Banerjee, S.; Wong, S. S. *Nano Lett.* **2002,** *2*, **49**. (b) Niyogi, S.; Hamon, M. A.; Hu, H.; Zhao, B.; Bhowmik, P.; Sen, R.; Itkis, M. E.; Haddon, R. *Acc. Chem. Res.* **2002**, *35,* **1105**. (c) Wang, Y.; Iqbal, Z.; Mitra, S. *J. Am. Chem. Soc.* **2006,** *128*, **95**. (d) Peng, H.; Alemany, L. B.; Margrave, J. L.; Khabashesku, V. N. *J. Am. Chem. Soc.* **2003,** *125*, **5174**. (e) Wang, Y.; Iqbal, Z.; Mitra, S. *J. Am. Chem. Soc.* **2006,** *128*, **95**. (f) Zhu, J.; Kim, J.; Peng, H.; Margrave, J. L.; Khabashesku, V. N.; Barrera, E. V *Nano Lett.* **2003,** *3*, **1107**.

16 *(a) NIST Vibrational Spectroscopy Database (via Internet: http://srdata.nist.gov/vb.).* (b) Pinchas, S.; Laulicht, I. *Infrared Spectra of Labeled Compounds, Academic Press: London,* **1971; Chapter 9**.

17 Lee, C. J.; Park, J. H.; Huh, Y.; Lee, J. Y. *Chem. Phys. Lett.* **2001,** *343,* **33**.

18 Chiang, I. W.; Brinson, B. E.; Huang, A. Y.; Willis, P. A.; Bronikowski, M. J.; Margrave, J. L.; Smalley, R. E.; Hauge, R. H. *J. Phys. Chem. B* **2001**, *105,* **8297**.

19 (a) Rao, A. M.; Eklund, P. C.; Bandow, S.; Thess, A.; Smalley, R. E. *Nature* **1997,** *388,* **257**. (b) Bubert, H.; Haiber, S.; Brandl, W.; Marginean, G.; Heintze, M.; Brüser, V. *Diam. Rel. Mater.* **2003**, *12*, **811**.

20 (a) Ebbesen, T. W.; Hiura, H.; Bisher, M. E.; Treacy, M. M. J.; Shreeve-Keyer, J. L.; Haushalter, R. C. *Adv. Mater.* **1996**, *8,* **155.** (b) Ang, L. M.; Hor, T. S. A.; Xu, G. Q.; Tung, C. H.; Zhao, S.; Wang, J. L. S. *Chem. Mater.* **1999**, *11,* **2115.** (d) Ye, X. R.; Lin, Y. H.; Wai, C. M. *Chem. Commun.* **2003, 642.**

21 Georgakilas, V.; Gournis, D.; Tzitzios, V.; Pasquato, L.; Guldi, D. M.; Prato, M. *J. Mater. Chem.* **2007**, *17,* **2679**. (b) Menon, M.; Andriotis, A. N.; Froudakis, G. E. *Chem. Phys. Lett.* **2000,** *320,* **425.** (b) Lee, K. Y.; Kim, M.; Lee, Y. W.; Lee, J.-J.; Han, S. W. *Chem. Phys. Lett.* **2007,** *440,* **249.**

22 Worsley, K. A.; Kalinina, I.; Bekyarova, E.; Haddon, R. C. *J. Am. Chem. Soc.* **2009,** *131,* **18153**.

23 (a) Nguyen, K. T.; Shim, M. *J. Am. Chem. Soc.* **2009**, *131*, **7103**. (b) Lee, S. Y.; Choi, W. C.; Jeon, C.; Park, C.; Yang, J. H.; Kwon, M. H. *Appl. Phys. Lett.* **2008,** *93,* **103101.**

24 Sathe, B. R.; Kakade, B. A.; Mulla, I. S.; Pillai, V. K.; Late, D. J.; More, M. A.; Joag, D. S. *App. Phys. Lett.* **2008,** *92,* **253106.**

25 Shrestha, S.; Choi, W. C.; Song, W.; Kwon, Y. T.; Shrestha, S. P.; Park, C.; *Carbon* **2010,** *48,* **54.**

26 Fang, X.; Bando, Y.; Gautam, U.; Ye, C.; Golberg, D. *J. Mater. Chem.* **2008,** *18,* **509.**

CHAPTER 6

Conclusions and Future Prospects

This chapter deals with the major conclusions of the present study with respect to the shape-selective synthesis of Rh nanostructures, heterostructure formation of Rh nanoclusters with carbon nanotubes and their effects on structure-property relationship. Related promising developments and daunting challenges in this broad area are also discussed to map the futuristic applications of these fascinating nanomaterials in view of their fundamental and technological interest. Finally, some of the future prospects and precautions for processing Rh nanostructures and contiguous materials are also explained within the broad perspective of nanotechnology and its societal impacts for device applications. It also outlines several limitations of both nanostructured Rh as well as their hybrid materials along with few suggestions. Despite these limitations, the results of present study are believed to be useful to understand several fundamental phenomena of metal nanostructures for fabricating nanoscale devices in future.

High aspect ratio nanomaterials of Rh has emerged as a major theme in contemporary nanotechnology due to its immense application possibilities. Rhodium is an especially promising nanomaterial due to its remarkable electronic, electrochemical, optical, and catalytic properties. Despite its high cost, the manipulation of the electronic structure of Rh at the nanoscale has strong implications on the development of high-throughput Rh nanostructures for enhancing their activity for potential applications. Accordingly, the present thesis outlines the potential utility of several attempts for the synthesis of various Rh nanostructures by solution, electrochemical and chemical vapour deposition approaches along with some of their respective merits and demerits over each others. Rh in reduced dimensions is an excellent material for the efficient transport of electrons/phonons and optical excitations, although the ultimate potential of these nanostructures is strongly dependent upon the ability to precisely control their morphology (which include size, shape and dimensionality), composition, crystal structure and phase purity at subnanometer length scale. As this unique physical and chemical properties could be controlled remarkably by tuning their morphology characteristics, unraveling the critical parameters responsible for achieving the size and shape selective synthesis of Rh is critical to the function and more importantly for integrating in many nanoscale devices. Despite the immense knowledge in this area, the synthesis of these nanostructures with high selectivity for special applications is still in an early stage of development. A number of challenges such as difficulty of precisely controlling the aspect ratio, lack of selectivity and uniformity in size distribution, difficulties of scale-up, cost effectiveness remain to be addressed before these materials to find viable applications. A thorough understanding of the growth mechanism is a key step towards achieving selective growth of nanostructures, which is of particular significance both for the creation of new materials as well as for the fabrication of devices using these structures. The main objectives of the present investigation have been formulated to address some of these important challenges related to the synthesis, characterization and possible applications (especially in electrocatalysis and field emission) of high aspect ratio nanostructures of Rh. This system is selected because of its

outstanding role as multifunctional catalysts in many industrial applications, including fuel cells, in addition to other more recent use in plasmonics, molecular electronics, field emission and so on.

Accordingly, chapter 1 demonstrates a critical review of the synthesis of Rh nanostructures using various methods including chemical, electrochemical and gas phase deposition strategies. Since, only limited progress has been achieved in synthesizing these materials with precise morphological control and better shape distribution, that too often in the presence of different types of capping molecule/surfactants, we have demonstrated the potential utility of polyfunctional molecules to synthesize high aspect ratio (nanochains, nanorods, nanoneedles) Rh nanostructures and other nonspherical nanostructures in Chapter 2. At the end of this chapter, the electro-catalytic activity of these nanostructures has also been explored towards formic acid oxidation, as an important test reaction for micro-fuel cells. Although, the presence of different types of capping molecule/surfactants is a critical parameter for achieving the shape-selective synthesis of these nanostructures, their presence could drastically hamper their potential benefits to some extent.

To overcome the inherent limitations of organic molecule capped structures, while keeping the objective to achieve the shape selective synthesis of Rh nanostructures for various applications, we demonstrate the potential utility of galvanic displacement approach for the synthesis of highly oriented nanostructures of Rh with Al as a sacrificial material through micro-galvanic cell formation in chapter 3. Tunable surface plasmon resonance (SPR) of these nanosturctures has been illustrated based on their surface roughness. Further, the role of the applied potential, concentration of Rh source, pH, temperature, presence of capping molecules and their effect on the diffusion of reactant (Rh^{3+}) and product (Rh^{0}) species toward and away from the surface of the Al has been elucidated towards the evolution of unique nanostructures of Rh. At the end of this chapter we have also compared the electrocatalytic performance of different anisotropic morphologies of Rh towards formaldehyde oxidation reaction, and these results are relevant for developing new anode materials in fuel cell technology.

Apart from the shape and monodispersity of nanostructures, a precise control of their crystallographic orientation is also a determining factor for selectivity and hence modulation of these planes of nanostructures is significant for the development of molecular-scale electronic devices, emitters for field emissions, selective catalytic reactions etc. However, only a limited progress has been made on the synthesis of oriented, capping free metallic nanostructures for various applications using above explained chemical and electrochemical synthetic approaches. This limitation arises mainly because of the challenges due to the presence of surface stabilizer, their separation, purification and recycling aspects. However, the presence of external capping molecules on the surface of nanostructures may alter their loading on electrode surface, which in turn could hamper some of their activity. In this context, we have demonstrated in chapter 4, the utility of chemical vapor deposition (CVD) approach to overcome the above mentioned problems of these approaches for producing high quality Rh nanostructures with different orientations like cubes, pyramids and hexagons. Further, a comparative electrocatalytic performance of these nanostructures towards formic acid oxidation has been correlated with their crystallographic orientation obtained from X-ray diffraction analysis. More importantly, four probe conductivity measurements reveal a systematic variation in the conductivity with their respective shapes. Field emission behavior from hexagonal Rh nanostructures has been discussed at the end as a typical example, in order to demonstrate the utility of these findings for applications. For example, the presence of sharp tips of the nanopotrusions with a higher areal density is indicated to be responsible for a stable current density along with their excellent current and mechanical stability toward ions bombardment.

It is well known that hybrid nanostructures are expected to show remarkable properties through co-operative interactions especially for desired applications. For example, Li and coworkers have recently reported Au-based hybrid magnetic nanostructures, including Au-Co core-shell and Au-Ni spindly nanostructures for tunable magnetic features. Carbon nanotubes and Rh are already considered to be good emitters, and these desirable properties may be further enhanced by making use of the electronic

properties (work function and the structure of density of states). As a result of this we have demonstrated in chapter 5, a unique hetero-junction formation based on the controlled decoration of Rh-nanospheres (2.3 nm) on acid functionalized MWNTs (~150 nm) with their enhanced field emission behavior compared to that of Rh nanospheres prepared by same method and also individual MWCNTs.

Thus the main results of this thesis unravel few issues related to the shape selective synthesis of Rh nanostructures, their heterostructures with carbon nanotubes along with their structure-property relationship and related effects on various properties. In the entire thesis, we have focused mainly on Rh and their carbon nanotube based heterostructures because of their outstanding role as multifunctional catalysts in many applications, particularly in fuel cells and field emission based devices. We have explored the uniqueness of plane oriented growth of Rh synthesized by chemical vapour deposition without the assistance of surfactants/capping molecule and also foreign species which is beneficial from their application point of view, in terms of blights of contamination. More importantly, we have demonstrated how the properties unique to nanostructures vary with morphology by considering their application in electrocatalysis, in a semi-quantitative manner.

Thus the major accomplishments of the present investigations could be summarized as follows-

- Fabrication of high aspect ratio nanostructures of Rh along with their assemblies using polyfunctional molecules.
- Preparation of oriented nanosturctures of Rh including, cubes, pyramids, hexagons etc., by chemical vapour deposition approach.
- Synthesis of Rh nanostructures by galvanic displacement approach with Al for their tunable optical features.
- Synthesis and functionalization of carbon nanotubes followed by their heterostructure formation with Rh nanoclusters.

- Comparative formaldehyde and formic acid oxidation studies of these Rh nanostructures with commercial Rh and their investigations based on the structure-property correlations of interest to fuel cells.
- Enhanced field emission studies form Rh nanostructures and Rh/MWNT heterostructures.

However, there are a number of unsolved issues that remain to be addressed before these materials could be exploited commercially. Even though, chemical vapor deposition allows a precise control of morphology without the aid of any surfactants/capping molecule, the nanostructures synthesized through reduction often proceed through the modulation of temperature of system which makes surface passivation through the oxide formation which in turn retards their reactivity. For example, in electrocatalysis, better performance of a catalyst requires the absence of surface passivating agents (capping molecules, surface oxide impurities) [5]. More importantly, the nanostructures which are used as catalysts should have high uniformity in size and shape distribution to precisely quantify the catalytic influence. As a result, much more efforts are essential to resolve these issues before realizing their complete potential. In addition, several existing gaps in our understanding need to be filled by important investigations focusing on structure-property correlations. For example, to envisage the electronic application of these metallic, one dimensional as well as hybrid morphologies, understanding of several fundamental and fascinating issues about the electronic properties such as the coherence of extended states, single electron behavior, difficulty of having individually addressable electronic contacts, the role of finite size and symmetry breaking and related phenomena is essential [6].

Furthermore, there are several daunting tasks like addressing the environmental concern and societal impact of these materials since very little is known about the long term impact of these materials especially how they behave inside living organisms. Based on previous studies on asbestos and chrysolite, we expect many of these nanostructures to be perhaps environmentally hazardous. Researchers dealing with these types of nanostructures should take great caution while handling. In this regard, a systematic, but

rigorous evaluation on how these nanostructures will impact our environment and health is urgently needed.

Our novel approaches, for the shape selective synthesis of Rh nanostructures and its processing offer an unprecedented opportunity to obviate many limitations of currently employed materials, opening new possibilities of manipulating the properties and stability to give enhanced performance. Despite steady progress during the couple of years, several key limitations need to be kept in mind before these results could commercially be exploited, as illustrated bellow:

- The understanding of the nucleation, growth kinetics and thermodynamics of these structures are necessary to resolve several fundamental issues related to the structural manipulation of these materials.
- Suitable methods to prepare shape selective nanostructures, organic-inorganic or inorganic-bio hybrid materials are to be developed, since they often have novel functions.
- Adequate strategies to realize high yield of Rh nanostructure, especially nanowires and nanotubes, must await further advances in synthesis (e.g., atomic layer deposition; ALD) and fabrication of devices with more accurate control.
- Magnetic properties of some of these Rh nanostructures have potential applications in various device fabrications, and these need to be considered further.
- A proper understanding of the role of commonly used materials for the building of nanostructures as well as the interface of nanoparticle/organic or biomolecules need to be evaluated. Since the toxicity is also expected to increase for nanomaterials compared to its bulk, these assessments may help to extend their applications in several social sectors.
- Assembling various shaped and high aspect ratio nanostructures in well defined domains to understand their coupled optical, electrical or magnetic response is still a daunting challenge.

- More details on both the preparation and characterization of the heterostructures, core shell and alloys of Rh with other materials are needed to prove their potential applications.
- Recycling potential of these nanostructured electrocatalyst has not been pursued, which is important for exploiting their utility in practical applications.

Since, some of these disadvantages restrict the full potential of commercial applications of these Rh based structures, further work is essential to alleviate some of these problems. Despite these limitations, the present approach offers enough scope to design different shaped nanostructures through a simple route with better reproducibility. In addition to the shape-dependent electrocatalysis, the present approach is also believed to unravel many shape-dependent fundamental phenomena of these nanomaterials. More significantly since these methods of shape-tuning are very general, we hope that apart from high aspect ratio nanostructures this could be extended to the synthesis of other potential anisotropic metallic and semiconducting nanostructures.

References:

1. Bhushan, B. (Ed.) *Springer handbook of nanotechnology* **2004**, Spinger-Verlag Berlin Heidelberg New York.
2. Bard, A. J. *Integrated Chemical Systems: A Chemical Approach to Nanotechnology* **2004,** Wiley, New York.
3. Roco, M. C., Bainbridge, W. S., *Societal Implications of Nanoscience and Nanotechnology; Eds. National Science Foundation Report*: **2001**.Arlington, VA; Kluwer Academic Publishers: Boston, MA.
4. Dresselhaus, M. S.; Dresselhaus, G.; Avouris, Ph. (Eds.) *Carbon Nanotubes; Synthesis, Structure, Properties and Applications* **2001** (Springer-Verlag Berlin Heidelberg New York).
5. Buatier, F.; Toma, E. A.; Molle, E. S.; Lizzit, E. L.; Petaccia, E. A. *Nanoscale Res. Lett.* **2007,** *2,* **251**.
6. Somorjai, G.A. *Introduction to Surface Chemistry and Catalysis* **1994** (Wiley, New York).
7. Crucq, A. (ed.), *Catalysis and Automotive Pollution Control II, Studies in Surface Science and Catalysis*, **1991,** *71*(Elsevier, Amsterdam).
8. Martensson, N.; Nilsson, A. *Springer Series in Surface Science,* **1994,** *35* ed. by W. Eberhardt (Springer-Verlag, Berlin).
9. Murray, C. B.; Kagan, C. R.; Bawendi, M. G. *Annu. Rev. Mater. Sci.* **2000,** *30,* **545**.
10 Saito, R.; Dresselhaus, G.; Dresselhaus, N. *Physical Properties of Carbon Nanotubes*, Imperial College, London, **1998**.

List of Publications

1. *Enhanced Electrocatalytic Performance of Interconnected Rh Nano-chains towards Formic Acid Oxidation* **Bhaskar R. Sathe**, Beena K. Balan, Vijayamohanan K. Pillai *Energy and Environmental Science* ***(In press, 2010).***

2. *Synthesis of Rh-carbon Nanotube based Heterostructures and Their Enhanced field emission characteristics* **Bhaskar R. Sathe,** Bhalchandra A. Kakade, Ajay Kushwaha, Mohammed Aslam, Vijayamohanan K. Pillai *Chem. Comm.* **2010,** 46, 5671.

3. *Tunable Optical Features from Self-organized Rhodium Nanostructures* **Bhaskar R. Sathe**, Beena K. Balan, Vijayamohanan K. Pillai *Appl. Phys. Letts.* **2010**, 96, 233102.

4. *Effect of Fe_3O_4 on Morphology of Fe–SnO_2 Hyperbranched Heterostructures* **Bhaskar R. Sathe,** Pravin S. Walke, Imtiaz S. Mulla, Vijayamohanan K. Pillai *Chem Phys Letts.* **2010**, 493, 121.

5. *Preparation and Characterization of Rh Nanostructures through the Evolution of Microgalvanic Cells and Their Enhanced Electrocatalytic Activity for Formaldehyde Oxidation* **Bhaskar R. Sathe**, Dhanraj B. Shinde, Vijayamohanan K. Pillai *J. Phys.Chem. C* **2009**, 113, 9316.

6. *A Facile, Single-step Route to Synthesize Sb-doped SnO_2 Nanowires and Hyper-branched Structures* **Bhaskar R. Sathe,** Pravin Walke, Vivek J. P., Mrudula Patil, Imtiaz S Mulla, Vijayamohanan K. Pillai, *Sci of Adv. Maters.* **2009,** 1, 38.

7. *Near-Complete Phase Transfer of Single-Wall Carbon Nanotubes by Covalent Functionalization using Oxalyl Chloride* Bhalchandra A. Kakade, Sanjay D. Patil, **Bhaskar R. Sathe,** Suresh P. Gokhale, Vijayamohanan K. Pillai *J. Chem. Sci.* **2009,** 120, 599.

8. *Development of In-doped SnO_2 nanowire arrays and its field emission* Ashok Bhise, Dattatray Late, **Bhaskar R. Sathe**, D. S. Joag, I. S. Mulla, Vijayamohanan K. Pillai *J. Surface Science* **2009,** 11, 114 **.**

9. *Enhanced Field Emission from Hexagonal Rhodium Nanostructures* **Bhaskar R. Sathe,** Bhalchandra A. Kakade, Imtiaz S. Mulla, Vijayamohanan K. Pillai, Dattatray J. Late, Mahendra A. More, Dilip S. Joag *Appl. Phys. Letts.* **2008,** 92, 253106.

10. *Electrochemical Sensing of Sulphur Dioxide: A Comparison using Dodecanethiol and Citrate Capped Gold Nanoclusters* **Bhaskar R. Sathe**, Mandar S. Risbud, Imtiaz S. Mulla and Vijayamohanan K. Pillai *J. Nanosci. and Nanotechnol.* **2008,** 8, 3184.

11. *Selective Cis-Dihydroxylation of Olefins using Recyclable Homogeneous Molybdenum Acetylide Catalyst* Ankush V. Biradar, **Bhaskar R. Sathe,** Mohan K. Dongare, Shubhangi B. Umbarkar *J. Mole. Cats. A* **2008,** 285, 111.

12. *High-Purity Synthesis of Scrolled Mats of Multi-walled Carbon Nanotubes using Temperature Modulation* Bhalchandra A. Kakade, Hatem Allouche, Subhramania Mahima, **Bhaskar R. Sathe,** Vijayamohanan K. Pillai *Carbon* **2008,** 46, 567.

13. *Copper Phthalocyanine Films Deposited by Liquid Interface Recrystallization Technique (LLIRCT)* K. R. Patil, S. D. Sathaye, R. Hawaldar, **Bhaskar R. Sathe,** A. B. Mandale and A. Mitra *J. Colloid Interface Sci.* **2007,** 315, 747.

14. *Template-Assisted Synthesis of Ruthenium Oxide Nanoneedles: Electrical and Electrochemical Properties* Mahima Subhramannia, Beena K. Balan, **Bhaskar R. Sathe**, Imtiaz S. Mulla and Vijayamohanan K. Pillai *J. Phys. Chem. C* **2007,** 111, 16593.

15. *Surface State-mediated Electron Transfer at nanostructured ZnO multipod/Electrolyte Interfaces* Meera Parthasarathy, Niranjan S. Ramgir, **Bhaskar R. Sathe**, Imtiaz S. Mulla, Vijayamohanan K. Pillai *J. Phys. Chem. C* **2007**, 111, 13092.

16. *Quantized Double Layer Charging Behavior of* $Rh_{2057}(TDA)_{321}$ *Clusters using Differential Pulse and Cyclic Voltammetry* Bhalchandra A. Kakade, Shashidhar Shintri, **Bhaskar Sathe**, S. B. Halligudi, and Vijayamohanan K. Pillai *Adv. Mater.* **2007,** 19, 272.

17. *Highly Sensitive Nanostructured Platinum Electrocatalysts for CO Oxidation: Implications for CO Sensing and Fuel cell Performance* **Bhaskar R. Sathe,** Mandar S. Risbud, Sanjay Patil, K. S. Ajayakumar, R. C. Naik, I. S. Mulla, Vijayamohanan K. Pillai *Sensors and Actuators: Physical* **2007,** 138, 1.

Erratum